Development of Supramolecular Channels for the Selective Transport of Chloride via Hydrogen and Halogen Bond Interactions

विद्या वाचस्पति की
उपाधि की अपेक्षाओं की आंशिक पूर्ति में प्रस्तुत शोध प्रबंध

A thesis submitted in partial fulfillment of the requirements of the degree of Doctor of Philosophy

द्वारा / By

छात्र का नाम / रश्मि शर्मा Rashmi Sharma)

पंजीकरण सं. / Registration No.: 20163468

शोध प्रबंध पर्यवेक्षक / Thesis Supervisor: Prof. Pinaki Talukdar

भारतीय विज्ञान शिक्षा एवं अनुसंधान संस्थान पुणे
INDIAN INSTITUTE OF SCIENCE EDUCATION AND RESEARCH PUNE

2023

Dedicated To

My Family...

CERTIFICATE

Certified that the work incorporated in the thesis entitled "***Development of Supramolecular Channels for the Selective Transport of Chloride via Hydrogen and Halogen Bond Interactions***" submitted by **Ms. Rashmi Sharma** was carried out by the candidate, under my supervision. The work presented here or any part of it has not been included in any other thesis submitted previously for the award of any degree or diploma from any other university or institution.

Date: 10 June 2023

Prof. Pinaki Talukdar
(Research Advisor)

DECLARATION

I declare that this written submission represents my ideas in my own words and where other's ideas have been included; I have adequately cited and referenced the original sources. I also declare that I have adhered to all principles of academic honesty and integrity and have not misinterpreted or fabricated any idea/data/fact/source in my submission. I understand that violation of above will cause for disciplinary action by the Institute and can also evoke the penal action from the sources which have thus not been properly cited or from whom proper permission has not been taken when needed.

Date: 10 June 2023

Rashmi Sharma

Acknowledgment

My Ph.D. tenure has been a journey of new learning in science and as a person, which has shaped me in terms of intellectual reasoning, independence, and self-assurance. This thesis would not have been possible without the help and support of the many people I have had the pleasure of meeting throughout my time in IISER Pune.

First and foremost, I would like to give my sincerest appreciation to Prof. Pinaki Talukdar for his exemplary guidance, great ideas, and generous provision of research independence. I would like to take this chance to express my gratitude to him for providing me with the chance to work in such a well-equipped research facility. His interest in chemistry and his upbeat outlook have been great sources of inspiration to me over the years of our conversations. I learned a lot about research and critical thinking from him, and he has always been optimistic about my potential as a researcher. I appreciate his unwavering belief in me and his unwavering support through the challenging period.

My heartfelt gratitude goes out to Prof. Harinath Chakrapani sir (Department of Chemistry, IISER Pune) and Prof. Vaishali Shinde (Department of Chemistry, Pune University) ma'am, members of my Research Advisory Committee (RAC), for their constructive suggestions and time during our meetings. Thanks to these suggestions I was able to improve the design and execution of my research experiments. I am really grateful to them for taking the time, effort, and providing such encouraging feedback.

Being a part of the Indian Institute of Science Education and Research (IISER), Pune, is an incredible privilege. I would like to express my gratitude to everyone associated with IISER Pune, and particularly to those who worked tirelessly to create this great institution, home to advanced laboratories and other research resources. At the Indian Institute of Science Education and Research (IISER), Pune, India, I would like to express my gratitude to both the outgoing and incoming directors, Prof. K. N. Ganesh and Prof. Jayant Udgaonkar, respectively. Prof. M. Jayakannan, Prof. H. N. Gopi, and Prof. Nirmalya Ballav, the former and current Chair of the Chemistry Department, as well as the entire department's professors and employees, have been tremendous resources to me. I was constantly impressed by the welcoming research environment at IISER Pune.

Most significantly, I'd like to acknowledge the contributions of my collaborators Amal Vijay from Prof. Arnab Mukherjee's lab at IISER Pune and Susmita Sarkar from Prof. Jagannath Mondal's lab at TIFR Hyderabad, without their help, this work would not have achieved the quality it has now.

Dr. C.V. Ramana (NCL, Pune), with whom I began my research career as a project assistant, has my deepest gratitude. The foundational research and laboratory training I have received has been greatly facilitated by Dr. Srinivas Kolluru (NCL, Pune). Working with them always gave me a boost of confidence. What I picked up from them, practically and philosophically, will serve me well for the rest of my life. It was an honor to work under their direction.

I am grateful to the technical staff and assistants in the institute who ensured that the characterization instruments were always up and running. I appreciate the office staff from the department and the institute for their pleasant cooperation regarding administrative formalities. I thank all non-teaching and technical staff for their support, particularly Mr. Mayuresh Kulkarni, Mr. Mahesh Jadhav, Mr. Ganesh Dimbar, Mr. Sandip Kanade, Mr. Sanjay Kumar Meena, Dr. Dipali Dalvi, Ms. Sayalee Damle, Ms. Hemlata Phadke, Mr. T. S. Yathish, Ms. Megha Paygude, Mr. Sureshchandra Prajapat, Mr. Nitin Dalvi and Dr. Sandeep Mishra (NMR), Mr. Tushar, Mr. Ravindra Malothu (XRD).

It's my pleasure to thank all the former and present lab members; Dr. Tanmoy Saha, Dr. Arundhati, Dr. Sopan Shinde, Dr. Javid Ahmad Malla, Dr Harshali, Dr. Debashis, Dr. Manzoor Ahmad, Avishikta, Anjana, Nihar, Arkajit, Anurag Naveen, Swati, Abhishek, Sandip, Akram, Ravi, Parappa, Paras, Kshitij, Ankit, Debarati, and Umesh for making my journey wonderful. It was indeed a great experience of working with them. I would especially like to thank Dr. Sopan, Dr. Tanmoy and Dr. Javid for constantly helping and guiding me during my tenure. Avishikta and Sandip, my lab buddies, are wonderful people who have been there for me through thick and thin. Having them as companions in and out of the lab has lightened the burden of my Ph.D. journey.

I wish to thank all my friends for their support and help at different stages of my life. I would like to thank all my batch-mates (PhD batch August-2016) especially, Subhajit, Ruma, Padmini, Sandhya, and Anand, wish all success in the future. I particularly wish to thank my friend Dr. Subhajit for his constant support in the lows and for celebrating achievements and being the encouragement throughout the Ph.D. journey. I would like to thank members of Prof. Sujit K. Gosh's group for their help in solving crystals. Being an integral part of Chemphilic Team -2019 as coordinator was indeed a memorable experience. I thank my friends in IISER and NCL, Prashant, Amit Sahu, Upendra, Mayank, Jayant, Shailendra, Deepak, Ravi, Sardha, Manish, Visakha, Uday, Simantani, Kunjan, Amit Yadav, Salam, Keerti, Rahul, Tumpa, Rashi, Isha, Suraj for their company during this Ph.D. tenure and helping me learn new things in

different aspects of life. I would especially like to thank my master's friends, Ankur, Neha, Naveen, Manish, and Pradeep, for always sticking by my side and enriching my life.

Prashant has been an incredible support system for me here in Pune, and I cannot express my gratitude enough. His unflagging support and lively conversation over ice creams provided the inspiration I needed to make it through the long journey.

For the fantastic and unforgettable occasions lived during my Ph.D., I would also like to thank my on-campus sports comrades from various teams. They have brightened some of the low points of my Ph.D. journey and made them easier to handle.

I am highly thankful to the Department of Science & Technology, DST-INSPIRE, Government of India, for my research scholarship and financial support during the course of my Ph.D. Moreover, I like to thank the Royal Society of Chemistry (RSC) for publishing several research articles produced during the course of my research as well as for giving permission for a reprint of copyrighted materials.

Finally, I want to express my deep appreciation to my family specially my mumma and papa for their unwavering love and support throughout the years. Despite coming from a rather traditional background, my parents have always encouraged me to follow my passions and supported me in realizing my goals, for which I will be eternally grateful. They have always prayed earnestly on my behalf, and I have no doubt that I would not be where I am today without their support. My brothers and sisters have always been my rock, and for that I am eternally grateful.

Rashmi Sharma

Table of Contents

A

α	Alpha
Å	Angstrom
abs	Absorbance
A^-	Anion
Aq.	Aqueous
Ar	Aromatic
Ac	Acetyl
ATP	Adenosine Tri-Phosphate

B

β	Beta
br	Broad singlet
BLM	Bilayer lipid membrane or Black lipid membrane

C

c	Concentration
Δ	Change in
Conc.	Concentration
Calc	Calculated
CCDC	Cambridge Crystallographic Data Centre
CF	Carboxyfluorescein
$CHCl_3$	Chloroform
CH_2Cl_2	Dichloromethane
$CDCl_3$	Deuterated chloroform
CH_3CN	Acetonitrile
CLC	Chloride channel
CLCA	Calcium-activated chloride channel
cm	Centimeter
CsCl	Cesium chloride

D

δ	Delta (Chemical shift)
°C	Degree Celsius
d	Diameter
d	Doublet
dd	Doublet of doublet
DFT	Density functional theory
DPhPC	2-diphytanoyl-*sn*-glycero-3-phosphocholine
DMSO	Dimethylsulfoxide
DMF	Dimethylformamide
DCM	Dichloromethane

E

EYPC	L-α-phosphatidylcholine from egg-yolk
EC_{50}	Effective concentration at half maximal activity
e.g.	*Exempli gratia*
em	Emission
EtOAc	Ethylacetate
EtOH	Ethanol
Et_3N	Triethylamine
EDTA	Ethylenediaminetetraacetic acid
EDC·HCl	1-(3-Dimethylaminopropyl)-3-ethylcarbodiimide hydrochloride
ESI	Electrospray ionization

F

F_t	Fluorescence intensity at time *t*
FCCP	Carbonyl cyanide-p-trifluoromethoxyphenylhydrazone

G

g	Gram
g	Corrected conductance
G	Free energy
G_{hyd}	Free energy of hydration

H

Hz	Hertz
h	Hour
HPTS	8-Hydroxypyrene-1,3,6-trisulfonate trisodium salt
HOBt	Hydroxybenotriazole
HEPES	4-(2-hydroxyethyl)-1-piperazineethanesulfonic acid
HCl	Hydrochloric acid
HPLC	High performance liquid chromatography
HRMS	High Resolution Mass Spectrometry

I

I_F	Normalized Fluorescence Intensity
IR	Infrared spectroscopy
ISE	Ion selective electrode

J

J	Coupling constant

K

k	Rate constant
kcal	kilocalorie
KBr	Potassium bromide

KCl	Potassium chloride
KOH	Potassium hydroxide

L

λ	Lambda
LAH	Lithium aluminium hydride
LiCl	Lithium chloride
LUV	Large unilamellar vesicle
logP	Partition Coefficient

M

m	Multiplet
M	Molar
μM	Micromolar
μL	Microliter
M.P.	Melting Point
MHz	Mega hartz
min	Minute(s)
max	Maximum
mg	Milligram(s)
MD	Molecular Dynamics
mol	Mole(s)
mmol	Millimole(s)
mM	Millimolar
mL	Milliliter
MeOH	Methanol
m/z	Mass to charge ratio

N

n	Hill coefficient

nm	Nanometer
nM	Nanomolar
NMR	Nuclear magnetic resonance
Na_2SO_4	Sodium sulfate
NaBr	Sodium bromide
NaCl	Sodium chloride
$NaClO_4$	Sodium perchlorate
NaF	Sodium fluoride
$NaNO_3$	Sodium nitrate
NaOAc	Sodium acetate
NaOH	Sodium hydroxide
NaSCN	Sodium thiocyanate
NaI	Sodium iodide

O

obs	Observed
ORTEP	Oak ridge thermal ellipsoid plot

P

pA	Picoampere
p	*para*
Ph	Phenyl
ppm	Parts per million
pS	Picosiemens

R

R	Ideal gas constant
ρ	Resistivity
RT	Room temperature

RbCl	Rubidium chloride

S

s	Second
SCXRD	Single Crystal X-ray diffraction

T

t	Triplet
td	Triplet of doublet
t	Time
T_x	Triton X-100
TBA	Tetrabutyl ammonium
TLC	Thin Layer Chromatography
THF	Tetrahydrofuran
TFA	Trifluoroacetic acid

U

UV	Ultra-violet

V

V_m	Membrane Potential
vis.	Visible
V	Volt
V_{rev}	Reversible Potential
Val	Valinomycin

W

wt.	Weight

X

X	Halogen
XB	Halogen bonding

Y

Y	Fractional fluorescence intensity

The thesis entitled **"Development of Supramolecular Channels for the Selective Transport of Chloride via Hydrogen and Halogen Bond Interactions"** comprises five chapters.

Synopsis

The fundamental objective of this thesis is to introduce artificial ion channel and to work on their development in terms of better activity and selectivity by incorporating different ways to mediate ion transport across the lipid bilayer. The research during my doctoral study was mainly focused on the design, synthesis, and characterization of biomimetic artificial ion channels which have shown remarkable ion transport capabilities and selectivity. In particular, this thesis mainly deals with the unimolecular or supramolecular architecture of artificial ion channels for the selective transport of chloride ions mediated via hydrogen bonds and halogen bonds. We have successfully developed new approaches that ensure the better activity and selectivity of these supramolecular architectures in the membrane phase. These studies would pave a new way for the development of synthetic ion transporters.

Initially, the ideal kind of substrate i.e., cholic acid was used to introduce a selectivity filter to tune the ion selectivity of the synthetic ion channel. Next, for the enhanced selectivity for chloride, we have incorporated multiple ion selectivity sites by employing bis-1,3-diol moiety for the self-assembly of the ion transporter. The above-mentioned systems were transported ion mediated via hydrogen bonding.

Further, we went ahead to explore the advantage of halogen bonding in the enhancement of ion transport activity. And to surprise the systems turn out to be very efficient with very low EC_{50} values showing how halogen bonding mediated ion transport systems can help in building more efficient synthetic ion channels. An interesting correlation between ion transport activity and lipophilicity was achieved by anion transport systems by utilizing monoiodo- and dihalo- moieties.

Chapter 1: Introduction to Membrane Transport

Lipid membranes of biological origin exhibit impermeability to solutes of high polarity and serve as protective barriers for cells and their organelles. The efficient functioning of cellular activities necessitates the exchange of polar solutes, including cations, anions, water, amino acids, ATP, and carbohydrates, across cellular membranes. Integral membrane proteins such as channels and carriers facilitate the selective transport of ions by overcoming the hydrophobic barriers present in phospholipid bilayer membranes. The selective ion transport process is

essential for maintaining various cellular functions such as cell proliferation, cellular signalling, pH regulation, and osmotic pressure regulation. This process plays a vital role in disseminating information contained within the cellular components. Significant attention has been directed towards investigating the structures and mechanisms of action of these entities, leading to the development of synthetic systems by chemists that mimic their natural counterparts. Chloride ion (Cl^-) is of paramount importance in human physiology, as it represents the predominant extracellular anion in the human organism. Various medical conditions such as Bartter's syndrome, osteopetrosis, Dent's disease, and cystic fibrosis have been associated with the pathophysiology of defective chloride channels. Nonetheless, the investigation of chloride ion transport mechanisms has been comparatively neglected in comparison to cation transporters, with regard to both naturally occurring and artificially produced compounds. Several designs have been proposed for the fabrication of ion channels utilising small organic molecules. The potential of these channels in selective chloride transport has been investigated, with a focus on the role of hydrogen bonding and halogen bonding interactions. The initial phase of the study involved the production of two distinct varieties of self-assembled supramolecular channels that incorporate hydrogen bonding interactions to facilitate the targeted transportation of chloride ions.

However, chloride ion transport systems have received less attention than cation transporters, both in terms of natural and synthesized molecules. We have presented a number of designs for fabricating ion channels based on small organic molecules and studied their applications in selective chloride transport aided by hydrogen bonding and halogen bonding interactions.

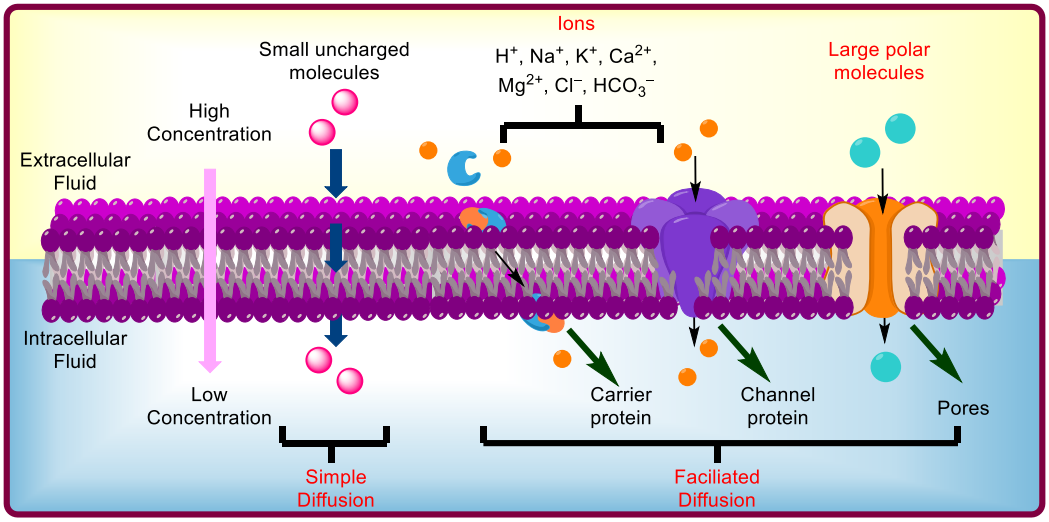

Figure 1. Schematic representation of transport process by ion carriers, ion channels, and ion pumps.

Chapter 2: Bis(cholyl)-based chloride channels with oxalamide and hydrazide selectivity filters

The responsiveness of biological membranes depends on the presence of selective ion channels. Because of their intricate structure and functioning, mimicking naturally existing ion channels is a difficult undertaking. We have found a means to mimic the intricate CLC channels, which will pave the path for the repair or replacement of broken chloride channels. To achieve this, we have designed a chloride-selective ion channel based on a bis(cholate)-based barrel stave assembly, with oxalamide and hydrazide as the core motif. To efficiently bind anions, we designed the synthetic ion channels **1a** and **1b**, which are based on bis(cholyl) and contain selectivity filers in the form of oxalamide and hydrazide linkers, respectively. The binding affinity, lipophilicity, and membrane permeability of the system were optimised by selecting two linkers. The half maximum activity (EC_{50}) values of the transporter were determined through dose-responsive ion transport tests to be 13.95 ± 0.193 μM, i.e., 27.7 mol %, relative to lipid content for isoform **1a**, and 7.95 ± 0.575 μM, i.e., 13.76 mol %, for isoform **1b**. Monitoring the efflux of chloride ion at varying concentrations using a lucigenin assay indicated that this ion channel, which was found to be the most active, is anion-selective. Further mechanistic investigations revealed the presence of an antiport mechanism (X^-/OH^-). The proposed transporter functions as a channel, not a carrier, as demonstrated by the conductance experiments (BLM). The creation of chloride-selective ion channels with a diameter of 3.67 ± 0.42 Å and a (P_{Cl^-}/P_{K^+}) = 1.69 was confirmed by tests of the conductance across a planar bilayer.

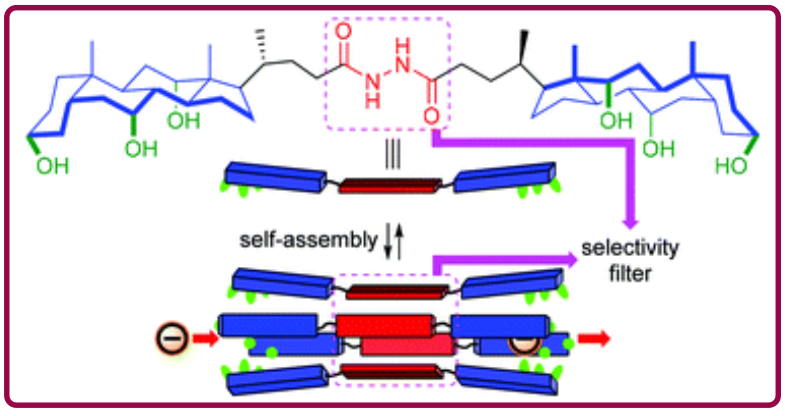

Figure 2. Structures (A) and self-assembly processes (B) of bis(chloyl)-linked oxalamide **1a** and hydrazide **1b** derivatives.

Chapter 3: Self-assembled anion channel formation by bis(1,3-propanediol)-linked meta - dipropynylbenzene-based small molecules

It is still a challenging task to create synthetic ion channels with recurring ion-recognition sites, particularly for small-molecule-based ion channels. As 1,3-diol moieties are known to produce various intermolecular and intramolecular H-bonding patterns that are utilized to develop hydrogels, channels, and polymers. In this chapter, we discussed the 1,3-di-hydroxyl moiety as a promising approach for the development of novel supramolecular ion channels with single-file ion recognition sites. We have designed two bis(1,3–di-hydroxyl)-linked molecules one with ester methylcyclohexane, **1** and another with amide methylcyclohexane, **2** substitutions to examine the effect of extra intermolecular H-bonding over channel activity, stability and selectivity for ions in lipid bilayer membrane. Half maximum activity (EC_{50}) values of 17.19 μM, i.e., 25.65 mol% relative to lipid content were obtained from dose-responsive ion transport studies of the transporter for **2**; however, the EC_{50} could not be calculated for **1** due to solubility difficulties (precipitation) at higher concentrations. Monitoring the efflux of chloride ion at different concentrations using a lucigenin test demonstrated that the most active ion channel, ion channel **2**, is anion selective. Mechanistic investigations added support for the existence of an X^-/OH^- antiport mechanism. The proposed transporter functions as a channel, not a carrier, as demonstrated by the conductance experiments (BLM). The formation of chloride-selective ion channels with a diameter of 3.56 ± 0.11 Å and a $(P_{Cl^-}/P_{K^+}) = 17.44$ was confirmed by investigations of the conductance across a planar bilayer.

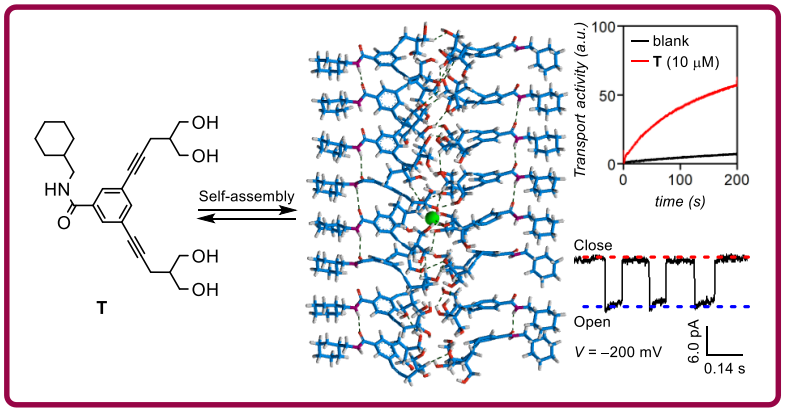

Figure 3. Self-assembly of individual monomers, **1** and **2** into barrel-rosette channel.

Chapter 4: Halogen bond-driven artificial Cl^- selective channel constructed from 5-iodoisophthalamide-based molecules

This chapter covers a system with an optimum balance between ion binding and ion releasing capabilities, allowing it to display adept ion channel behavior within a lipid bilayer. Small molecules that can self-assemble into a highly efficient and stable bilayer-based system have been synthesized to achieve high levels of ion selectivity. Compounds **1a-1c** with 5-iodo-isophthalamide substitutions were synthesized and characterized here. These molecules construct a supramolecular structure through a process of intelligent self-assembly. This complex aids in the selective transport of Cl^- ions through the membrane of lipid-based cells. Of the three transporters evaluated, transporter **1b** exhibited the highest level of ion transport efficiency, as evidenced by an EC_{50} value of 0.79 μM and a Hill coefficient of approximately 2, as determined through the utilization of a widely recognized HPTS assay. Comprehensive investigations have revealed the selectivity of **1b** towards Cl^-, and the primary mode of ion transport was identified as Cl^-/anion antiport. The transporter under consideration operates in the capacity of a channel, rather than a carrier, as evidenced by the results of the cholesterol assay and conductance experiments conducted on a bilayer lipid membrane. The study has verified the development of ion channels that are selective towards chloride, possessing a diameter of 3.81 ± 0.42 Å and a (P_{Cl^-}/P_{K^+}) ratio of 1.83. This was achieved through the examination of conductance across a planar bilayer. The aforementioned studies are expected to offer appealing methodologies for the development of effective ion channel systems with selectivity towards chloride ions.

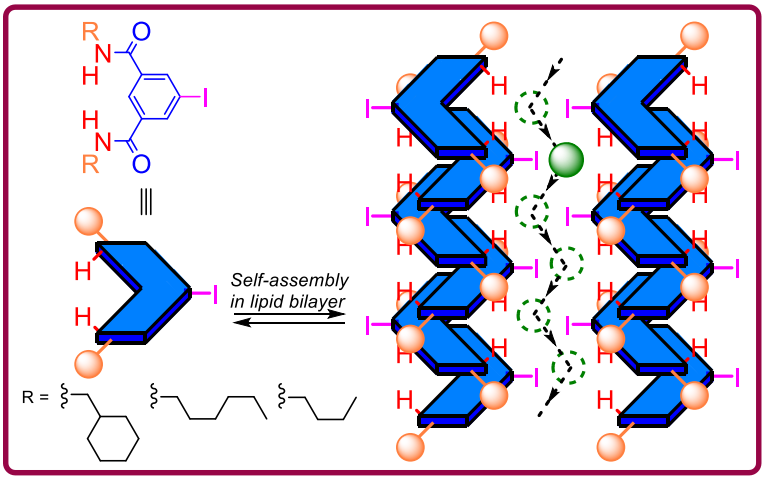

Figure 4. Chemical structure of compounds **1a-1c** and possible self-assembly in the lipid bilayer membrane.

Chapter 5: Transmembrane Cl^- selective channel by meta directed halogen bond donors

The special chemical properties of halogens are widely used in compounds available on the market to enhance or provide brand-new functions. The use of halogens has significantly increased in modern medical chemistry. Their increased lipophilicity, which raises cellular permeability, is to blame for this. We have successfully synthesized **1a-1c** in anticipation of improving the viability of artificial ion transporters to replace defective ones. Among other derivatives, transporter **1a** (diiodo-based) demonstrated the most effective ion transport activity (EC_{50} = 0.65 μM and Hill coefficient 4). The assembly of **1a** through I-carbonyl interaction is seen in the single-crystal X-ray structure, with the remaining iodine pointing into the cavity. The major transport mechanism for **1a** was identified by in-depth mechanistic research as the channel-mediated anion antiport mechanism as studied by cholesterol assay and planar bilayer conductance studies. The conductance study across planar bilayer has confirmed the development of ion channels that are selective towards chloride ions. These ion channels have a diameter of 3.68 ± 0.12 Å and exhibit a (P_{Cl^-}/P_{K^+}) ratio of 4.07.

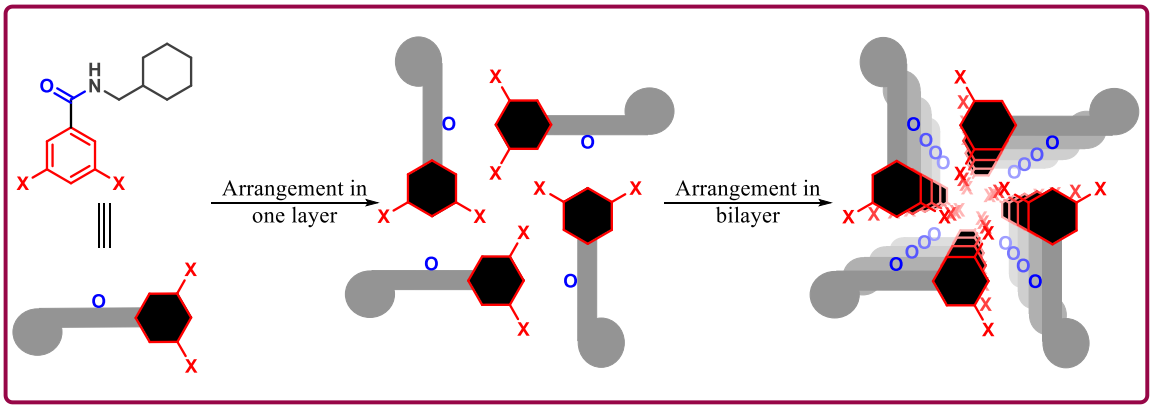

Figure 5. Chemical structure of compounds **1a-1c** and possible self-assembly in the lipid bilayer membrane.

Chapter 1

Introduction to Membrane Transport

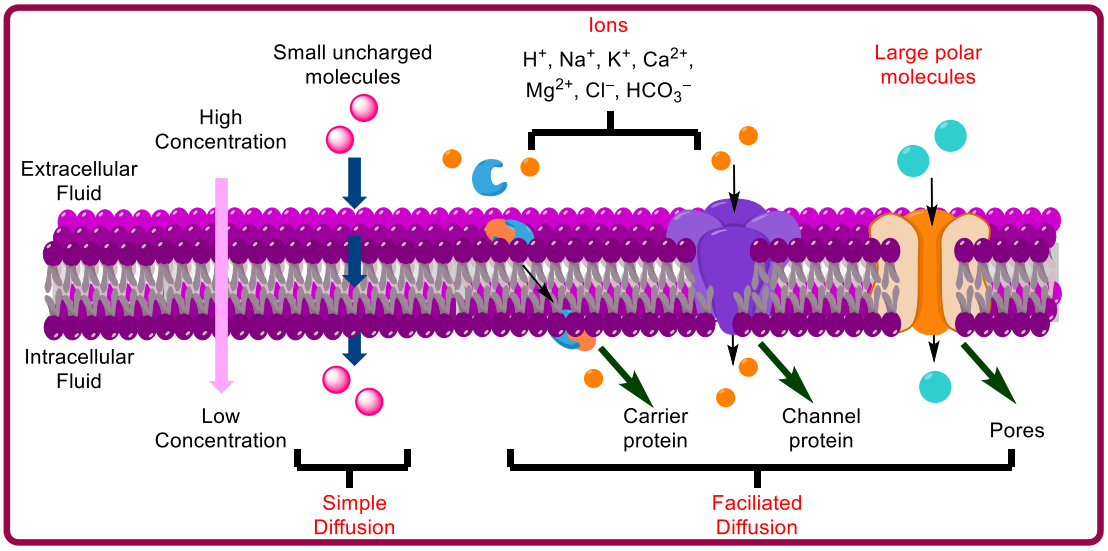

1.1 Cell and Cell Membrane

A cell is the basic structural and functional unit of all living organisms. It is the smallest unit of life that is capable of performing all the functions essential for life, such as metabolism, reproduction, and response to stimuli. Cells vary in size, shape, and function, but they all share certain features, including a plasma membrane, cytoplasm, and genetic material in the form of DNA. The plasma membrane encloses the cell and separates its internal environment from the external environment, and it regulates the movement of materials in and out of the cell.[1]

The cell membrane is a complex and dynamic structure that plays a vital role in maintaining the integrity and function of cells. The lipid bilayer is a fundamental component of biological membranes, which are thin, flexible structures that surround cells and organelles.

Components of lipid bilayer

The lipid bilayer is composed of two layers of phospholipids, each consisting of a hydrophilic head group and two hydrophobic fatty acid tails. The hydrophilic head group is composed of a charged or polar phosphate group and a glycerol molecule, which is a three-carbon alcohol. The hydrophobic fatty acid tails are composed of long chains of hydrocarbons that are insoluble in water. The hydrophobic tails of the phospholipids form the interior of the lipid bilayer, while the hydrophilic head groups are exposed to the aqueous environment on either side of the membrane. The hydrophobic tails are arranged in a tail-to-tail orientation, with the fatty acid chains of one layer facing the fatty acid chains of the other layer. The most common phospholipids in the membrane are phosphatidylcholine, phosphatidylethanolamine, phosphatidylserine, and sphingomyelin. This arrangement allows the lipid bilayer to form a stable and impermeable barrier between the cell and its environment. The thickness of the lipid bilayer varies depending on the types of lipids present and their degree of saturation. The average thickness of a biological membrane is approximately 3-4 nanometers (nm), with the hydrophobic region of the bilayer comprising about 2 nm and the hydrophilic head groups on either side comprising about 1 nm. The thickness of the bilayer can also vary depending on the specific location in the cell, with some membranes being thinner or thicker than others. The thickness of the lipid bilayer is important for its function as a barrier, as it determines which molecules can cross the membrane and how quickly they can do so. Molecules that are small and nonpolar, such as

oxygen and carbon dioxide, can diffuse through the lipid bilayer easily, while larger or charged molecules require specialized transport proteins to cross the membrane. The thickness of the lipid bilayer can also affect its fluidity and permeability, as thicker membranes are generally less fluid and more difficult to penetrate.[2]

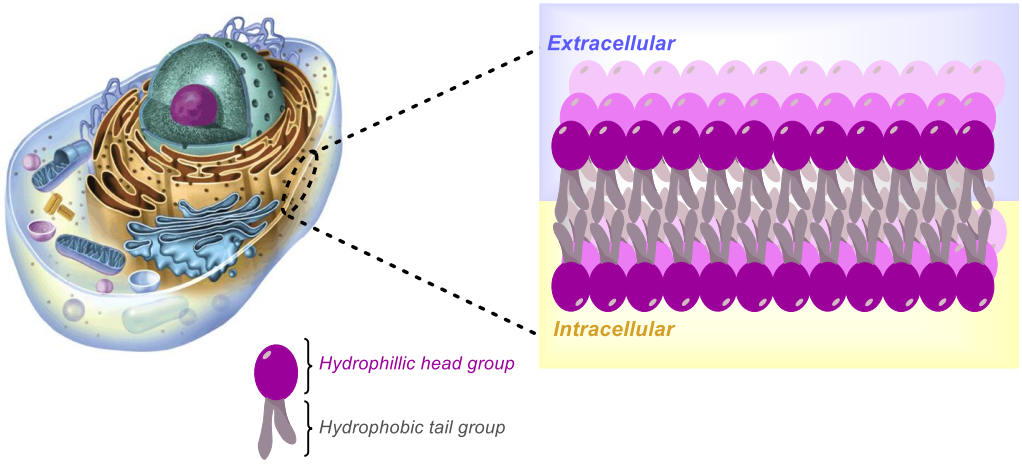

Figure 1.1. Schematic representation of eukaryotic cell and structure of lipid bilayer. The image has been adapted from https://o.quizlet.com/ZuhjESaLG1Y1A6vfAcT0YQ_b.png

The lipid bilayer is not a static structure, but rather a dynamic and constantly changing entity. Lipid molecules can move laterally within the membrane and can also rotate and flip-flop between the two layers. The fluidity of the membrane can also change in response to changes in temperature or other environmental factors.

One of the main functions of the cell membrane is to control the exchange of materials between the cell and its environment. The lipid bilayer is selectively permeable, meaning that it allows certain substances to pass through while preventing others from entering or leaving the cell. Small, non-polar molecules such as oxygen and carbon dioxide can diffuse freely across the lipid bilayer, while larger or polar molecules require specialized transport proteins to facilitate their movement. The lipid bilayer is selectively permeable, which means that it allows certain molecules to pass through while excluding others. Small, nonpolar molecules such as oxygen and carbon dioxide can diffuse through the lipid bilayer easily, while larger or charged molecules require specialized transport proteins to cross the membrane.

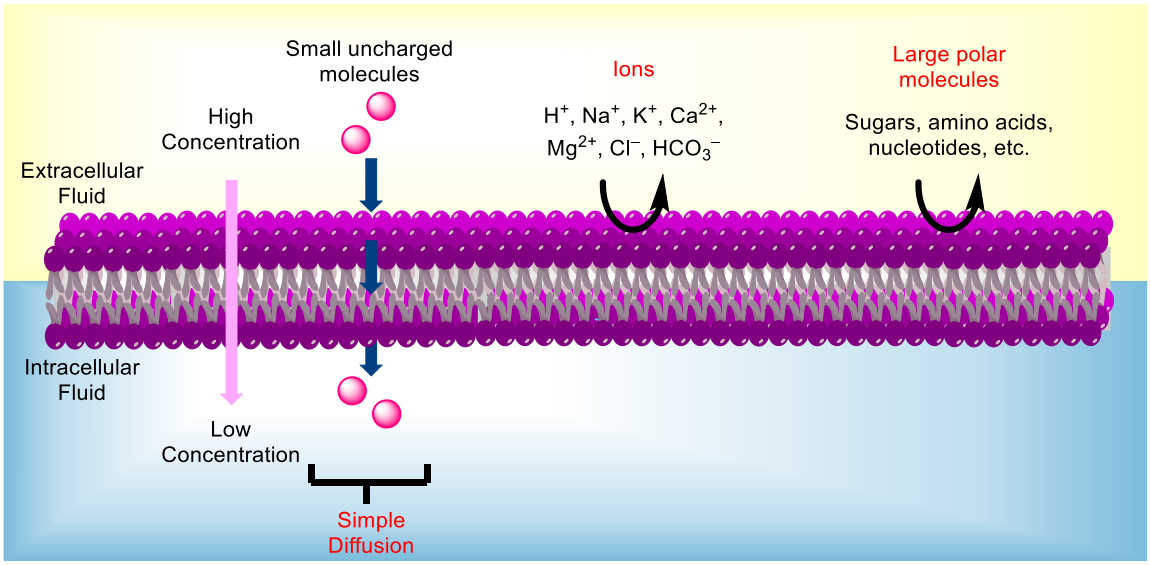

Figure 1.2. Representation of the transport processes across the cell membrane for different solutes.

1.2 Mechanism of Ion Transport[75]

Active and passive ion transport are two distinct mechanisms that are distinguished based on the energy required for the transportation process across cellular membranes.

1.2.1 Active Ion Transport

Primary active transport: This type of transport directly utilizes energy from ATP hydrolysis to transport ions against their electrochemical gradient. Examples of primary active transport include the sodium-potassium pump, which pumps three sodium ions out of the cell and two potassium ions into the cell, and the calcium pump, which pumps calcium ions out of the cell or into the endoplasmic reticulum.

Secondary active transport: This type of transport indirectly utilizes energy stored in the electrochemical gradient of one ion to transport another ion against its electrochemical gradient. Examples of secondary active transport include the sodium-glucose transporter, which moves glucose into cells against its concentration gradient by using the energy stored in the sodium gradient, and the sodium-calcium exchanger, which moves calcium ions out of cells against their gradient by using the energy stored in the sodium gradient.

1.2.2 Passive Ion Transport

Diffusion: This type of transport occurs when ions move from an area of high concentration to an area of low concentration. Diffusion can occur through the lipid bilayer of the cell membrane or through ion channels. Examples of diffusion include the movement of oxygen and carbon dioxide across the cell membrane by simple diffusion, and the movement of potassium ions through potassium channels.

Facilitated diffusion: This type of transport occurs when ions move across the membrane with the help of a transporter protein. Transporter proteins include ion channels and ion exchangers. Examples of facilitated diffusion include the movement of glucose into cells through the glucose transporter and the movement of chloride ions through chloride channels.[3]

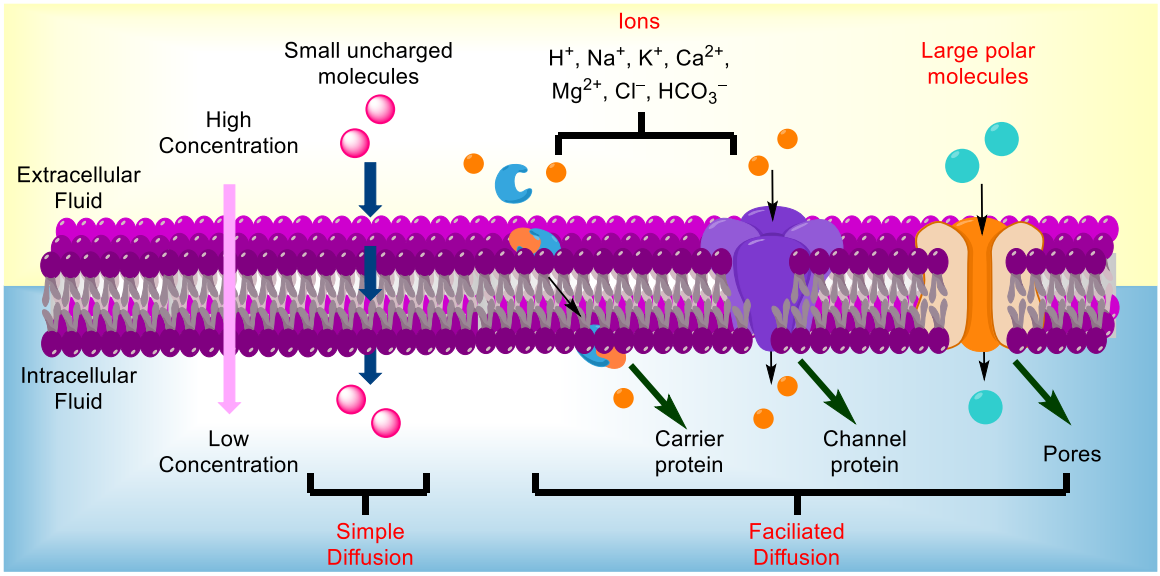

Figure 1.3. Schematic representation of transport process by ion carriers, ion channels, and ion pumps.

Differentiation based on the number of substances being transported, the direction of transport, and the energy requirements for transport.

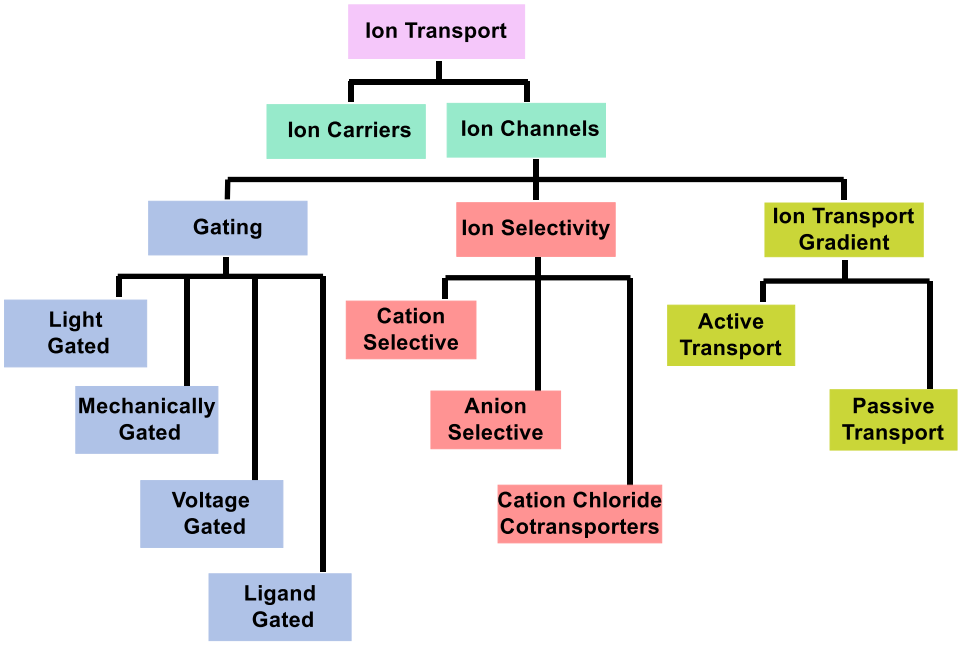

Figure 1.4. Characterisation of ion transport systems.

1.2.3 Antiport: Antiport involves the simultaneous movement of two different ions or molecules across the membrane in opposite directions. This type of transport is also known as counter-transport. Antiporters are transmembrane proteins that use energy, usually in the form of ATP, to move the ions or molecules against their concentration gradient. An example of an antiporter is the sodium-calcium exchanger, which uses the energy stored in the sodium gradient to move calcium ions out of the cell. Another example of an antiporter is the chloride-bicarbonate exchanger, which exchanges chloride ions for bicarbonate ions across the membrane.

1.2.4 Symport: Symport involves the movement of two different ions or molecules across the membrane in the same direction. This type of transport is also known as co-transport. Symporters are transmembrane proteins that use the energy stored in the electrochemical gradient of one ion or molecule to move the other ion or molecule against its concentration gradient. An example of a symporter is the sodium-glucose transporter, which moves glucose molecules into the cell by using the energy stored in the sodium gradient.

1.2.5 Uniport: Uniport involves the movement of a single ion or molecule across the membrane in one direction. This type of transport is passive, meaning it does not require energy input. Uniporters are transmembrane proteins that allow the diffusion of ions or molecules down their concentration gradient. An example of a uniporter is the glucose

transporter, which allows glucose molecules to diffuse into the cell down their concentration gradient.[4-9]

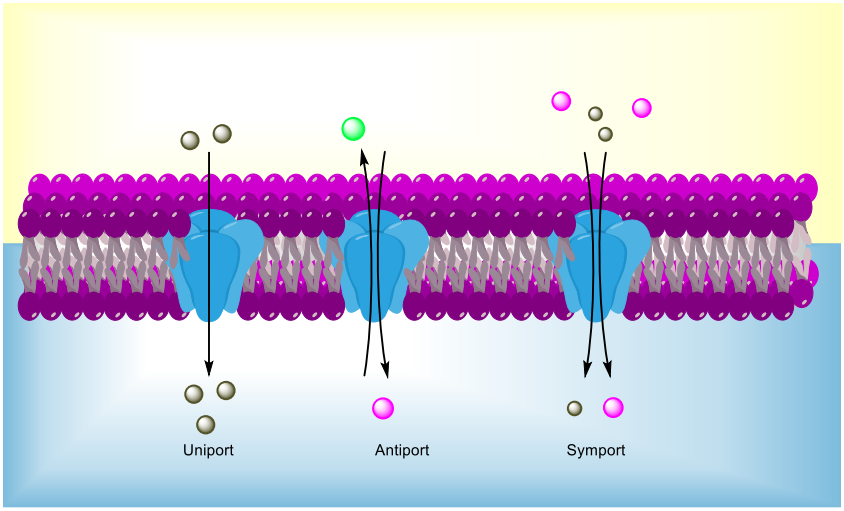

Figure 1.5. Schematic representation of different transport modes across the lipid bilayer membrane.

1.3 Supramolecular Interactions (Non-Covalent Interactions)

Supramolecular interactions refer to non-covalent interactions between molecules or ions that lead to the formation of larger, more complex structures. These interactions are responsible for the self-assembly of molecules and play a critical role in the function of biological systems, as well as in materials science and nanotechnology. There are several types of supramolecular interactions, including hydrogen bonding, van der Waals interactions, electrostatic interactions, hydrophobic interactions, and π -π stacking.[10-14]

I. Hydrogen bonding: Hydrogen bonding is a type of electrostatic interaction that occurs between a hydrogen atom that is covalently bonded to a highly electronegative atom (such as nitrogen, oxygen, or fluorine) and an unshared pair of electrons on another electronegative atom. This interaction is responsible for the formation of secondary structures in proteins and nucleic acids, such as alpha helices and beta sheets.

Hydrogen bonds are divided into three categories, based on the strength of interaction, as determined by the depth of the interaction potential D_e at the complex's minimum. Weak, moderate, and strong hydrogen bonds are the three categories, with energetic boundaries at roughly 2 and 15 kcal/mol. The weak hydrogen bonds include less polar X-H groups in proton donors, such as C-H or P-H groups, or less polar acceptors, such as the N_2 molecule in the N_2···HF complex. The group of moderate hydrogen bonds includes water dimer or

hydrogen fluoride dimer, carboxylic acids, base pairs of nucleic acids, and typical hydrogen bonds forming within or between proteins. The strong hydrogen bonds are composed of ionic species, with interaction energies of about 15, 30, 35, and 40 kcal/mol for $Cl^{-}\cdots H_2O$, $F^{-}\cdots H_2O$, $H_3O+\cdots H_2O$, and $F^{-}\cdots HF$, respectively. In addition, $H\cdots F^{-}$ distances of about 1.3 Å are closer to typical chemical bond distances than to H···Y hydrogen bond distances of about 2 Å. Strong hydrogen bonds cause significant distortion of the monomer's structure. The hydrogen bonding between ions and water is the main mechanism of the hydration processes. Most hydrogen-bonded molecules exhibit all of the features described in section VI to some extent. However, some complexes have X-H vibrations that are blue-shifted, and in those cases, the hydrogen-bonded classification is appropriate if the equilibrium geometry has a nearly linear X-H···Y shape, and the bond is reasonably strong.[15]

Example: The complementary base pairing between adenine and thymine in DNA is stabilized by hydrogen bonding.

II. Van der Waals interactions: Van der Waals interactions are weak attractions between atoms or molecules that arise from fluctuations in electron density. These interactions include dipole-dipole interactions, which occur between polar molecules, and London dispersion forces, which occur between nonpolar molecules.

Example: The formation of micelles in aqueous solution is driven by van der Waals interactions between the hydrophobic tails of the surfactant molecules.

III. Electrostatic interactions: Electrostatic interactions are strong attractions between positively and negatively charged ions or between polar molecules.

Example: The binding of enzymes to their substrates is often mediated by electrostatic interactions between charged amino acid residues and the substrate molecules.

IV. Hydrophobic interactions: Hydrophobic interactions arise from the tendency of nonpolar molecules to avoid contact with water molecules. This leads to the self-assembly of nonpolar molecules in aqueous solution, as they cluster together to minimize their exposure to water.

Example: The folding of proteins is driven by the burial of hydrophobic amino acid residues in the protein's interior, away from the aqueous environment.

V. π-π stacking: π -π stacking refers to the interaction between two aromatic rings in which the electron clouds of the rings overlap. This interaction is important in the structure and function of DNA and RNA, as well as in the binding of ligands to receptors.[16]

Example: The interaction between the nucleotide bases in DNA is stabilized by π-π stacking between the aromatic rings of adjacent bases.

VI. Metal-ligand coordination: This type of interaction involves the binding of a metal ion to a ligand molecule, typically through the donation of electron pairs from the ligand to the metal ion. Metal-ligand coordination is important in many biological processes, such as oxygen transport by hemoglobin.

Example: The binding of iron ions to heme molecules in hemoglobin and myoglobin is an example of metal-ligand coordination.

VII. Host-guest interactions: This type of interaction involves the binding of a guest molecule within a cavity or pocket formed by a larger host molecule. Host-guest interactions are important in many biological processes, such as enzyme catalysis and receptor-ligand binding.

Example: The binding of a drug molecule to a receptor protein is an example of a host-guest interaction.

VIII. π-π* interactions: This type of interaction involves the interaction between a filled π orbital (π) and an empty π* orbital. These interactions are important in the photochemistry of organic molecules and in the stabilization of transition states in chemical reactions.

Example: The stabilization of a transition state in a chemical reaction by π-π* interactions between the substrate molecule and the catalyst.

IX. Anion-π interactions: This type of interaction involves the interaction between a negatively charged anion and an aromatic ring. Anion-π interactions are important in the binding of anions to receptors and in the stabilization of negatively charged transition states in chemical reactions.

Example: The binding of chloride ions to the anion-binding site of the acetylcholinesterase enzyme is an example of anion-π interactions.

X. Sigma-hole interactions: This is another type of supramolecular interaction that involves the interaction between a positive sigma-hole region of a molecule and a negative or electron-rich region of another molecule. These interactions are important in many fields, including materials science, drug discovery, and catalysis.

The sigma-hole is a region of positive electrostatic potential on an atom that is bonded to an electronegative atom such as fluorine, chlorine, or iodine. This positive region can interact with negatively charged atoms or molecules such as oxygen, nitrogen, or sulfur, which have lone pairs of electrons or negative charges.[17, 18]

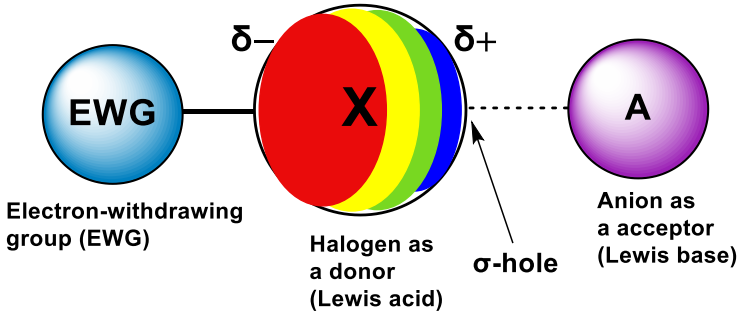

Figure 1.6. Schematic representation of sigma hole.

Examples of sigma-hole interactions include:

Halogen bonding: This is a type of sigma-hole interaction that involves the interaction between the sigma-hole on a halogen atom (e.g., iodine, chlorine) and a negative or electron-rich region of another molecule. Halogen bonding is important in the design of new drugs and materials.

Chalcogen bonding: This is a type of sigma-hole interaction that involves the interaction between the sigma-hole on a chalcogen atom (e.g., sulphur, selenium) and a negative or electron-rich region of another molecule. Chalcogen bonding is important in the design of new materials and catalysts.

Tetrel bonding: This is a type of sigma-hole interaction that involves the interaction between the sigma-hole on a tetrel atom (e.g., silicon, germanium) and a negative or electron-rich region of another molecule. Tetrel bonding is important in the design of new materials and catalysts.

Strength of sigma-hole

The strength of the sigma-hole depends on various factors, including the electronegativity of the atom, the size of the atom, and the polarizability of the atom. Generally, the strength of the sigma-hole follows the order: iodine > bromine > chlorine > fluorine.

This order can be explained by the increase in size of the halogen atom from fluorine to iodine, which results in a greater distance between the positively charged sigma-hole and the negatively charged electron-rich species. Additionally, as the size of the halogen atom increases, the polarizability of the atom also increases, making it more likely to form a supramolecular interaction.

The strength of the sigma-hole can also be affected by the surrounding chemical environment and the geometry of the molecule. For example, the presence of electron-withdrawing groups in the vicinity of the sigma-hole can weaken its interaction strength. Similarly, the orientation of the molecule can affect the accessibility and geometry of the sigma-hole, thereby influencing its interaction strength.

1.4 Hydrogen Bonding versus Halogen Bonding[19-24]

Hydrogen bonding and halogen bonding are both types of supramolecular interactions that involve the formation of non-covalent bonds between atoms or molecules. However, there are several key differences between these two types of interactions.

Nature of the bond: Hydrogen bonding involves the interaction of a hydrogen atom with a highly electronegative atom, such as oxygen or nitrogen. The hydrogen atom is partially positive due to the electronegativity of the nearby atom, while the electronegative atom is partially negative. This creates a dipole-dipole interaction between the two atoms.

Halogen bonding, on the other hand, involves the interaction of a halogen atom, such as chlorine or bromine, with a highly electronegative atom or group, such as oxygen or nitrogen. The halogen atom is partially negative due to its high electronegativity, while the electronegative atom or group is partially positive. This creates a dipole-dipole interaction similar to hydrogen bonding.

Strength of the bond: Hydrogen bonds are generally stronger than halogen bonds. This is because the hydrogen atom is smaller and more polarizable than halogen atoms, which makes it more effective at forming a dipole-dipole interaction with nearby electronegative atoms.

Directionality of the bond: Hydrogen bonds are highly directional, meaning they form along a straight line between the hydrogen atom and the electronegative atom. This is due to the linear geometry of the molecule. In contrast, halogen bonds are less directional and can form along a range of angles between the halogen atom and the nearby electronegative group.

Occurrence in nature: Hydrogen bonding is a common interaction in biological systems, where it plays a key role in the structure and function of proteins, DNA, and other biomolecules. Halogen bonding is less common in nature but has been observed in some biological systems and can be used in the design of synthetic molecules and materials.

Applications: Both hydrogen bonding and halogen bonding have potential applications in the design of new materials and drugs. For example, hydrogen bonding can be used to design new catalysts, sensors, and drug molecules. Halogen bonding can be used to design new materials with specific properties, such as improved solubility or conductivity.

1.5 Importance of Ion Transport

The property of fluidity exhibited by the lipid bilayer is of significant importance for its proper functioning. The fluidic nature of the lipid bilayer is contingent upon the inherent characteristics of the constituent lipid molecules. The packing of saturated fatty acid tails is denser, resulting in increased membrane rigidity, whereas unsaturated fatty acid tails possess bends that impede tight packing and promote membrane fluidity. The fluidity of the membrane can be influenced by cholesterol molecules, which can reduce the mobility of lipid molecules by closely packing with them.

The selective permeability of the lipid bilayer is significantly influenced by the proteins that are integrated within it. The two primary classifications of membrane proteins are integral proteins and peripheral proteins. Integral proteins are situated within the lipid bilayer and traverse its complete width, whereas peripheral proteins are affixed to the surface of the lipid bilayer. Both categories of proteins have the capacity to act as channels or transporters, enabling selective molecules to traverse the membrane, or as receptors, facilitating the detection and response of the cell to environmental signals.

The cellular membrane is also involved in the process of cellular signalling and intercellular communication. The process of signal transduction pathways entails the interaction between distinct molecules and receptor proteins located on the cellular membrane. This interaction

initiates a series of intracellular events that culminate in a cellular response. The cellular membrane comprises distinct lipid rafts that are abundant in cholesterol and sphingolipids. These specialised structures are responsible for organising and regulating the signalling molecules present within the membrane.

1.6 Natural Ion Transporters

Nature exhibits a range of ion channels, consisting of one or more subunits of proteins. For instance, the voltage-dependent anion channel (VDAC) is a unimolecular ion channel,[25] composed of a single protein unit, which is capable of switching between specific on-off states based on the membrane potential. Another example is Gramicidin A, which is a dimeric ion channel formed by self-assembly of two identical helical peptides, with a selective structure for cations.[26] The KcsA channel, which is highly selective towards potassium, is another example, consisting of four identical alpha-helical peptide units that self-assemble to create an hourglass-shaped channel structure.[27] In addition, there are naturally occurring ion carriers like prodigiosin and valinomycin, which can transport Cl^- and K^+ ions, respectively. Amphotericin-B, a natural antibiotic, is another example of an amphiphilic nonpeptide molecule that forms an oligomeric cation-selective ion channel, with a hydrophilic pore made up of hydroxyl functionalities and a hydrophobic outer surface composed of polyene moieties.[28] Additionally, there are naturally occurring ion carriers such as prodigiosin[29] and valinomycin,[30] which can transport Cl^- and K^+ ions, respectively. Lastly, the heptameric structure of alpha-hemolysin, found in Staphylococcus aureus, forms a larger size pore in the membrane for the transport of solutes like water, DNA, and toxins.[31]

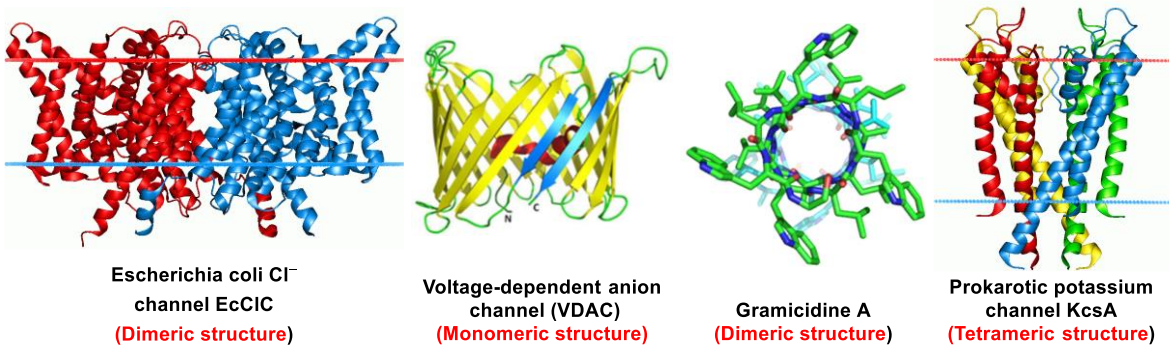

Figure 1.7. Some of the natural ion channels.

1.7 Designing Principles for Synthetic Ion Channel

Designing principles for synthetic ion channels have been inspired by natural ion channels. Some of the principles include:

1.7.1 Mimicking the structure of natural channels: Synthetic ion channels can be designed by mimicking the structure of natural channels. This involves studying the structure and function of natural channels and using this information to design synthetic channels with similar properties.

1.7.2 Selectivity: Natural channels are highly selective for specific ions. Synthetic channels can be designed to have similar selectivity by incorporating specific functional groups that interact with specific ions.

1.7.3 Size and geometry: The size and geometry of the channel can also be used to control ion selectivity. For example, channels with a larger diameter tend to be more selective for larger ions, while smaller channels tend to be more selective for smaller ions.

1.7.4 Hydrophobicity: The hydrophobicity of the channel can also be used to control ion selectivity. Hydrophobic channels tend to be more selective for non-polar ions, while hydrophilic channels tend to be more selective for polar ions.

1.7.5 Charge distribution: The charge distribution within the channel can also be used to control ion selectivity. For example, channels with a positive charge tend to be more selective for anions, while channels with a negative charge tend to be more selective for cations.

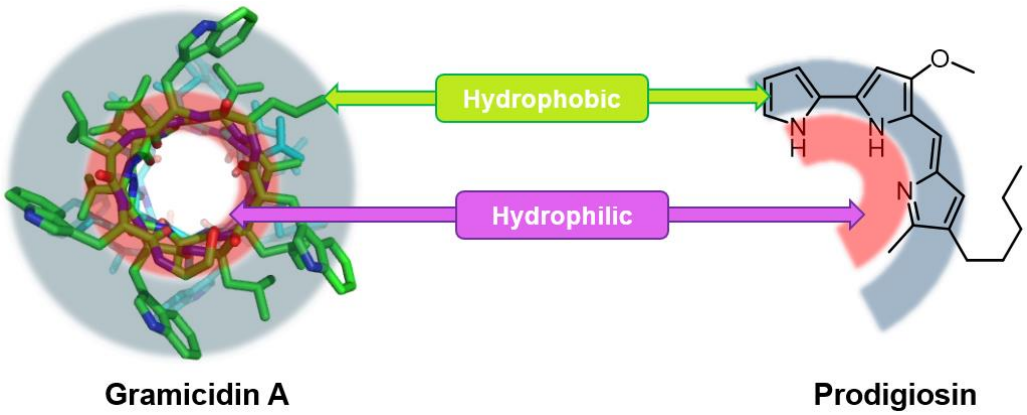

Figure 1.8. Representation of the hydrophilic interior and hydrophobic surface of natural ion transporting agents.

Some examples of synthetic ion channels that have been designed based on natural ion channels include:[32-53]

Cucurbituril-based ion channels: These channels are inspired by the pore structure of natural ion channels and use cucurbituril molecules as building blocks.

Rotaxane-based ion channels: These channels are inspired by the gating mechanism of natural ion channels and use rotaxane molecules to control ion transport.

Pillararene-based ion channels: These channels are inspired by the hydrophobicity of natural ion channels and use pillararene molecules to anchor the channel in the cell membrane.

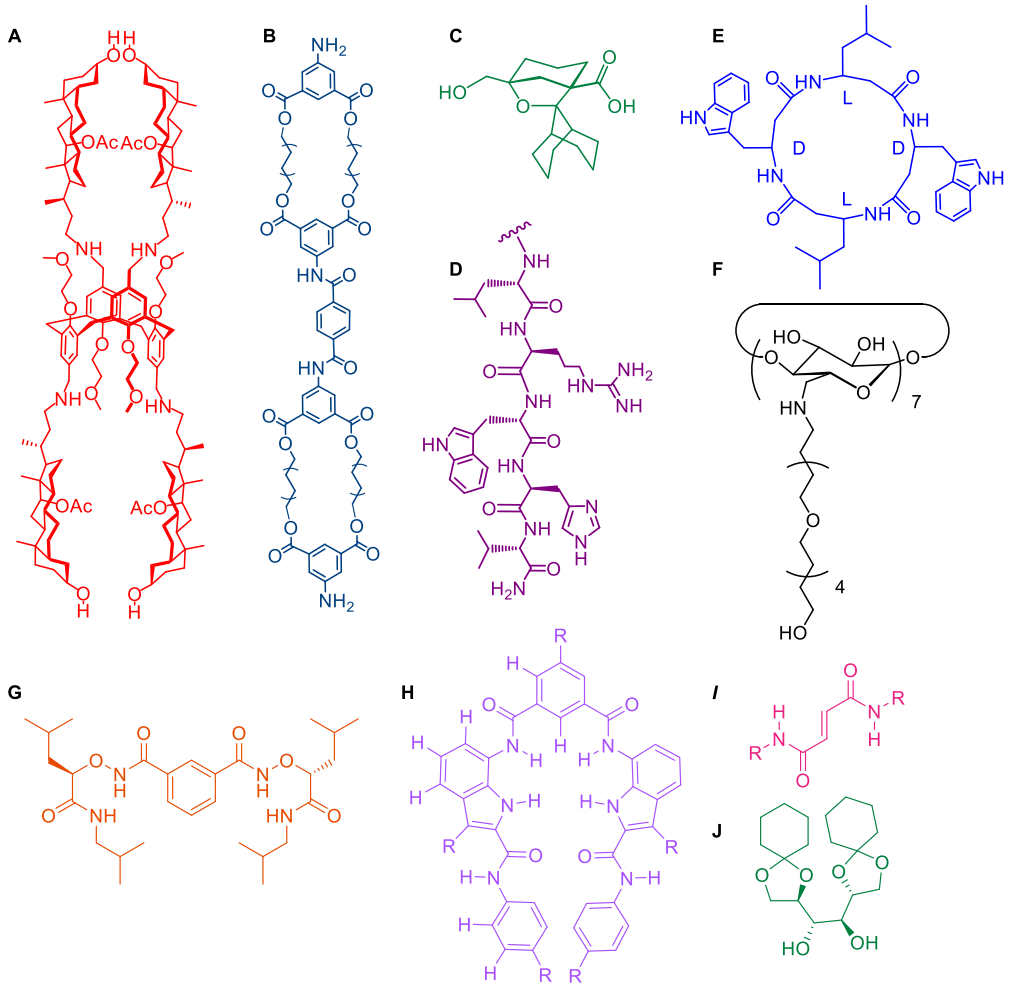

Figure 1.9. Structures of some of the reported synthetic ion channels based on designing principles.

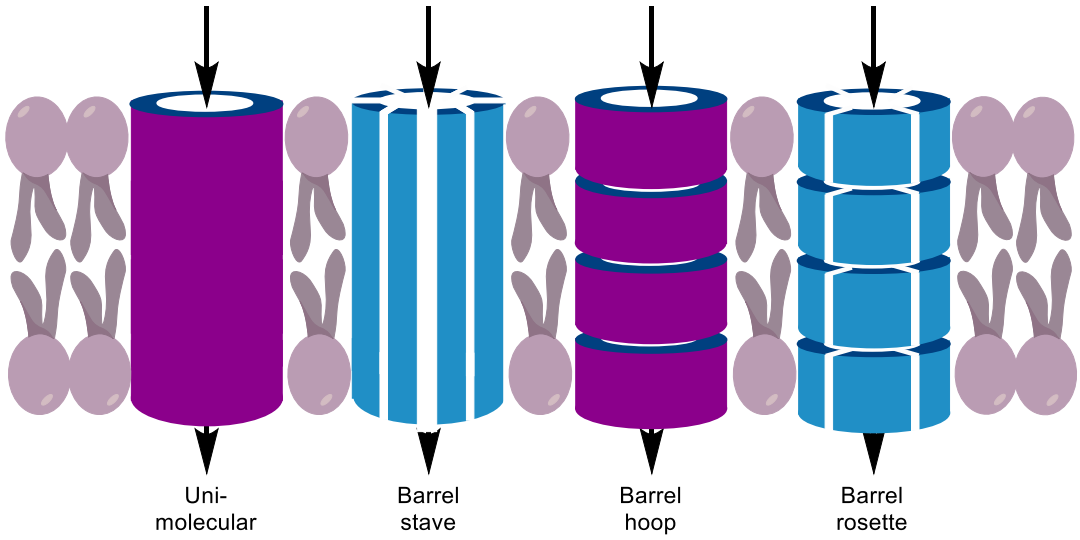

Figure 1.10. Schematic representation of various possible ion channel assemblies.

Calixarene-based ion channels: These channels are inspired by the size and shape of natural ion channels and use calixarene molecules to achieve selective ion transport.

The self-assembly of these synthetic ion channels is crucial for their functionality. Different types of self-assemblies are possible, and they are often inspired by natural ion channel structures. Here are explanations of various types of self-assemblies for synthetic ion channels:

Unimolecular Channels:

Description: Unimolecular channels refer to synthetic ion channels that consist of a single molecular entity. These molecules are typically amphiphilic, containing both hydrophilic and hydrophobic regions. The hydrophobic regions interact with the lipid membrane, while the hydrophilic regions create a pathway for ion transport.

Barrel-Stave Channels:

Description: Barrel-stave channels are assemblies where multiple synthetic molecules come together to form a cylindrical structure within the lipid bilayer. The hydrophobic portions of the molecules align to create a channel or pore, while the hydrophilic portions face the interior of the pore, facilitating ion transport.

Barrel Hoop Channels:

Description: Toroidal channels, also known as barrel hoop channels, involve the formation of a lipid-lined pore within the membrane. The synthetic ion channel induces a curvature in the lipid bilayer, and the hydrophilic portions of the channel interact with both the water-filled pore and the lipid headgroups.

Barrel-Rosette Channels:

Description: Barrel-rosette channels involve the assembly of synthetic molecules into a rosette-like structure within the lipid bilayer. These structures can form multiple small channels or a central pore for ion transport.

These different self-assemblies highlight the versatility of synthetic ion channels and their ability to mimic various structural motifs found in natural ion channels. Researchers design these synthetic channels to achieve specific functions, such as ion selectivity, transport rates, and stability, by carefully engineering the molecular structure and interactions. The choice of self-assembly strategy depends on the desired properties and intended applications of the synthetic ion channel.

1.8 Importance of Chloride Transport across the Cell Membrane

To understand the importance of chloride in transport across the cell membrane firstly we must analyse the importance of anion. Anions are ubiquitous and crucial to many different functions in the body. DNA and adenosine triphosphate (ATP) are two examples of polyanionic molecules with crucial roles in biology. To prevent their thyroids from absorbing radioactive iodine (^{131}I), people at risk of radioactive exposure commonly take potassium iodide (KI) tablets, as iodide (^{127}I) is essential for hormone production in the thyroid glands.[54] Chloride transport channels in the body that are either dysfunctional or not produced enough cause cystic fibrosis.[55] Since fluoride can effectively prevent tooth decay, it is frequently added to both toothpaste and water supplies.[56] Certain anions present serious dangers to ecosystems and should be avoided at all costs. High concentrations of nitrate and phosphate in soil water and nearby lakes and rivers have led to eutrophication, marked by excessive development of algae, due to the abuse of nitrate- and phosphate-rich fertilizers in intensive arable farming.[57] Anion cyanide is extremely poisonous and can be found in cigarette smoke and other forms of industrial waste.[58] Nuclear waste often contains the radioactive anion pertechnetate. Disposal and storage issues have been brought to the forefront due to its extremely long half-life (>200,000 years) and high solubility in water.[59]

Some naturally occurring anions are damaging to human health, in addition to those released by humans. More than 300 million people throughout the world are at risk due to arsenic contamination in their groundwater in the form of $H_2AsO_4^-$ or $HAsO_4^{2-}$.[60] Arsenic is toxic to humans in large enough doses that it causes skin lesions, cancer, and foetal abnormalities when exposed over long periods of time.[61] The field of anion recognition has advanced quickly as the significance of anions in biological and environmental processes has become more generally understood. An increasing number of anion receptors have been identified, and these receptors have found use in a wide variety of contexts, including sensing, extraction, and catalysis.[62-64]

The concentration of chloride ions in the body is tightly regulated and plays a critical role in various physiological processes. Chloride is the major extracellular anion and contributes to the osmotic pressure and pH balance of the body fluids. The normal concentration of chloride in the plasma of healthy adults is between 95 and 105 mmol/L.

Chloride ions are also important in maintaining the electrical potential of cells, especially in neurons and muscle cells. Chloride ions can move across the cell membrane through specific ion channels, which help to maintain the resting membrane potential and allow for the generation of action potentials.

Chloride ions also play a crucial role in the production of stomach acid, which is necessary for the digestion of food. The transport of chloride ions into the stomach epithelial cells is facilitated by the proton-potassium ATPase pump, which pumps hydrogen ions into the stomach lumen in exchange for potassium ions and chloride ions.

Additionally, chloride ions are involved in the regulation of fluid and electrolyte balance in the body. The concentration of chloride in the body is regulated by various hormones such as aldosterone, which stimulates the reabsorption of chloride ions in the kidneys.

Abnormal chloride ion concentrations can have significant health implications. For example, cystic fibrosis is a genetic disorder that affects the transport of chloride ions across cell membranes, resulting in thick mucus accumulation in various organs. Other conditions such as metabolic alkalosis and renal tubular acidosis can also result in abnormal chloride ion concentrations and lead to health problems.[65-70]

1.9 Chloride Ion Transporters in Therapeutics

Chloride ion transporters play a crucial role in various physiological processes and their dysfunction has been implicated in several diseases. Therefore, modulation of chloride ion transporters has therapeutic potential. Here are some examples:

1.9.1 Cystic fibrosis: Cystic fibrosis is a genetic disease caused by mutations in the cystic fibrosis transmembrane conductance regulator (CFTR) gene, which encodes a chloride channel. This results in reduced chloride secretion in the lungs, leading to thickened mucus and bacterial infections. Several drugs have been developed to target CFTR, including ivacaftor, lumacaftor, and tezacaftor. These drugs can improve chloride ion transport and have shown clinical benefits in cystic fibrosis patients.

1.9.2 Edema: Edema is a condition characterized by the accumulation of fluid in tissues, which can be caused by impaired chloride ion transport. Loop diuretics, such as furosemide and bumetanide, are commonly used to treat edema. These drugs inhibit the $Na^+/K^+/2Cl^-$ co-transporter in the kidneys, leading to increased chloride ion excretion and reduced fluid accumulation.

1.9.3 Epilepsy: Chloride ion transporters also play a role in the regulation of neuronal excitability, and dysfunction of these transporters can contribute to epilepsy. The anti-epileptic drug vigabatrin acts by irreversibly inhibiting the enzyme GABA transaminase, which degrades GABA, a neurotransmitter that activates chloride ion channels. This leads to increased chloride ion influx and neuronal inhibition, reducing seizures.

1.9.4 Cancer: Chloride ion transporters are also involved in cancer progression and metastasis. The chloride intracellular channel protein 1 (CLIC1) has been shown to be upregulated in several cancers, and knockdown of CLIC1 has been shown to inhibit cancer cell proliferation and migration. Therefore, CLIC1 has been proposed as a potential target for cancer therapy.[71-74]

Some examples of synthetic ion transporters that gained attention for its potential therapeutic applications:

1. Gramicidin A: Gramicidin A is a naturally occurring ion channel-forming peptide, but synthetic derivatives have been engineered for therapeutic purposes. Researchers have modified gramicidin A to enhance its stability and selectivity for specific ions. These

modified peptides have been explored for their potential in treating certain diseases, particularly in the context of ion channelopathies.

2. Amphotericin B: Amphotericin B is an antifungal drug that acts as a polyene ionophore. While it is a natural product, efforts have been made to modify its structure to improve its selectivity and reduce its toxicity. Amphotericin B and its derivatives have been investigated not only for their antifungal properties but also for their ability to transport ions across membranes, suggesting potential applications beyond antifungal therapy.

3. Tripodal Tris-thioureas: Researchers have designed synthetic tripodal tris-thioureas that act as chloride transporters. These molecules have shown promise in facilitating chloride transport across lipid bilayers and may have applications in conditions associated with dysfunctional chloride channels, such as cystic fibrosis.

4. Synthetic Anionophores: Various synthetic anion transporters have been developed to facilitate the transport of anions across cell membranes. For instance, researchers have explored the use of synthetic carriers based on urea and thiourea motifs to transport anions like chloride and bicarbonate. These compounds are designed to mimic the function of natural anion channels.

1.10 Techniques Used to Study Synthetic Ion Transporters

The investigation of synthetic ion transport systems is conducted through the utilisation of the model cell membrane, which can take the form of either spherical membranes (vesicles) in which transport in and out of the vesicles is examined or planar bilayer membranes (in BLMs) on patches of synthetic or natural membranes, whole cells or sheets of tissue. These membranes are comprised of lipids. The following is a concise analysis of the methodologies employed in investigating ion transportation mechanisms across bilayer membranes.

1.10.1 Vesicle-based Methodology

Most techniques use small spherical membranes, called unilamellar vesicles, which range from 0.1 to 1 μm in diameter and are made of bilayer membranes. These vesicles are created by a variety of methods, such as passing lipid suspensions through a nano porous filter. Water-soluble components (ions, indicators) are generally trapped inside the vesicles. Components that remain outside the vesicles are removed, for example, by dialysis, and

replaced with a different set of components to create concentration gradients across the membrane, which can be released by active transporters. Several techniques are available to detect anion transport, such as the use of fluorescent dyes that respond to the appearance or disappearance of anions. For instance, (1) pyranine, HPTS is a pH-sensitive dye that is widely used to detect anion transport, shows an increment in fluorescence if there is an influx of OH^- or efflux of H^+ ions while (2) lucigenin detects the exchange of halides with oxoanions such as nitrate. Additionally, (3) safranin O is a potential-sensitive dye that can identify the small amount of electrogenic transport possible in vesicular systems. Moreover, other types of fluorescent dyes such as (4) Carboxyfluorescein (CF), (5) ANTS-DPX, and (6) calcein are suitable for monitoring ion transport using established procedures. CF and ANTS-DPX can differentiate between ion channels and transmembrane pores with diameters exceeding 10 nm. They can also be used to investigate the impact of substances on the stability of the lipid bilayer membrane.

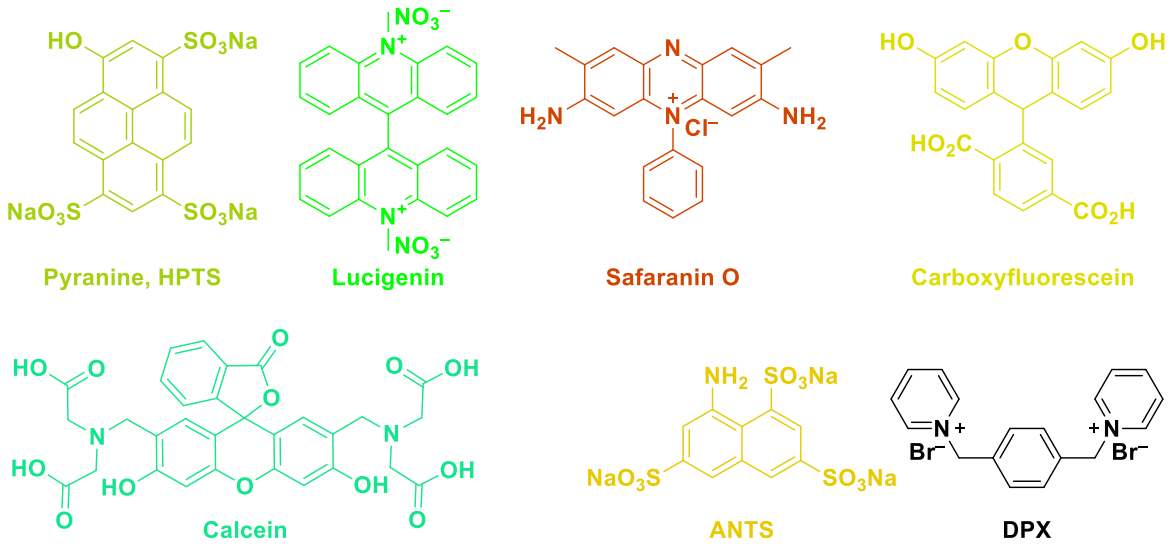

Figure 1.11. Representation of the structure of the different dyes used in vesicle method.

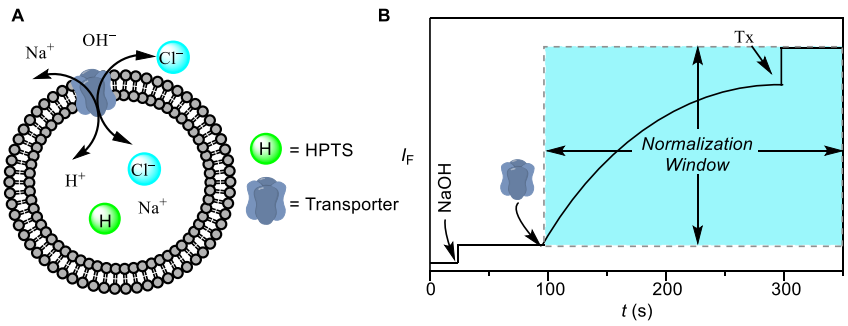

Figure 1.12. Representation of fluorescence-based ion transport assay in spherical vesicles.

Commercially available ion-selective electrodes are an alternative to fluorescence, where vesicle-encapsulated chloride ions are invisible to a chloride-selective electrode but can be detected if released by a transporter. NMR spectroscopy can also differentiate between anions inside and outside vesicles if a suitable shift reagent is present on one side of the membrane. However, kinetic experiments are limited by the relatively slow response time of the electrode, and lengthy acquisition times are required to observe the inherently weak signal in NMR spectroscopy.

1.10.2 Ion Transport Study in Planar Bilayers

Planar lipid bilayer membranes (BLMs) are widely used as a model system to investigate the properties of ion channels and transporters. The BLM technique allows researchers to directly measure the transport of ions across a bilayer, which can provide valuable insights into the structure and function of ion channels and transporters. In the BLM technique, a lipid monolayer (often 1,2-diphytanoyl-sn-glycero-3-phosphocholine (DPhPC) is used, although other lipids can also be used depending on the specific research question) is spread across a small hole in a Teflon partition (size of the hole is typically in the range of 150-250 μm) that separates two compartments filled with electrolyte solutions. The lipid monolayer is then allowed to self-assemble into a bilayer, which separates the two compartments. The bilayer has insulating properties, which means that it prevents the flow of ions between the compartments. However, the presence of ion channels or transporters in the bilayer can create a conductive pathway, allowing ions to flow across the bilayer. The transport of ions across the bilayer can be detected by measuring the current flowing across the membrane. This current can be generated by applying a voltage across the membrane using a pair of electrodes placed in the two compartments. The current is typically measured using a high-sensitivity current amplifier, which can detect picoampere currents.

One of the advantages of the BLM technique is that it allows researchers to study ion channels and transporters in isolation from other cellular components. This makes it possible to investigate the properties of these molecules in a controlled environment, which can provide valuable insights into their structure and function. The BLM technique has been used to study a wide range of ion channels and transporters, including voltage-gated ion channels, ligand-gated ion channels, mechanosensitive channels, and ion transporters.

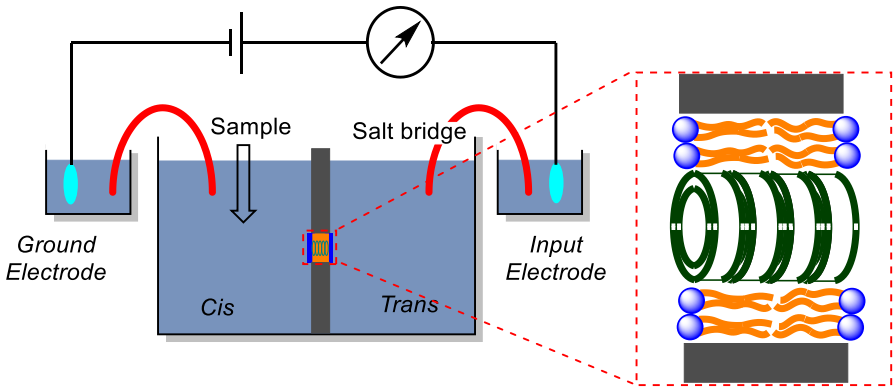

Figure 1.13. Systematic representation of black lipid membrane experiment.

1.11 References

1 B. Alberts, A. Johnson, J. Lewis, M. Raff, K. Roberts, and P. Walter, Molecular Biology of the Cell. 4th edition. New York: Garland Science, 2002.

2 H. Lodish, A. Berk, S. L. Zipursky, P. Matsudaira, D. Baltimore, and J. Darnell, Molecular cell biology, W. H. Freeman, 2000.

3 B. Alberts, A. Johnson, J. Lewis, M. Raff, K. Roberts, and P. Walter, Molecular Biology of the Cell. Garland Science. Chapter 11, Cell Membrane Transport of Small Molecules and the Electrical Properties of Membranes, 2002.

4 B. Alberts, A. Johnson, J. Lewis, M. Raff, K. Roberts, and P. Walter, Molecular biology of the cell (6th ed.) Garland Science, 2015.

5 D. L. Nelson, and M. Cox. M, Lehninger principles of biochemistry (7th ed.), W. H. Freeman, 2017.

6 H. Lodish, A. Berk, S. L. Zipursky, P. Matsudaira, D. Baltimore, and J. Darnell, Molecular cell biology (4th ed.), W. H. Freeman, 2000.

7 D. Voet, J. G. Voet, and C. W. Pratt, Fundamentals of biochemistry: Life at the molecular level (5th ed.), Wiley, 2016**.**

8 G. M. Cooper, R. E. Hausman, and C. Hausman, The cell: A molecular approach (8th ed.), Sinauer Associates, 2017**.**

9 E. R. Kandel, J. H. Schwartz, T. M. Jessell, S. A. Siegelbaum, and A. J. Hudspeth, Principles of neural science (5th ed.), McGraw-Hill Education, 2012.

10 I. M. Klotz, Supramolecular interactions in biological systems, *J. Mol. Recognit.*, 2009, **22**, 1–2.

11 D. N. Reinhoudt, Supramolecular chemistry: From molecules to nanomaterials, *J. Nanopart. Res.*, 2007, **9**, 983–1001.

12 G. M. Whitesides and B. Grzybowski, Self-assembly at all scales, *Science*, 2002, **295**, 5564, 2418–2421.

13 J. R. Nitschke, and C. J. Rogers, *Chem. Soc. Rev.*, 2005, **34,** 363–374.

14 Schalley, C. A. (Ed.), Analytical methods in supramolecular chemistry (2nd ed.), Wiley-VCH, 2011.

15 P. Hobza, and M. Kabeláč, *Chem. Soc. Rev.*, 2005, **34**, 762–771.

16 D. A. Dougherty, *Science*, 1996, **271**, 163–168.

17 P. Politzer, J. S. Murray, and T. Clark, *Phys. Chem. Chem. Phys.*, 2013, **15**, 11178–11189.

18 L. Mendez, G. Henriquez, S. Sirimulla and M. Narayan, *Molecules*, 2017, **22**, 1397.

19 T. Steiner, *Angew. Chem. Int. Ed.*, 2002, **41**, 48–76.

20 P. Auffinger, F. A. Hays, E. Westhof, and P. S. Ho, *Proc. Natl. Acad. Sci.*, 2004, **101**, 16789–16794.

21 P. Politzer, J. S. Murray, and T. Clark, *Phys. Chem. Chem. Phys.*, 2013, **15**, 11178–11189.

22 P. Metrangolo, and G. Resnati, *Chem. Eur. J.*, 2011, **17**, 274–279.

23 G. A. Jeffrey, An introduction to hydrogen bonding (Vol. 9), Oxford University Press, 1997.

24 C. A. Hunter, *Angew. Chem. Int. Ed.*, 2004, **43**, 5310–5345.

25 M. Bayrhuber, T. Meins, M. Habeck, S. Becker, K. Giller, S. Villinger, C. Vonrhein, C. I. Griesinger, M. Zweckstetter, and K. Zeth, *Proc. Nat. Acad. Sci.*, 2008, **105**, 15370–15375.

26 B. Roux, and M. Karplus, *Biophys. J.*, 1991, ***59***, 961–981.

27 D. A. Doyle, J. M. Cabral, R. A. Pfuetzner, A. Kuo, J. M. Gulbis, S. L. Cohen, B. T. Chait, and R. MacKinnon, *Science*, 1998, **280**, 69–77.

28 G. Fujii, J. -E. Chang, T. Coley, and B. Steere, *Biochemistry*, 1997, **36**, 4959–4968.

29 J. L. Seganish, and J. T. Davis, *Chem. Commun*., 2005, 5781–5783.

30 G. Stark, B. Ketterer, R. Benz, and P. Läuger, *Biophys. J*., 1971, **11**, 981–994.

31 L. Song, M. R. Hobaugh, C. Shustak, S. Cheley, H. Bayley, and J. E. Gouaux, *Science,* 1996, **274**, 1859–1866.

32 I. Tabushi, Y. Kuroda, and K. Yokota, *Tetrahedron Lett.,* 1982, **23**, 4601–4604.

33 N. Madhavan, E. C. Robert, and M. S. Gin, *Angew. Chem., Int. Ed*., 2005, **44**, 7584–7587.

34 N. Madhavan, and M. S. Gin, *Chem. Bio. Chem*., 2007, **8**, 1834–1840.

35 N. Maulucci, F. De Riccardis, C. B. Botta, A. Casapullo, E. Cressina, M. Fregonese, P. Tecilla, and I. Izzo, *Chem. Commun*., 2005, 1354–1356.

36 E. Biron, F. Otis, J. C. Meillon, M. Robitaille, J. Lamothe, P. Van Hove, M. E. Cormier, and N. Voyer, Design, *Bioorg. Med. Chem.*, 2004, **12**, 1279–1290.

37 P. K. Eggers, T. M. Fyles, K. D. Mitchell, and T. J. Sutherland, *Org. Chem*., 2003, **68**, 1050–1058.

38 M. Yoshii, M. Yamamura, A. Satake, and Y. Kobuke, *Org. Biomol. Chem*., 2004, **2**, 2619–2623.

39 H. Ishida, Z. Qi, M. Sokabe, K. Donowaki, and Y. J. Inoue, *Org. Chem.*, 2001, **66**, 2978–2989.

40 D. T. Bong, T. D. Clark, J. R. Granja, and M. R. Ghadiri, *Angew. Chem. Int. Ed.*, 2001, **40**, 988–1011.

41 J. Sánchez-Quesada, M. P. Isler, and M. R. Ghadiri, *J. Am. Chem. Soc.*, 2002, **124**, 10004–10005.

42 S. Fernandez-Lopez, H. S. Kim, E. C. Choi, M. Delgado, J. R. Granja, A. Khasanov, K. Kraehenbuehl, G. Long, D. A. Weinberger, K. M. Wilcoxen, M. R. Ghadiri, *Nature*, 2001, **412**, 452–455.

43 T. D. Clark, L. K. Buehler, and M. R. Ghadiri, *J. Am. Chem. Soc.*, 1998, **120**, 651–656.

44 M. R. Ghadiri, J. R. Granja, and L. K. Buehler, *Nature*, 1994, **369**, 301-304.

45 C. Pérez, C. G. Espínola, C. Foces-Foces, P. Núñez-Coello, H. Carrasco, and J. D. Martín, *Org. Lett.*, 2000, **2**, 1185–1188.

46 S. L. Forman, J. C. Fettinger, S. Pieraccini, G. Gottarelli, and J. T. Davis, *J. Am. Chem. Soc.*, 2000, **122**, 4060–4067.

47 N. Sakai, Y. Kamikawa, M. Nishii, T. Matsuoka, T. Kato, and S. Matile, *J. Am. Chem. Soc.*, 2006, **128**, 2218–2219.

48 N. Sakai, N. Majumdar, and S. Matile, *J. Am. Chem. Soc.*, 1999, **121**, 4294–4295.

49 P. Talukdar, N. Sakai, N. Sordé, D. Gerard, V. M. F. Cardona, and S. Matile, *Bioorg. Med. Chem.,* 2004, **12**, 1325–1336.

50 R. Sharma, A. Vijay, A. Mukherjee and P. Talukdar, *Org. Biomol. Chem.*, 2022, **20**, 2054–2058.

51 D. Mondal, M. Ahmad, B. Dey, A. Mondal and P. Talukdar, *Nat. Commun.*, 2022, **13**, 6507.

52 A. Roy, A. Gautam, J. A. Malla, S. Sarkar, A. Mukherjee and P. Talukdar, *Chem. Commun.*, 2018, **54**, 2024–2027.

53 T. Saha, S. Dasari, D. Tewari, A. Prathap, K. M. Sureshan, A. K. Bera, A. Mukherjee and P. Talukdar, *J. Am. Chem. Soc*., 2014, **136**, 14128–14135.

54 C. Reiners, and R. Schneider, *Radiat. Environ. Biophys*., 2013, **52**, 189–193.

55 G. R. Cutting, *Nat. Rev. Genet.,* 2015, **16**, 45-56.

56 N. H. de Leeuw, *J. Phys. Chem. B,* 2004, **108**, 1809–1811.

57 D. W. Schindler, *Limnol*. *Oceanogr.*, 2006, **51**, 356–363.

58 C. A. Johnson, *Appl. Geochem.*, 2015, **57**, 194–205.

59 E. A. Katayev, G. V. Kolesnikov, and J. L. Sessler, *Chem. Soc. Rev*., 2009, **38**, 1572–1586.

60 P. Ravenscroft, H. Brammer, K. S. Richards, Arsenic pollution: A global synthesis, Wiley-Blackwell, Chichester, U.K., Malden, MA, 2009.

61 R. Quansah, F. A. Armah, D. K. Essumang, I. Luginaah, E. Clarke, K. Marfoh, S. J. Cobbina, E. Nketiah-Amponsah, P. B. Namujju, S. Obiri, M. Dzodzomenyo, *Environ. Health Perspect.*, 2015, **123**, 412–421.

62 N. H. Evans, and P. D. Beer, *Angew. Chem. Int. Ed.,* 2014, **53**, 11716–11754.

63 N. Busschaert, C. Caltagirone, W. Van Rossom, P. A. Gale, *Chem. Rev*., 2015, **115**, 8038–8155.

64 P. Molina, F. Zapata, A. Caballero, *Chem. Rev*. 2017, **117**, 9907–9972.

65 T. J. Jentsch, V. Stein, F. Weinreich, and A. A. Zdebik, *Physiol. Rev*., 2002, **82**, 503–568.

66 M. B. Burg, and J. D. Ferraris, *Contrib. Nephrol*., 2008, **159**, 44–58.

67 M. Haas, and B. Forbush, *J. Bioenerg. Biomembr.*, 2000, **32**, 185–198.

68 K. Kaila, and R. Miles, *Epilepsia*, 2010, **51**, 52-52.

69 K. Strange, *J. Am. Soc. Nephrol.*, 1992, **3**, 12–27.

70 R. Dutzler, E. B. Campbell, M. Cadene, B. T. Chait, and R. MacKinnon, *Nature*, 2002, **415**, 287–294.

71 S. M. Rowe, S. Miller, E. J. Sorscher, *N. Engl. J. Med*., 2005, **352**, 1992–2001.

72 D. H. Ellison, H. Velázquez, and F. S. Wright, *Kidney Int*., 1990, **38**, 1095–1100.

73 W. Löscher, and M. A. Rogawski, *Epilepsia*, 2012, **53**, 12–25.

74 S. Zhang, X. M. Wang, Z. Y. Yin, W. X. Zhao, J. Y. Zhou, B. X. Zhao, and P. G. Liu, *APMIS*. 2013, **121**, 1047–1053.

75 M. Gashi, M. Mirhom, *J Psychiatry Neurosci.*, Sinauer Associates, 2017, 25–33.

Chapter 2

Bis(cholyl)-based chloride channels with oxalamide and hydrazide selectivity filters

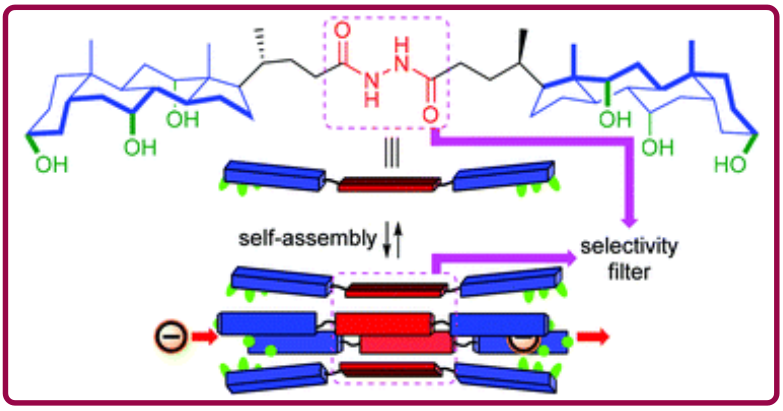

2.1 Introduction

A key part in the continued existence of live cells is played by the biological membrane and the movement of ions across the membrane.[1–3] They serve a critical and vital role in the control of biological functions and the passage of ions across the membrane with great selectivity and specificity because they are responsible for maintaining the enzymes and other molecules in their proper location within the cells. Small neutral molecules, such as water, carbon dioxide, and other similar molecules, are able to easily diffuse through the phospholipid membrane due to the amphiphilic nature of the membrane. On the other hand, the transport of charged species across the lipid membrane requires the assistance of a specialised type of protein and molecule that can act as a membrane-spanning channel or carrier and provide a selective passage for the charged species.[4–7]

Since chloride ion is the most abundant soluble anion in the body, proper maintenance of chloride milieu is a crucial parameter for ensuring that normal functions are carried out.[8–11] A group of potentially fatal conditions known collectively as "channelopathies" is linked to an abnormal concentration of chloride ions, which can be brought on by a dysfunctional channel.[12–16] These channelopathies could be exemplified by a variety of neurodegenerative disorders and epilepsies, as well as cystic fibrosis and a variety of renal ailments such as Dent's disease.[15,17,18] In order to treat channelopathies, many treatment approaches are utilised, one of these approaches is the activation of secondary chloride ion channels. For instance, in the case of cystic fibrosis, activating TMEM 16A helps to restore chloride concentrations in faulty cells.[19,20] Channel replacement treatment is one of the alternative therapeutic methods. In this type of therapy, a dysfunctional channel is offered to be replaced by other functioning channels, which may include synthetic channels. The chloride ion channels that are found in biological systems can be roughly categorised into a variety of distinct categories, such as ligand-gated channels, CLC voltage gated ion channels, volume regulated anion channels, and so on.[21,22] These CLC channels are the most prevalent in terms of number, and since they may be further subdivided into a wide variety of subtypes, they have been the subject of more research than any other class of chloride channels. It has been hypothesised, based on the crystal structure of CLC channels, that these channels feature a selectivity filter that is positioned inside the pore and that this filter leads to chloride recognition through electrostatic interactions.[10,23–27] As a result, imitating these channels in an accurate manner is necessary in order to successfully replace them in cases of channelopathies. The research published to date has provided ample

evidence of the existence of synthetic anion channels.[28–36] However, the design principle of a synthetic channel mimicking the CLC channels in terms of selectivity filter and shape was recently reported by Wen-Long Huanga et al. The authors of this study used a 1,3-alternate tetraoxacalix[2]arene[2]triazine as the selectivity filter at the centre of the channel, which was then flanked by four transmembrane arms (Figure 2.1B).[37] Despite this, there has been no report of a supramolecular channel in this domain up to this point. In this chapter, we describe the study of the first supramolecular channel in which the central core functions as a selectivity filter and, in the presence of chloride ion, has a smaller width than it does when the ion is absent.

A Cl^- selective bis(cholate) ion channel was synthesised by connecting cholic acid derived amine to fumaryl chloride and a corresponding maleamide derivative as a negative control for self-assembly. The work of the P. Talukdar group that was reported in 2018 served as inspiration for the design principle of this channel (Figure 2.1A).[38] In that study, the researchers created a Cl^- selective bis(cholate) ion channel. Nevertheless, the middle fumaramide core of the channel was rigid enough, and it provided a static path that Cl^- recognition and transport could take. We hypothesised that if this fumaramide core's stiff centre could be replaced with a hydrazine or oxalyl core, it may respond to the presence or absence of Cl^- ions to form a selectivity filter. This would be possible because hydrazine and oxalyl cores have a smaller

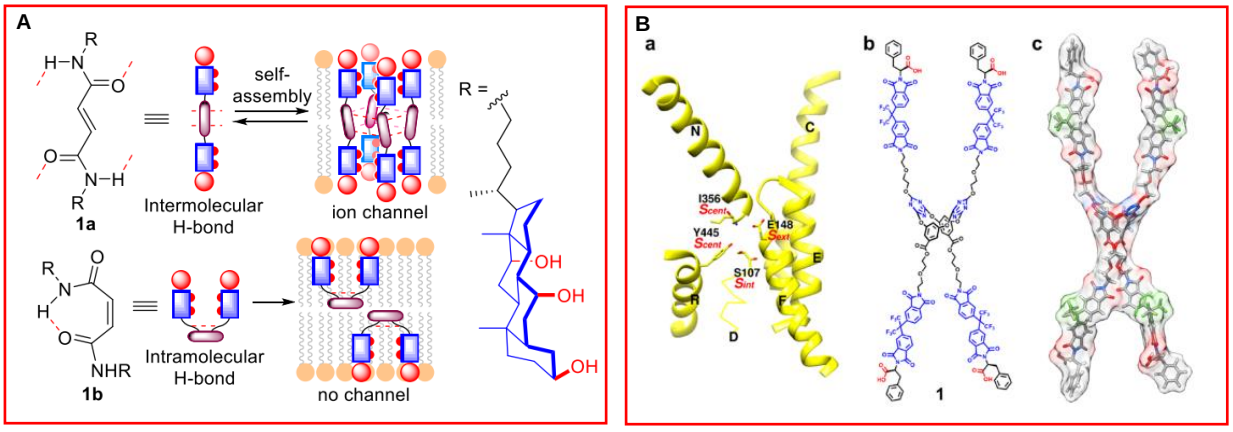

Figure 2.1 Barrel stave ion channel model for bis-cholic acid derivatives (A). Artificial channel molecule that mimics the shape and function of the ClC channel selective pore (B).

size than fumaramide cores and do not contain such conjugated rigid systems.[33,39–46] The side chains were also cholic acid derivatives, but they possessed well-defined amphiphilicity on their faces, which allowed them to bridge the bilayer membrane (Figure 2.2). Investigations using fluorescence and BLM techniques, as well as investigations using MD modelling

techniques, revealed that the channels that were created have chloride selectivity. Because of its distinct hydrophobic β-face for the van der Waals interactions with the membrane and a hydrophilic α-face (three OH groups are present on the α-face), the flat, rigid lipophilic backbone of cholic acid is used as the side chain. Because firstly, they provide extra symmetry and defined self-assembly of molecules (via. intermolecular H-bonding between two monomeric molecules) to have a rigid structure in the lipid membrane and therefore improving its selectivity; secondly, one monomer strand can now easily span the thickness of phospholipid membrane; and thirdly, the hydroxyl group present will ensure the continuity of hydrophobic interactions, it provides an excellent recognition site for anions through O–H···anion interactions.[33,40,44,47,48] The incorporation of two spacers that are chemically distinct gave some light on the implications of these effects for activity and selectivity.

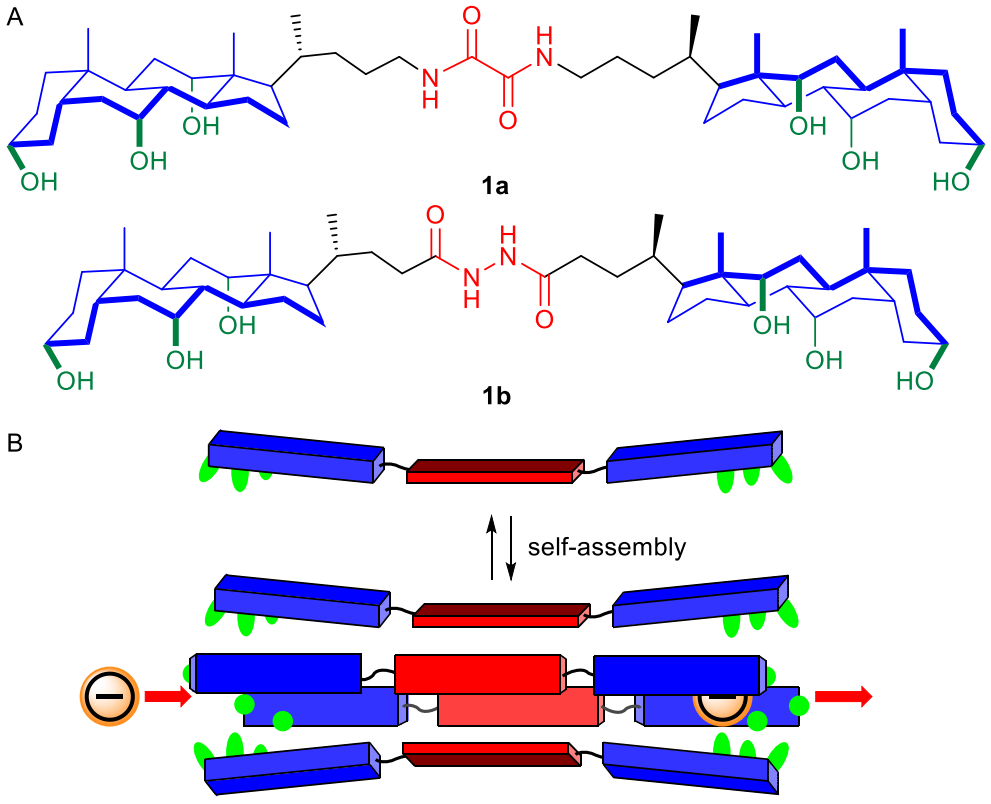

Figure 2.2 Structures (A) and self-assembly processes (B) of bis(chloyl)-linked oxalamide **1a** and hydrazide **1b** derivatives.

2.2 Result and Discussion

2.2.1 Synthesis

The bis(cholyl)-linked oxalamide **1a** was synthesized from cholic acid using a process that involved converting the terminal acid group to the amine by a reported protocol. The cholic-acid-derived amine was then linked to oxalyl chloride to furnish **1a** in 16% yield. The bis(cholyl)-linked hydrazide **1b** was synthesized by reacting cholic-acid-derived chloride with hydrazine monohydrate in 18% yield (Scheme 1).[49]

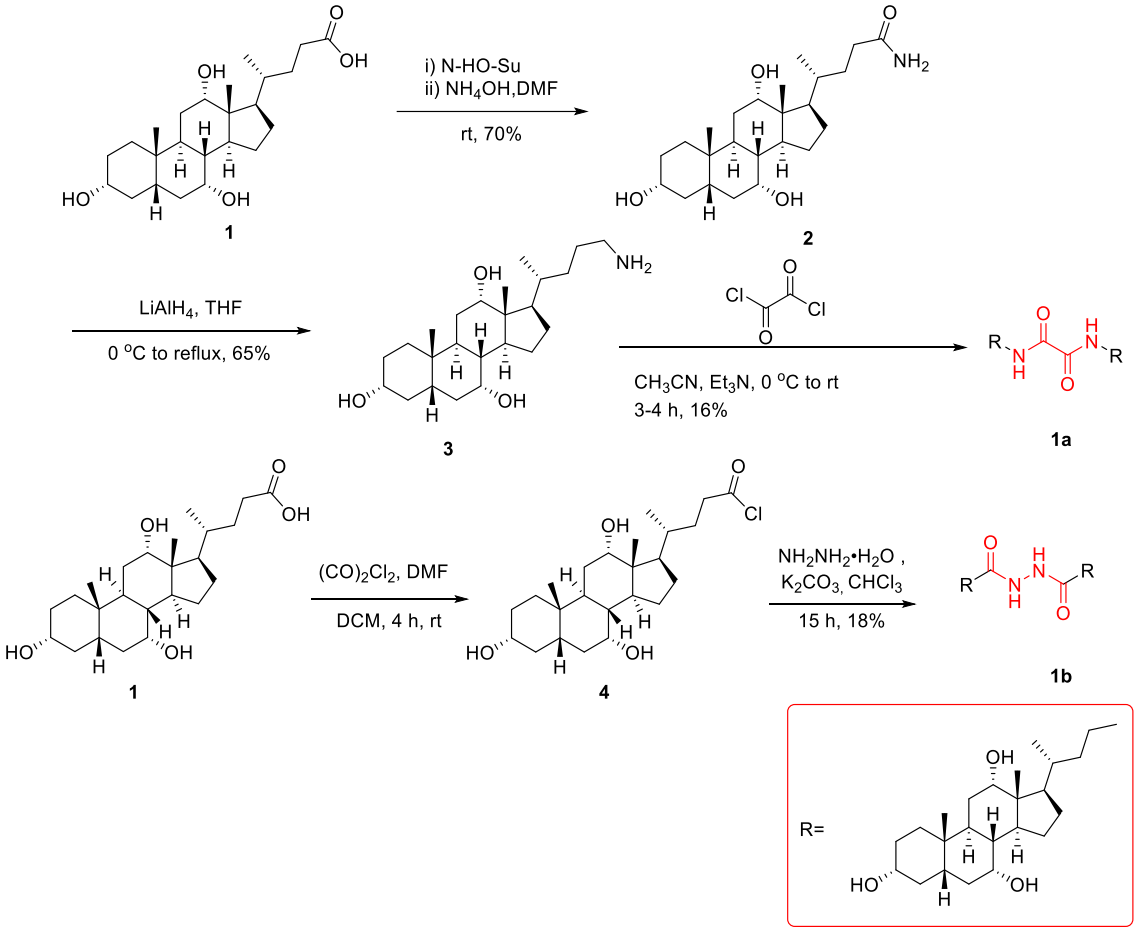

Scheme 2.1 Synthesis of oxalamide derivative **1a** and hydrazide derivative **1b**.

2.2.2 Ion Transport Studies

In order to investigate the ion transport capabilities of **1a** and **1b**, a model lipid bilayer membrane was constructed using egg-yolk phosphatidylcholine (EYPC) and prepared in the form of large unilamellar vesicles (LUVs). The EYPC-LUVs were created through the entrapment of the pH-sensitive fluorescent dye, 8-hydroxy-1,3,6-pyrenetrisulfonate (HPTS).

Subsequently, a pH gradient of 0.8 units (pH_{in} = 7.0 and pH_{out} = 7.8) was induced by means of 0.5 M NaOH. This resulted in an increase in the fluorescence intensity of the HPTS dye, provided that the ion transport process was functioning.[50,51] When subjected to similar conditions, the efficacy of compound **1b** was observed to be significantly greater than that of **1a**, as depicted in Figure 2.3. The EC_{50} values of 13.95 ± 0.193 μM (Figure. 2.4) and 7.95 ± 0.575 μM (Figure. 2.5) were obtained for **1a** and **1b**, respectively, indicating a dose-responsive ion transport activity. These values correspond to 27.7 mol% and 13.76 mol%, respectively, relative to lipid concentration. The self-assembly of monomers in the lipid bilayer membrane is responsible for the formation of the ion channel, as indicated by the Hill coefficients of n = 3.83 for **1a** and n = 4.06 for **1b**.[33,38,45,52]

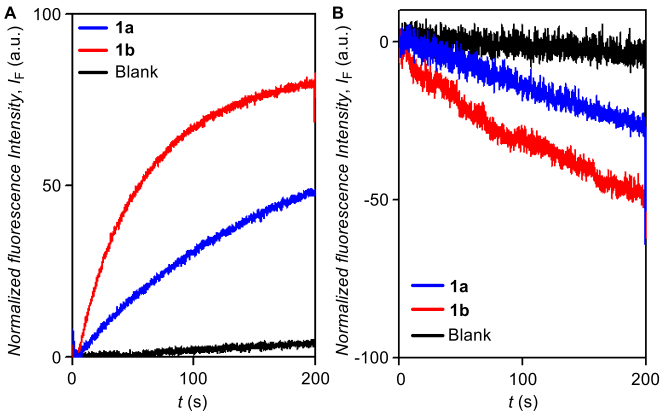

Figure 2.3 Comparison of activities of **1a** and **1b** (14 μM concentration) across EYPC-LUVs⊃HPTS (A). Comparison of activities of **1a** and **1b** (20 μM concentration) across EYPC-LUVs⊃Lucigenin (B).

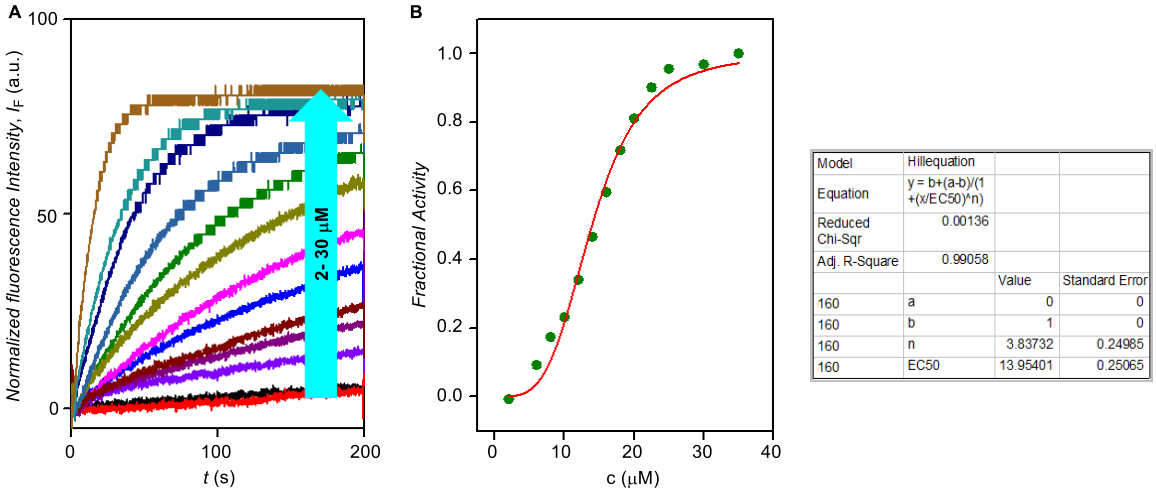

Model	Hillequation		
Equation	y = b+(a-b)/(1 +(x/EC50)^n)		
Reduced Chi-Sqr	0.00136		
Adj. R-Square	0.99058		
		Value	Standard Error
160	a	0	0
160	b	1	0
160	n	3.83732	0.24985
160	EC50	13.95401	0.25065

Figure 2.4 Concentration dependent activity of compound **1a** across EYPC–LUVs⊃HPTS (A). Hill plot analysis of compound **1a** (B) at 160 s.

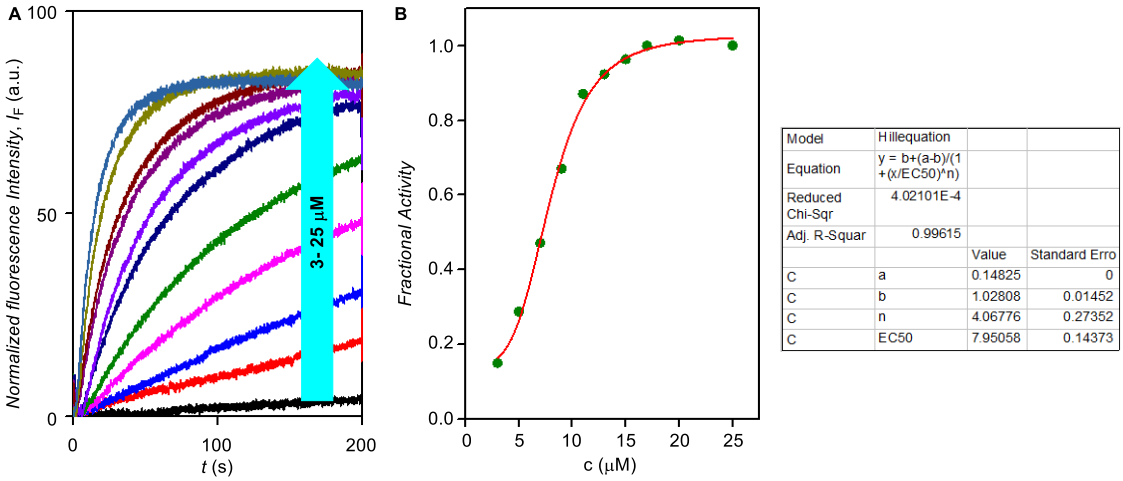

Figure 2.5 Concentration dependent activity of compound **1b** across EYPC–LUVs⊃HPTS (A). Hill plot analysis of compound **1b** (B) at 160 s.

2.2.3 Ion Selectivity Studies

The ion transport capabilities exhibited by **1a** and **1b** have instigated an inquiry into their ion selectivity and the mechanism by which they transport ions. The study employed the HPTS assay to examine the selective transportation of cations or anions through the channel. The transport function was probed through manipulation of the extravesicular ions. The transport activity of each compound was assessed in the presence of intravesicular NaCl and extravesicular isoosmolar MCl (where M^+ = Li^+, K^+, Rb^+, and Cs^+).[50,53] The results indicated that there were no significant changes in transport activity (Figure. 2.6B, 2.7B). This suggests that the presence of alkali cations did not affect ion transport by **1a** or **1b**, thereby eliminating the possibility of H^+/M^+ antiport and OH^-/M^+ symport mechanisms. Consequently, the transport mechanism was limited to either OH^-/X^- antiport or H^+/X^- symport. The study proceeded to investigate anion selectivity by modifying the extravesicular anions and analysing variations in ion transport rate using a pH gradient of 0.8 (pH_{in} 7.0 and pH_{out} 7.8). The investigation involved different NaX (X^- = Cl^-, Br^-, I^-, NO_3^-, ClO_4^-, OAc^-, and SCN^-) salts, which exhibited significant differences in ion transport rates, thus confirming the influence of anions in ion transport (Figure. 2.6A, 2.7A).[50]

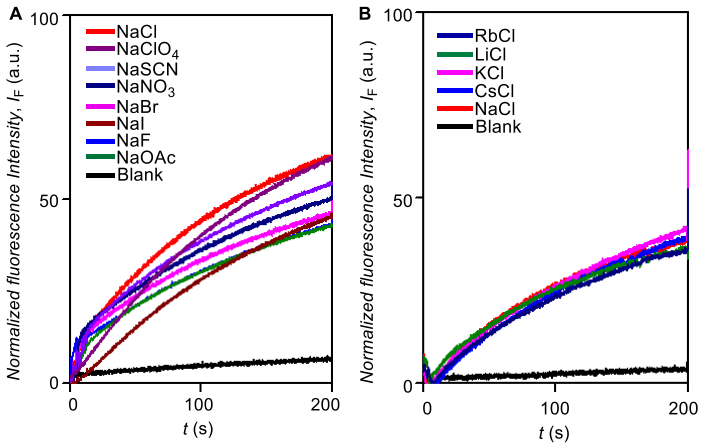

Figure 2.6 Anion selectivity of compound **1a** (A) at 17.5 µM and cation selectivity of **1a** (B) at 16.5 µM.

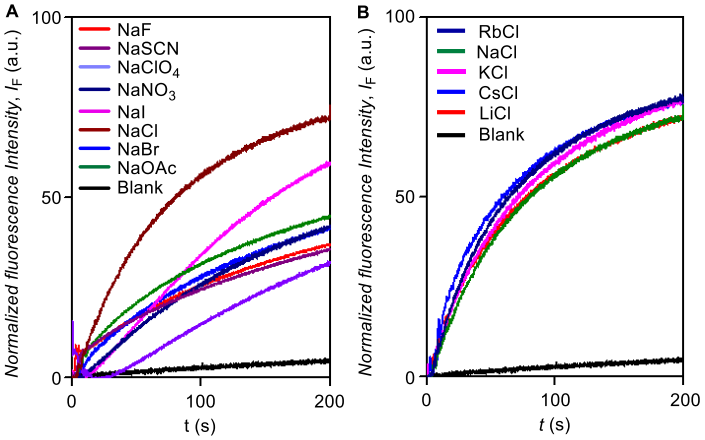

Figure 2.7 Anion selectivity (A) and cation selectivity of **1b** (B) at 9 µM.

2.2.4 Chloride Transport Assay

The transport mechanism was assessed through the quantification of Cl^- influx across EYPC liposomes containing lucigenin dye, in the presence of $NaNO_3$ and iso-osmolar extravesicular NaCl. This evaluation was conducted to gain further insight into the transport mechanism. The lucigenin dye has been observed to exhibit measurable fluorescence quenching when exposed to Cl^- ions.[54,55] The experimental results indicate that each compound exhibited a concentration-dependent influx of chloride ions, as demonstrated in Figure 2.8 and 2.9. The results demonstrate that the hydrazide system exhibited superior anion transport as evidenced by the significantly higher activity observed in **1b** compared to **1a**, as depicted in Figure 3A. The alteration of the cation in the extravesicular buffer, specifically M^+ which includes Li^+, K^+, Rb^+, and Cs^+, did not yield any discernible variation in the rate of Cl^- influx as depicted in Figure 2.10A. This finding effectively eliminates the possibility of M^+/Cl^- symport during the transportation process. At a concentration of 10 µM, there was no observed leakage of the

ANTS dye from EYPC–LUVs⊃ANTS/DPX (λ_{em} = 520 nm with λ_{ex} = 353 nm) for compound **1a** and **1b**. This confirms that the vesicle integrity was maintained in the presence of the cholyl derivatives, as shown in Figure 2.10B, 2.10C. The aforementioned findings provide additional corroboration that the compound in question does not generate significant transmembrane pores.

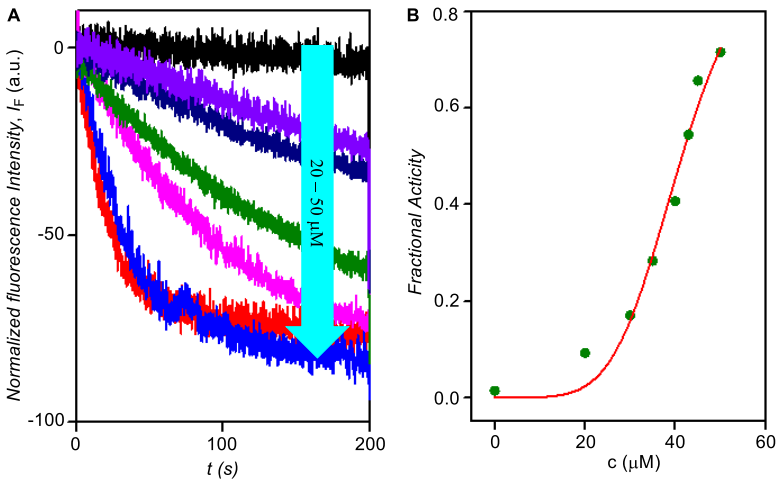

Figure 2.8 Concentration dependent activity of compound **1a** across EYPC–LUVs⊃lucigenin. (A). Hill plot analysis of compound **1a** (B).

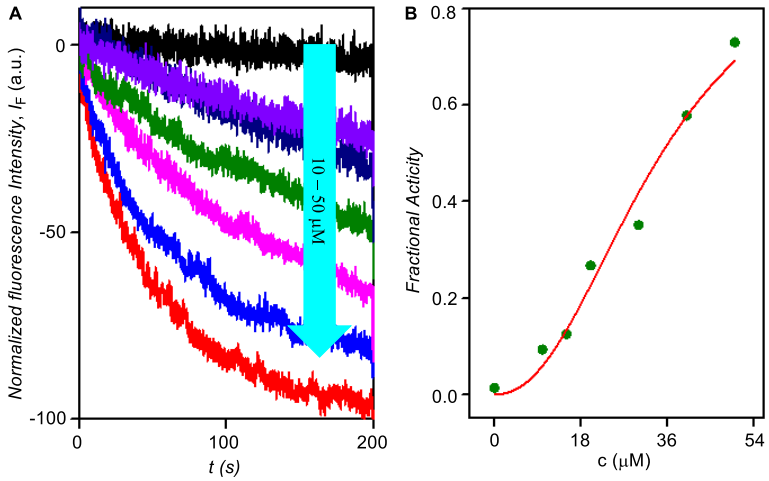

Figure 2.9 Concentration dependent activity of compound **1b** across EYPC–LUVs⊃lucigenin (A). Hill plot analysis of compound **1b** (B).

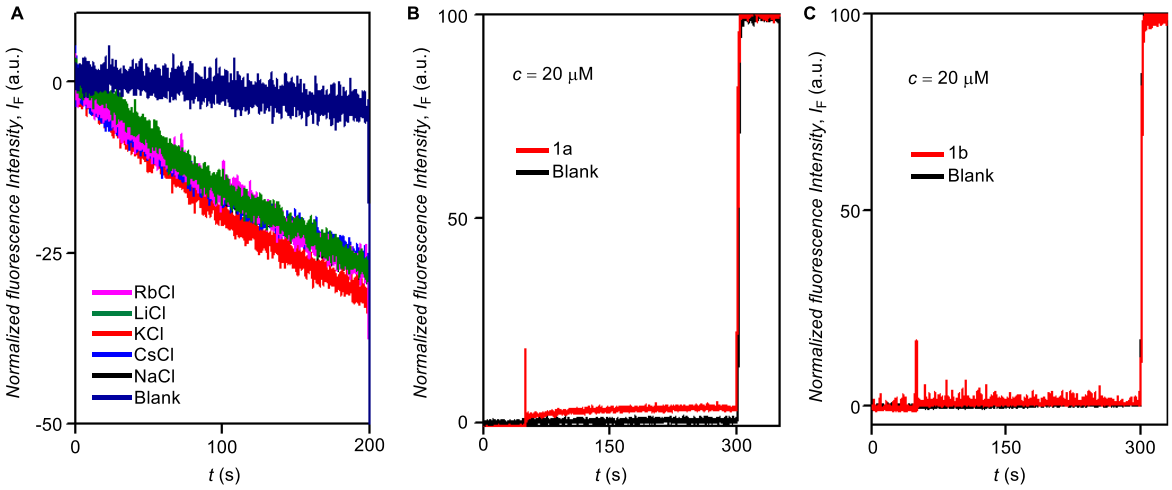

Figure 2.10 Influence of extravesicular cations in the Cl^- influx by **1a** at 20 μM (A). ANTS–DPX leakage assay in the presence of compound **1a** (B) and compound **1b** (C).

2.2.5 Planar Bilayer Conductance Studies

In order to determine the mechanism of ion transport, the electrical conductance of the planar lipid bilayer membrane was measured for **1b**, with the aim of discerning whether the process occurs through channel formation or a carrier mechanism.[31,55,56] A planar lipid bilayer was formed using 1,2-diphytanoyl-sn-glycero-3-phosphocholine (DPhPC) lipid. The bilayer was created by placing it over an orifice that connected two electrolyte chambers, namely the cis and trans chambers. Both chambers contained a 1 M solution of KCl. The introduction of **1b** (c = 20 μM) into the cis chamber of the electrolyte solution resulted in a noteworthy conduction of ions. The formation of ion channels at the planar bilayer is evidenced by the distinct single channel opening and closing events observed in **1b** recordings at both +100 mV and –200 mV, as depicted in Figure 2.11A, 2.11B. The researchers have determined that the pore's single channel conductance is G = 42.5 ± 0.9 pS and its diameter is d = 3.67 ± 0.42 Å. The study demonstrated a linear correlation between current and voltage (I–V) within the range of –100 mV to +100 mV, both in symmetrical and unsymmetrical KCl environments. The plot of current-voltage relationship obtained under unsymmetrical KCl conditions yielded the ion permeability ratio of (P_{Cl^-}/P_{K^+}) = 1.69, thus verifying the anion selectivity of the channel (Figure 2.11C).

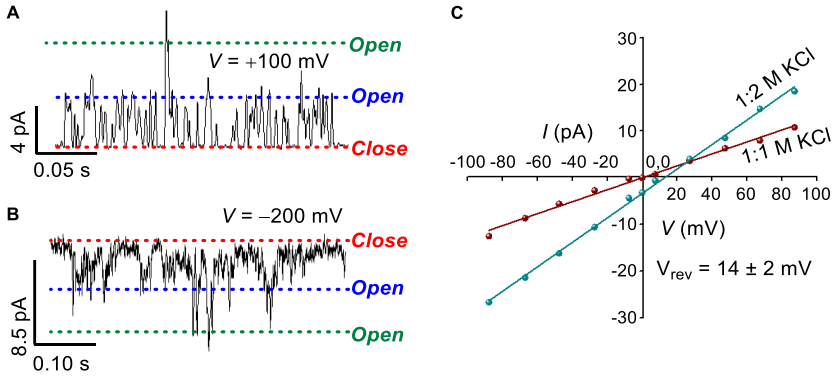

Figure 2.11 Single-channel conductance of **1b** (20 μM) recorded (A) at +100 mV and (B) at −200 mV under symmetrical KCl solutions. (C) I−V plots of **1b** under symmetrical and unsymmetrical concentrations of KCl.

2.2.6 Molecular Modelling of Ion Channel

These findings prompted us to develop a theoretical model for the suggested channel. The **1a** and **1b** was initially optimized using steepest descent method[57] for 10000 steps. The optimized **1a** and **1b** structures were then placed in the DPhPC lipid bilayer membrane and constructed two different systems, each consisting of four units. Afterward, the Molecular Dynamics simulations were carried out by using an explicit pre-equilibrated phospholipid bilayer of 128 DPhPC (1,2-diphytanoyl-*sn*-glycero-3-phosphocholine) obtained from Lipidbook[58], using GROMACS 2019.6.[59] The optimized channel was inserted in a box of 128 POPC molecules using inflategro methodology[60] at the proper density (area per lipid) of ~ 0.83 nm^2. To solvate the system, ~11000 SPC[61] model water molecules were added to the system. GROMOS-53a6 united atom force field[62] was used for DPhPC molecules. The automated topology builder[63] created by Malde et al. was used to create the all-atom topology parameters of the channel with GROMOS-53a6 force field. The average interaction energy between the individual channel and the chloride ion was calculated when the ion was at the centre of the channel. It is found that the hydrazide based, **1b** (more active) channel is found to stabilize the chloride ion more than the oxalamide based, **1a** channel (less active). The interaction energy between **1b** channel and chloride ion was found to be −14.4 kJ/mol, and that of **1a** and chloride ion was found to be −11.5 kJ/mol, respectively (Figure. 2.12D). This extra stabilization of the ion by the **1b** accounts for the active ion transport through this channel. The interaction energy profiles show that channel-ion interaction, as well as channel-channel interactions, are significant to stabilize the system in phospholipid membrane (Figure. 2.13B). In another interpretation, both channel-ion and channel-channel interactions stabilize the system, but the latter does not obstruct the channel-ion interaction. Figure. 2.12E illustrates the number of contacts made between the

channel and the chloride ion within the cut-off distance of 0.5 nm, indicating that **1b** has a stronger interaction with chloride for more period of time than **1a**, owing to the use of hydrazide as a selectivity filter. In the instance of **1a**, the total number of interactions decreased to zero after 500 ps because the ion had reached the bulk water.

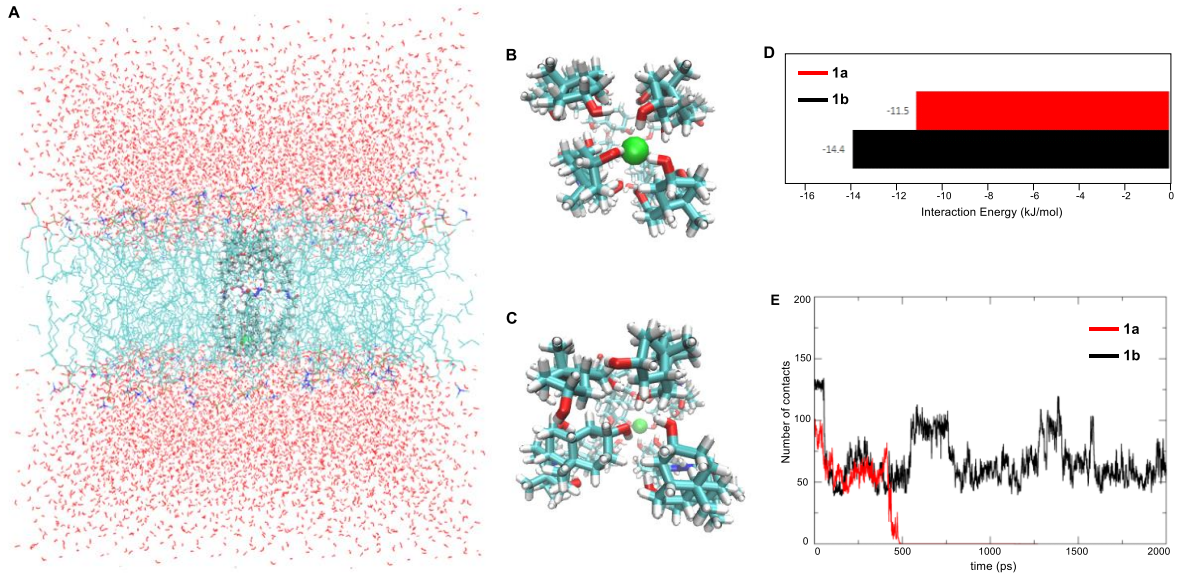

Figure 2.12 Equilibrated channel−DPPC/water system (A). Top view, when chloride ion is at the edge of the channel during simulation (B). Top view, when chloride ion is at the middle of the channel during simulation (C). Bar chart comparing the interaction energy between channels and chloride ion (D). Variation of contacts between channel and chloride ion within the cut-off distance of 0.5 nm (E).

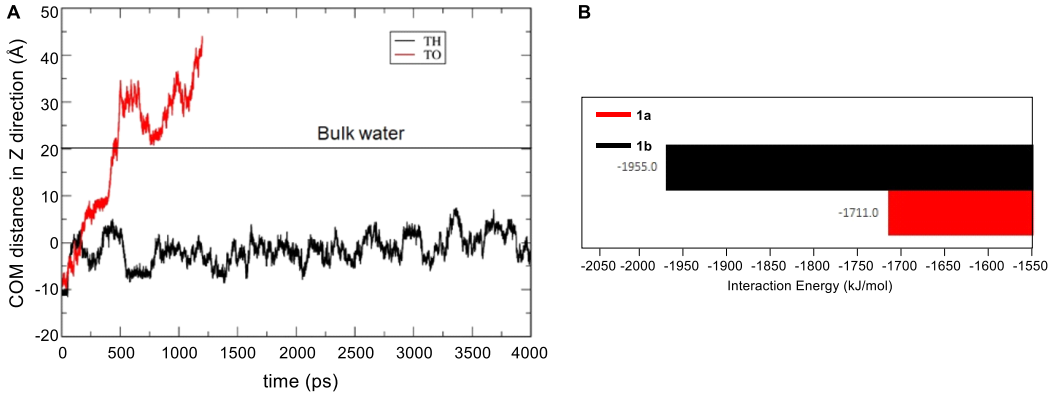

Figure 2.13 The centre of mass (COM) distance between the channel and the chloride ion (A). Bar chart comparing the interaction energy between channels and channel strands (B).

2.3 Conclusion

In summary, we have developed new bis(cholyl)-linked oxalamide and hydrazide analogues, which self-assemble among themselves in the barrel-stave model to construct

anion selective ion channels. In the self-assembled structures, oxalamide and hydrazide connectors worked as selectivity filters. Fluorescence-based ion transport experiments confirmed the formation of a supramolecular ion channel by bis(cholyl) analogues. The bis(cholyl) system with the hydrazide connector showed better activity (EC_{50} = 7.95 ± 0.57 μM) than the one with the oxalamide connector (EC_{50} = 13.95 ± 0.19 μM). The hydrazide system favoured anion transport with prominent chloride ion selectivity and no role of cations in the mechanism. Planar bilayer conductance measurements confirmed the formation of an ion channel of 3.67 ± 0.42 Å diameter and provided an additional support for chloride selectivity. Theoretical investigations confirmed that the hydrazide core served as a better selectivity filter compared to the oxalamide core as it provided stronger chloride binding. Moreover, the anion binding was observed primarily at the core of the channel.

2.4 Experimental Section

2.4.1 General Methods

All chemical reactions were performed under a nitrogen atmosphere. All reagents and solvents for synthesis were purchased from commercial sources (Sigma-Aldrich, Spectrochem) and used further without purification. The column chromatography was carried out using Merc silica (100-200/230-400 mesh size). The thin layer chromatography was performed on E. Merck silica gel 60-F254 plates. Egg yolk phosphatidylcholine (EYPC) as a solution of chloroform (25 mg/mL), mini extruder, polycarbonate membrane of 100 nm and 200 nm were purchased from Avanti Polar Lipid. HEPES, HPTS, Lucigenin, NaOH, Triton-X, and all inorganic salts were obtained as molecular biology grade from Sigma-Aldrich.

2.4.2 Physical Measurements

The ^{1}H NMR spectra were recorded at 400 MHz whereas ^{13}C at 101 MHz. The residual solvent signals were considered as an internal reference ($CDCl_3$ δ_H = 7.26 ppm, DMSO–d_6 δ_H =2.50, CD_3CN δ_H = 1.94) to calibrate spectra. The chemical shifts were reported in ppm. Following abbreviations were used to indicate multiplicity patterns m: multiplet, s: singlet, d: doublet, t: triplet, q: quartet, dd: doublet of doublet, td: triplet of doublet. Coupling constants were measured in Hz. Infra-red (IR) spectra were measured in cm^{-1} using FT–IR spectrophotometer. Melting points were measured on micro melting point apparatus. High-resolution mass spectra

(HRMS) were recorded on electrospray ionization time-of-flight (ESI-TOF). Fluorescence experiments were recorded on Fluoromax-4 from Jobin Yvon Edison equipped with an injector port and magnetic stirrer in a microfluorescence cuvette. All buffer solutions were prepared from the autoclaved water. Adjustment of pH of buffer solutions was made using Helmer pH meter. The extravesicular dye was removed by performing gel chromatography using Sephadex G-50. The fluorescence data were processed using OriginPro 8.5.

2.4.3 Synthesis

Synthesis of compound 2: Synthesis of compound **2** was done according to known protocol.[49] Cholic acid (1.07 g, 2.62 mmol), DCC (590 mg, 2.86 mmol), and *N*-hydroxysuccinimide (430 mg, 3.78 mmol) were dissolved in anhydrous THF and CH_3CN (10:1 mL), and stirred at room temperature for 8 h. After completion of the reaction, the white solid formed was filtered out and the filtrate was concentrated *in vacuo* to give a white foam (88% yield). A portion of this solid (350 mg, 0.700 mmol) was dissolved in anhydrous DMF and NH_4OH (27% aqueous solution) was added. After 12 h of stirring at 50 °C, the mixture was poured into brine. The precipitate was collected by suction filtration, washed with water (2 × 10 mL), and purified with column chromatography over silica gel using CH_2Cl_2/CH_3OH (8:1) as the eluent to give **2** (213.5 mg, 75% yield) as white powder. ^{1}H NMR spectrum was matched with the data of the reported compound.

Synthesis of compound 3: Synthesis of compound **3** was also done according to known protocol.[49] Compound **2** (310 mg, 0.760 mmol) was dissolved in anhydrous THF under N_2. $LiAlH_4$ (288 mg, 7.60 mmol) was added slowly. The reaction mixture was heated to reflux for 12 h. A small amount of ethyl acetate was added slowly to quench the $LiAlH_4$, which was then filtered and the filtrate was collected and concentrated *in vacuo*. The residue was purified with column chromatography over silica gel using CH_2Cl_2/CH_3OH (10:1) and CH_3OH/Et_3N (50:1) as the eluents to give **3** (194 mg, 65% yield) as white solid. ^{1}H NMR spectrum of the synthesized compound was matched with reported data.

Synthesis of compound 1a: Compound **4** (400 mg, 1.01 mmol) was dissolved in anhydrous THF (15 mL) under N_2. Triethylamine (0.63 mL, 0.45 mmol) was added dropwise to a solution of amine at 0 °C. Oxalyl chloride (0.19 mL, 0.22 mmol) was added dropwise and stirred at room temperature for 14 h. The precipitate was filtered off, and the solution was evaporated in vacuo. The pure product **1a** was isolated by flash column chromatography over silica gel using

CH_2Cl_2/CH_3OH (10:1) as white solid (185 mg, 16% yield). **M.P.:** 165-167 °C; **IR** (neat, ν/cm^{-1}): 3418, 2930, 2864, 1713, 1635, 1552, 1461, 1378, 1304, 1167, 977). **^{1}H NMR (400 MHz, DMSO-*d*$_6$, δ):** 7.96 (d, *J* = 7.5 Hz, 1H), 4.33 (d, *J* = 3.9 Hz, 2H), 4.11 (s, 2H), 4.01 (s, 2H), 3.77 (d, *J* = 7.6 Hz, 2H), 3.60 (s, 2H), 3.42 (s, 2H), 3.17 (s, 2H), 3.06 (s, 2H), 2.89 (s, 2H), 2.73 – 2.59 (m, 2H), 2.15 (ddd, *J* = 23.9, 18.5, 11.8 Hz, 6H), 1.97 (dd, *J* = 19.6, 9.8 Hz, 4H), 1.78 (d, *J* = 12.9 Hz, 4H), 1.64 (d, *J* = 12.7 Hz, 9H), 1.41 (s, 6H), 1.35 (s, 6H), 1.23 (s, 9H), 1.14 – 1.11 (m, 2H), 0.92 (s, 6H), 0.80 (s, 6H), 0.58 (s, 6H). **^{13}C NMR (101 MHz, DMSO-*d*$_6$):** 169.5, 71.3, 70.7, 66.5, 46.3, 45.9, 41.7, 35.5, 35.1, 34.6, 33.6, 32.6, 31.2, 30.5, 29.2, 28.7, 27.6, 26.44, 24.1, 23.1, 22.8, 22.4, 17.4, 14.9, 12.5. **HRMS (ESI):** Calc. for $C_{52}H_{86}N_2O_8$ $[M+H]^+$: 841.6228; Found: 841.6201.

Synthesis of compound 1b: To a solution of Cholic acid (500 mg, 1.22 mmol) and DMF (0.1 mL) in CH_2Cl_2 (60 mL) was added oxalyl chloride (0.51 mL, 0.60 mmol) dropwise at 0 °C. The reaction mixture was then stirred at room temperature for 2 h, and distilled in vacuo to afford cholyl chloride as a colourless liquid (522 mg). Cholyl chloride (209 mg, 0.489 mmol) was added to a solution of hydrazine monohydrate (0.118 mL, 0.244 mmol) and K_2CO_3 (1 g) in $CHCl_3$ (10 mL) at 0 °C. The reaction mixture was stirred at same temperature for 1 h, and then allowed to warm to room temperature. After 18 h, the compound was extracted with ethyl acetate (3 × 50 mL). The organic layer was dried over Na_2SO_4 and then evaporated in vacuo. The crude product was purified with column chromatography over silica gel using $CHCl_3/CH_3OH$ (10:1) as the eluents to give **1b** as white solid (75 mg, 18% yield). **M.P.:** 145-147 °C; **IR** (neat, ν/cm^{-1}): 3435, 2925, 2854, 1744, 1630, 1460, 1381, 1184, 1083, 1031, 909. **^{1}H NMR (400 MHz, DMSO-*d*$_6$, δ):** 11.89 (s, 2H), 4.31 (d, *J* = 4.4 Hz, 2H), 4.11 (d, *J* = 3.5 Hz, 2H), 4.00 (d, *J* = 3.4 Hz, 2H), 3.78 (d, *J* = 2.8 Hz, 2H), 3.61 (s, 2H), 3.43 (d, *J* = 60.9 Hz, 2H), 3.24 – 3.10 (m, 4H), 2.34 – 2.25 (m, 2H), 2.21 (dd, *J* = 10.4, 4.2 Hz, 2H), 2.12 (dd, *J* = 19.0, 6.5 Hz, 4H), 1.99 – 1.94 (m, 2H), 1.79 (dd, *J* = 14.4, 4.8 Hz, 4H), 1.68 – 1.65 (m, 2H), 1.62 (s, 2H), 1.47 – 1.40 (m, 6H), 1.34 (dd, *J* = 9.9, 4.2 Hz, 4H), 1.23 (s, 12H), 0.92 (d, *J* = 6.4 Hz, 6H), 0.87 – 0.83 (m, 4H), 0.81 (s, 6H), 0.58 (s, 6H). **^{13}C NMR (101 MHz, DMSO-*d*$_6$):** δ 175.5, 71.3, 70.7, 66.5, 47.7, 46.4, 45.9, 41.6, 35.4, 35.1, 34.6, 33.5, 32.4, 31.7, 30.5, 28.7, 27.5, 26.4, 25.5, 24.7, 23.1, 22.8, 17.3, 12.6. **HRMS (ESI):** Calc. for $C_{52}H_{86}N_2O_8$ $[M+H]^+$: 813.5915; Found: 813.5993.

2.4.4 Ion Transport Studies

Ion transporting activity studies across EYPC–LUVs⊃HPTS[50,54]

Preparation of HEPES buffer and stock solutions: The HEPES buffer of pH = 7.0 was prepared by dissolving an appropriate amount of solid HEPES (10 mM) and NaCl (100 mM) in autoclaved water. The pH was adjusted to 7.0 by addition of aliquots from 0.5 M NaOH solution. The stock solution of all carriers was prepared using HPLC grade DMSO.

Preparation of EYPC–LUVs⊃HPTS in NaCl: In 10 mL clean and dry round bottom flask thin transparent film of egg yolk phosphatidylcholine (EYPC) was formed using a 1 mL EYPC lipid (25 mg/mL in $CHCl_3$) by providing continuous rotation and purging nitrogen gas. The transparent thin film was completely dried under high vacuum for 4-5 h. After that, the transparent thin film was hydrated with the addition of 1 mL HEPES buffer (1 mM HPTS, 10 mM HEPES, 100 mM NaCl, pH =7.0) and the resulting suspension was vortexted at 10 minutes interval during 1 hour. This hydrated suspension was subjected to 15 cycles of freeze and thaw (N_2 gas, 55 °C) followed by extrusion through 100 nm (pore size) polycarbonate membrane for 21 times, to get vesicles of average 100 nm diameter. The unentrapped HPTS dyes were removed by size exclusion chromatography using Sephadex G-50 (Sigma-Aldrich) with eluting of HEPES buffer (10 mM HEPES, 100 mM NaCl, pH =7.0). Finally, collected vesicles were diluted to 6 mL to get EYPC–LUVs⊃HPTS. *Final conditions:* ~ 5 mM EYPC inside: 1 mM HPTS, 10 mM HEPES, 100 mM NaCl, pH = 7.0, outside: 10 mM HEPES, 100 mM NaCl, pH = 7.0.

Ion transport activity by HPTS assay: In a clean and dry fluorescence cuvette, 1975 μL of HEPES buffer (10 mM HEPES, 100 mM NaCl, pH =7.0) and 25 μL of EYPC–LUVs⊃HPTS vesicle was added. The cuvette was placed in slowly stirring condition using a magnetic stirrer equipped in a fluorescence instrument (t = 0 s). The time-dependent HPTS emission intensity was monitored at λ_{em} = 510 nm (λ_{ex} = 450 nm) by creating a pH gradient between intravesicular and extravesicular system by adding 0.5 M NaOH (20 μL) at t = 20 s, transporter at t = 20 s. Then different concentrations of transporter molecules in DMSO were added at t = 100 s. Finally, the vesicle was lysed by adding of 10% Triton X-100 (25 μL) at t = 300 s to destroy the pH gradient (Figure. 2.14).

The time axis was normalized according to Equation 1:

$$t = t - 100 \qquad \text{(Equation 1)}$$

The time of compound addition can be normalized to t = 0 s and time of Triton-X 100 addition was normalized to t = 200 s.

The time-dependent data were normalized to percent change in fluorescence intensity using Equation 2:

$$I_F = [(I_t - I_0)/ (I_\infty - I_0)] \times 100) \qquad \text{(Equation 2)}$$

where, I_0 is the initial intensity, I_t is the intensity at time t, and I_∞ is the final intensity after the addition of Triton X-100.

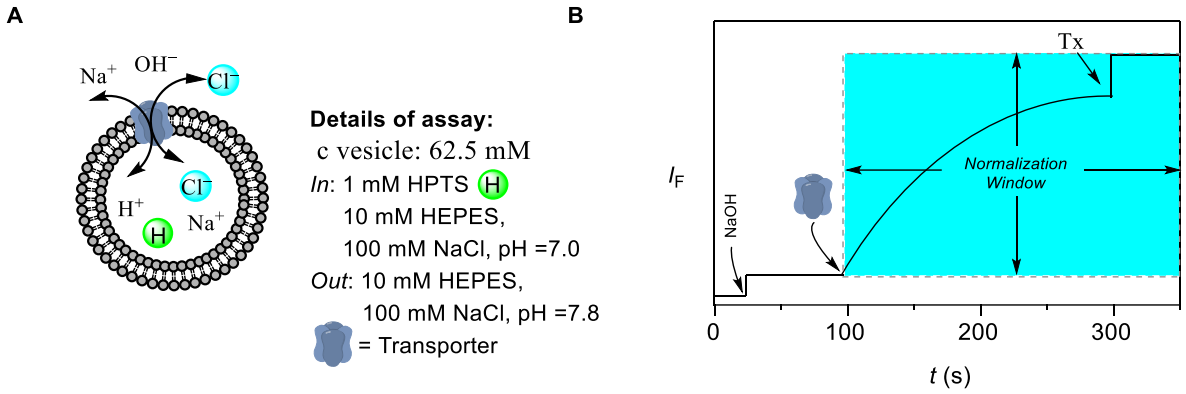

Figure 2.14 Representations of fluorescence-based ion transport activity assay using EYPC–LUVs⊃HPTS (A), and illustration of ion transport kinetics showing normalization window (B).

Dose-response activity:

The fluorescence kinetics of each transporter at different concentration was studied as a course of time. The concentration profile data were evaluated at t = 290 s to get effective concentration, EC_{50} (i.e., the concentration of transporter needed to achieve 50 % chloride efflux) using Hill equation (Equation 3):

$$Y = Y_\infty + (Y_0 - Y_\infty)/[1 + (c/EC_{50})^n] \qquad \text{(Equation 3)}$$

where, Y_0 = fluorescence intensity just before the transporter addition (at t = 0 s), Y_∞ = fluorescence intensity with excess transporter concentration, c = concentration of transporter compound, and n = Hill coefficient (i.e., indicative for the number of monomers needed to form an active supramolecule).

Ion selectivity studies across EYPC–LUVs⊃HPTS

Preparation of EYPC–LUVs⊃HPTS: The vesicles were prepared by the following reported protocol.

Preparation of buffer and stock solutions: The HEPES buffer solution of 10 mM HEPES and 100 mM salts were prepared by dissolving appropriate amounts of solid HEPES and salts (NaCl, NaF, NaBr, NaI, $NaNO_3$, NaSCN, NaOAc, $NaClO_4$, LiCl, KCl, RbCl, and CsCl) in autoclaved water, followed by adjustment of pH = 7.0 using 0.5 M NaOH. The stock solution of the most active transporter was prepared in HPLC grade DMSO.

Anion selectivity assay: In a clean and dry fluorescence cuvette 1975 μL HEPES buffer (10 mM HEPES, 100 mM NaX, pH = 7.0; where X = F^-, Cl^-, Br^-, I^-, OAc^-, NO_3^-, SCN^- and ClO_4^-) was taken, followed by addition of 25 μL EYPC–LUVs⊃HPTS. The resulting solution was slowly stirred in fluorescence instrument equipped with the magnetic stirrer (t = 0 s). The fluorescence intensity of HPTS was observed at λ_{em} = 510 nm (λ_{ex} = 450 nm) as a course of time, with creating pH gradient by addition of 20 μL 0.5 M NaOH at t = 20 s, followed by addition of transporter **1d** (as a DMSO solution) at t = 100 s to initiate ion transport and finally vesicle was lysed for complete destruction of pH gradient by addition of 25 μL 10% Triton X – 100 at t = 300 s. The time-dependent data were normalized to percent change in intensity using Equation 2 ($I_F = [(I_t - I_0)/ (I_\infty - I_0)] \times 100$), where I_0 is the initial intensity, I_t is the intensity at time t, and I_∞ is the final intensity after addition of Triton X-100).

Cation selectivity assay: In a similar way, cation selectivity of transporter **1d** (as a DMSO solution) was explored by changing extravesicular HEPES buffer solution (10 mM HEPES, 100 mM MCl, pH = 7.0) of chloride salts (MCl) of different cations (M = Li^+, Na^+, K^+, Rb^+, Cs^+). Using the same condition, no difference in fluorescence intensity was observed for different cations. The fluorescence data were normalised to percent change in intensity as a course of time using Equation 2 ($I_F = [(I_t - I_0)/ (I_\infty - I_0)] \times 100$), where I_0 is the initial intensity, I_t is the intensity at time t, and I_∞ is the final intensity after addition of Triton X-100).

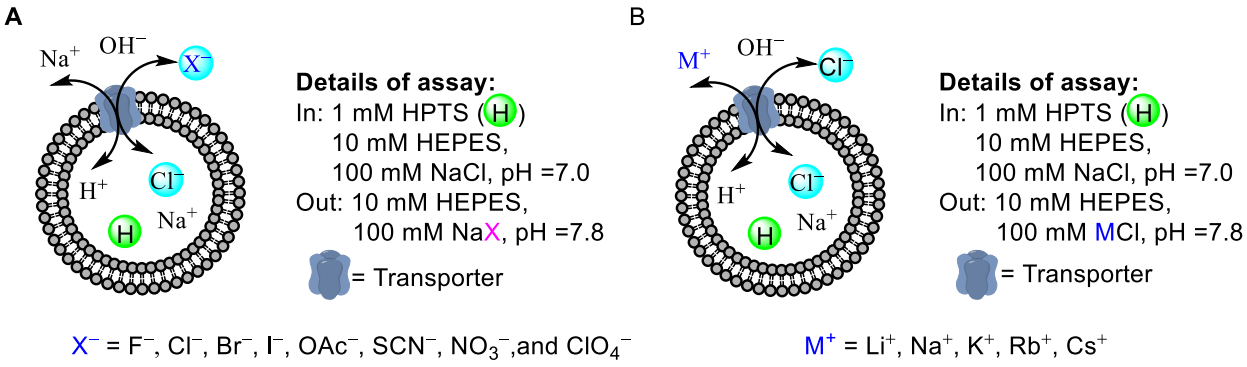

Figure 2.15 Schematic representations of fluorescence-based anion (A) and cation selectivity (B) assays.

Chloride transport activity across EYPC–LUVs⊃lucigenin vesicles

Preparation of EYPC-LUVs⊃lucigenin vesicles[54]

In a 10 mL clean and dry round bottom flask the thin transparent film of egg yolk phosphatidylcholine (EYPC) was formed by drying 1 mL egg yolk phosphatidylcholine (EYPC, 25 mg/mL in $CHCl_3$) with providing continuous rotation and purging nitrogen. The transparent thin film was kept on high vacuum for 4 h to remove all trace of $CHCl_3$. Then the transparent thin film was hydrated with 1 mL aqueous $NaNO_3$ (200 mM, 1 mM Lucigenin) with occasional vertexing at 10-minute interval for 1 h. The resulting suspension was subjected for freeze and thaw cycles (≥15, liquid nitrogen, 55 ° C water bath) and 21 times extrusion through 200 nm pore size polycarbonate membrane. The size exclusion chromatography (using Sephadex G-50) was performed to remove extracellular dye using 200 mM $NaNO_3$ solution as eluent, finally collected vesicles were diluted to 4 mL. Final conditions: ~5 mM EYPC; inside: 200 mM $NaNO_3$, 1 mM lucigenin, pH 7.0; outside: 200 mM $NaNO_3$.

Ion transport activity by Lucigenin assay

In clean and dry fluorescence cuvette 1975 µL 200 mM $NaNO_3$ solution and 25 µL EYPC-LUVs⊃lucigenin was taken. This suspension was placed in a slowly stirring condition in fluorescence instrument equipped with a magnetic stirrer (at $t = 0$ s). The fluorescence intensity of lucigenin was monitored at λ_{em} = 535 nm (λ_{ex} = 450 nm) as a course of time. The chloride gradient was created by addition of 33.3 µL NaCl (2.0 M) at t = 20 s between intra and extra vesicular system, followed by addition of transporter at t = 100 s. Finally, vesicles were lysed by addition of Triton X-100 at t = 300 s for the complete destruction of chloride gradient.

The time-dependent data were normalized to percent change in fluorescence intensity using Equation 4:

$$I_F = [(I_t - I_0) / (I_\infty - I_0)] \times -100) \qquad \text{(Equation 4)}$$

Where, I_0 is the initial intensity, I_t is the intensity at time t, and I_∞ is the final intensity after the addition of Triton X-100.

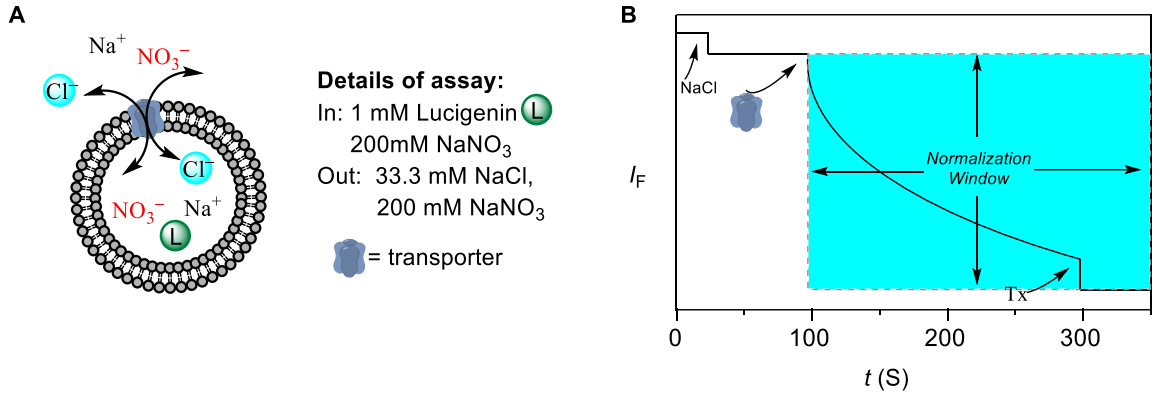

Figure 2.16 Representations of fluorescence-based ion transport activity assay using EYPC–LUVs⊃lucigenin (A), and illustration of ion transport kinetics showing normalization window (B).

Involvement of cation in transport process:

The involvement of cations in the transport process was evaluated from the lucigenin-based assay. The preparation of solutions and vesicles are similar as described in above section. In assay condition the chloride salt of various cation (M^+ = Li^+, Na^+, K^+, Rb^+ and Cs^+) were added to evaluate the contribution of cation in transport process.

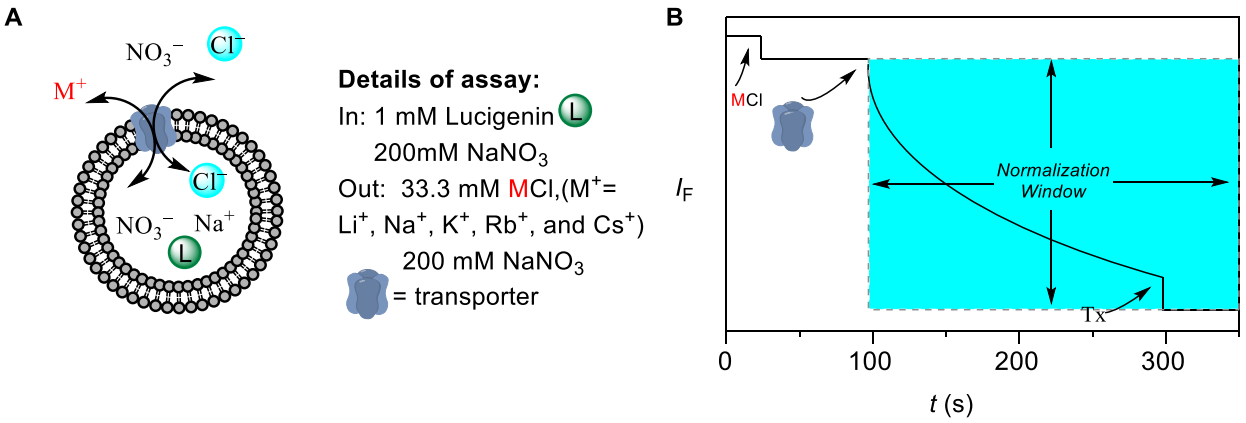

Figure 2.17 Representations of chloride influx activity assay using EYPC–LUVs⊃lucigenin by varying extravesicular cations (A), and illustration of chloride influx kinetics showing normalization window (B).

Cation transport activity: In a clean and dry fluorescence cuvette 1950 μL of $NaNO_3$ solution (200 mM) was added followed by addition of 50 μL of EYPC/cholesterol- LUVs⊃lucigenin. The cuvette was placed in the fluorescence instrument in slowly stirring condition by a magnetic stirrer equipped with the instrument (at t = 0 s). The time course of lucigenin fluorescence emission intensity, F_t was observed at λ_{em} = 535 nm (λ_{ex} = 450 nm). 33.3 μL of 2 M MCl (M^+ = Li^+, Na^+, K^+, Rb^+ and Cs^+) was added to the cuvette at t = 25 s to create the chloride gradient between the intra and extra vesicular system. Transporter molecules were added at t = 100 s in different concentration and finally 25 μL of 10% Triton X-100 was added at t = 300 s to lyse those vesicles resulting destruction of chloride gradient (Fig. S8).

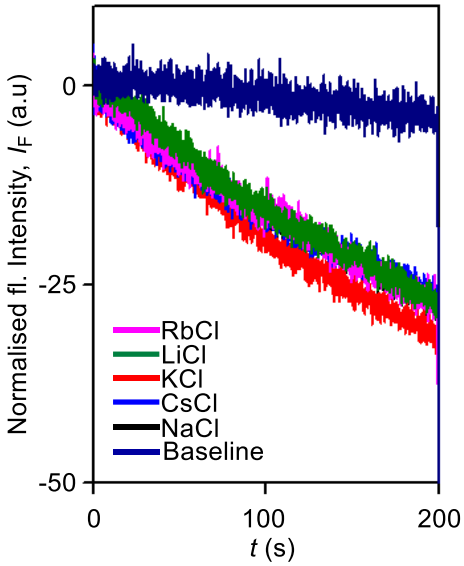

Figure 2.18 Influence of extravesicular cations in the Cl^- influx by **1a** at 20 μM.

Evaluation of membrane stability and channel nature by ANTS-DPX assay

EYPC-LUVs were loaded with anionic fluorophore ANTS (8-aminonaphthalene-1,3,6-trisulfonic acid disodium salt) and cationic quencher DPX (1,1-[1,4-phenylenebis(methylene)] bis[pyridinium]bromide) (Figure. 2.19). Efflux of either ANTS or DPX through pores formed by **1a** was followed by an increase in ANTS emission intensity.[64]

The following buffers were prepared by known method.[65]
Buffer A: 12.5 mM ANTS, 45.0 mM DPX, 5 mM TES, 20 mM KCl, pH = 7.0
Buffer B: 5 mM TES, 100 mM KCl, pH = 7.0.

Preparation of EYPC-LUVs⊃ANTS/DPX vesicles: A thin film of EYPC lipid was prepared by evaporating a solution (1 mL) of EYPC lipid (25 mg/mL) in $CHCl_3$ evaporated slowly by a

stream of nitrogen and then in vacuo (6 h), and then hydrated with 1 mL buffer A, followed by vortex treatment (4 times). The resulting suspension was subjected to > 5 freeze-thaw cycles (using liquid N_2 to freeze and a warm water bath to thaw), and 19 times extruded using a Mini-Extruder through a 100 nm polycarbonate membrane (Avanti). External ANTS/DPX was removed by gel filtration (Sephadex G-50) using buffer B and diluted with the same buffer to 3 mL to give EYPC-LUVs⊃ ANTS/DPX stock solution.

ANTS/DPX-assay: In a clean and dry fluorescence cuvette, 50 µL of above lipid solution and 1950 µL buffer B were added. The compound **1a** was added at 50 seconds and kept in slowly stirring condition by a magnetic stirrer equipped with the fluorescence instrument (at t = 0 s). The time course of fluorescence emission intensity, F_t was monitored at λ_{em} = 520 nm (λ_{ex} = 353 nm). Finally, at t = 300 s, 25 µL of 10% Triton X-100 was added to lyse all vesicles for 100% dye efflux. Fluorescence intensities (F_t) were normalized to fractional emission intensity I_F using Equation S4.

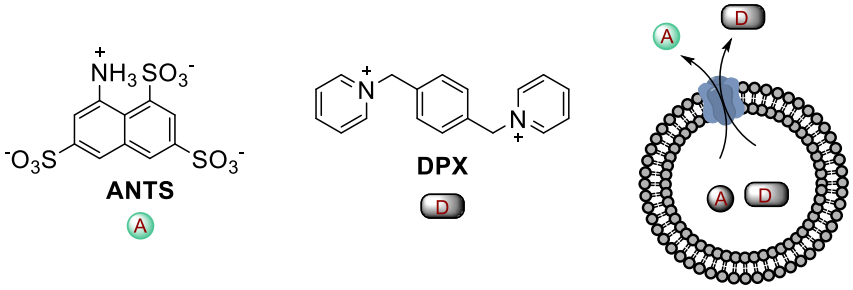

Figure 2.19 Structure of ANTS and DPX dyes and representation of ANTS–DPX assay.

2.4.5 Planar Bilayer Conductance Measurements[66]

Bilayer membrane (BLM) was formed across an aperture of 150 µM diameter in a polystyrene cup (Warner Instrument, USA) with lipid diphytanoylphosphatidylcholine (Avanti Polar Lipids), dissolved in *n*-decane (18 mg/mL). Both chambers (*cis* and *trans*) were filled with symmetrical solution, containing 1 M KCl. The *trans* compartment was held at virtual ground and the *cis* chamber was connected to the BC 535 head-stage (Warner Instrument, USA) via matched Ag-AgCl electrodes. Compound **1a** (20 µM) was added to the *trans* chamber and the solution was stirred with a magnetic stirrer for 30 min. Channel formation was confirmed by the distinctive channel opening and closing events after applying voltages. Currents were low pass filtered at 1 kHz using pClamp9 software (Molecular Probes, USA) and an analog-to-digital converter (Digidata 1440, Molecular Probes). All data were analyzed by the software pClamp 9.

The complete data trace observed for ten minutes contained a series of opening and closing events at some indefinite intervals. From a large and complete trace, a small portion is presented above (Figure. 2.11A, B). The average current was calculated from this trace and then conductance and other calculations were made accordingly.

Calculation of ion channel diameter: Diameter of artificial ion channel was calculated according to Hille's equation,

$$1/g = (l + \pi d/4) \times (4\rho / \pi d^2) \qquad \text{(Equation 5)}$$

Where, g = corrected conductance (obtained by multiplying measured conductance with the Sansom's correction factor) = 3.37×10^{-10} S, l = length of the ion channel = 34 Å, and ρ = resistivity of the 1 M KCl solution = 9.47 Ω·cm).

Anion selectivity by Planar Bilayer Conductance Measurements:

The *cis* and *trans* chambers were filled with unsymmetric solutions of KCl. The *cis* chamber was filled with 2 M KCl solution and the *trans* chamber was filled with 1 M KCl. The compound **1a** (20 µM) was added to the *trans* chamber and stirred for 20 minutes. The reversal potential was calculated to be 14 ± 2 mV.

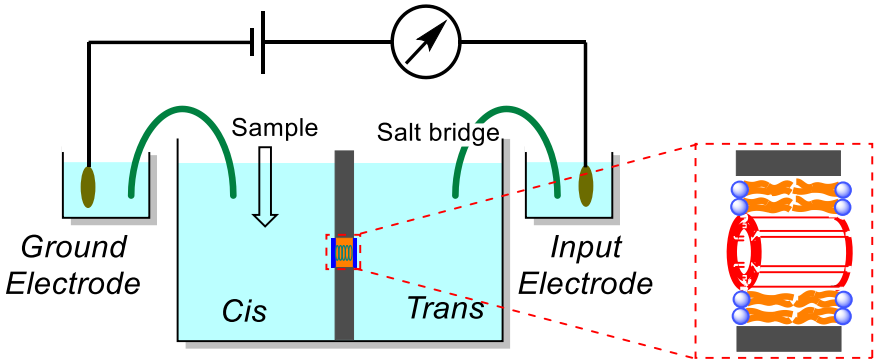

Figure 2.20 Systematic representation of black lipid membrane experiment.

2.4.6 Theoretical Studies (*Done in collaboration with Amal Vijay and Prof. Arnab Mukherjee from Chemistry Department, IISER Pune*)

The theoretical calculations were carried out using GROMACS 2019.6 software to get more insights about the pattern of intermolecular hydrogen bonding among the bis(cholyl) derivative units. This optimized hydrazide and oxalamide based channels were then placed in the DPhPC

lipid bilayer membrane and constructed two different systems. Afterward, the Molecular Dynamics Simulations were carried out by using an explicit pre-equilibrated phospholipid bilayer of 128 DPHPC (1,2-diphytanoyl-*sn*-glycero-3-phosphocholine) obtained from Lipidbook.[67] The optimized channel was inserted in a box of 128 POPC molecules using inflategro methodology[60] at the proper density (area per lipid) of ~ 0.83 nm^2. To solvate the system, ~11000 SPC[61] model water molecules were added to the system. GROMOS-53a6 united atom force field[62] was used for DPhPC molecules. The automated topology builder[68] created by Malde, et al. was used to create the all-atom topology parameters of the channel with GROMOS-53a6[69] force field. Initially the ions were kept near the bottom of the channel and the system was energy minimized using steepest descent method for 50000 steps. This was followed by equilibration for 1 ns at constant 323 K temperature and 1 bar pressure using Nosé-Hoover thermostat[70] and Parrinello-Rahman barostat[71] with a coupling constant of 0.5 ps and 5 ps, respectively. The time step of each simulation was taken as 2 fs. PME[72] electrostatics was used for electrostatic interactions using a 12 Å cut-off with the van der Waals (vdW) cut-off set at 12 Å. Position restraints of 500 kJ/mol nm^2 is applied to the heavy atoms of the channel molecules. The simulation box was found to be approximately 7.4X7.7X9.0 nm^3 for both the channels. A final 10 ns molecular dynamics simulation at constant 323 K temperature and 1 bar pressure was carried out using Nosé-Hoover thermostat[70] and Parrinello-Rahman barostat[71] with a coupling constant of 0.5 ps and 2 ps respectively with similar electrostatics and vdW as in equilibration process. Initially the chloride ion was placed at the starting of the channels made of hydrazide and oxalamide units. The centre of mass (COM) distance between the channel and the chloride ion was calculated for the 10 ns trajectory (Figure. 2.13A). It was found that the ions get separated from the channel and come to the bulk water within 500 ps in the case of oxalamide channel. While in the case of hydrazide channel it is found that the ions are stabilized at the middle of the channel (COM distance nearly 0Å) indicating that the individual hydrazide units are stabilizing the chloride ion compared to oxalamide channel. Further, the average interaction energy between the channel molecules was calculated. It is found that the channelchannel interaction is more favoured by the oxalamide derivative than that by hydrazide derivative in this case.

2.4.7 NMR Spectra

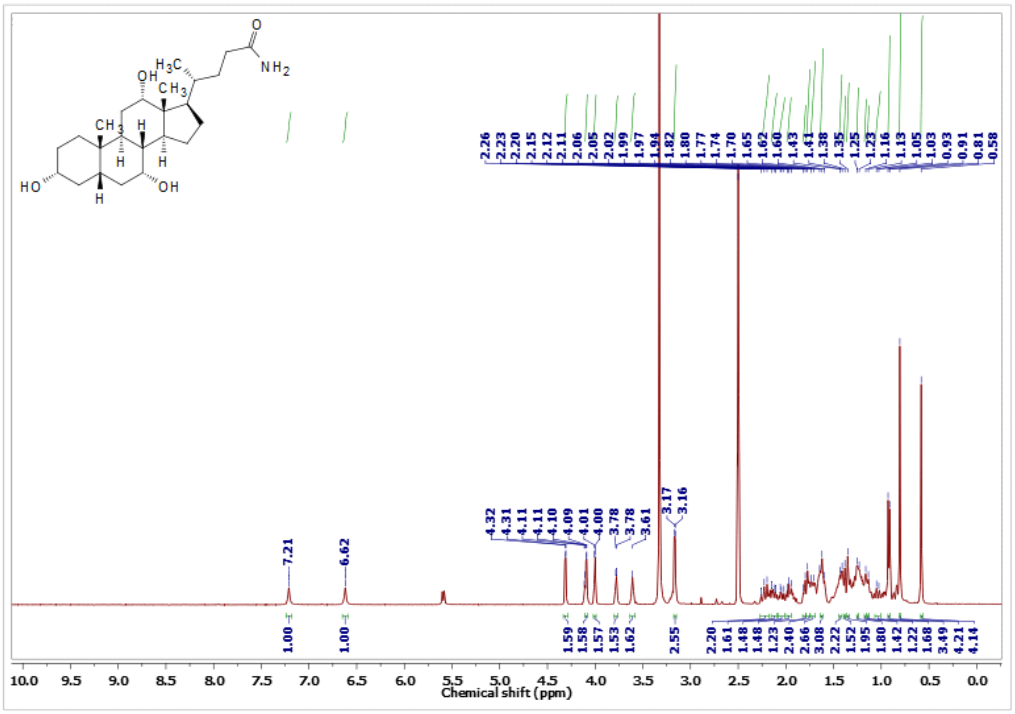

Figure 2.21 ^{1}H NMR spectrum of **2** in DMSO-d_6.

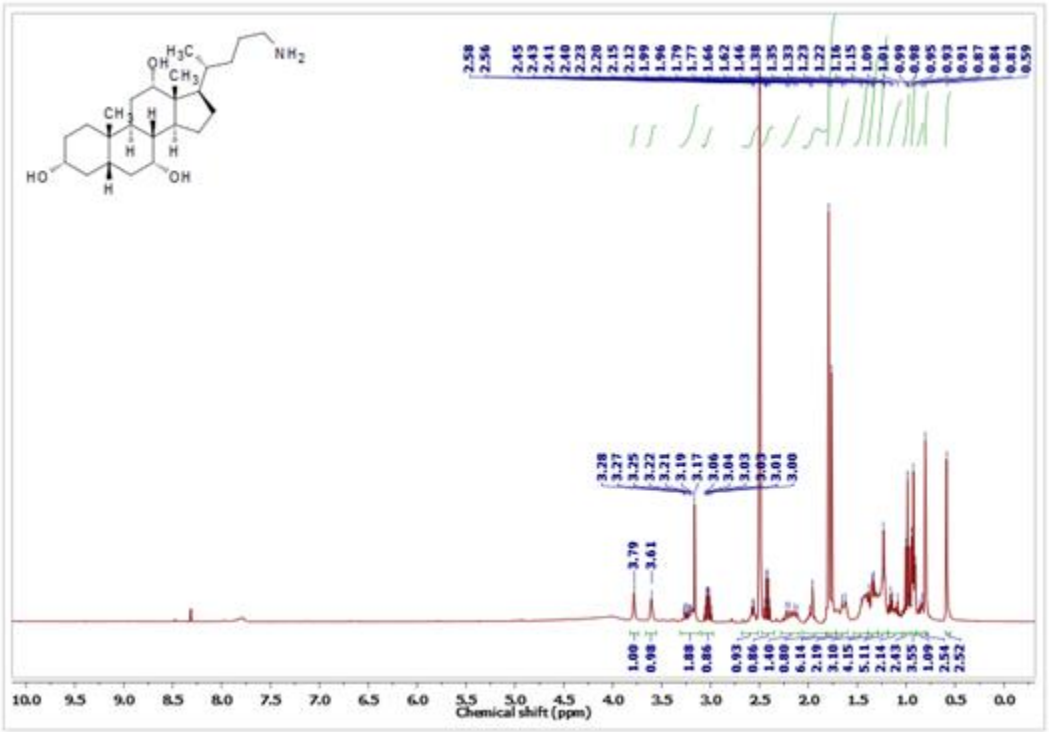

Figure 2.22 ^{1}H NMR spectrum of **3** in DMSO-d_6.

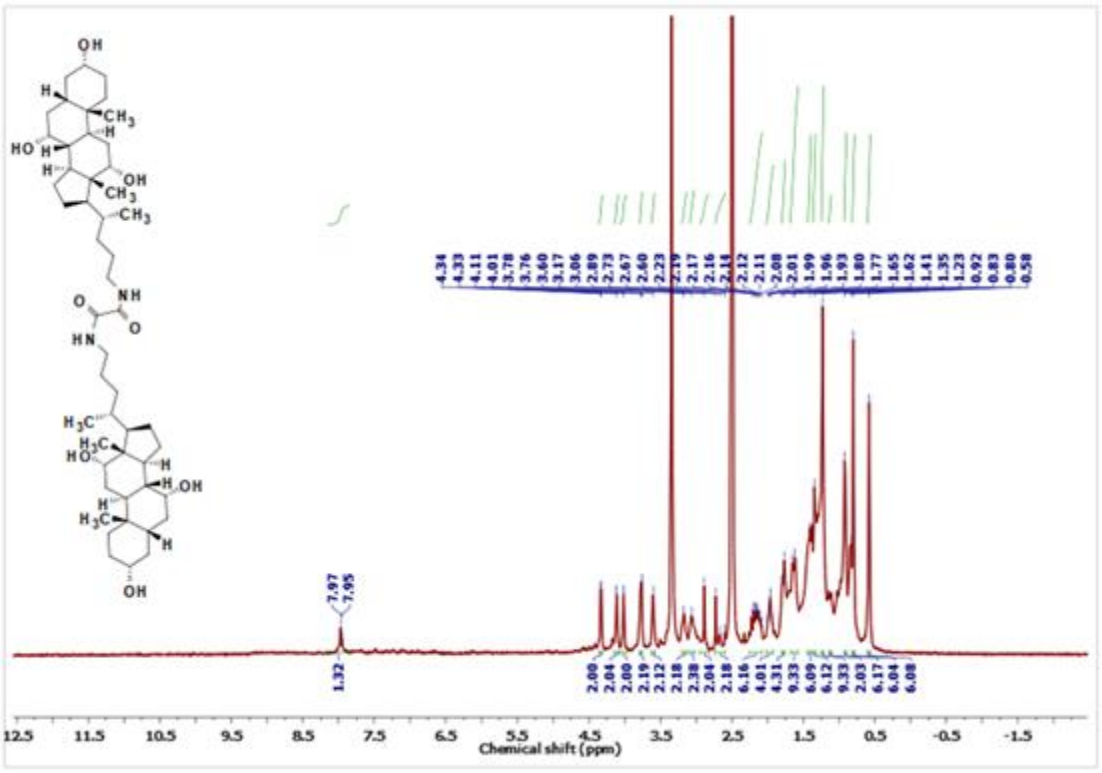

Figure 2.23 ^{1}H NMR spectrum of **1a** in DMSO-d_6.

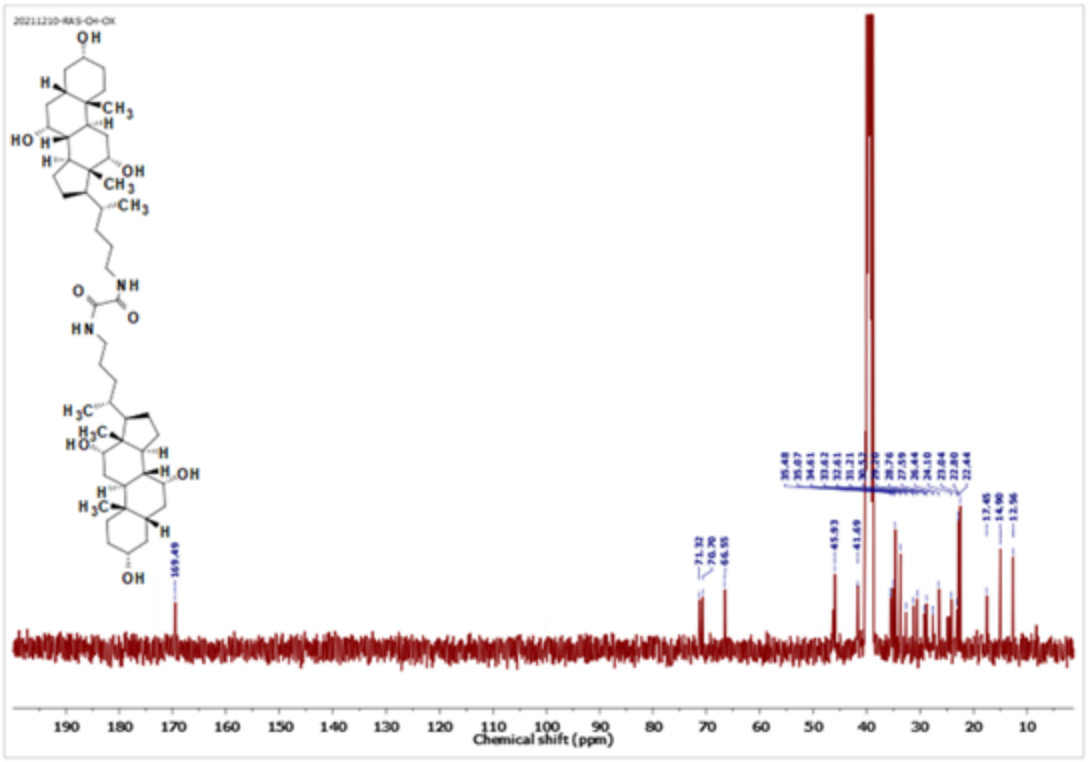

Figure 2.24 ^{13}C NMR spectrum of **1a** in DMSO-d_6.

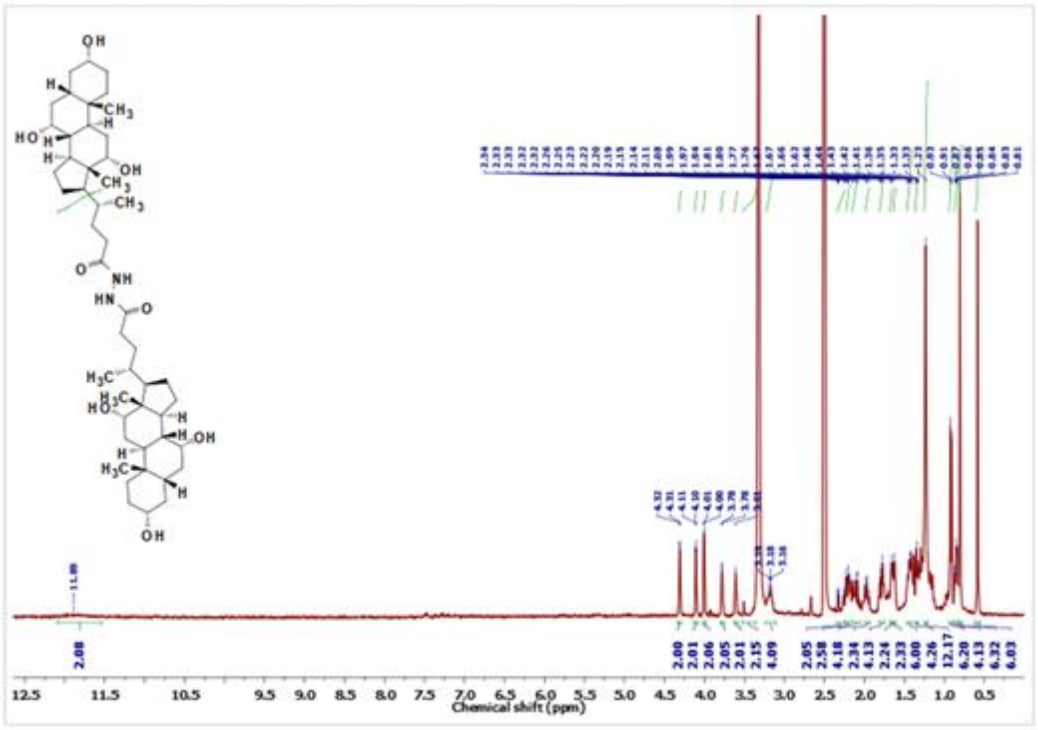

Figure 2.25 ^{1}H NMR spectrum of **1b** in DMSO-d_6.

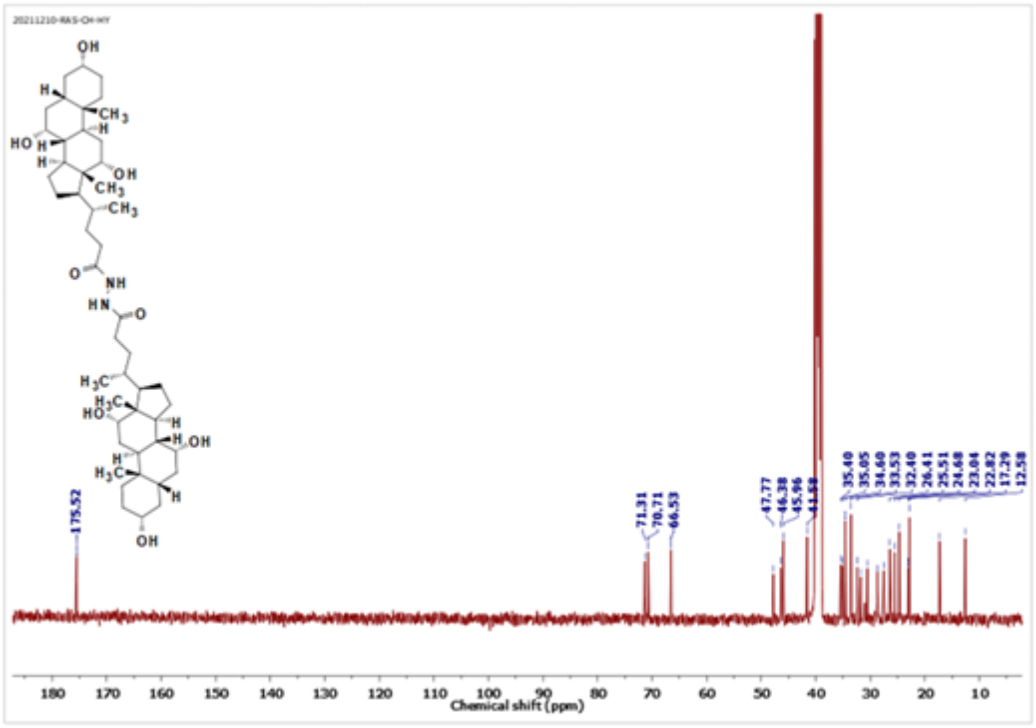

Figure 2.26 ^{13}C NMR spectrum of **1b** in DMSO-d_6.

2.5 References

1 T. W. Allen, O. S. Andersen and B. Roux, *Proc. Natl. Acad. Sci. U. S. A.*, 2004, **101**, 117–122.

2 P. Agre, *Angew. Chemie Int. Ed.*, 2004, **43**, 4278–4290.

3 R. MacKinnon, *Angew. Chem. Int. Ed. Engl.*, 2004, **43**, 4265–4277.

4 L. H. Pinto, G. R. Dieckmann, C. S. Gandhi, C. G. Papworth, J. Braman, M. A. Shaughnessy, J. D. Lear, R. A. Lamb and W. F. Degrado, *Proc. Natl. Acad. Sci. U. S. A.*, 1997, **94**, 11301–11306.

5 O. S. Smart, J. Breed, G. R. Smith and M. S. P. Sansom, *Biophys. J.*, 1997, **72**, 1109–1126.

6 J. M. Diamond and E. M. Wright, *Annu. Rev. Physiol.*, 1969, **31**, 581–646.

7 O. S. Andersen, *Biophys. J.*, 1983, **41**, 147–165.

8 *Recommended Dietary Allowances*, National Academies Press, 1989.

9 C. Duran, C. H. Thompson, Q. Xiao and H. C. Hartzell, *Annu. Rev. Physiol.*, 2009, 72, 95–121.

10 T. J. Jentsch and M. Pusch, *Physiol. Rev.*, 2018, **98**, 1493–1590.

11 E. N. W. Howe, N. Busschaert, X. Wu, S. N. Berry, J. Ho, M. E. Light, D. D. Czech, H. A. Klein, J. A. Kitchen and P. A. Gale, *J. Am. Chem. Soc.*, 2016, **138**, 8301–8308.

12 J. T. Davis, O. Okunola and R. Quesada, *Chem. Soc. Rev.*, 2010, **39**, 3843–3862.

13 R. Planells-Cases and T. J. Jentsch, *Biochim. Biophys. Acta - Mol. Basis Dis.*, 2009, **1792**, 173–189.

14 H. Von Der Maase, L. Sengelov, J. T. Roberts, S. Ricci, L. Dogliotti, T. Oliver, M. J. Moore, A. Zimmermann and M. Arning, *J. Clin. Oncol.*, 2005, **23**, 4602–4608.

15 R. D. Vaughan-Jones, K. W. Spitzer and P. Swietach, *J. Mol. Cell. Cardiol.*, 2009, **46**, 318–331.

16 J. Y. Choi, D. Muallem, K. Kiselyov, M. G. Lee, P. J. Thomas and S. Muallem, *Nature*, 2001, **410**, 94–97.

17 D. Bok, G. Galbraith, I. Lopez, M. Woodruff, S. Nusinowitz, H. BeltrandelRio, W. Huang, S. Zhao, R. Geske, C. Montgomery, I. Van Sligtenhorst, C. Friddle, K. Platt, M. J. Sparks, A. Pushkin, N. Abuladze, A. Ishiyama, R. Dukkipati, W. Liu and I. Kurtz, *Nat. Genet.*, 2003, **34**, 313–319.

18 A. Rousselle and D. Heymann, 2002, **30**, 533–540.

19 Alan S. Verkman and Luis J. V. Galietta, *Nat. Rev. Drug Discov.*, 2009, **8**, 153–171.

20 A. K. M. Lam and R. Dutzler, *Nat. Commun.*, 2021, **12**, 786.

21 M. J. Ackerman and D. E. Clapham, *N. Engl. J. Med.*, 1997, **336**, 1575–1586.

22 F. M. Ashcroft, *Nature*, 2006, **440**, 440–447.

23 R. Dutzler, E. B. Campbell, M. Cadene[2], B. T. Chait[2] and R. Mackinnon, *Nature*, 2002, **415,** 287–294.

24 R. Dutzler, *FEBS Lett.*, 2004, **564**, 229–233.

25 T. J. Jentsch, V. Stein, F. Weinreich and A. A. Zdebik, *Physiol. Rev.*, 2002, 82, 503–568.

26 E. Park, E. B. Campbell and R. MacKinnon, *Nature*, 2017, **541**, 500–505.

27 A. K. Koster, C. A. P. Wood, R. Thomas-Tran, T. S. Chavan, J. Almqvist, K. H. Choi, J. Du Bois and M. Maduke, *Proc. Natl. Acad. Sci. U.S.A.*, 2018, **115,** E4900–E4909.

28 C. Chhun and A. R. Schmitzer, *Medchemcomm*, 2011, **2**, 987–990.

29 P. Xin, S. Tan, Y. Wang, Y. Sun, Y. Wang, Y. Xu and C. P. Chen, *Chem. Commun.*, 2017, **53**, 625–628.

30 N. Madhavan, E. C. Robert and M. S. Gin, *Angew. Chemie - Int. Ed.*, 2005, **44**, 7584–7587.

31 W. Si, Z. T. Li and J. L. Hou, *Angew. Chemie - Int. Ed.*, 2014, **53**, 4578–4581.

32 M. Maduke, C. Miller and J. A. Mindell, *Annu. Rev. Biophys. Biomol. Struct.*, 2000, **29**, 411–438.

33 Y. Kobuke and T. Nagatani, *J. Org. Chem.*, 2001, **66**, 5094–5101.

34 J. Montenegro, M. R. Ghadiri and J. R. Granja, *Acc. Chem. Res.*, 2013, **46**, 2955–2965.

35 T. Saha, A. Roy, M. L. Gening, D. V. Titov, A. G. Gerbst, Y. E. Tsvetkov, N. E. Nifantiev and P. Talukdar, *Chem. Commun.*, 2014, **50**, 5514–5516.

36 A. Martinez-Cuezva, S. Valero-Moya, M. Alajarin and J. Berna, *Chem. Commun.*, 2015, **51,** 14501–14504

37 W. L. Huang, X. D. Wang, Y. F. Ao, Q. Q. Wang and D. X. Wang, *J. Am. Chem. Soc.*, 2020, **142**, 13273–13277.

38 J. A. Malla, A. Roy and P. Talukdar, *Org. Lett*, 2018, **20**, 5991–5994.

39 P. Bandyopadhyay, V. Janout, L. H. Zhang, J. A. Sawko and S. L. Regen, *J. Am. Chem. Soc.*, 2000, **122**, 12888–12889.

40 P. Bandyopadhyay, V. Janout, L. H. Zhang and S. L. Regen, *J. Am. Chem. Soc.*, 2001, **123**, 7691–7696.

41 C. Goto, M. Yamamura, A. Satake and Y. Kobuke, *J. Am. Chem. Soc.*, 2001, **123**, 12152–12159.

42 Y. M. Lu, L. Q. Deng, X. Huang, J.-X. Chen, B. Wang, Z.-Z. Zhou, G.-S. Hu and W.-H. Chen, *Org. Biomol. Chem.*, 2013, **11**, 8221–8227.

43 A. J. Ayling, M. N. Pérez-Payán and A. P. Davis, *J. Am. Chem. Soc.*, 2001, **123**, 12716–12717.

44 W. H. Chen, X. B. Shao and S. L. Regen, *J. Am. Chem. Soc.*, 2005, **127**, 12727–12735.

45 M. Yoshii, M. Yamamura, A. Satake and Y. Kobuke, *Org. Biomol. Chem.*, 2004, **2**, 2619–2623.

46 C. P. Wilson and S. J. Webb, *Chem. Commun.*, 2008, 4007–4009.

47 H. Li, H. Valkenier, L. W. Judd, P. R. Brotherhood, S. Hussain, J. A. Cooper, O. Jurček, H. A. Sparkes, D. N. Sheppard and A. P. Davis, *Nat. Chem.*, 2016, **8**, 24–32.

48 J. Shen, Y. Gu, L. Ke, Q. Zhang, Y. Cao, Y. Lin, Z. Wu, C. Wu, Y. Mu, Y. L. Wu, C. Ren and H. Zeng, *Nat. Commun.*, 2022, **13**, 5985–5985.

49 Y. Zhou, E. H. Ryu, Y. Zhao and L. K. Woo, *Organometallics*, 2007, **26**, 358–364.

50 A. Roy, D. Saha, P. S. Mandal, A. Mukherjee and P. Talukdar, *Chem. - A Eur. J.*, 2017, **23**, 1241–1247.

51 S. Litvinchuk, G. Bollot, J. Mareda, A. Som, D. Ronan, M. R. Shah, P. Perrottet, N. Sakai and S. Matile, *J. Am. Chem. Soc.*, 2004, **126**, 10067–10075.

52 C. Goto, M. Yamamura, A. Satake and Y. Kobuke, *J. Am. Chem. Soc.*, 2001, **123**, 12152–12159.

53 T. Saha, S. Dasari, D. Tewari, A. Prathap, K. M. Sureshan, A. K. Bera, A. Mukherjee and P. Talukdar, *J. Am. Chem. Soc.*, 2014, **136**, 14128–14135.

54 A. Roy, D. Saha, A. Mukherjee and P. Talukdar, *Org. Lett.*, 2016, **18**, 5864–5867.

55 T. Saha, A. Gautam, A. Mukherjee, M. Lahiri and P. Talukdar, *J. Am. Chem. Soc.*, 2016, **138**, 16443–16451.

56 T. M. Fyles, *Chem. Soc. Rev.*, 2007, **36**, 335–347.

57 W. H. T. Press; S. A. Teukolsky; W. T. Vetterling; B. P. Flannery, *Numerical Recipes: The Art of Scientific Computing*, Cambridge University Press, Third Edit., 2007.

58 J. Domański, P. J. Stansfeld, M. S. P. Sansom and O. Beckstein, *J. Membr. Biol.*, 2010, **236**, 255–258.

59 B. Hess, C. Kutzner, D. Van Der Spoel and E. Lindahl, *J. Chem. Theory Comput.*, 2008, **4**, 435–447.

60 T. H. Schmidt and C. Kandt, *J. Chem. Inf. Model.*, 2012, **52**, 2657–2669.

61 H.J.C. Berendsen, J.P.M. Postma and J. Hermans, *D. Reidel Publishing Company*, 1981,

331–342.

62 C. Oostenbrink, A. Villa, A. E. Mark and W. F. Van Gunsteren, *J. Comput. Chem.*, 2004, **25**, 1656–1676.

63 A. K. Malde, L. Zuo, M. Breeze, M. Stroet, D. Poger, P. C. Nair, C. Oostenbrink and A. E. Mark, *J. Chem. Theory Comput.*, 2011, **7**, 4026–4037.

64 N. Sakai and S. Matile, *J. Am. Chem. Soc.*, 2002, **124**, 1184–1185.

65 P. Talukdar, N. Sakai, N. Sordé, D. Gerard, V. M. F. Cardona and S. Matile, *Bioorganic Med. Chem.*, 2004, **12**, 1325–1336.

66 C. Ren, X. Ding, A. Roy, J. Shen, S. Zhou, F. Chen, S. F. Yau Li, H. Ren, Y. Y. Yang and H. Zeng, *Chem. Sci.*, 2018, **9**, 4044–4051.

67 J. Domański, P. J. Stansfeld, M. S. P. Sansom and O. Beckstein, *J. Membr. Biol.*, 2010, **236**, 255–258.

68 A. K. Malde, L. Zuo, M. Breeze, M. Stroet, D. Poger, P. C. Nair, C. Oostenbrink and A. E. Mark, *J. Chem. Theory Comput*, 2011, **7**, 4026–4037.

69 B. Hess, C. Kutzner, D. Van Der Spoel and E. Lindahl, *J. Chem. Theory Comput.*, 2008, **4**, 435–447.

70 S. Nosé, *Mol. Phys.*, 1984, **52**, 255–268.

71 M. Parrinello and A. Rahman, *J. Appl. Phys.*, 1981, **52**, 7182–7190.

72 T. Darden, D. York and L. Pedersen, *J. Chem. Phys.*, 1993, **98**, 10089–10092.

Chapter 3

Self-assembled anion channel formation by bis(1,3-propanediol)-linked meta - dipropynylbenzene-based small molecules

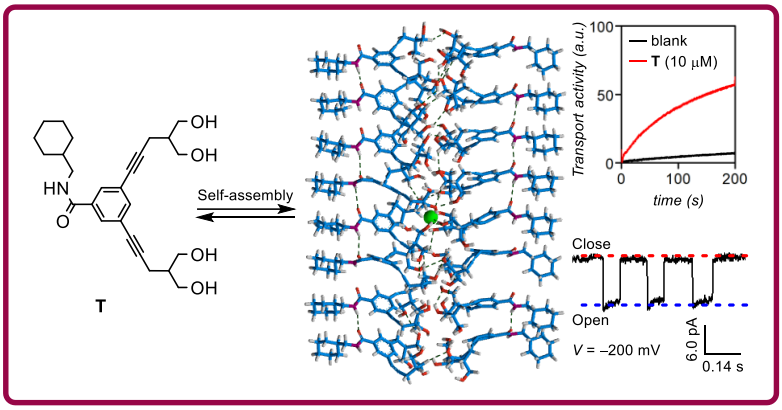

3.1 Introduction

The specificity of naturally occurring ion channels towards different ions is attributed to their ion selectivity, which is facilitated by the presence of multiple ion binding sites. The channel's lumen presents numerous binding sites for selective ions, thereby facilitating their translocation across the lipophilic regions of the cellular membrane. The arduous discovery has led to the emergence of unimolecular ion channels or self-assembled supramolecular ion channels. The development of synthetic ion channels with repeating ion-recognition sites is a challenging task, particularly for small-molecule-based ion channels. Despite the abundance of reports on self-assembled ion channels, several factors such as the poorly preorganized geometry of monomers, unpredictable self-assembly, and lack of well-arranged binding sites contribute to this challenge. Previously, synthetic ion channel designs that included multiple ion recognition sites were primarily selective towards cations.[1–9] However, Matile and colleagues recently published findings on transmembrane supramolecules that possess single-file multiple anion recognition sites.[10] It has been observed that rigid-rod molecules based on oligonaphthalene-diimide[10,11] and oligoperylenediimide[12] make π-slides in lipid vesicles. When studying ion transport with these supramolecules, the anion interactions at each recognition site along the channel direction accounted for their selectivity (Figure 3.1). The single channel conductance of these molecules, however, is poorly understood. In 2014, our group reported a mannitol-based anion channel that self-assembles via 1,2-diol mediated H-bonding, with the hydroxyl groups serving as single-file anion recognition sites inside the channel.[13] The 1,2-diol motif was utilised at both termini of a stiff 1,3-diethynylbenzene nucleus to create a proficient chloride channel structure, which exhibited cellular apoptosis mediated by chloride. According to the theoretical calculation, the 1,2-diol arms present in the 1,3-diethynylbenzene-based channel are involved in the formation of an intermolecular hydrogen bonded network, which serves to stabilise the overall structure of the channel. The high prevalence of hydroxyl (−OH) groups present in these locations prompted us to contemplate it as the recognition motif.[14–20] The notion is subject to debate, as all synthetic ion channels that incorporate a −OH group exhibit selectivity towards cations.[3,21–23] The selectivity in these synthetic channels is attributed to the recognition of cation by a pair of oxygen atoms that are not bonded to any other atoms.[24] The −OH group is widely recognised as the most prominent hydrogen bond donor group for anion recognition.[25–27] This suggests that it can potentially be utilised in the development of anion selective ion channels.

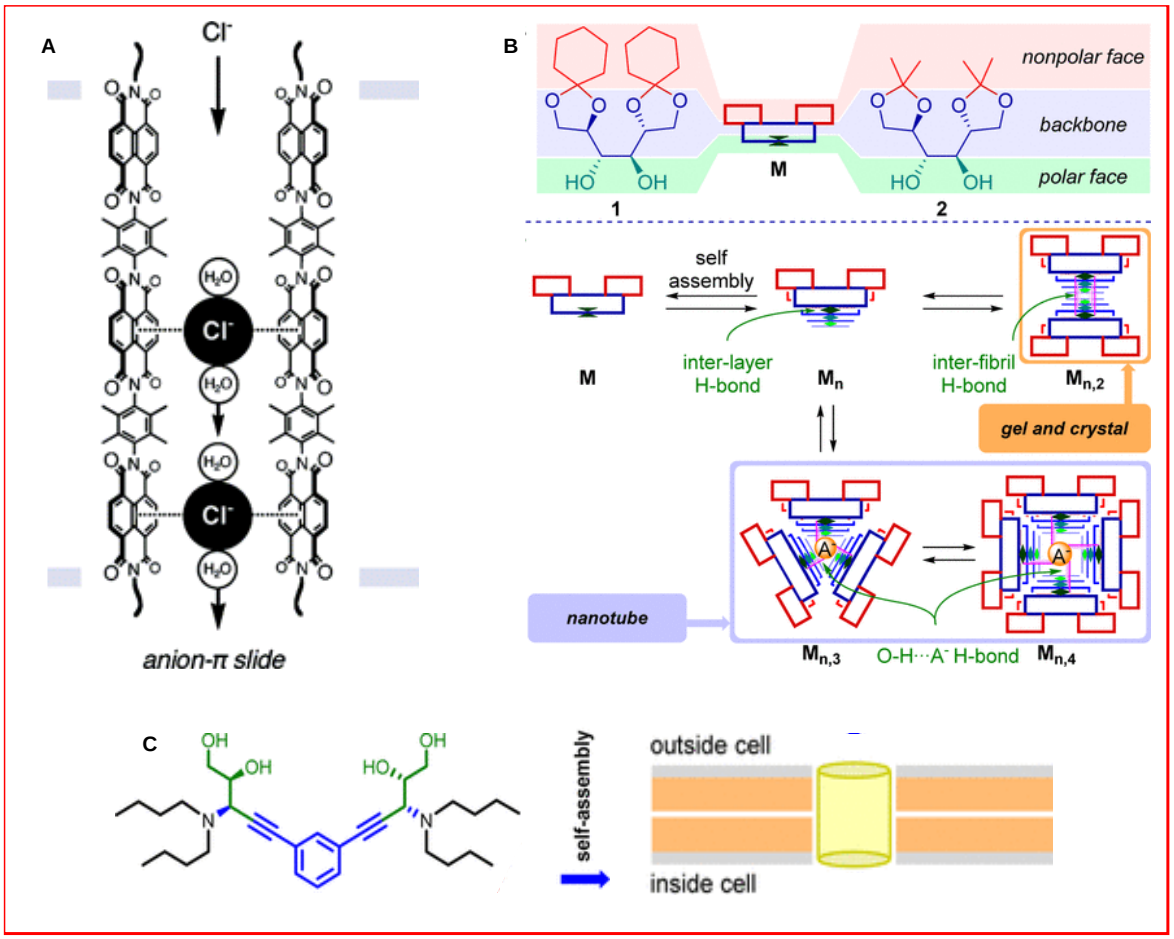

Figure 3.1 Self-assembled rigid oligo(aromatic diimide) rods based on anion−π interactions (A). Self-assembled mannitol-based rosette ion channel for selective chloride transport (B). Vicinal diols self-assembled supramolecular barrel-rosette ion channel (C).

The 1,3-diol motif is closely associated with the 1,2-diol motif and is recognised for its involvement in numerous self-assembly mechanisms via hydrogen bonding interactions.[28–32] The 1,3-diol moiety is considered to be a compelling system for the development of novel supramolecular ion channels that possess single-file ion recognition sites. The present study details the creation and advancement of synthetic ion channels utilising two bis(1,3-diol)-linked molecules, denoted as **1** and **2** in Figure 3.2. The channel-forming molecules were designed by linking two 2-ethynylpropane-1,3-diol moieties to the C-3 and C-5 positions of a central phenyl ring. Additionally, the central phenyl ring contains either an ester or amide moiety at its C-1 position. Alkyne spacers were utilised to prevent the formation of intramolecular hydrogen bonds between two arms' hydroxyl groups and to ensure adequate width for the resulting channel. It was hypothesised that the formation of a nanotubular assembly of dimeric rosettes would occur in each system through the intra- and intermolecular

H-bonding interactions of hydroxyl groups (as depicted in Figure 3.2). Furthermore, the intermolecular hydrogen bonding interactions of amide functional groups would confer enhanced stability to the channel created by compound **2** as compared to that formed by compound **1**. It was hypothesised that the disparity in stability between **2** and **1** would lead to enhanced ion transportation through the channel by the former.

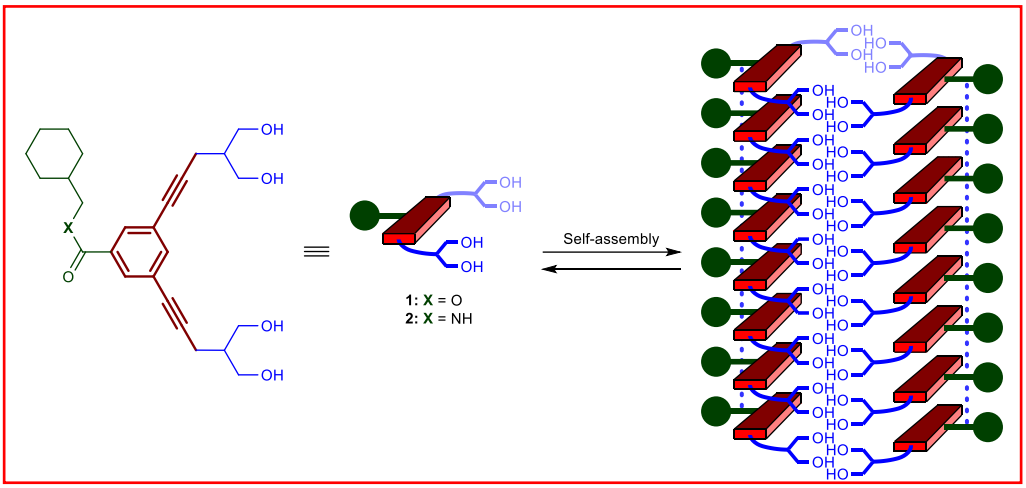

Figure 3.2 Self-assembly of individual monomers, **1** and **2** into barrel-rosette channel.

3.2 Results and Discussion

3.2.1 Synthesis

Compounds **1** and **2** were synthesized from compounds **4** and **5** respectively. The synthesis of compounds **1** and **2** is described in Scheme 1. At first, 3,5-diiodobenzoic acid **3** was synthesized according to the reported protocol.[33] Similarly, 2-(prop-2-yn-1-yl)propane-1,3-diol **6** was prepared from diethyl malonate following the reported protocol.[34] Then the reaction of compound **3** with (bromomethyl)cyclohexane in the presence of K_2CO_3 in DMF provided compound **4** with 85% yield. Subsequently, the reaction of compound **4** with **6** in the presence of $(Ph_3P)_2PdCl_2$, CuI, and Et_3N afforded the bis(diol) **1** in 78% yield. On the other hand, the coupling of compound **3** with cyclohexylmethanamine in the presence of EDC·HCl, HOBT, and Et_3N in DMF provided **5** with 83% yield. Compound **5** was then converted to **2** with 86% yield by reacting with **6** in the presence of $(Ph_3P)_2PdCl_2$, CuI, and Et_3N (Scheme 1). All compounds were purified by column chromatography and characterized by ^1H NMR, ^{13}C NMR, HRMS, and IR.

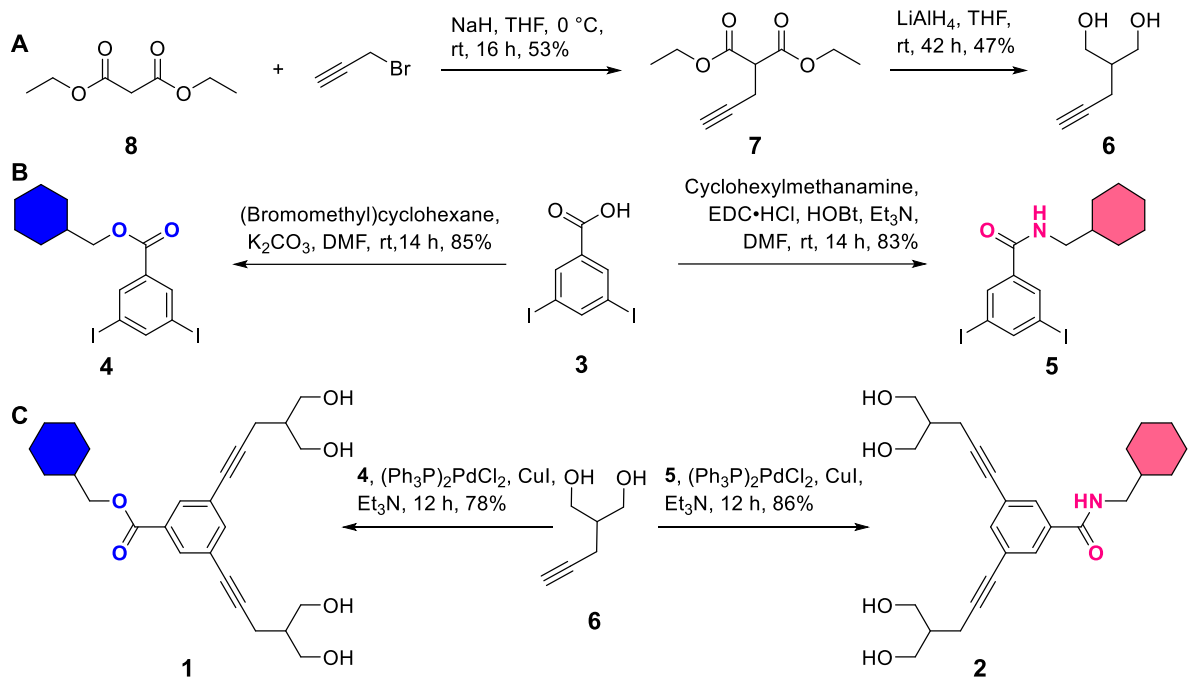

Scheme 3.1. Synthesis of bis-1,3-diol ester derivative **1** and amide derivative **2**.

3.2.2 Crystallographic Studies

The crystal structures of **2** was obtained from the MeOH solvent system which crystalizes in triclinic space group (P-1). X-ray single-crystal structures give a fair indication of the self-assembly in solid state and their propensity to build OH channel superstructures and potential for self-organization in bilayer membranes. The single crystal structure of **2** revealed that each unit is connected through a continuous intermolecular N–H···O hydrogen bonding between two layers giving it a barrel-rosette type of assembly. Additionally compound **2** crystalizes in a parallelly displaced stacking along a-axis in which both the hydroxyl groups (pair 1) of one arm are pointed toward up-ward direction, whereas the hydroxyl groups (pair 2) connect to the other arm are pointed in opposite direction to each other (i.e., up and down) (Figure 3.4). The pair of hydroxyl groups (pair 1) directed in same direction exhibit strong hydrogen bonding through intermolecular O–H···O interactions with the hydroxyl groups in opposite layer (pair 2), giving rise to a six-membered intermolecular hydrogen bonded network system. CPK model makes it abundantly clear that the parallelly displaced structure lacks enough cavity for the chloride ion to pass through it (Figure 3.5). We suggested a different arrangement of molecules in the lipid bilayer membrane to allow the flow of ions as the cavity in the solid state is insufficient for this process (Figure 3.14A).

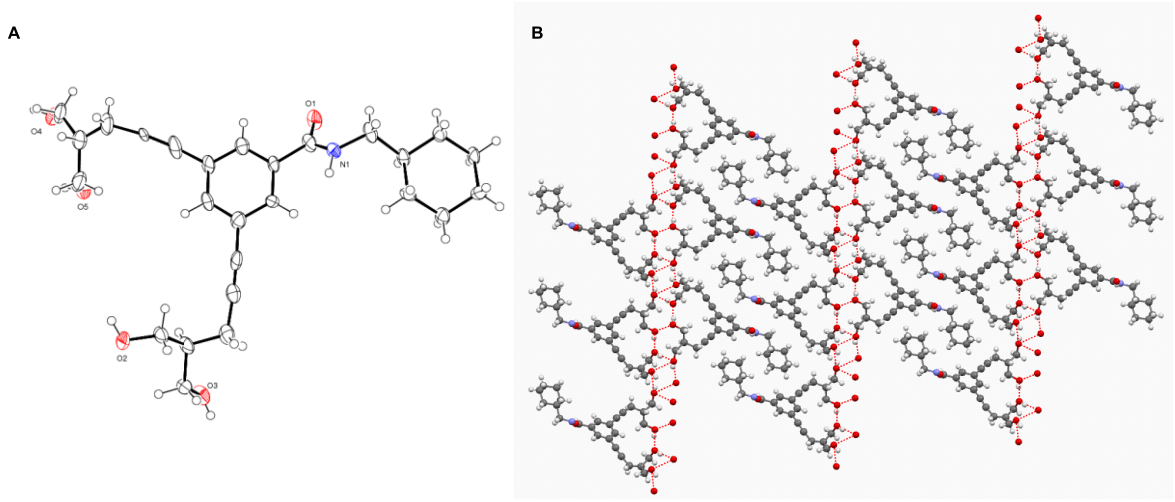

Figure 3.3. ORTEP diagram of **2** (A). Hydrogen bonded network of **2** in the solid state (B).

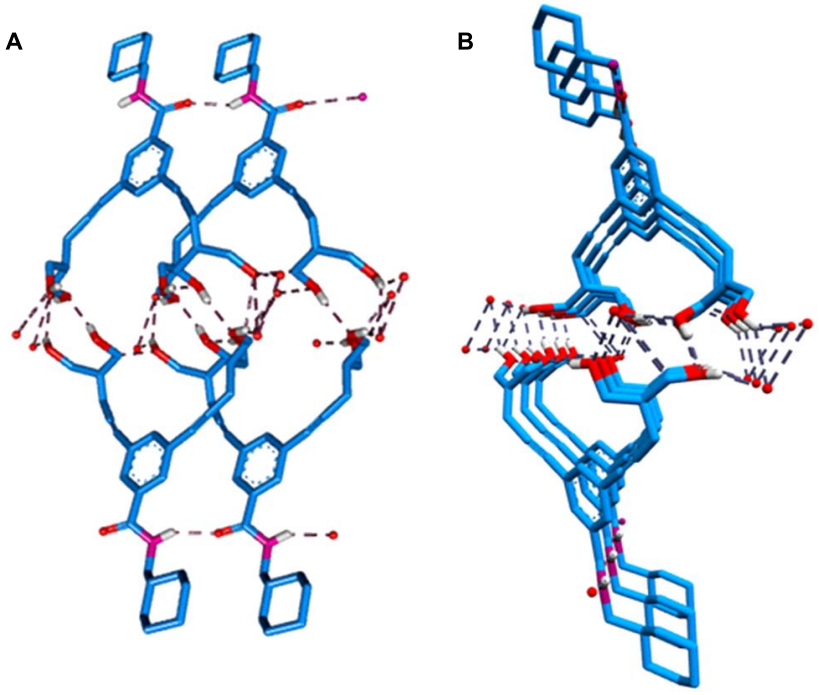

Figure 3.4 Solid state packing of **2**, Side view (A), Top view (B) (dots denotes the atom from another molecule, omitted for clarity).

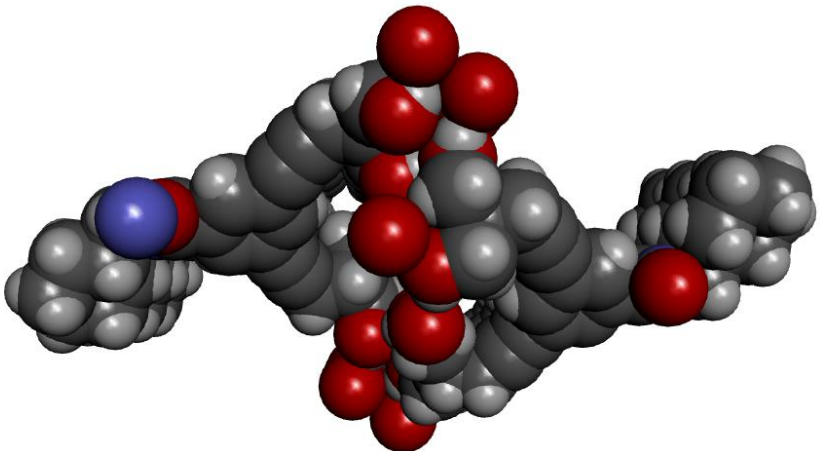

Figure 3.5. Three molecules are stacked in two adjacent layers facing each other in the space fill model for **2** (along a-axis).

3.2.3 Ion Transport Studies

Compounds **1** and **2** were examined for their ion transport capabilities across large unilamellar vesicles (LUVs) prepared from egg yolk phosphatidylcholine (EYPC) lipid by encasing 8-hydroxypyrene-1,3,6-trisulfonate (HPTS) dye and NaCl, and after applying a ΔpH of 0.8 (pH_{out} = 7.8 and pH_{in} = 7.0), ion transport activities were monitored by measuring the increment in HPTS fluorescence at λ_{ex} = 450 nm (λ_{em} = 510 nm) with time.[10,35] The comparison of ion transport activity at the identical concentration of 10 μM confirmed a better ion transport efficiency of **2**, as evidenced by its faster equilibration of the applied pH gradient compared to **1** (Figure 3.6). Such higher transport activity of **2** can be corroborated to the additional intermolecular H-bonding between the amide moieties providing the extra rigidity and stability to the channel in the lipid bilayer membrane. Concentration dependent ion transport activity of **2** (5–80 μM) (Figure 3.7B, 3.7C) followed by Hill analysis provide the EC_{50} = 17.19 μM (i.e., 25.65 mol% with respect to the lipid) confirming the compound as an efficient transmembrane transporter. The Hill coefficient (n) value of 1.83 supports that the dimeric form of **2** acts as the active structure for the supramolecular nanochannel assembly. The EC_{50} calculation could not be performed on **1** due to its precipitation observed at higher concentrations (Figure 3.7A).

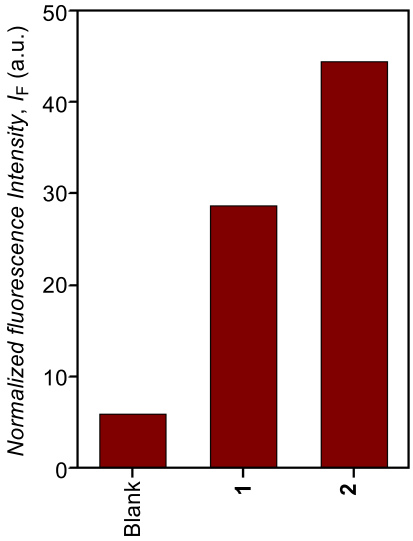

Figure 3.6 Comparison of activities of **1** and **2** (10 μM concentration) across EYPC-LUVs⊃HPTS recorded at 200 s after sample addition.

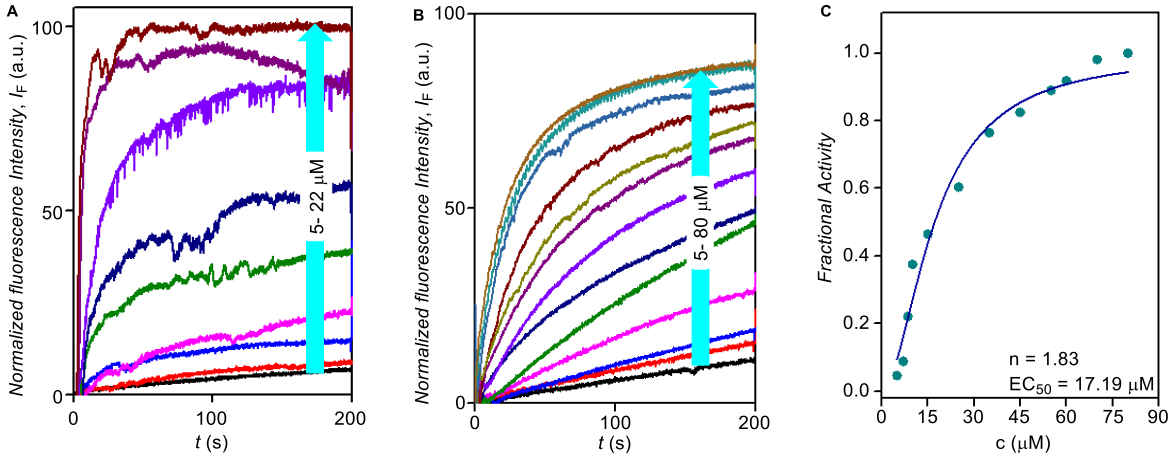

Figure 3.7. Dose-response curve of ester **1** (A), amide **2** (B) derivative across EYPC-LUVs⊃HPTS. (C) Hill analysis of compound **2** at 170 s.

3.2.4 Ion Selectivity Studies and Transport Mechanism

To scrutinize the ion selectivity and transport mechanism, the most active compound **2** was selected. By varying the extravesicular ions in the HEPES buffer solution, selectivity studies on compound **2** were carried out. The ion transport activity altered insignificantly when the metal ions in the extravesicular buffer containing trapped HPTS and isoosmolar NaCl were varied among Li^+, Na^+, K^+, Rb^+ and Cs^+ (Figure 3.8B). These findings demonstrate that cations are not engaged in the rate-limiting steps of the ion transport process by **2**. However, substituting the anions of the extravesicular sodium salts among F^-, Cl^-, Br^-, OAc^-, and NO_3^-

resulted in a substantial variation in ion transport activity, indicating the activity sequence: Cl^- > F^- > OAc^- > Br^- ≈ NO_3^- that confirmed the involvement of anions in the ion transport mechanism (Figure 3.8A).

To evaluate the preferential ion selectivity between OH^- and Cl^-, the transport activity was measured in the presence of valinomycin, a K^+ selective ionophores. In a typical experiment, KCl was added to the extravesicular buffer along with iso-osmolar intravesicular NaCl, and the collapse of the imposed pH gradient by **2** was observed in the presence and absence of valinomycin. If compound **2** facilitates superior OH^- transport over Cl^-, a cooperative increase in the pH gradient collapse rate is anticipated. In contrast, if the transport of Cl^- is enhanced by the presence of molecule **2**, no cooperative effect is observed. Comparable rates of pH gradient collapse were found when the ion transport activity of **2** was measured in the absence and presence of valinomycin (Figure 3.8C). Therefore, the experiments indicated preferential selectivity of **2** towards Cl^- over OH^-, i.e., Cl^- ≫ OH^-.

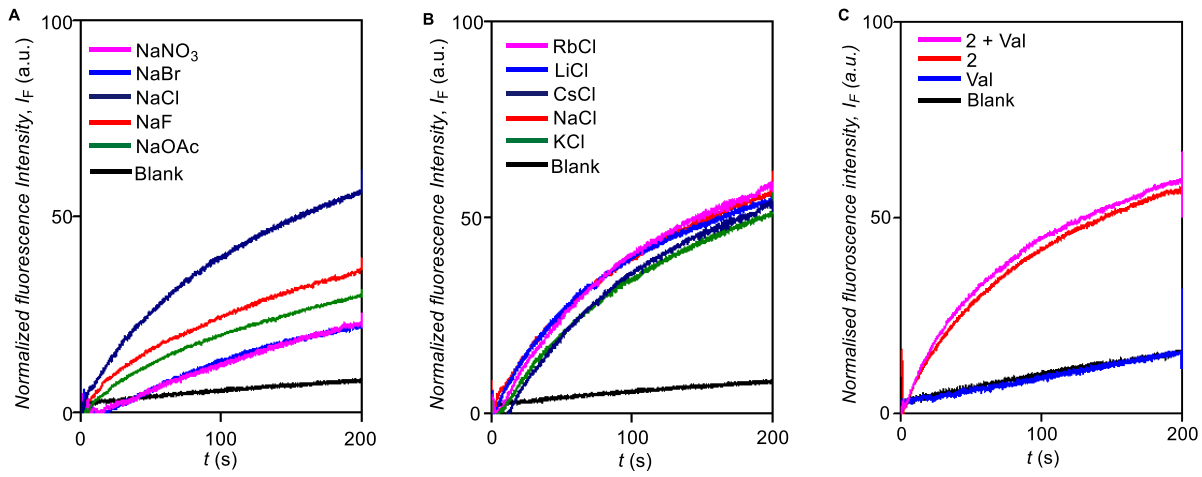

Figure 3.8. Anion selectivity (A) and cation selectivity of **2** at 17 μM (B) across EYPC-LUVs⊃HPTS. Ion transport activity of **2** (18 μM) determined across EYPC–LUVs⊃HPTS in the absence and presence of valinomycin (C).

3.2.5 Chloride Transport Assay

The Cl^- ion transport activity of **2** was explored across LUVs in-depth by measuring the fluorescence intensity of intravesicular lucigenin dye at λ_{em} = 535 nm with λ_{ex} = 450 nm. To confirm the Cl^- ion transport activity of **2**, EYPC-LUVs were prepared by entrapping lucigenin dye (i.e., EYPC- LUVs⊃lucigenin) and $NaNO_3$ salt, and a

Cl^-/NO_3^- gradient was applied by adding NaCl (2 M) to the additional vesicular buffer. The quenching of lucigenin fluorescence caused by the influx of Cl^- ion by **2** was timed. The addition of **2** caused a significant dimming of fluorescence, confirming the influx of Cl^- across the lipid bilayer membrane transport activity (Figure 3.9A). Furthermore, the Cl^- influx rate did not change significantly when the cations in the extravesicular buffer were altered among Li^+, K^+, Rb^+, and Cs^+, excluding the potential role of M^+/Cl^- symport in the transport process (Figure 3.9B). Finally, valinomycin (V), a K^+ selective transporter, was used to get direct experimental insight into the favored transporting mechanism for **2**.[36] EYPC-LUVs⊃lucigenin was suspended in KCl solution with intravesicular $NaNO_3$, and the ion transport rate of **2** was measured in the absence and presence of valinomycin. Cl^- influx got significantly faster when **2** and valinomycin were studied together than when **2** was analyzed alone, showing a coordinated action of two transporters (Figure 3.10A). These observations revealed antiport as the primary transport mechanism by compound **2**. Using vesicles with encapsulated ANTS-DPX dye, the impact of **2** on the lipid bilayer membrane was also investigated. The EYPC-LUV⊃ANTS-DPX (λ_{em} = 520 nm with λ_{ex} = 353 nm) were prepared using a standard method (Figure 3.10B, 3.10C). The absence of significant dye leakage from vesicles suggested that the compound does not disrupt the integrity of the lipid bilayer membrane or create large transmembrane pores.

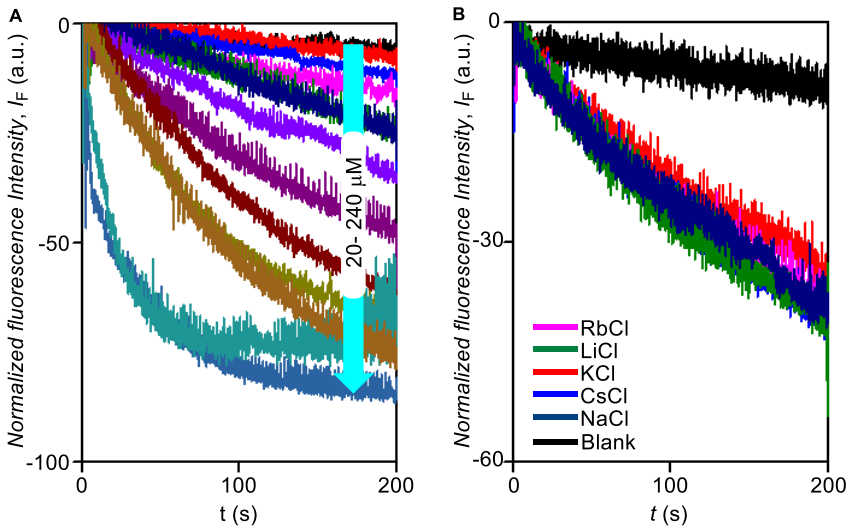

Figure 3.10. Concentration-dependent activity of compound **2** across EYPC-LUVs⊃lucigenin (A) and influence of extravesicular cations in the Cl^- influx by **2** across EYPC-LUVs⊃lucigenin.

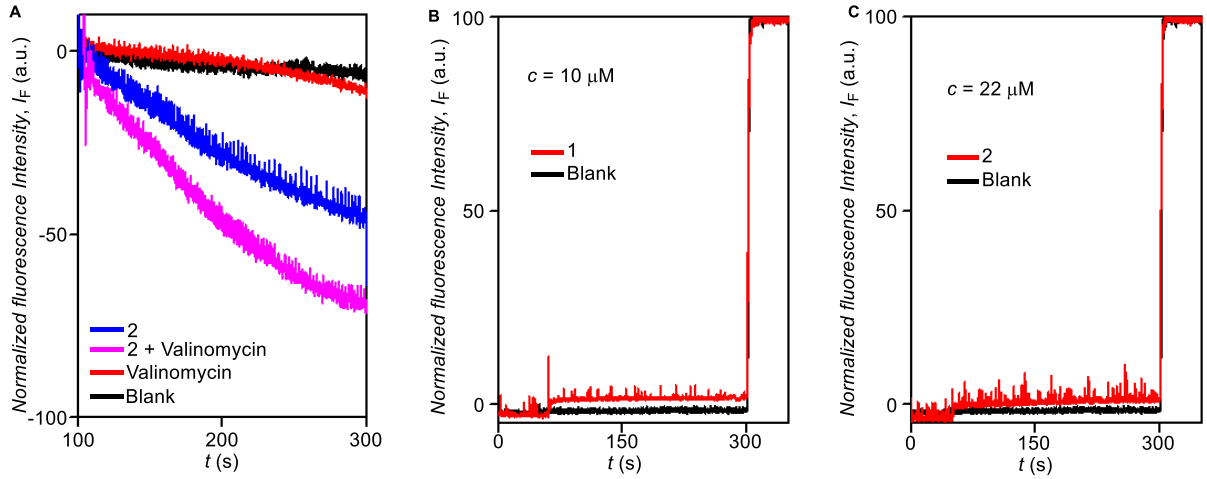

Figure 3.11. Comparison of Cl^- influx activity of **2** in the absence and in the presence of valinomycin (1.25 μM) across EYPC-LUVs⊃lucigenin (A) ANTS–DPX leakage assay in presence of compound **1** (B) and compound **2** (C).

3.2.6 Transporter Mechanism (Cholesterol Method)

The fluidity of the EYPC/cholesterol membrane changes when the amount of cholesterol in it changes, and this should have an impact on carriers by altering their mobility. However, since transmembrane channels span the entire membrane, they shouldn't be impacted. Increasing cholesterol levels will lower the membrane's fluidity to slow down a carrier's rate of transit but won't show any change in the fluorescence of the channel.[36]

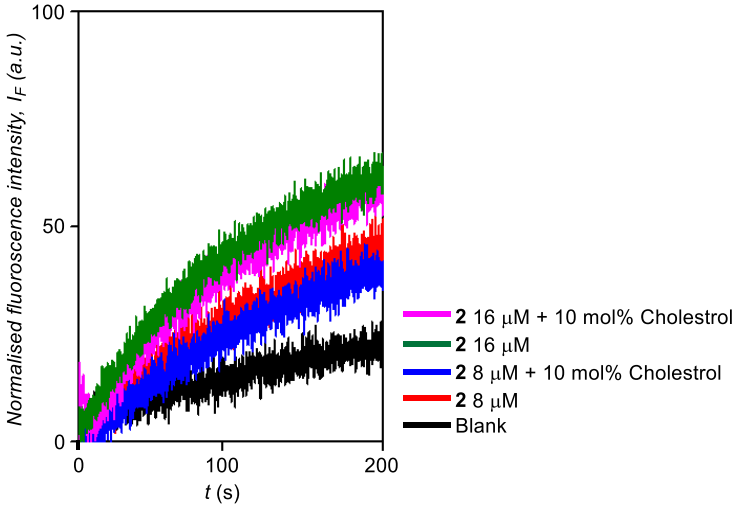

Figure 3.12 Effect of the amount of cholesterol in the EYPC/cholesterol membrane on transport by **2** (10 mol%, of cholesterol in the membrane).

3.2.7 Planar Bilayer Conductance Studies

Planar bilayer conductance studies, in which the ionic conductance across the planar lipid bilayer membrane was examined, demonstrated the development of transmembrane ion channels by compound **2**. A planar lipid bilayer membrane made of diphytanoyl phosphatidylcholine (diPhyPC) lipid was utilized to separate the two chambers (cis and trans chambers) holding unbuffered KCl (1.0 M) solution in this typical experiment.[13] The addition of **2** (10.0 μM) in the cis chamber exhibited distinct channel openings and closings at various holding potentials, suggesting the formation of ion channels (Figure 3.13A, 3.13B). The single-channel conductance was determined to be 42.5 ± 0.9 pS, and the channel diameter was calculated to be 3.56 ± 0.11 Å using the Hille equation (Equation 5). The variation of current with voltage (I–V plot) in the presence of the symmetric solution of KCl (1.0 M each) exhibited a linear variation, i.e., ohmic behavior, confirming the channel's nondipole nature. When the channel's ion selectivity was studied using unsymmetric KCl solutions in two chambers (1.0 M in cis and 2 M in trans), it was discovered that the rate of Cl^- transport is greater than the rate of K^+ transport, with a permeability ratio (P_{Cl^-}/P_{K^+}) = 17.44. (Figure 3.13C). These findings confirmed the anion selectivity for the channel.

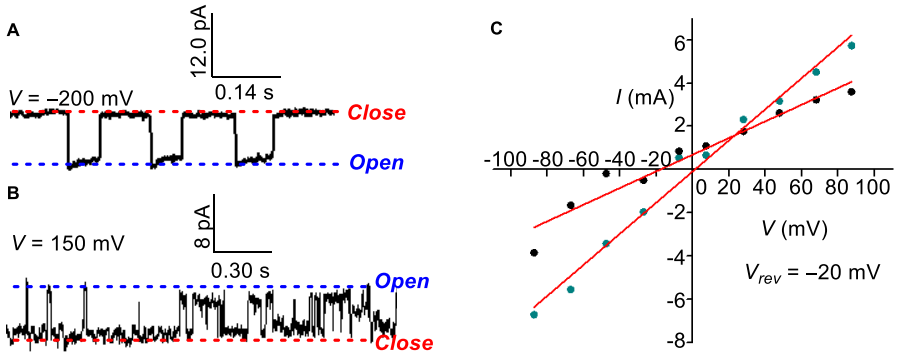

Figure 3.13. Single-channel conductance of **2** (10 μM) recorded at –200 mV (A) at 150 mV under symmetrical KCl solutions (B). I–V plots of **2** under symmetrical (•) and unsymmetrical (•) concentrations of KCl (C).

3.2.8 Molecular Modelling of Ion Channel

To investigate the driving force and mechanism of Cl^- ion permeation, we performed MD simulations of single channel-membrane (DPHPC) system at 200 mM NaCl for 10 ns equilibration followed by 50 ns production run (Figure 3.14A). The partial density profiles of all system components are shown in Figure 3.16, along with orientation distribution and time-dependent density profiles of channel components, which indicate the stability of the system.

A permeation event involving a Cl^- ion was observed between 19.4 ns and 26.0 ns (Figure 3.17). Figure 3.14B shows the position of chloride ion during the permeation. When Cl^- ion comes to the boundary of the channel, it forms hydrogen bond (HB) with hydroxyl and phenyl hydrogens of the channel while retaining its HBs with bulk water (as a transitory intermediate state) before completely getting inserted into the channel (Figure 3.18, 3.19). In the channel, Cl^- ion is surrounded by water, albeit less compared to bulk water. These results indicate that the channel-bulk water interface plays a critical role in the permeation pathway. Since the permeation event is rare (only one event in 50 ns simulation), it does not provide a statistically viable mechanism. Therefore, to probe into the equilibrium free energy and associated mechanism of Cl^- ion permeation, we used state-of-the-art multiple walker metadynamics[37] simulations by positioning a reference chloride ion at various parts of the channel obtained from the permeation event observed in normal MD simulation. The final free energy surface is obtained by reweighting[38] the trajectory with respect to the permeation distance (distance of the Cl^- ion from the center of the channel) and coordination number between the Cl^- ion and water molecules. The initial structure and time evaluation of the permeation distance for each of the independent walker is shown in the Figure 3.20A and 3.20B, respectively. The free energy surface for the permeation is shown in the Figure 3.14C, which shows a stable minimum ("A") at the permeation distance 0.2 nm and Cl^--H_2O coordination number 3. The transition state is observed near the exit of the channel, indicated by the state "B." A flat minimum "C" is observed when the ion reaches the bulk water (minima states are shown in Figure 3.15). The free energy change for permeation is found to be –2.9 kcal/mol. The minimum free energy path describing the permeation pathway is shown by dotted lines in the free energy surface.

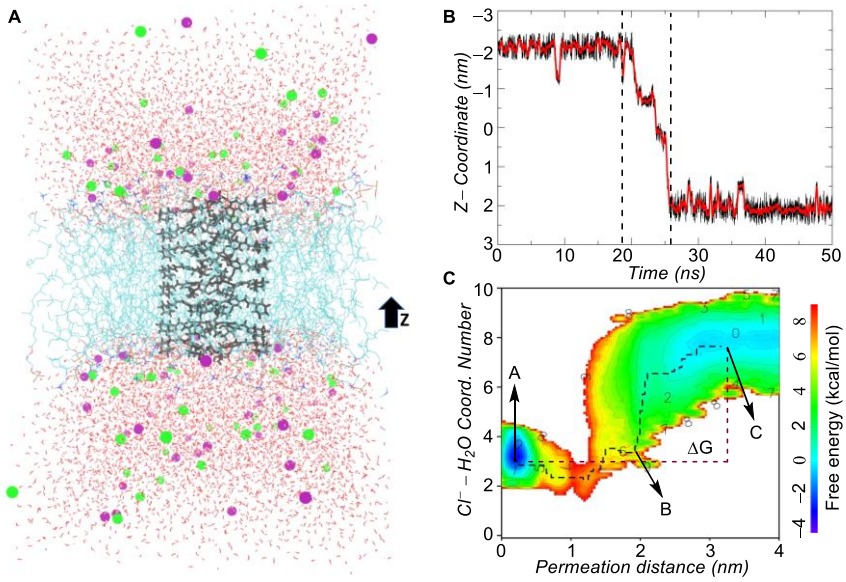

Figure 3.14. Representation of the system with channel inserted in bilayer and solvated with water and 200 mM ion concentration of sodium (purple) and chloride (green) (A). The variation in the position of the chloride ion along Z-Coordinate (channel axis) with respect to time (black) and its running average of 100 frames (red) (B). Free energy surface for the permeation of chloride ion constructed using multiple walker meta dynamics simulations. The permeation pathway in indicated by black dotted lines. The free energy minimum "A" appears at the centre of the channel (permeation distance close to 0). Transition state B and minimum C correspond to the position of the ion in the channel exit and in bulk water (C).

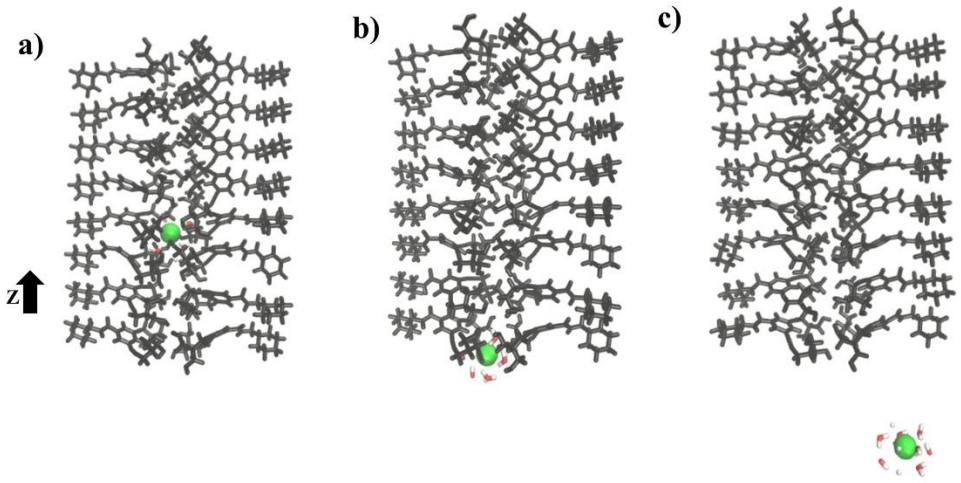

Figure 3.15. Structural representation of minima states, corresponding to the permeation of chloride ion from free energy plots shown in Figure 3.14. Cl^- ion is shown green colour with surrounded water molecules (red colour) minima state "A" (permeated state) (A), minima state "B" (Transition state) (B), and minima state "C" (Free state) (C).

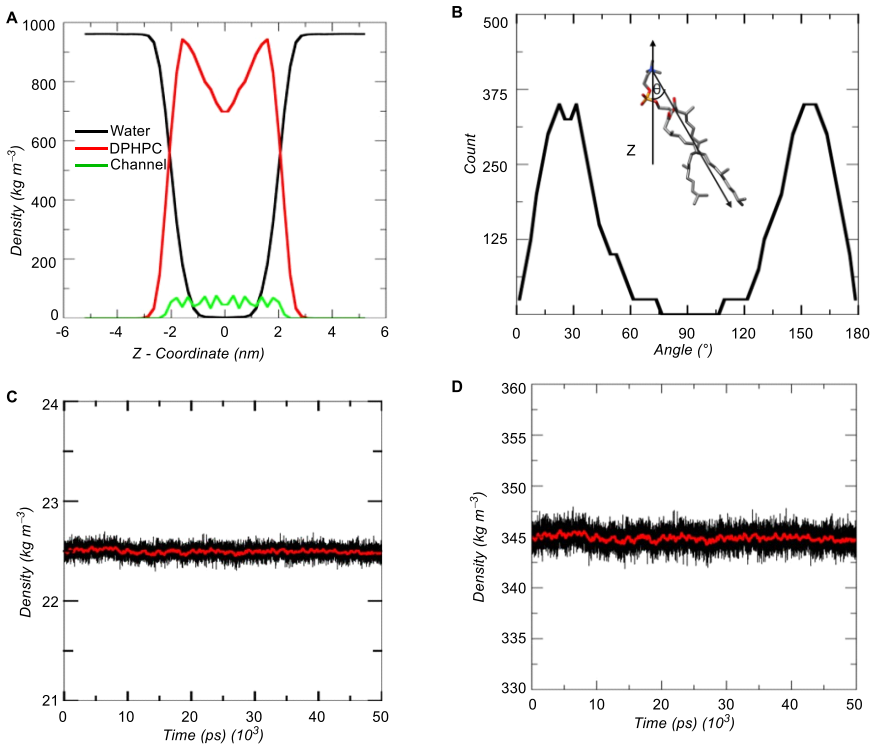

Figure 3.16. Partial density profile of water, DPHPC, and channel present in the system with respect to Z – coordinate (A), Distribution of angle formed by channel axis (Z – direction) and a vector connecting the head group to the long tail end of the alkyl group of the DPHPC. The figure shows two clear peaks near 20° to 32° and 150° to 160°, corresponding to two oppositely oriented molecules in two layers (B), time evolution of the density of channel present in the system (C), time evolution of the density of DPHPC present in the system (D).

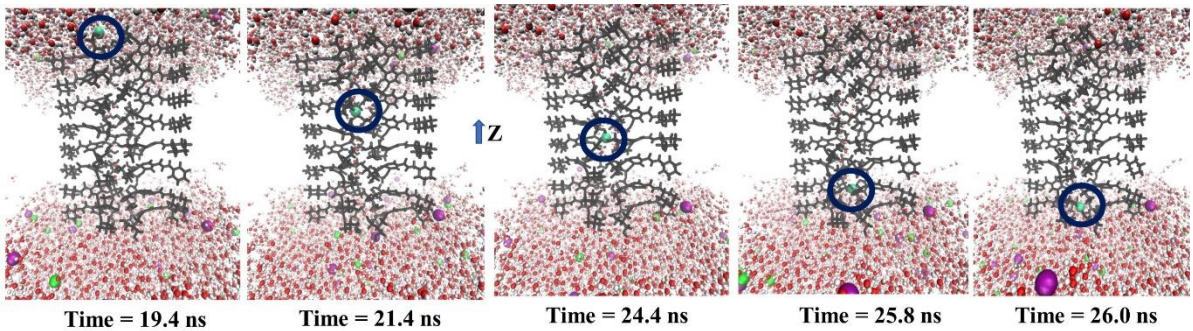

Figure 3.17. A closer view of channel in black (lipid molecules omitted for clarity), water molecules (red), sodium ion (purple), and chloride ions (green; permeating ion is encircled in blue) at different timepoint.

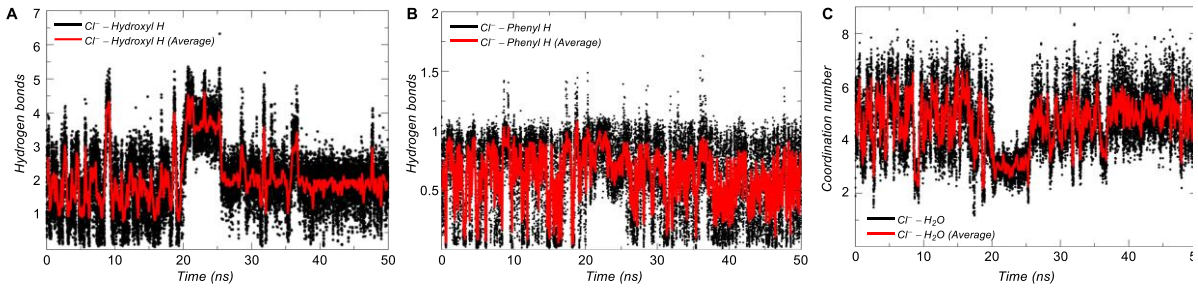

Figure 3.18. Evolution of closest chloride ion (with respect to virtual centre of the channel) permeated through the channel. Variation of Hydrogen bonds between Hydroxyl group and chloride ion with respect to time (A), the variation of hydrogen bonds between phenyl hydrogens and the chloride ion with respect to time (B) and the variation in the coordination number between chloride ion and water molecules with respect to time (C).

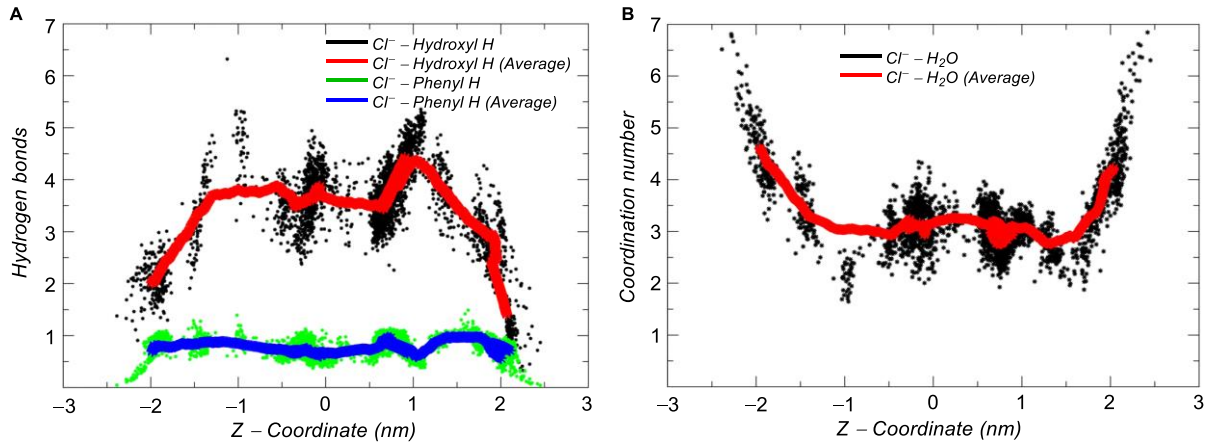

Figure 3.19. Variation of hydrogen bonds between the permeated chloride ions with hydroxyl groups of channel and phenyl hydrogens. The starting and ending residues of the channel have the values –2.2 nm and 2.2 nm respectively (A) and variation of coordination number between chloride ion and water molecule in the system during the permeation pathway (B).

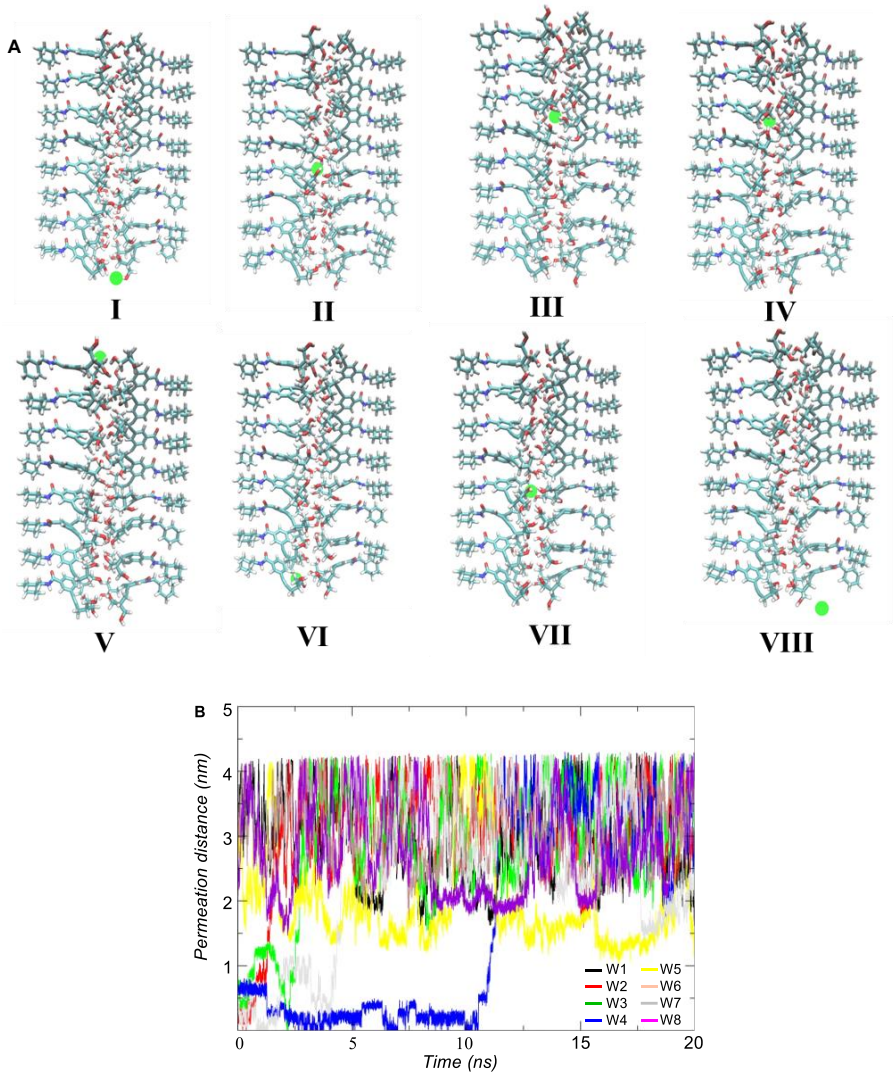

Figure 3.20. Structure of Cl^- and channel in the system used as initial configuration for multiple-walker meta dynamics simulation. The starting geometry with reference Cl^- ion (green) of each of these walkers is shown. (A). Variation of permeation distance with respect to time for each of the walker used for the simulation. The colour code for each of the walker is shown in the inset (B).

3.3 Conclusion

In conclusion, we have developed two bis(1,3-propanediol) based supramolecular synthetic ion channel systems relying primarily on the hydrogen bonding interactions. These channel forming molecules also contain either an ester or amide arm, and the amide linked system displayed better ion transport activity over the ester-based system. The amide-based system favoured anion transport with strong chloride ion selectivity and no cation participation in the process. Planar bilayer conductance measurements corroborated to the formation of ion channels with diameter of 3.56 ± 0.11 Å and $(P_{Cl^-}/P_{K^+}) = 17.44$. The geometry-optimized structure of the postulated amide-based channel with internal chloride ions

validated the establishment of a C═O···H–N hydrogen-bonded channel and anion recognition via –OH···anion interactions.

3.4 Experimental Section

3.4.1 General Method

All reactions were carried out under the nitrogen atmosphere. All the chemicals were purchased from commercial sources and were used as received unless stated otherwise. Solvents were dried by standard methods prior to use or purchased as dry. Thin layer chromatography (TLC) was carried out with E. Merck silica gel 60-F_{254} plates and column chromatography was performed over silica gel (100-200 mesh) obtained from commercial suppliers. Egg yolk phosphatidylcholine (EYPC) lipid was purchased from Avanti Polar Lipids as a solution dissolved in chloroform (25 mg/mL). HEPES buffer, HPTS dye, ANTS-DPX system, Triton X-100, NaOH, and all inorganic salts of molecular biology grade were purchased from Sigma. Gel-permeation chromatography was performed on a column of Sephadex LH-20 gel (25×300 mm, V_0 = 25 mL). Large unilamellar vesicles (LUV) were prepared from EYPC lipid by using a mini extruder, equipped with a polycarbonate membrane either of 100 nm or 200 nm pore size, obtained from Avanti Polar Lipids.

3.4.2 Physical Measurements

The ^{1}H and ^{13}C NMR spectra were recorded on 400 MHz Jeol ECS-400 (or 101 MHz for ^{13}C) spectrometers using either residual solvent signals as an internal reference or from internal tetramethylsilane on the δ scale relative to chloroform (δ 7.26 ppm), dimethylsulphoxide (δ 2.50 ppm), acetone (δ 2.05 ppm) for ^{1}H NMR and chloroform (δ 77.20 ppm), dimethylsulphoxide (δ 39.50 ppm), acetone (δ 29.84 and 206.26 ppm) for ^{13}C NMR. The chemical shifts (δ) are reported in ppm and coupling constants (J) in Hz. The following abbreviations are used: s (singlet), d (doublet) m (multiplet), and td (triplet of doublet) while describing ^{1}H NMR signals. High-resolution mass spectra (HRMS) were obtained from the MicroMass ESI-TOF MS spectrometer. Fluorescence spectra were recorded by using Fluoromax-4 from Jobin Yvon Edison equipped with an injector port and a magnetic stirrer. 10 mM HEPES (with 100 mM NaCl or other salts as per necessity) buffer solutions were used for the fluorescence experiment and the pH of the buffers was adjusted to 7.0 or 8.0 by NaOH and the pH of the buffer solutions was measured using Helmer pH meter. FT-IR spectra were obtained using NICOLET 6700 FT-IR spectrophotometer as KBr disc and reported in cm^{-1}.

Melting points of all the compounds were measured using a VEEGO Melting point apparatus. All melting points were measured in open glass capillary and values are uncorrected. All fluorescence data were processed either by Origin 8.5 or Kaleida Graph and finally, all data were processed through Chem Draw Professional 15.

3.4.3 Synthesis

Synthesis of *diethyl 2-(prop-2-yn-1-yl) malonate*, 7, $C_{10}H_{14}O_4$: Compound **7** was synthesized by a reported protocol.[34] The product was purified by column chromatography (SiO_2, EtOAc/C_6H_{14} = 5:95 – 10:90) to yield product **7,** diethyl 2-(prop-2-yn-1-yl) malonate as transparent liquid (Yield = 53%). **^{1}H NMR** (400 MHz δ, $CDCl_3$): δ 1.28 (t, 6H); 2.01 (t, 1H); 2.78 (dd, 2H); 3.56 (t, 1H); 4.23 (m, 4H). Characterization data of the synthesized compound was matched with reported data.[S1]

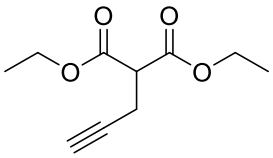

Synthesis of *2-(prop-2-yn-1-yl) propane-1,3-diol*, 6, $C_6H_{10}O_2$: Compound **6** was synthesized by a reported protocol.[34] The product was purified by column chromatography (SiO_2, $CHCl_3$/MeOH = 5:95 – 10:90) to yield the product **6**, 2-(prop-2-yn-1-yl) propane-1,3-diol as transparent viscous liquid (Yield = 47%). **^{1}H NMR** (400 MHz δ, $CDCl_3$): δ 3.64 (m, 4H); 2.3 (dd, 2H); 2.26 (t, 1H); 1.86 (m, 1H). Characterization data of the synthesized compound was matched with reported data.[34]

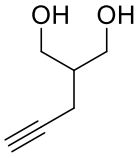

Synthesis of *3,5-diiodobenzoic acid*, 3, $C_7H_4I_2O_2$: Compound **3** was synthesized by a reported protocol.[33] The crude product **3**, 3,5 – diiodobenzoic acid was purified by column chromatography (SiO_2, $CHCl_3$/MeOH = 5:95 – 8:92) to give a white solid (Yield = 62.6%). **^{1}H NMR** (400 MHz, DMSO-d_6): δ 13.53 (s, 1H), 8.35 (t, J= 1.5 Hz, 1H), 8.19 (d, J= 1.5 Hz, 2H). Characterization data of the synthesized compound was matched with reported data.[33]

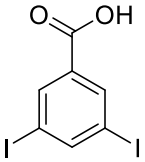

Synthesis of *cyclohexyl methyl 3,5-diiodobenzoate*, 4, $C_{14}H_{16}I_2O_2$: 3,5- diiodobenzoic acid, **3** (500 mg, 1.33 mmol, 1 equiv.) and K_2CO_3 (462 mg, 3.34 mmol, 2 equiv.) were stirred in DMF under nitrogen atmosphere. After, that bromomethyl cyclohexane (474 mg, 0.38 mL, 3.34 mmol, 2.5 equiv.) was added to it and kept on stirring overnight at room temperature.[39] Completion of the reaction was monitored by Thin Layer Chromatography (TLC). The reaction mixture was partitioned between ethyl acetate (organic phase, 50 mL each time) and brine solution (aqueous phase). Three repetitions of extraction followed by drying of the combined organic layer over

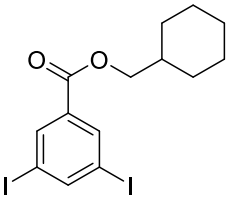

anhydrous sodium sulfate were done. The solvent was evaporated under reduced pressure. The crude product **4**, cyclohexylmethyl 3,5-diiodobenzoate was purified by column chromatography (SiO_2, $CHCl_3$/MeOH = 3:97 – 5:95) to yield the viscous liquid (Yield = 43.72 %). **^{1}H NMR** (400 MHz δ, $CDCl_3$): δ 8.29 (d, J= 8.3 Hz, 2H); 8.22 (t, J = 8.22 Hz, 1H); 4.12 (d, J = 4.12 Hz, 2H); 1.81 – 1.72 (m, 7H); 1.3 – 1.2 (m, 4H). **^{13}C NMR** (101 MHz δ, $CDCl_3$): δ 163.9, 149.2, 137.8, 133.8, 94.5, 71.0, 37.2, 29.8, 26.4, 25.7. **IR** (neat, ν/cm^{-1}) 3428, 3071, 2923, 2851, 2111, 1721, 1545, 1451, 1414, 1254, 1120, 976, 874, 761, 709, 661, 556.

Synthesis of *N-(cyclohexylmethyl)-3,5-diiodobenzamide*, 5, $C_{14}H_{17}I_2NO$: 3,5-diiodobenzoic acid, **4** (500 mg, 1.33 mmol, 1 equiv.), EDC·HCl (568 mg, 4.00 mmol, 3 equiv.) and HOBT (495 mg, 3.2 mmol, 2.4 equiv.) were added to an oven-dried 100 mL round bottom flask under a nitrogen atmosphere. After that triethylamine (0.8 mL, 5.89 mmol, 2.5 equiv.) and then DMF (10 mL) was added to the flask. Finally, cyclohexylmethylamine (0.3 mL, 2 mmol, 1.5 equiv.) was added dropwise to the round bottom flask. Then the round bottom flask was left, stirring overnight.[40] Completion of the reaction was monitored using Thin Layer Chromatography (TLC). The reaction mixture was partitioned between ethyl acetate (organic phase, 50 mL each time) and brine solution (aqueous phase) in a separating funnel, and the organic layer was extracted three times. The combined organic layer was dried over anhydrous sodium sulfate and the solvent was removed under reduced pressure. The crude product **5**, N-(cyclohexylmethyl)-3,5-diiodobenzamide was purified by column chromatography (SiO_2, $CHCl_3$/MeOH = 3:97 – 5:95) to yield colorless solid (Yield = 83%). **^{1}H NMR** (400 MHz δ, $CDCl_3$): δ 8.16 (t, J = 8.16 Hz, 1H); 8.01(d, J = 8.01 Hz, 2H); 6.07 (s, 1H); 3.26 (t, J = 3.28 Hz, 2H); 1.77 – 1.73 (m, 5H); 1.26 – 1.20 (m, 6H). **^{13}C NMR** (101 MHz δ, $CDCl_3$): δ 166.9, 137.9, 134.5, 128.6, 98.3, 46.4, 38.1, 31.1, 26.5, 25.9. **IR** (neat, ν/cm^{-1}) 3886, 3840, 3723, 3673, 3606, 3256, 3070, 2916, 2850, 2315, 1728, 1621, 1531, 1437, 1359, 1306, 1269, 1214, 1142, 1026, 962, 901, 859, 778, 730, 692, 553.

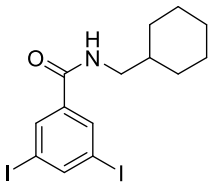

Synthesis of *cyclohexylmethyl 3,5-bis(5-hydroxy-4-(hydroxymethyl)pent-1-yn-1-yl)benzoate*:, 1, $C_{26}H_{34}O_6$: Cyclohexylmethyl 3,5-diiodobenzoate **6** (100 mg, 0.21 mmol, 1 equiv.) was taken in a 100 mL round bottom flask and triethyl amine (4 – 5 mL) was added to it. The round bottom flask was degassed for 30 – 40 minutes by bubbling nitrogen gas through

the mixture. Then $PdCl_2(PPh_3)_2$ (5 mg, 0.01 mmol, 0.08 equiv.), CuI (4 mg, 0.02 mmol, 0.11 equiv.) and compound **3** (92 mg, 0.8 mmol, 3 equiv.) were added one by one to the solution in the round bottom flask containing Compound **6.** The solution was stirred for about 6 h after which the completion of the reaction was monitored by Thin Layer Chromatography (TLC).[41] The reaction mixture was partitioned between ethyl acetate (organic phase, 50 mL each time) and brine solution (aqueous phase) in a separating funnel, and the organic layer was extracted three times. The combined organic layer was dried over anhydrous sodium sulfate and the solvent was removed under reduced pressure. The product **1**, cyclohexylmethyl 3,5-bis(5-hydroxy-4-(hydroxymethyl)pent-1-yn-1-yl)benzoate was purified by column chromatography (SiO_2, $CHCl_3$/MeOH = 1:99 – 5:95) to yield a viscous liquid (Yield = 78%). **^{1}H NMR** (400 MHz δ, $CDCl_3$): δ 7.89 (d, J = 7.89 Hz, 2H); 7.54 (t, J = 7.55 Hz, 1H); 4.10 (d, J = 4.10 Hz, 2H); 3.91 – 3.81 (m, 8H); 2.74 (s, 4H); 2.53 (d, J = 2.53 Hz, 4H); 2.09 – 2.03 (m, 2H); 1.77 – 1.73 (m, 7H); 1.26 – 1.20 (m, 2H); 1.07 – 1.00 (m, 2H). **^{13}C NMR** (101 MHz δ, $CDCl_3$): δ 165.7, 138.6, 131.7, 131.1, 124.3, 89.4, 80.6, 41.84, 37.3, 29.8, 26.5, 25.8, 18.5. **IR** (neat, ν/cm^{-1}) 3388, 2928, 2858, 2314, 2232, 1707, 1444, 1390, 1337, 1230, 1108, 1023, 894., 729, 608, 555, 516; **HRMS (ESI):** Calcd. $C_{26}H_{34}O_6$ $[M+H]^+$: 443.2355, Found: 443.2357.

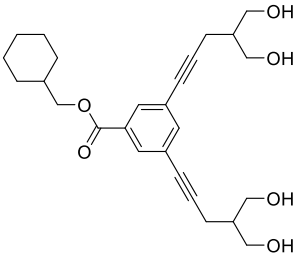

Synthesis of *N-(cyclohexylmethyl)-3,5-bis(5-hydroxy-4-(hydroxymethyl)pent-1-yn-1- yl) benzamide*, 2, $C_{26}H_{35}NO_5$: N-(cyclohexylmethyl)-3,5-diiodobenzamide, **5** (150 mg, 0.32 mmol, 1 equiv.) was taken in a 100 mL round bottom flask and triethyl amine (4 – 5 mL) was added to it. The round bottom flask was degassed for 30 – 40 minutes by bubbling nitrogen gas through the mixture. Then $PdCl_2(PPh_3)_2$ (7 mg, 0.01 mmol, 0.032 equiv.), CuI (6 mg, 0.03 mmol, 0.11 equiv.) and compound **3** (164 mg, 1.44 mmol, 4.5 equiv.) were added one by one to the solution in the round bottom flask containing compound **5.** The solution was stirred for about 6 hours after which the completion of the reaction was monitored by Thin Layer Chromatography (TLC).[41] The reaction mixture was partitioned between ethyl acetate (organic phase, 50 mL each time) and brine solution (aqueous phase) in a separating funnel, and the organic layer was extracted three times. The combined organic layer was dried over anhydrous sodium sulfate and the solvent was removed under reduced pressure. The product **2** was purified by column chromatography (SiO_2, $CHCl_3$/MeOH

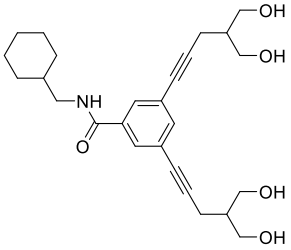

= 1:99 – 5:95) to yield product N-(cyclohexylmethyl)-3,5-bis(5-hydroxy-4-(hydroxymethyl) pent-1-yn-1-yl)benzamide, **2** as a light brown solid (Yield = 86%). **^{1}H NMR** (400 MHz δ, MeOH–d_4) 7.73 (d, J = 7.73 Hz, 2H); 7.49 (t, J = 7.5 Hz, 1H); 3.73 – 3.64 (m, 8H); 3.61 – 3.55 (m, 1H); 3.18 (d, J = 3.18 Hz, 2H); 2.55 (d, J = 2.55 Hz, 4H); 1.97 – 1.91 (m, 2H); 1.78 – 1.73 (m, 5H); 1.29 – 1.23 (m, 4H); 1.02 – 0.96 (m, 2H). **^{13}C NMR** (101 MHz δ, $CDCl_3$): δ 136.9, 135.2, 124.5, 129.4, 89.5, 80.6, 64.1, 46.6, 41.9, 38.1, 30.9, 26.5, 25.9, 18.4. **IR** (neat, ν/cm^{-1}): 3360, 2926, 2722, 2166, 1639, 1546, 1448, 1267, 1030, 893.14, 729.25. **HRMS (ESI):** Calcd. $C_{26}H_{34}O_6$ $[M+H]^+$: 442.2515, Found: 442.2519.

3.4.4 Ion Transport Experiments

Ion transporting activity studies across EYPC–LUVs ⊃ HPTS:

Preparation of HEPES buffer and stock solutions: The HEPES buffer of pH = 7.0 was prepared by dissolving an appropriate amount of solid HEPES (10 mM) and NaCl (100 mM) in autoclaved water. The pH was adjusted to 7.0 by adding aliquots from 0.5 M NaOH solution. The stock solution of all carriers was prepared using HPLC grade DMSO.

Preparation of EYPC–LUVs ⊃ HPTS in NaCl: The vesicles were prepared by the reported protocol.[42–44]

Ion transport activity by HPTS assay: In clean and dry fluorescence cuvette, 1975 μL of HEPES buffer (10 mM HEPES, 100 mM NaCl, pH =7.0) and 25 μL of EYPC–LUVs⊃HPTS vesicle was added. The cuvette was placed in a slowly stirring condition using a magnetic stirrer equipped in a fluorescence instrument (t = 0 s). The time-dependent HPTS emission intensity was monitored at λ_{em} = 510 nm (λ_{ex} = 450 nm) by creating a pH gradient between intra and extra vesicular system by the addition of 0.5 M NaOH (20 μL) at t = 20 s. Then different concentrations of transporter molecules in DMSO were added at t = 100 s. Finally, the vesicle was lysed by the addition of 10% Triton X–100 (25 μL) at t = 300 s to disrupt the pH gradient (Figure 3.21). The time-dependent data were normalized to percent change in fluorescence intensity using Equation 1:

$$I_F = [(I_t - I_0)/ (I_\infty - I_0)] \times 100) \qquad \text{(Equation 1)}$$

where I_0 is the initial intensity, I_t is the intensity at time t, and I_∞ is the final intensity after the addition of Triton X–100.

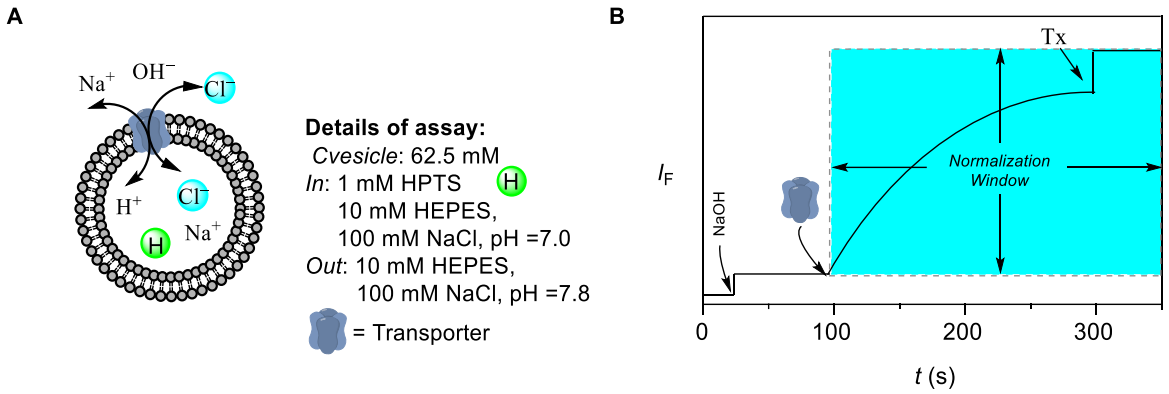

Figure 3.21. Representations of fluorescence-based ion transport activity assay using EYPC–LUVs⊃HPTS (**A**), and illustration of ion transport kinetics showing normalization window (**B**).

Dose-response activity:

The fluorescence kinetics of each transporter at different concentrations was studied as the course of time. The concentration profile data were evaluated at t = 170 s to get effective concentration, EC_{50} (i.e. the concentration of transporter needed to achieve 50% chloride efflux)[45] using Hill equation (Equation 2):

$$Y = Y_\infty + (Y_0 - Y_\infty)/[1 + (c/EC_{50})^n \quad \text{(Equation 2)}$$

where, Y_0 = fluorescence intensity just before the transporter addition (at t = 0 s), Y_∞ = fluorescence intensity with excess transporter concentration, c = concentration of transporter compound, and n = Hill coefficient (i.e. indicative of the number of monomers needed to form an active supramolecular channel).[46]

Ion selectivity studies across EYPC–LUVs⊃HPTS

Preparation of EYPC–LUVs ⊃ HPTS: The vesicles were prepared by the following reported protocol.[42,43,47]

Preparation of buffer and stock solutions: The HEPES buffer solution of 10 mM HEPES and 100 mM salts were prepared by dissolving appropriate amounts of solid HEPES and salts (NaCl, NaF, NaBr, $NaNO_3$, NaOAc, LiCl, KCl, RbCl, and CsCl) in autoclaved water, followed by adjustment of pH = 7.0 using 0.5 M NaOH. The stock solution of the most active transporter was prepared in HPLC grade DMSO.

Anion selectivity assay: In a clean and dry fluorescence cuvette 1975 μL HEPES buffer (10 mM HEPES, 100 mM NaX, pH = 7.0; where X = F^-, Cl^-, Br^-, OAc^-, and NO_3^-) was taken,

followed by the addition of 25 µL EYPC–LUVs⊃HPTS. The resulting solution was slowly stirred in a fluorescence instrument equipped with the magnetic stirrer (t = 0 s). The fluorescence intensity of HPTS was observed at λ_{em} = 510 nm (λ_{ex} = 450 nm) over a course of time, by creating pH gradient by addition of 20 µL 0.5 M NaOH at t = 20 s, followed by the addition of transporter **2** (as a DMSO solution) at t = 100 s to initiate ion transport and finally, vesicle was lysed for complete disruption of pH gradient by addition of 25 µL 10% Triton X – 100 at t = 300 s. The time-dependent data were normalized to percent change in intensity using Equation 1.

Cation selectivity assay: In a similar way, cation selectivity of transporter **2** (as a DMSO solution) was explored by changing extravesicular HEPES buffer solution (10 mM HEPES, 100 mM MCl, pH = 7.0) of chloride salts (MCl) of different cation (M = Li^+, Na^+, K^+, Rb^+, Cs^+). Using the same condition, no difference in fluorescence intensity was observed for different cations. The fluorescence data was normalised to percent change in intensity over course of time using Equation 1.

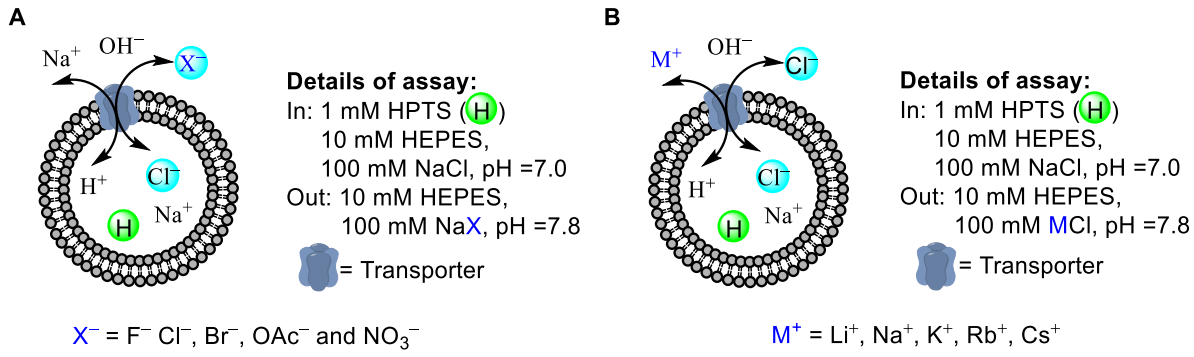

Figure 3.22. Schematic representations of fluorescence-based anion **(A)** and cation selectivity **(B)** assays.

Ion transport activity across EYPC–LUVs⊃HPTS in presence of valinomycin:[48,49]

In a clean fluorimetric cuvette 1975 µL of buffer solution (100 mM KCl, 10 mM HEPES, pH 7.0), 25 µL of above prepared vesicles solution were taken and placed in a fluorescence instrument equipped with a magnetic stirrer at t = 0 s. The fluorescence emission intensity of the HPTS dye, it was measured at λ_{em} = 510 nm (where λ_{ex} = 450 nm) for the time course of 0 to 350 s. At t = 20 s, 20 µL of 0.5 M NaOH solution was added to the same cuvette to generate a pH gradient (ΔpH = 0.8) between intra and extra vesicular medium. Then valinomycin (2.5 pM) was added at t = 50s followed by the addition of 18 µL solution of **2** in DMSO at t = 100

s. At t = 300 s, 25 µL of 10% triton X-100 was added to destroy all the vesicles for destructing the pH gradient. All the data was normalized using the Equation 1.

Comparable rates of pH gradient collapse were found when the ion transport activity of **2** was measured in the absence and presence of valinomycin. Therefore, the experiments indicated preferential selectivity of **2** towards Cl^- over OH^-, i.e., $Cl^- \gg OH^-$.

Chloride transport activity across EYPC–LUVs⊃lucigenin vesicles

Preparation of EYPC–LUVs⊃lucigenin vesicles: The vesicles were prepared by the reported protocol.[42,43,47]

Ion transport activity by Lucigenin assay:

In clean and dry fluorescence cuvette 1975 µL 200 mM $NaNO_3$ solution and 25 µL EYPC–LUVs⊃lucigenin was taken. This suspension was placed in a slowly stirring condition in fluorescence instrument equipped with a magnetic stirrer (at t = 0 s). The fluorescence intensity of lucigenin was monitored at λ_{em} = 535 nm (λ_{ex} = 450 nm) over a course of time. The chloride gradient was created by the addition of 33.3 µL NaCl (2.0 M) at t = 20 s between the intra and extra vesicular system, followed by the addition of a transporter at t = 100 s. Finally, vesicles were lysed by the addition of Triton X–100 at t = 300 s for the complete disruption of the chloride gradient.

The time-dependent data were normalized to percent change in fluorescence intensity using Equation 3:

$$I_F = [(I_t - I_0) / (I_\infty - I_0)] \times -100) \qquad \text{(Equation 3)}$$

Where, I_0 is the initial intensity, I_t is the intensity at time t, and I_∞ is the final intensity after the addition of Triton X–100.

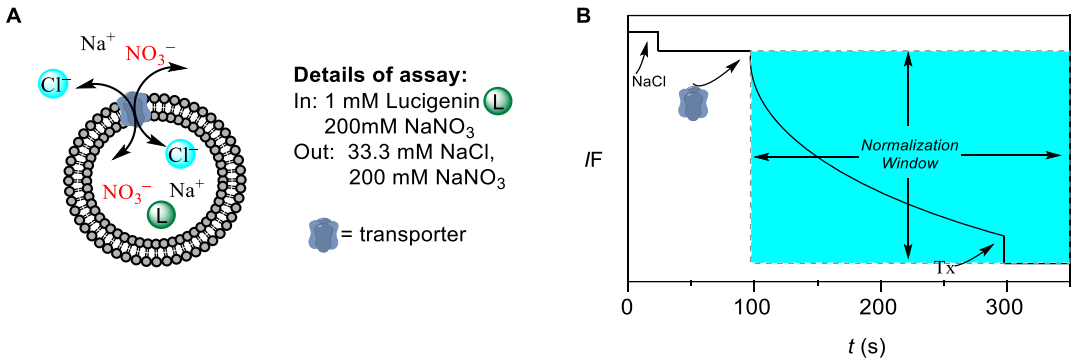

Figure 3.23. Representations of fluorescence-based ion transport activity assay using EYPC–LUVs⊃ Lucigenin (**A**), and illustration of ion transport kinetics showing normalization window (**B**).

Involvement of cation in transport process

The involvement of cations in the transport process was evaluated from the lucigenin-based assay. The preparation of solutions and vesicles are similar as described in the above section. In assay condition, the chloride salt of various cation (M^+ = Li^+, Na^+, K^+, Rb^+ and Cs^+) were added to evaluate the contribution of cation in transport process.

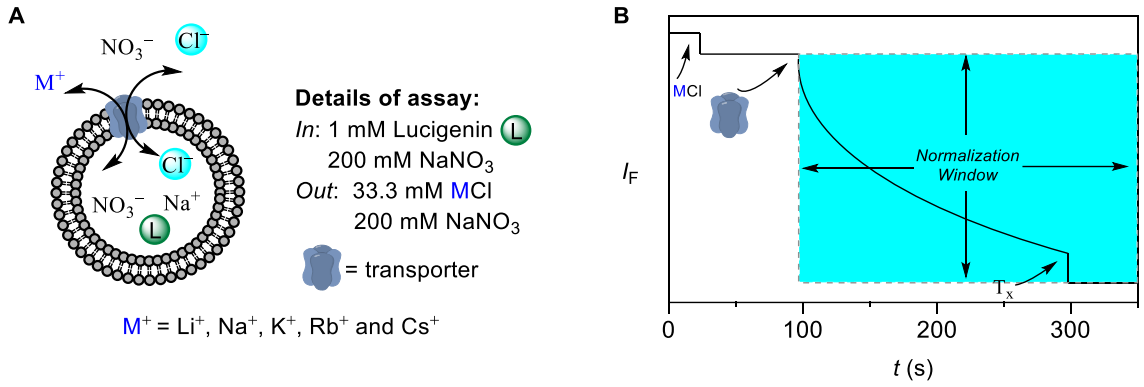

Figure 3.24. Representations of chloride influx activity assay using EYPC–LUVs⊃ Lucigenin by varying extravesicular cations (**A**), and illustration of chloride influx kinetics showing normalization window (**B**).

Cation transport activity: In a clean and dry fluorescence cuvette 1975 µL of $NaNO_3$ solution (200 mM) was added followed by the addition of 25 µL of EYPC–LUVs⊃lucigenin. The cuvette was placed in the fluorescence instrument in a slowly stirring condition by a magnetic stirrer equipped with the instrument (at t = 0 s). The time course of lucigenin fluorescence emission intensity, F_t was observed at λ_{em} = 535 nm (λ_{ex} = 450 nm). 33.3 µL of 2 M, MCl (M^+ = Li^+, Na^+, K^+, Rb^+ and Cs^+) was added to the cuvette at t = 25 s to create the chloride gradient between the intra and extra vesicular system. Transporter molecule **2** was added at t = 100 s in

different concentrations and, finally, 25 µL of 10% Triton X–100 was added at t = 300 s to lyse those vesicles resulting destruction of the chloride gradient (Figure 3.24).

Ion transport activity across EYPC–LUVs⊃lucigenin in the presence of valinomycin: The antiport mechanism (i.e. simultaneous transport of two different ions, in opposite directions, across the membrane)[13,35,50] of **2** was experimentally confirmed by lucigenin assay in the presence of valinomycin. The ion transport activity of **2** was monitored in vesicle entrapped with lucigenin (1 mM) and $NaNO_3$ (200 mM) suspended in KCl (2 M) solution with and without valinomycin. The remarkable enhancement in ion transport activity of **2** in the presence of valinomycin gave direct experimental insight into the antiport mechanism of ion transport.

Antiport mechanism: In clean and dry fluorescence cuvette 1975 µL 200 mM $NaNO_3$ solution and 25 µL EYPC–LUVs⊃lucigenin vesicles were taken and slowly stirred in a fluorescence instrument equipped with a magnetic stirrer (at t = 0 s). The time-dependent fluorescence intensity of lucigenin was monitored at λ_{em} = 535 nm (λ_{ex} = 455 nm). A solution of 2 M KCl (33.3 µL) was added at t = 20 s to create a chloride gradient between intra and extra vesicular system, followed by the addition of valinomycin (1.25 µM) at t = 50 s and transporter **2** (1.25 µM) at t = 100 s. Finally, the destruction of the chloride gradient was done by the addition of 10 % Triton X–100 (25 µL) at t = 300 s (Figure 3.23). The time-dependent data were normalized to percent change in fluorescence intensity using Equation 3.

Transporter Mechanism (Cholesterol Method)

The fluidity of the EYPC/cholesterol membrane changes when the amount of cholesterol in it changes, and this should have an impact on carriers by altering their mobility. However, since transmembrane channels span the entire membrane, they shouldn't be impacted. Increasing cholesterol levels will lower the membrane's fluidity to slow down a carrier's rate of transit but won't show any change in the fluorescence of the channel.[36]

Vesicles were prepared as before, but with 10 mol% of cholesterol added during the initial stage of vesicle preparation.[36]

Evaluation of membrane stability and channel nature by ANTS-DPX assay: EYPC–LUVs were loaded with anionic fluorophore ANTS (8-aminonaphthalene-1,3,6-trisulfonic acid disodium salt) and cationic quencher DPX (1,1-[1,4 phenylenebis(methylene)]bis[pyridinium]bromide) (Figure 3.25). Efflux of either ANTS or DPX through pores formed by **1** or **2** was followed by an increase in ANTS emission intensity.

The following buffers were prepared by a known method.

Buffer A: 12.5 mM ANTS, 45.0 mM DPX, 5 mM TES, 20 mM KCl, pH = 7.0

Buffer B: 5 mM TES, 100 mM KCl, pH = 7.0.

Preparation of EYPC–LUVs⊃ ANTS/DPX vesicles: A thin film of EYPC lipid was prepared by evaporating a solution (1 mL) of EYPC lipid (25 mg/mL) in $CHCl_3$ evaporated slowly by a stream of nitrogen and then in vacuo (6 h), and then hydrated with 1 mL buffer A, followed by vortex treatment (4 times). The resulting suspension was subjected to > 5 freeze-thaw cycles (using liquid N_2 to freeze and a warm water bath to thaw), and 19 times extruded using a Mini-Extruder through a 100 nm polycarbonate membrane (Avanti). External ANTS/DPX was removed by gel filtration (Sephadex G-50) using buffer B and diluted with the same buffer to 3 mL to give EYPC-LUVs⊃ ANTS/DPX stock solution.

ANTS/DPX assay: In a clean and dry fluorescence cuvette, 50 µL of the above lipid solution and 1950 µL buffer B were added. The compound **1** or **2** were added at 50 s and kept in a slowly stirring condition by a magnetic stirrer equipped with the fluorescence instrument (at t = 0 s). The time course of fluorescence emission intensity, F_t was monitored at λ_{em} = 520 nm (λ_{ex} = 353 nm).

Finally, at t = 300 s, 25 µL of 10% Triton X–100 was added to lyse all vesicles for 100% dye efflux. Fluorescence intensities (F_t) were normalized to fractional emission intensity I_F using Equation 2.

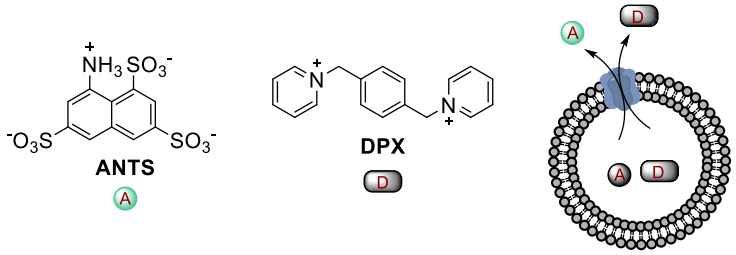

Figure 3.25. Representation of ANTS–DPX assay.

3.4.5 Planar Bilayer Conductance Measurements[51]

Bilayer membrane (BLM) was formed across an aperture of 150 µM diameter in a polystyrene cup (Warner Instrument, USA) with lipid diphytanoylphosphatidylcholine (Avanti Polar Lipids), dissolved in *n*-decane (18 mg/mL). Both chambers (*cis* and *trans*) were filled with symmetrical solution, containing 1 M KCl. The *trans* compartment was held at virtual ground and the *cis* chamber was connected to the BC 535 head-stage (Warner Instrument, USA) via

matched Ag–AgCl electrodes. Compound **2** (10 µM) was added to the *trans* chamber and the solution was stirred with a magnetic stirrer for 30 min. Channel formation was confirmed by the distinctive channel opening and closing events after applying voltages. Currents were low pass filtered at 1 kHz using pClamp9 software (Molecular Probes, USA) and an analog-to-digital converter (Digidata 1440, Molecular Probes). All data were analyzed by the software pClamp 9.

The complete data trace observed for 10 min contained a series of opening and closing events at some indefinite intervals. From a large and complete trace, a small portion is presented in the results and discussion part. The average current was calculated from this trace and then conductance and other calculations were made accordingly.

Calculation of ion channel diameter: Diameter of artificial ion channel was calculated according to Hille's equation,

$$1/g = (l + \pi d/4) \times (4\rho/\pi d^2) \qquad \text{(Equation 5)}$$

Where, g = corrected conductance (obtained by multiplying measured conductance with the Sansom's correction factor) = 3.37×10^{-10} S, l = length of the ion channel = 34 Å, and ρ = resistivity of the 1 M KCl solution = 9.47 Ω·cm).

Anion selectivity by Planar Bilayer Conductance Measurements

The *cis* and *trans* chambers were filled with unsymmetric solutions of KCl. The *cis* chamber was filled with 0.5 M KCl solution and the *trans* chamber was filled with 1 M KCl. The compound **2** (10 µM) was added to the *trans* chamber and stirred for 20 min. The reversal potential was calculated to be –20 ± 2 mV.

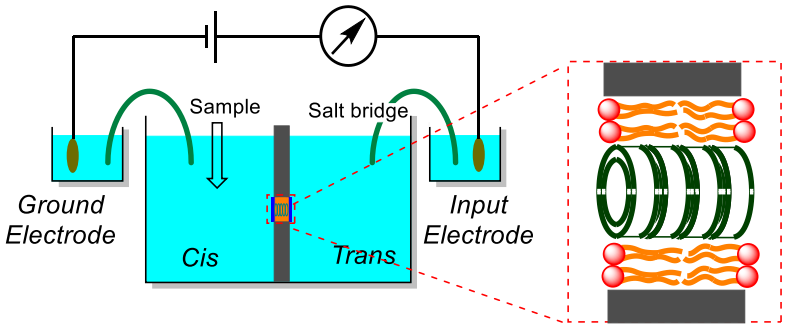

Figure 3.26. Systematic representation of black lipid membrane experiment.

3.4.6 Theoretical Studies (*Done in collaboration with Amal Vijay and Prof. Arnab Mukherjee from Chemistry Department, IISER Pune*)

System Preparation: Single channel-membrane system is constructed by embedding the quantum mechanically optimized synthetic ion channel in the DPHPC membrane and solvated it by 10586 water molecules, 63 Na^+ and 63 Cl^- ions (corresponding to 200 mM concentration). To solvate the system, ~11000 SPC model[52] water molecules were added to the system. The pre-equilibrated structure and parameters for DPHPC (1,2-diphytanoyl-sn-glycero-3-phosphocholine) obtained from Lipidbook.[53] The optimized channel was placed in the box of 128 DPHPC molecules using inflategro methodology.[54] The automated topology builder[55] created by Malde, et al. was used to develop the all-atom topology parameters of the channel with GROMOS-53a6 force field[56]. Molecular dynamics simulation was carried out using GROMACS 2019.6[57] package.

Molecular Dynamics simulation details: The system was minimized using the steepest descent method for 50000 steps. This was followed by equilibration for 10 ns at constant temperature for 323 K temperature and 1 bar pressure using Nosé-Hoover thermostat[58] and Parrinello-Rahman barostat[59] with a coupling constant of 0.5 ps and 5 ps, respectively. The time step of each simulation was taken as 2 fs. PME electrostatics [S30] was used for electrostatic interactions using a 12Å cut-off with the van der Waals (vdW) cut-off set at 12 Å. Position restraints of 500 kJ/mol nm^2 were applied to the heavy atoms of the channel molecules. The simulation box was found to be approximately 7.0X7.4X10.0 nm^3 for the system. A final 50 ns molecular dynamics simulation at constant 323 K temperature and 1 bar pressure was carried out using Nosé-Hoover thermostat[58] and Parrinello-Rahman barostat[59] with a coupling constant of 0.5 ps and 2 ps respectively with similar electrostatics and vdW as in equilibration process.

Free energy calculations for permeation events: we used state-of-the-art multiple walker metadynamics[S31] simulations by positioning a reference chloride ion at various parts of the channel. The initial configurations for constructing the multiple walker metadynamics simulation setup are obtained from the permeation event captured from the unbiased MD simulation trajectory. In this enhanced sampling approach, independent biased simulations are considered in parallel, and the bias contribution from each walker are considered for constructing the final free energy surface for the permeation process, till the last ion is out from the channel. A total of 8 walkers were constructed (each sampling different independent trajectory) and a total of 160 ns simulations (20 ns each) were performed using the Z-

Coordinate (displacement of Cl^- ion along Z-coordinate, hereafter referred as permeation distance) between the channel and reference chloride ion as a collective variable (CV) to study the permeation events. This CV quantitatively describe the position of ion inside and outside the channel in the simulation system. Near the centre the channel, the permeation distance has the value of 0 nm and when it reaches the bulk water it has a value greater than 2.5 nm. We considered a hill height of 0.2 kJ/mol, a bias factor of 10, and hills deposition rate of 1 ps and Gaussian widths of 0.05 nm for the metadynamics simulation.

Calculation of coordination number: The coordination number between the Cl^- ion and water molecules is calculated using the switching function described as follows Group A contains the reference chloride ion and Group B contains the oxygen atoms of the water molecules present in the system.

$$Coord.Number = \sum_{i \in A} \sum_{i \in B} s_{ij}$$

$$s_{ij} = \frac{1 - \left(\frac{r_{ij} - d_0}{r_0}\right)^n}{1 - \left(\frac{r_{ij} - d_0}{r_0}\right)^m}$$

r_{ij} describes the distance between the reference chloride ion and the neighbouring oxygen atoms of the water molecules. r_0 and d_0 values set to 0.35 nm and 0 nm respectively.

3.4.7 NMR

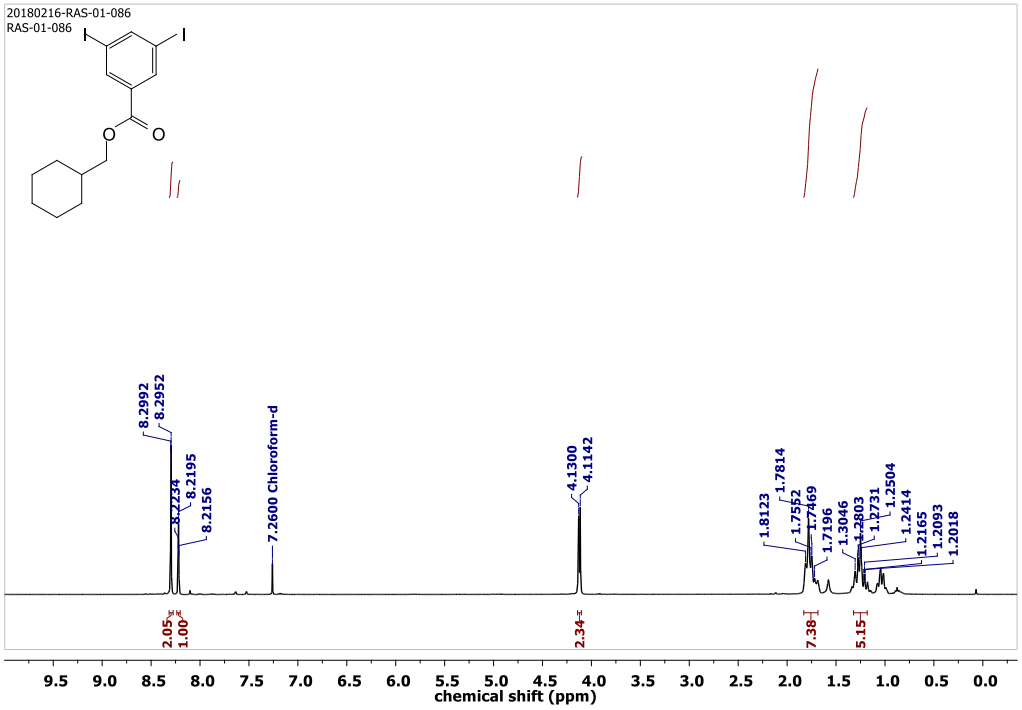

Figure 3.27. ^{1}H NMR (400 MHz) spectrum of **4** in $CDCl_3$.

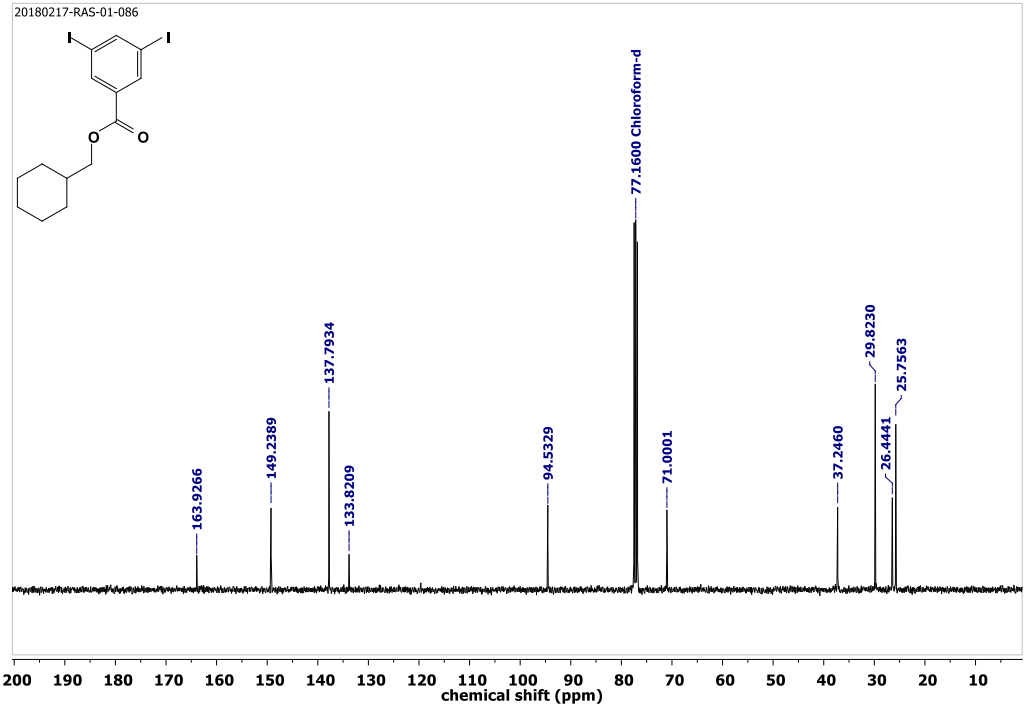

Figure 3.28. ^{13}C NMR (101 MHz) spectrum of **4** in $CDCl_3$.

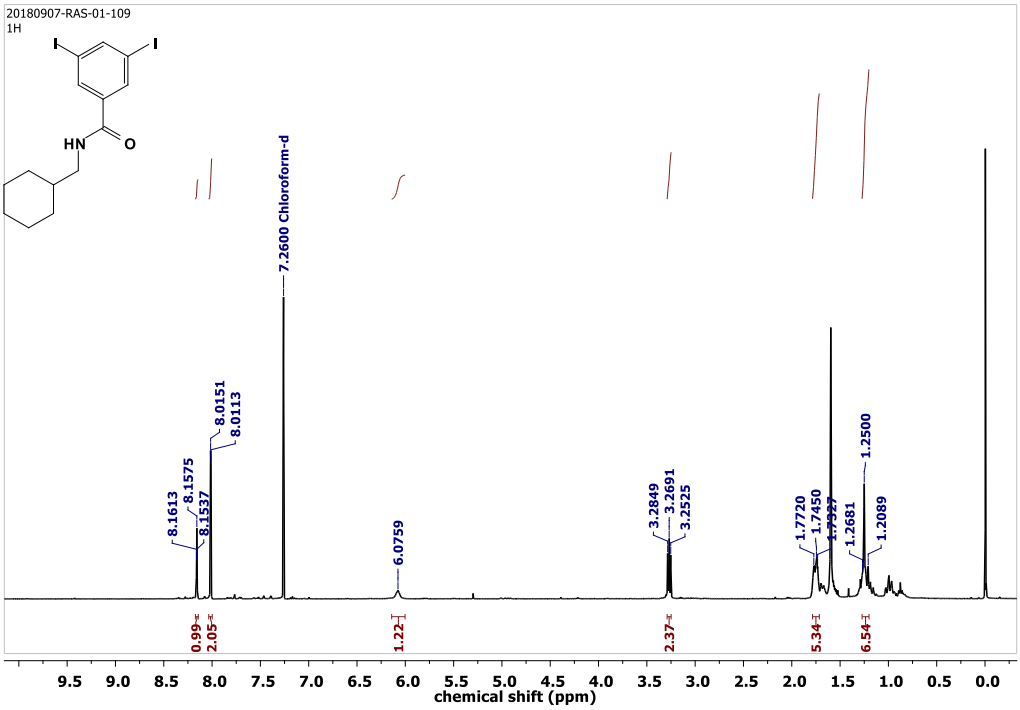

Figure 3.29. ^{1}H NMR (400 MHz) spectrum of **5** in $CDCl_3$.

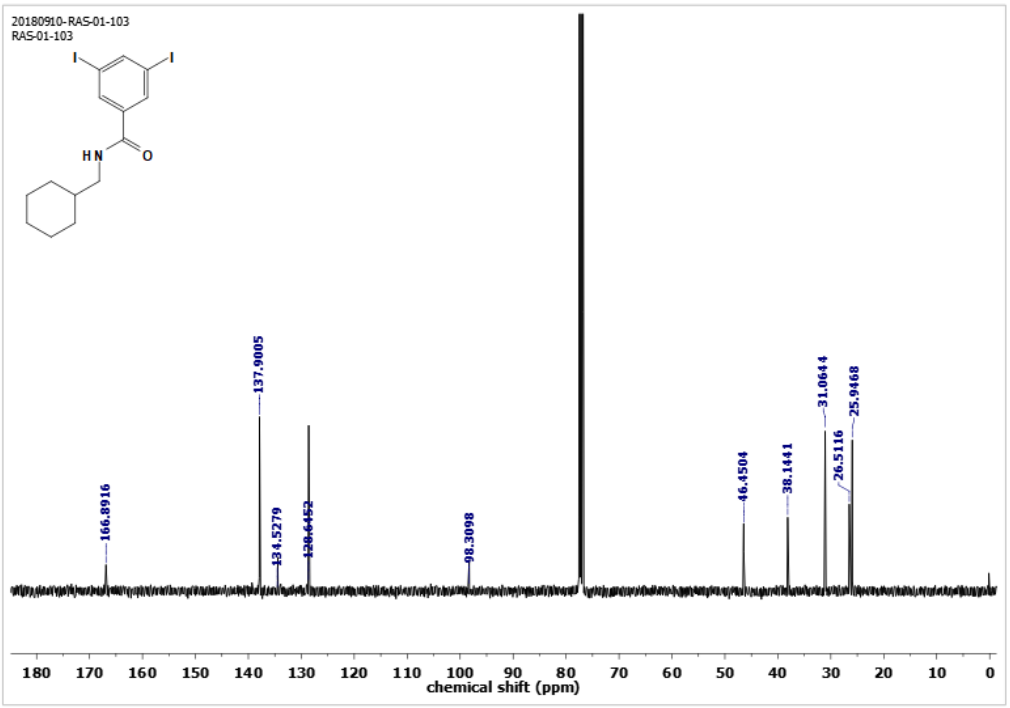

Figure 3.30. ^{13}C NMR (101 MHz) spectrum of **5** in $CDCl_3$.

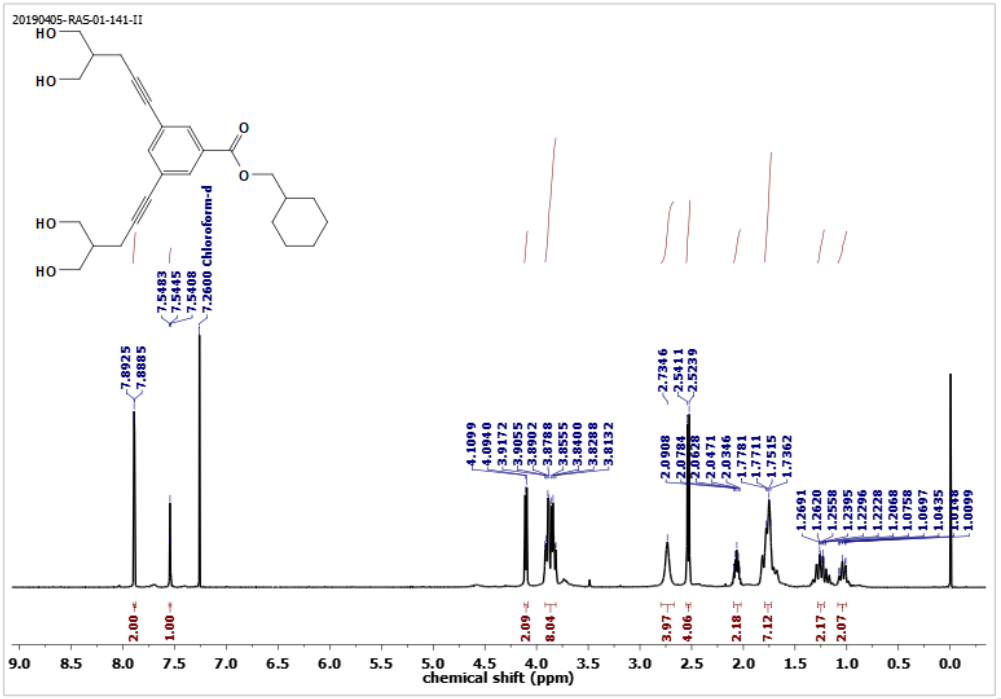

Figure 3.31. ^{1}H NMR (400 MHz) spectrum of **1** in $CDCl_3$.

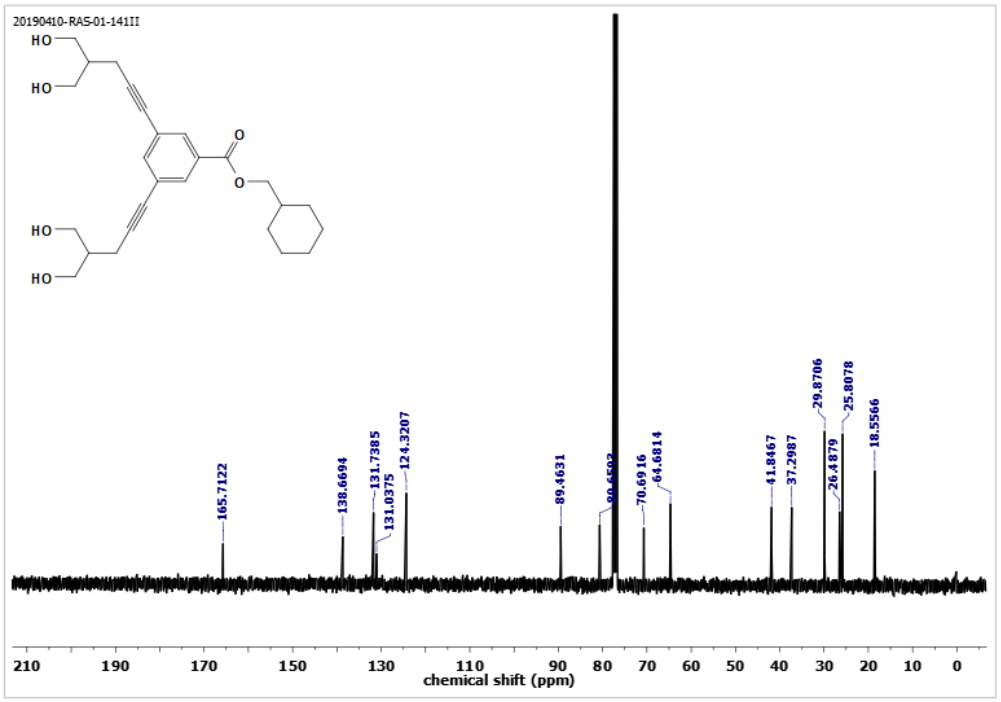

Figure 3.32. ^{13}C NMR (101 MHz) spectrum of **1** in $CDCl_3$.

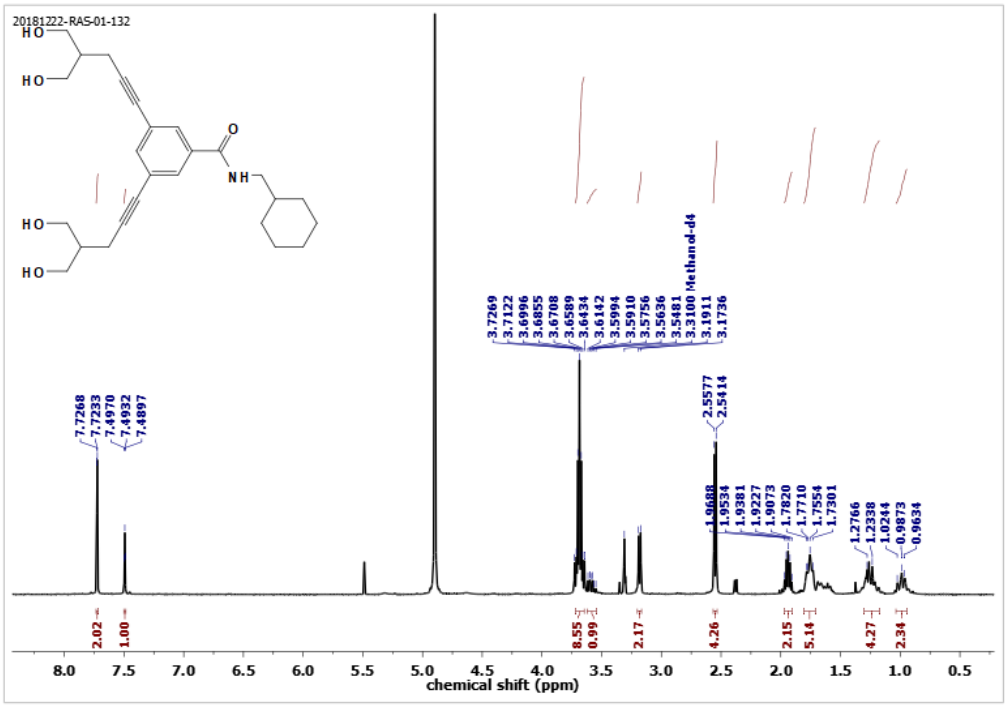

Figure 3.33. ^{1}H NMR (400 MHz) spectrum of **2** in MeOH–d_4.

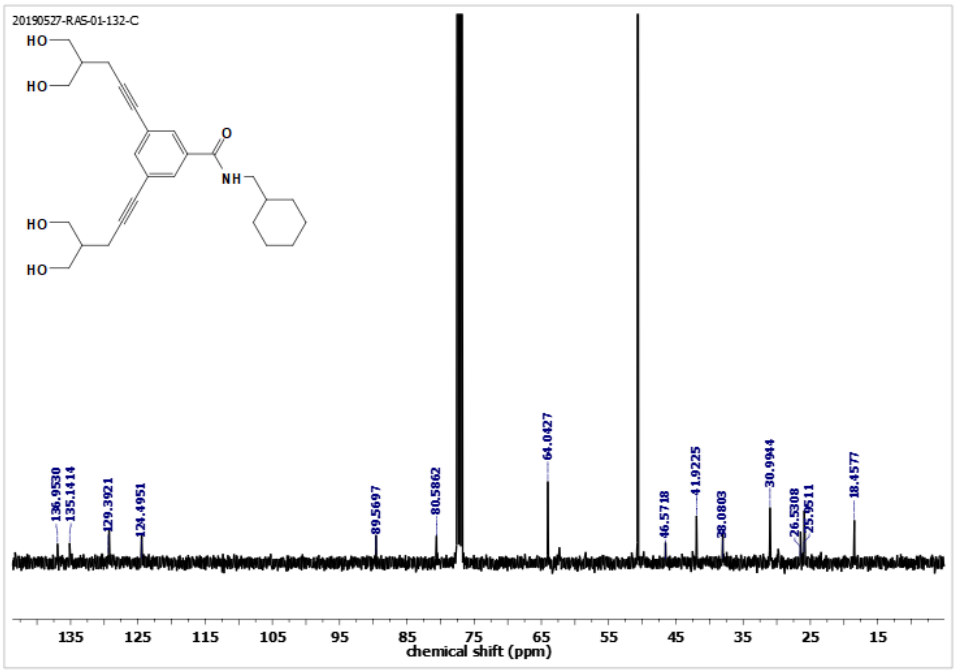

Figure 3.34. ^{13}C NMR (101 MHz) spectrum of **2** in. $CDCl_3$.

3.5 References

1 M. M. Tedesco, B. Ghebremariam, N. Sakai and S. Matile, *Angew. Chemie - Int. Ed.*, 1999, **38**, 540–543.

2 M. R. Ghadiri, J. R. Granja and L. K. Buehler, *Nature*, 1994, **369**, 301–304.

3 N. Sakai, K. C. Brennan, L. A. Weiss and S. Matile, *J. Am. Chem. Soc.*, 1997, **119**, 8726–8727.

4 N. Sakai, Y. Kamikawa, M. Nishii, T. Matsuoka, T. Kato and S. Matile, *J. Am. Chem. Soc.*, 2006, **128**, 2218–2219.

5 A. Hennig and S. Matile, in *Chirality*, 2008, **20,** 932–937.

6 H. Ishida, Z. Qi, M. Sokabe, K. Donowaki and Y. Inoue, *J. Org. Chem.*, 2001, **66**, 2978–2989.

7 J. Sá Nchez-Quesada, M. P. Isler and M. R. Ghadiri, *J. Am. Chem. Soc.*, 2002, **124**, 10004–10005.

8 S. Fernandez-Lopez, H. S. Kim, E. C. Choi, M. Delgado, J. R. Granja, A. Khasanov, K. Kraehenbuehl, G. Long, D. A. Weinberger, K. M. Wilcoxen and M. R. Ghadiri, *Nature*, 2001, **412**, 452–455.

9 T. D. Clark, L. K. Buehler and M. R. Ghadiri, *J. Am. Chem. Soc.*, 1998, **120**, 651–656.

10 V. Gorteau, G. Bollot, J. Mareda and S. Matile, *Org. Biomol. Chem.*, 2007, **5**, 3000–3012.

11 V. Gorteau, G. Bollot, J. Mareda, A. Perez-Velasco and S. Matile, *J. Am. Chem. Soc.*, 2006, **128**, 14788–14789.

12 A. Perez-Velasco, V. Gorteau and S. Matile, *Angew. Chemie - Int. Ed.*, 2008, **47**, 921–923.

13 T. Saha, S. Dasari, D. Tewari, A. Prathap, K. M. Sureshan, A. K. Bera, A. Mukherjee and P. Talukdar, *J. Am. Chem. Soc.*, 2014, **136**, 14128–14135.

14 N. Pelizzi, A. Casnati and R. Ungaro, *Chem. Commun.*, 1998, 2607–2608.

15 A. P. Davis, J. J. Perry and R. S. Wareham, *Tetrahedron Lett.*, 1998, **39**, 4569–4572.

16 O. Hayashida, M. Kato, K. Akagi and Y. Aoyama, *J. Am. Chem. Soc.*, 1999, **121**, 11597–11598.

17 A. Arduini, G. Giorgi, A. Pochini, A. Secchi and F. Ugozzoli, *J. Org. Chem.*, 2001, **66**, 8302–8308.

18 H. Miyaji and J. L. Sessler, *Angew. Chemie - Int. Ed.*, 2001, **40**, 154–157.

19 H. Tong, G. Zhou, L. Wang, X. Jing, F. Wang and J. Zhang, *Tetrahedron Lett.*, 2003, **44**, 131–134.

20 J. L. Sessler, P. Gale and W.-S. Cho, *Anion Receptor Chemistry*, The Royal Society of Chemistry, 2006.

21 L. A. Weiss, N. Sakai, B. Ghebremariam, C. Ni and S. Matile, *J. Am. Chem. Soc.*, 1997, **119**, 12142–12149.

22 C. Ni and S. Matile, *Chem. Commun.*, 1998, 755–756.

23 K. Yamashita, V. Janout, E. M. Bernard, D. Armstrong and S. L. Regen, *J. Am. Chem. Soc.*, 1995, **117**, 6249–6253.

24 K. E. Koenig, G. M. Lein, P. Stuckler, T. Kaneda and D. J. Cram, *J. Am. Chem. Soc.*, 1979, **101**, 3553–3566.

25 J. P. Clare, A. J. Ayling, J. B. Joos, A. L. Sisson, G. Magro, M. N. Pérez-Payán, T. N. Lambert, R. Shukla, B. D. Smith and A. P. Davis, *J. Am. Chem. Soc.*, 2005, **127**, 10739–10746.

26 A. P. Davis, J. F. Gilmer and J. J. Perry, *Angew. Chemie - Int. Ed.*, 1996, **35**, 1312–1315.

27 P. Ashokkumar, V. T. Ramakrishnan and P. Ramamurthy, *ChemPhysChem*, 2011, **12**, 389–396.

28 T. Saito, M. Morimoto, C. Akiyama, T. Matsumoto and K. Suzuki, *J. Am. Chem. Soc.*,

1995, **117**, 10757–10758.

29 A. Denichoux, L. Debien, M. Cyklinsky, M. Kaci, F. Chemla, F. Ferreira and A. Pérez-Luna, *J. Org. Chem.*, 2013, **78**, 134–145.

30 R. Long, J. Huang, W. Shao, S. Liu, Y. Lan, J. Gong and Z. Yang, *Nat. Commun. 2014 51*, 2014, **5**, 1–10.

31 L.-B. Huang, A. Hardiagon, I. Kocsis, C.-A. Jegu, M. Deleanu, A. Gilles, A. Van Der Lee, F. Sterpone, M. Baaden and M. Barboiu, *J. Am. Chem. Soc*, 2021, **143**, 4233.

32 T. Mondal, D. Basak, A. Al Ouahabi, M. Schmutz, P. Mésini and S. Ghosh, *Chem. Commun.*, 2015, **51**, 5040–5043.

33 M. Banno, T. Yamaguchi, K. Nagai, C. Kaiser, S. Hecht and E. Yashima, *J. Am. Chem. Soc.*, 2012, **134**, 8718–8728.

34 J. Mandal, S. Krishna Prasad, D. S. S. Rao and S. Ramakrishnan, *J. Am. Chem. Soc.*, 2014, **136**, 2538–2545.

35 P. Talukdar, G. Bollot, J. Mareda, N. Sakai and S. Matile, *J. Am. Chem. Soc.*, 2005, **127**, 6528–6529.

36 L. Rose and A. T. A. Jenkins, *Bioelectrochemistry*, 2007, **70**, 387–393.

37 P. Raiteri, A. Laio, F. L. Gervasio, C. Micheletti and M. Parrinello, *J. Phys. Chem. B*, 2005, **110**, 3533–3539.

38 M. Bonomi, A. Barducci and M. Parrinello, *J. Comput. Chem.*, 2009, **30**, 1615–1621.

39 D. Tadic, J. T. . Linders, J. L. Flippen-Anderson, A. E. Jacobson and K. C. Rice, *Tetrahedron*, 2003, **59**, 4603–4614.

40 N. Fresno, M. Macías-González, A. Torres-Zaguirre, M. Romero-Cuevas, P. Sanz-Camacho, J. Elguero, F. J. Pavón, F. Rodríguez De Fonseca, P. Goya and R. Pérez-Fernández, *J. Med. Chem.*, 2015, **58**, 6639–6652.

41 U. Dutta, S. Maity, R. Kancherla and D. Maiti, *Org. Lett.*, 2014, **16**, 6302–6305.

42 A. Roy, D. Saha, A. Mukherjee and P. Talukdar, *Org. Lett.*, 2016, **18**, 5864–5867.

43 P. Talukdar, N. Sakai, N. Sordé, D. Gerard, V. M. F. Cardona and S. Matile, *Bioorganic Med. Chem.*, 2004, **12**, 1325–1336.

44 N. Sordé and S. Matile, *J. Supramol. Chem.*, 2002, **2**, 191–199.

45 A. Vargas Jentzsch, D. Emery, J. Mareda, P. Metrangolo, G. Resnati and S. Matile, *Angew. Chemie - Int. Ed.*, 2011, **50**, 11675–11678.

46 S. Bhosale and S. Matile, *Chirality*, 2006, **18**, 849–856.

47 S. Matile and N. Sorde, *J. Supramol. Chem.*, 2002, **2**, 191–199.

48 N. Busschaert, L. E. Karagiannidis, M. Wenzel, C. J. E. Haynes, N. J. Wells, P. G. Young, D. Makuc, J. Plavec, K. A. Jolliffe and P. A. Gale, *Chem. Sci.*, 2014, **5**, 1118–1127.

49 M. Lisbjerg, H. Valkenier, B. M. Jessen, H. Al-Kerdi, A. P. Davis and M. Pittelkow, *J. Am. Chem. Soc.*, 2015, **137**, 4948–4951.

50 V. Gorteau, G. Bollot, J. Mareda, A. Perez-Velasco and S. Matile, *J. Am. Chem. Soc.*, 2006, **128**, 14788–14789.

51 C. Ren, X. Ding, A. Roy, J. Shen, S. Zhou, F. Chen, S. F. Yau Li, H. Ren, Y. Y. Yang and H. Zeng, *Chem. Sci.*, 2018, **9**, 4044–4051.

52 H. J. C. Berendsen, J. P. M. Postma, W. F. van Gunsteren and J. Hermans, in *D. Reidel Publishing Company*, 1981, 331–342.

53 J. Domański, P. J. Stansfeld, M. S. P. Sansom and O. Beckstein, *J. Membr. Biol.*, 2010, **236**, 255–258.

54 T. H. Schmidt and C. Kandt, *J. Chem. Inf. Model.*, 2012, **52**, 2657–2669.

55 A. K. Malde, L. Zuo, M. Breeze, M. Stroet, D. Poger, P. C. Nair, C. Oostenbrink and A. E. Mark, *J. Chem. Theory Comput*, 2011, **7**, 4026–4037.

56 C. Oostenbrink, A. Villa, A. E. Mark and W. F. Van Gunsteren, *J Comput Chem*, 2004,

25, 1656–1676.

57 B. Hess, C. Kutzner, D. van der Spoel and E. Lindahl, *J. Chem. Theory Comput.*, 2008, **4**, 435–447.

58 S. Nosé, *Mol. Phys.*, 1984, **52**, 255–268.

59 M. Parrinello and A. Rahman, *J. Appl. Phys.*, 1981, **52**, 7182–7190.

Chapter 4

Halogen bond-driven artificial Cl^- selective channel constructed from 5-iodoisophthalamide-based molecules

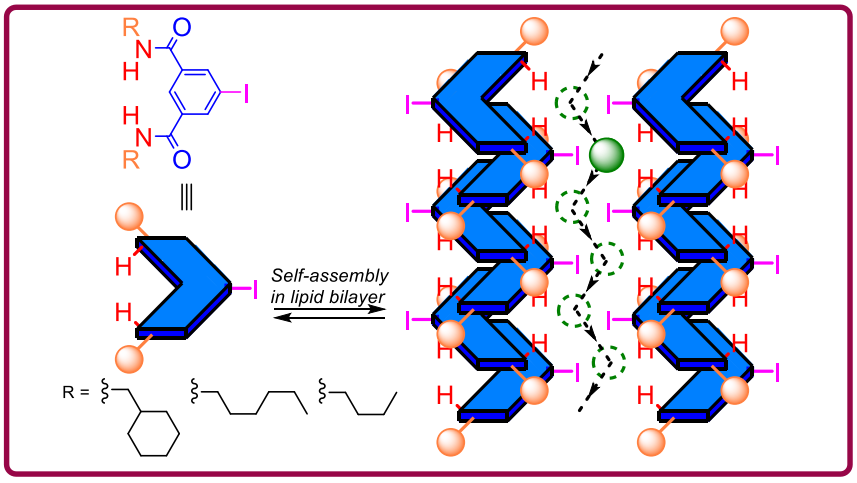

4.1 Introduction

While many different synthetic anion receptors have been discovered, so far only a small fraction have achieved the outstanding selectivity of naturally occurring anion-binding proteins. The problem is exacerbated by the fact that, unlike cations, anions have weaker coordination preferences and lower charge densities. Furthermore, their wide variety of geometries, protonation equilibria resulting from their pH sensitivity, and often high solvation enthalpies all work against the selective binding. Although HB is the most common non-covalent contact discovered to date among anion receptors, less common interactions have been increasingly exploited in recent years to increase the diversity of anion detection and selectivity. Solvophobic effects, anion- interactions, coordination bond formation with Lewis acidic metals and main group elements, and halogen bonding (XB) are all gaining ground as potential mechanisms for anion sensors.[1–4] The similar strength of XB to HB and, most notably, its greatly enhanced linear directionality (at least 175° in the gas phase) have led to its extensive exploitation in solid-state crystal engineering and materials design as an attractive non-covalent interaction between an electron-deficient halogen (group 17) atom and a Lewis base[5] Because of its comparable electronic, steric, geometric, and solvent impacts, XB typically improves the anion-binding affinities and selectivity compared to HB analogs in solution.[6–8]

Significant progress has been achieved in comprehending the mechanism of natural ion transporters through the utilization of various non-covalent interactions such as hydrogen bonding, anion-π, π-π, among others.[9–17] The XB-based supramolecular architecture has undergone significant advancements in supramolecular materials[18,19], rotaxanes, catenanes, macrocyclic hosts,[20] helical foldamers,[21] anion receptors, catalysts, and crystal engineering[10,22–26] in recent times.[27–35] Around 200 years ago, J.J. Colin fortuitously produced I···NH3 while conducting experiments in J.L. Gay-Lussac's laboratory, ultimately leading to the revelation of XB. This discovery established the foundation for the incorporation of novel non-covalent interactions within the scientific community. Halogen bonds exhibit greater stability and directionality when compared to hydrogen bonds.[10,22,24–26] The potential effectiveness of anion transport through halogen bonds can be attributed to their inherent lipophilicity. The utilization of halogen-bond assisted transport has significantly impacted anion selective transport, particularly for chloride ions. This is due to the minimal possibility of cation binding, which distinguishes this system from hydrogen-bond-assisted ion transport systems and enhances its efficacy. The body of evidence supporting the existence of halogen bonding in biological systems is expanding, and its application in the field of drug design is

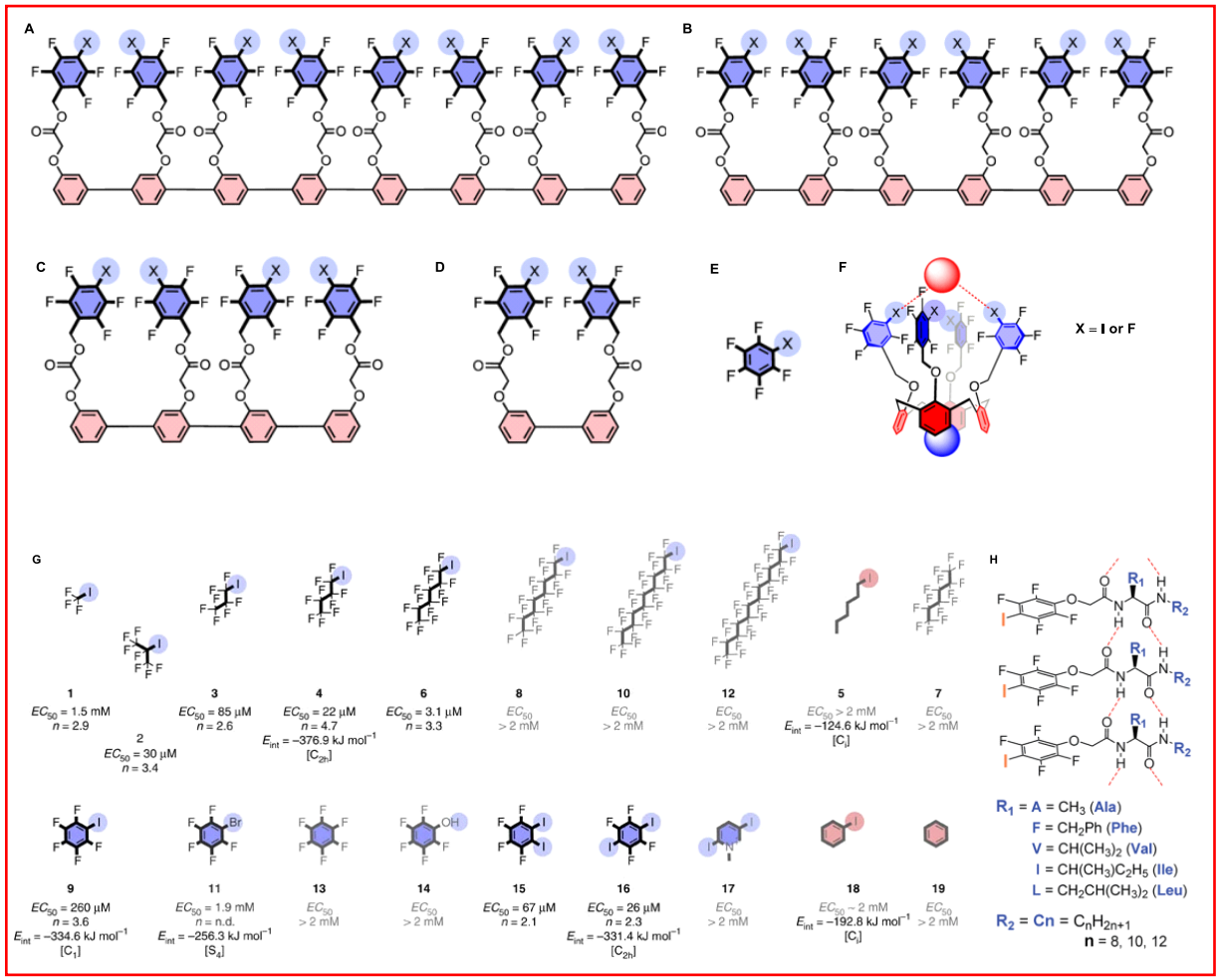

Figure 4.1. Halogen-bond mediated Cl- selective ion channels.[4,36,37]

increasingly feasible.[38–41] The presence of an excessive amount of fluorine causes a rise in the electron deficiency of iodine, which results in the expression of a strong binding affinity and a reduced capacity for anion transport. The electron deficiency and sigma-hole size of iodine atoms attached to a system can be diminished by replacing fluorine with an alternative electron-withdrawing group (EWG) element amide group. It appears that this arrangement is optimal for binding and transporting the anion. Both the inadequate release of ions and the robust binding can exert inhibitory effects on ion channel systems. The effectiveness of transportation operations is dependent on achieving an optimal level of binding, in accordance with the "Goldilocks principle".[3,42,43] The geometric properties of the motif are of interest due to the presence of the amide group, which contributes to both electron-withdrawing effects and intermolecular C=O···H−N hydrogen bonding interactions, resulting in enhanced stability. Additionally, the π-π stacking interactions facilitate the formation of a preorganized geometry of an active ion channel across the membrane, which is crucial for effective anion recognition. The lipophilic nature of iodine is expected to result in the formation of a distinctive assembly

within the bilayer. It is anticipated that certain iodine molecules will align themselves towards the internal cavity to facilitate ion binding, whereas others will face the phospholipid tails. The aforementioned configuration, in conjunction with the prioritization of preserving the potency of the halogen intermolecular interactions, resulted in a noteworthy augmentation of the transportation efficacy.[44–50] The present study has demonstrated that this particular approach exhibits superior efficacy in relation to transport activity and selectivity when compared to other ion channels that utilize fluorine as a replacement to create a sigma-hole over iodine.

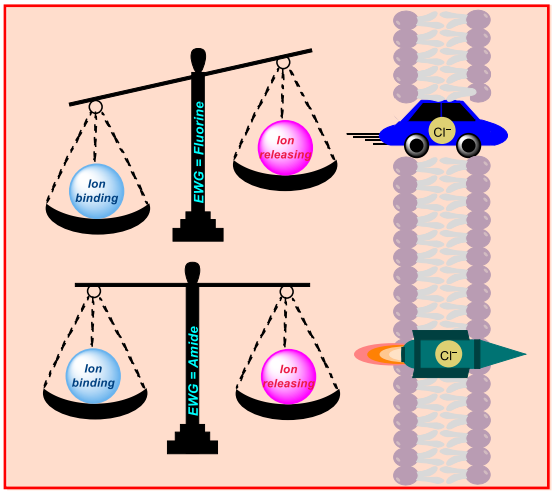

Figure 4.2. Illustration of EWG's influence on transporter molecule activity across lipid bilayer.

The studies in this chapter describes a system that exhibits proficient ion channel behaviour within a lipid bilayer owing to its optimal equilibrium between ion binding and ion-releasing capabilities. In order to attain elevated degrees of ion selectivity, minuscule molecules have been synthesized which possess the ability to spontaneously assemble into a bilayer-based system that is highly efficient and stable. In this chapter we have synthesised and characterized compounds **1a-1c**, which contain 5-iodo-isophthalamide substitutions.

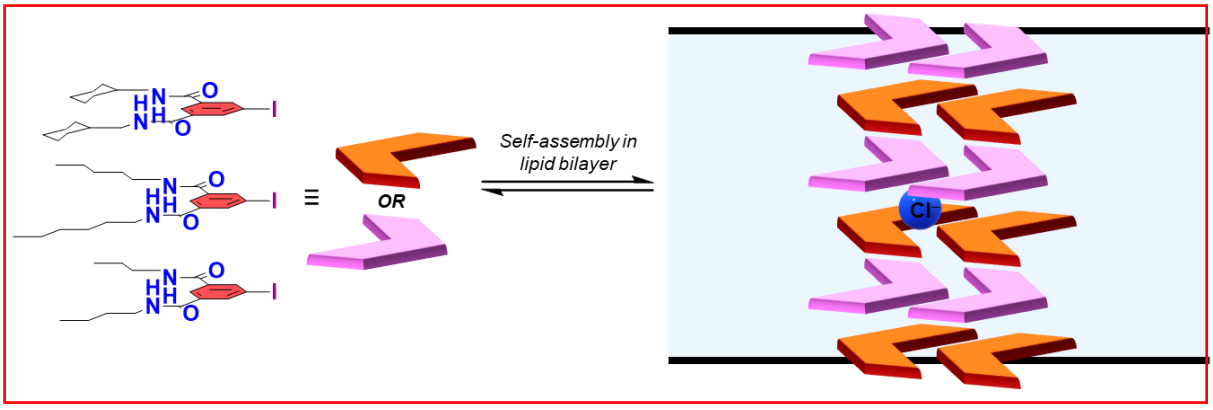

Figure 4.3. Chemical structure of compounds **1a-1c** and possible self-assembly in the lipid bilayer membrane.

These compounds exhibit intelligent self-assembly behaviour, resulting in the formation of a supramolecular assembly. This assembly selectively facilitates the translocation of Cl^- ions across the lipid membrane.

4.2 Results and Discussion

4.2.1 Synthesis

The compounds **1a-1c** were synthesized from 5-aminoisophthalic acid **2** by converting it to 5-iodoisophthalic acid using diazotization reaction and treating with urea and KI. 5-iodoisophthalic acid was then coupled with the respective amines using EDC·HCl as coupling reagent to get the di-carboxyamides **1a–1c** (Scheme 4.1). All compounds were purified by column chromatography, and the structures were confirmed by ^{1}H NMR, ^{13}C NMR, and HRMS data (details in Experimental Section).

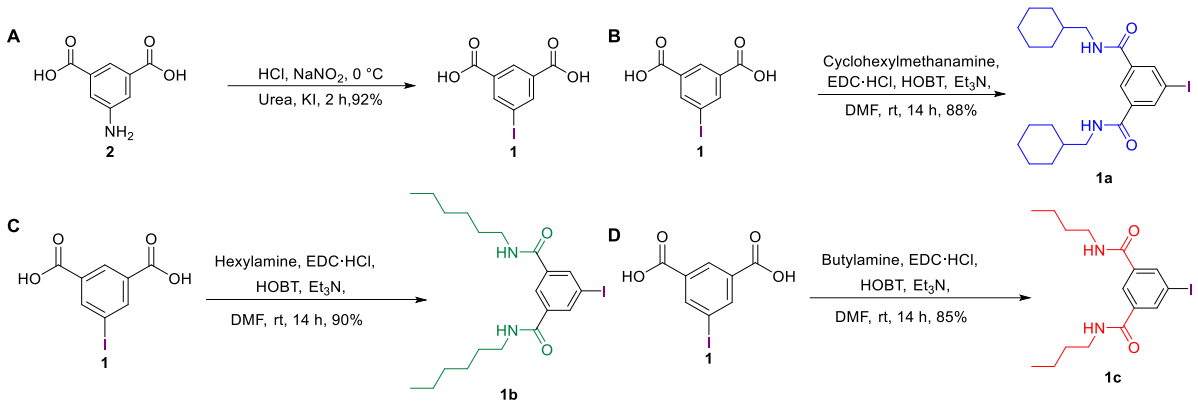

Scheme 4.1. Synthesis of compound **1a-1c**.

4.2.2 Crystallographic Studies

The MeOH solvent system was utilized to obtain crystal structures of **1b** that are appropriate for diffraction. The monoclinic space group crystallization of compound **1b** has been observed. X-ray diffraction analysis of single-crystal structures provides a reliable indication of the self-assembly phenomena in the solid state and their potential for self-organization in bilayer membranes. The arrangement of molecules is such that they are stacked in a sandwich-like manner, with each consecutive molecule oriented in the opposite direction. This results in a vertically slipped stacking pattern along the a-axis, ultimately forming an infinite stacked structure. In this particular scenario, the iodine atoms within a given unit cell exhibit antiparallel orientation. The underlying stratum exhibits an analogous configuration, albeit with molecules that are subject to supplementary symmetry operations, resulting in a reverse

orientation upon stacking. The units are linked by a persistent intermolecular N–H···O hydrogen bonding between two strata, resulting in a barrel-rosette configuration of the assembly. The stacking of barrels is observed to occur repeatedly along the b and c-axes, resulting in the formation of supramolecular assemblies. These assemblies are decorated with iodine atoms arranged in a zigzag pattern along the a-axis (Figure 4.4).

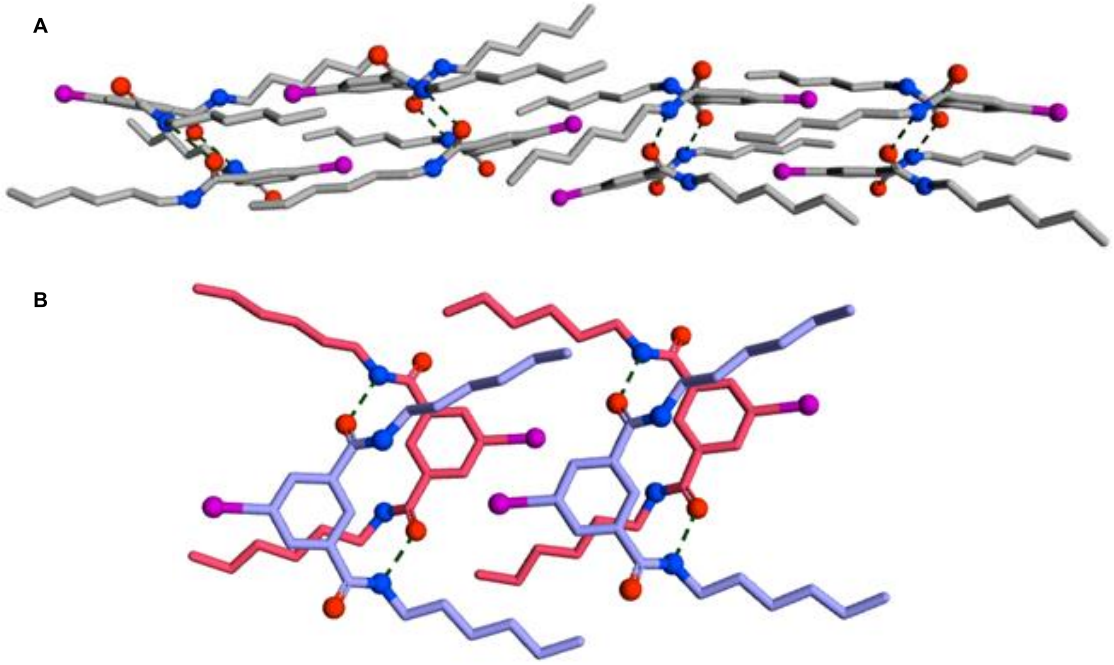

Figure 4.4. Solid state packing of **1b**.

4.2.3 Certification of self-assembly (FESEM)

Field Emission Scanning Electron Microscopy (FESEM) data was acquired for the **1a-1c** sample through methanol sample preparation, as illustrated in Figure 4.5. The identification of a unique elongated rod-like structure is significant as it validates the notable self-assembly property of **1a-1c**.

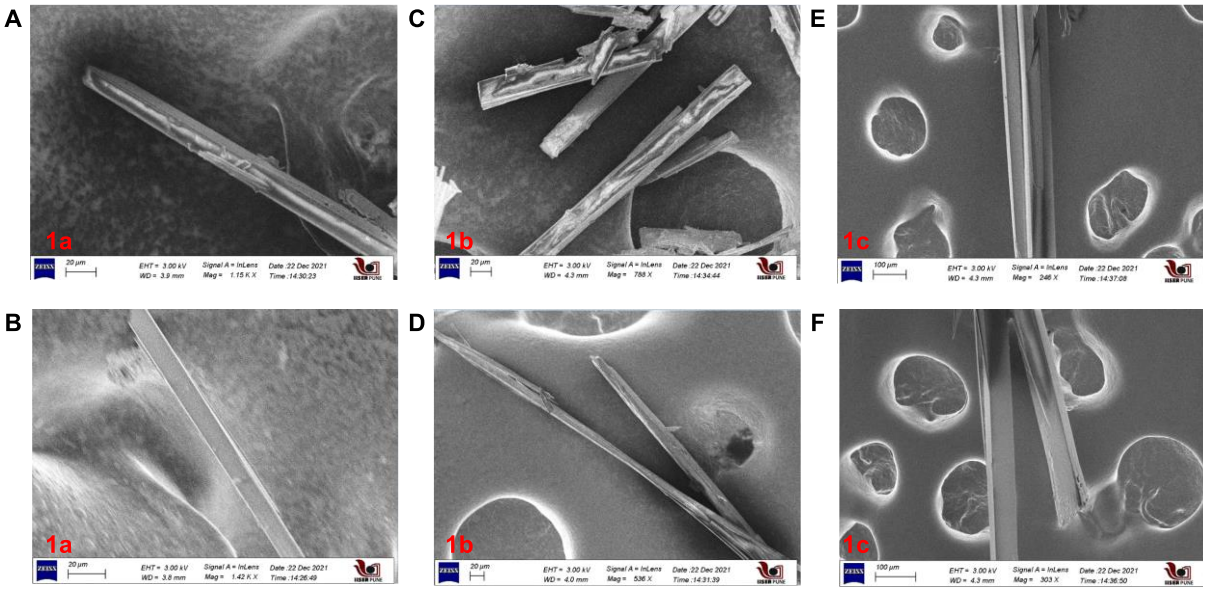

Figure 4.5. FESEM images of **1a** (A), (B); **1b** (C), (D), and **1c** (E), (F) showing distinct aggregation patterns recorded in methanol.

4.2.4 Ion Transport Studies

Ion transport activities of compounds **1a–1c** were evaluated across large unilamellar vesicles consisting of egg yolk phosphatidylcholine (EYPC–LUVs⊃HPTS) by 8-hydroxypyrene-1,3,6-trisulfonate (HPTS) based fluorometric methods. The EYPC vesicles, entrapping the pH-sensitive HPTS dye (pKa = 7.2), were prepared with internal and external pH 7.0, and a pH gradient was then applied by addition of NaOH (i.e., ΔpH = 0.8) in the extravesicular buffer. The collapse of the pH gradient upon the addition of **1a–1c** was monitored by the change in the dye fluorescence intensity at λ_{em} = 510 nm (λ_{ex} = 450 nm).[51,52] The comparison of activities provided the activity sequence: **1b** > **1a** > **1c**, inferring that compound **1b** works as the most efficient ion transporter (Figure 4.6). The dose-dependent activity data of compound **1b**, upon Hill analysis, provided the effective concentration at 50% activity, EC_{50} = 0.079 μM and Hill coefficient, n = 2.2 (Figure 4.7). The determined Hill coefficient (EC_{50}) value corroborates the supramolecular dimer formed by monomers of **1b** as the active rosette structure for the supramolecular nanochannel assembly.

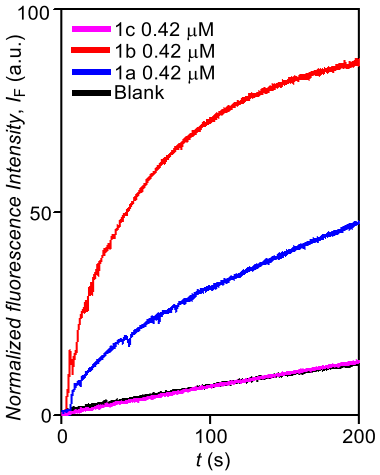

Figure 4.6. Comparison of ion transport activities of **1a-1c** across EYPC–LUVs⊃HPTS measured in the presence of an applied pH gradient (ΔpH = 0.8).

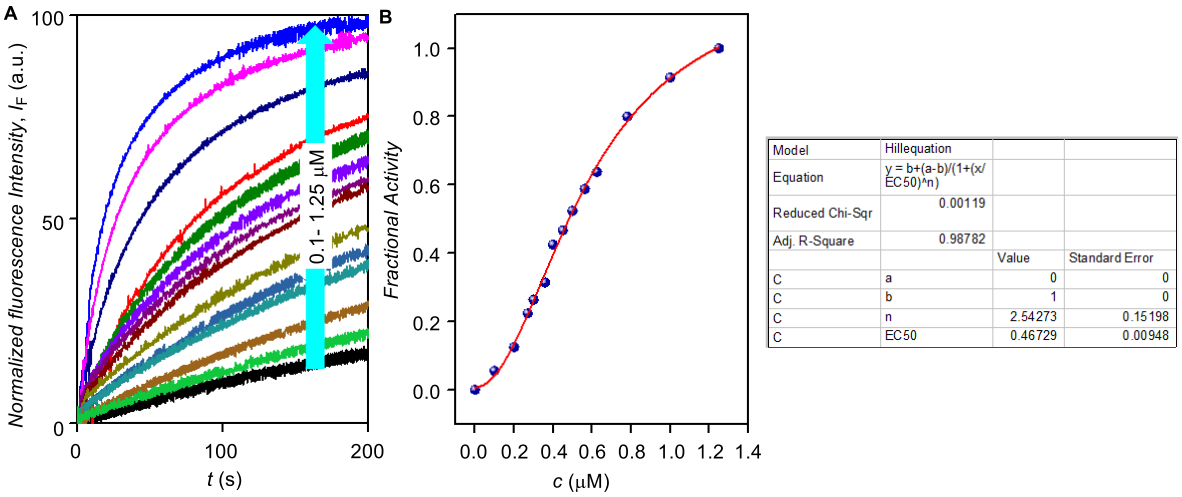

Model	Hillequation		
Equation	y = b+(a-b)/(1+(x/EC50)^n)		
Reduced Chi-Sqr	0.00119		
Adj. R-Square	0.98782		
		Value	Standard Error
C	a	0	0
C	b	1	0
C	n	2.54273	0.15198
C	EC50	0.46729	0.00948

Figure 4.7. Concentration dependent activity (A) and hill plot analysis of compound **1a** (B) across EYPC–LUVs⊃HPTS.

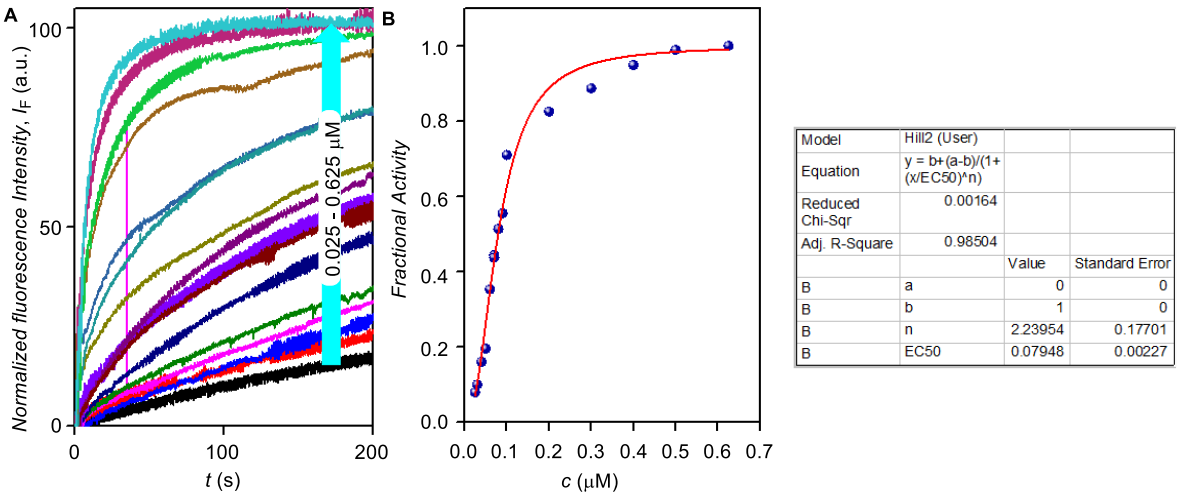

Model	Hill2 (User)		
Equation	y = b+(a-b)/(1+(x/EC50)^n)		
Reduced Chi-Sqr	0.00164		
Adj. R-Square	0.98504		
		Value	Standard Error
B	a	0	0
B	b	1	0
B	n	2.23954	0.17701
B	EC50	0.07948	0.00227

Figure 4.8. Concentration dependent activity (A) and hill plot analysis of compound **1b** (B) across EYPC–LUVs⊃HPTS.

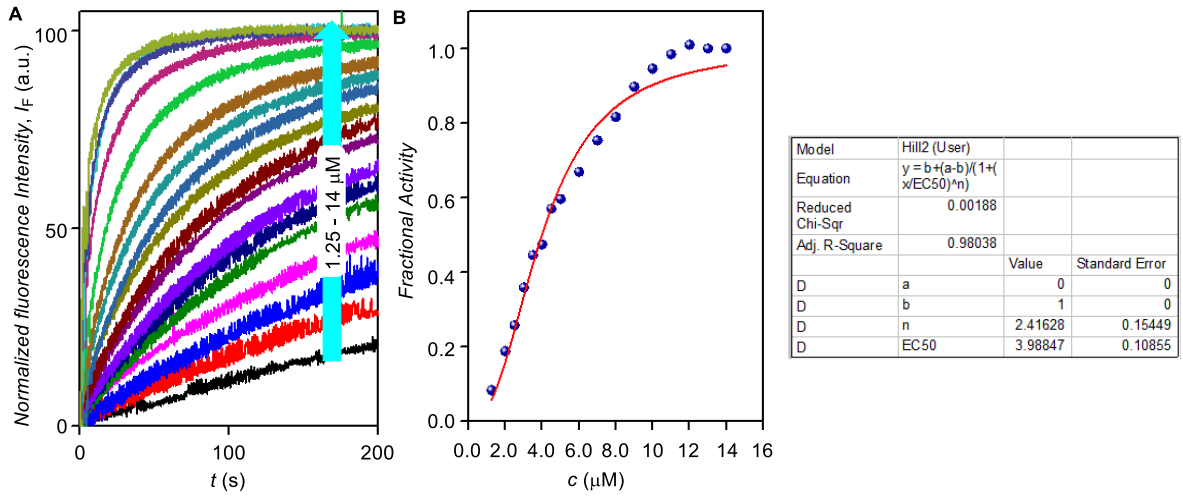

Model	Hill2 (User)		
Equation	y = b+(a-b)/(1+(x/EC50)^n)		
Reduced Chi-Sqr	0.00188		
Adj. R-Square	0.98038		
		Value	Standard Error
D	a	0	0
D	b	1	0
D	n	2.41628	0.15449
D	EC50	3.98847	0.10855

Figure 4.9. Concentration dependent activity (A) and hill plot analysis of compound **1c** (B) across EYPC–LUVs⊃HPTS.

4.2.5 Ion Selectivity Studies

The appreciable ion transport activity observed for compound **1b** led us to investigate the ion selectivity of the compound. Initially, the ion transport activity across EYPC–LUVs⊃HPTS was measured with intravesicular NaCl and an iso-osmolar extravesicular M^+/ Cl^- salt (where, M^+ = Li^+, Na^+, K^+, Rb^+, and Cs^+) were used to investigate the possible selectivity among the different cations. Variation of the external cations (M^+ = Li^+, Na^+, K^+, Rb^+, and Cs^+) in the aforementioned LUVs did not provide any noticeable difference in the ion transport rate, thus indicating no role of alkali metal cations in the transport process (Figure 4.10A). To determine the role of anions in the transport process, the anion selectivity study was performed by varying the extravesicular anions of NaX salt (X^- = Cl^-, Br^-, I^-, $NO3^-$, and $ClO4^-$), and the collapse of rates of the applied pH gradient was compared in the presence of **1b**. The results from this experiment provided the selectivity sequence as $Cl^- > ClO_4^- > Br^- > I^- > NO_3^-$ which confirmed that the highest selectivity was present for Cl^- (Figure 4.10B). Overall, these studies suggested the major involvement of alkali metal cations and inorganic anions in the transport process.

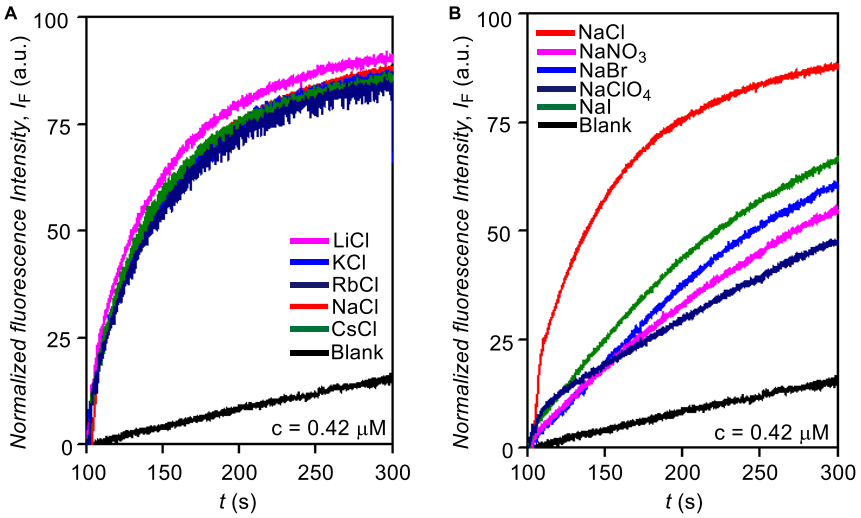

Figure 4.10. Anion selectivity (A) and cation selectivity of **1b** (B) across EYPC–LUVs⊃HPTS.

4.2.6 Chloride Transport Assay and Transport Mechanism

To further confirm the Cl^- ion transport activity of **1b**, the EYPC–LUVs were prepared by entrapping lucigenin dye (i.e., EYPC–LUVs⊃lucigenin) and $NaNO_3$ salt, and a Cl^-/NO_3^- gradient was applied by adding NaCl (2M) in the extravesicular buffer. The influx of the Cl^- was measured by monitoring the fluorescence intensity of intravesicular dye at λ_{em} = 535 nm (λ_{ex} = 450 nm). A dose-dependent quenching of lucigenin fluorescence was observed upon the addition of compound **1a** (Figure 4.11) and **1b** (Figure 4.12). These data indicated that the supramolecular channel formed by compound **1a** and **1b** allows the influx of Cl^- across liposomes. The Hill coefficient value provided additional evidence supporting the participation of two units of **1b** in the constitution of the active transporter. No change in transport activity was seen upon changing the extravesicular cation salts MCl (M^+ = Li^+, Na^+, K^+, Rb^+, Cs^+), excluding the potential role of M^+/Cl^- symport in the transport pro cess (Figure 4.13). In order to provide additional evidence for the antiport mechanism, compound **1b** was combined with valinomycin, a well-established potassium transporter, and the rate of ion transport was subsequently observed.[53] The extravesicular buffer was supplemented with KCl in order to establish a gradient of Cl^-/NO_3^-. Subsequently, the inclusion of valinomycin was carried out concomitantly with **1b** to observe their synergistic impact. The acceleration of the chloride transport rate was quantified in Figure 4.13, demonstrating the synergistic effect of chloride influx by **1b** and potassium influx by valinomycin. The Cl^-/NO_3^- antiport has been identified as the favoured transport mechanism involving **1b**, owing to the increased rate of Cl^- transport observed in the presence of valinomycin.

The effect of **1b** on the lipid bilayer membrane was checked by using vesicles with entrapped ANTS–DPX dye. The EYPC–LUV⊃ANTS–DPX (λ_{em} = 520 nm with λ_{ex} = 353 nm) were prepared according to the known procedure. No significant leakage of the dye from vesicles confirmed that the compound neither destroys the integrity of the lipid bilayer membrane nor large transmembrane pores are formed by the compound (Figure 4.13).

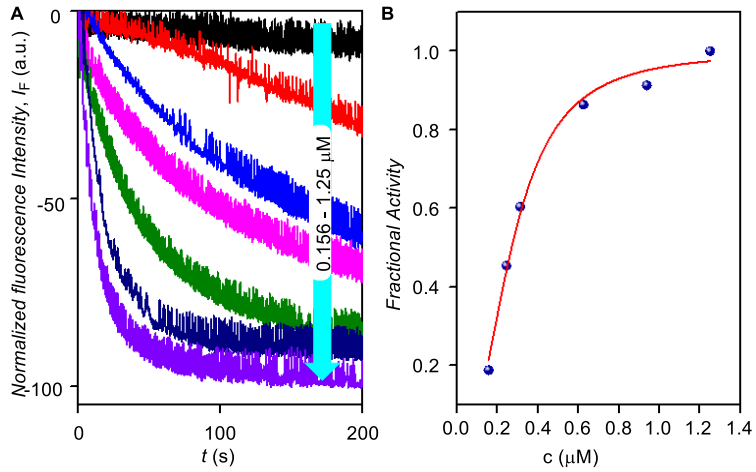

Model	Hill2 (User)		
Equation	y = b+(a-b)/(1+(x /EC50)^n)		
Reduced Chi-Sqr	8.96327E-4		
Adj. R-Square	0.99084		
		Value	Standard Error
B	a	0	0
B	b	1	0
B	n	2.3788	0.19824
B	EC50	0.26967	0.00846

Figure 4.11. Concentration dependent activity of compound **1a** across EYPC–LUVs⊃lucigenin. (A). Hill plot analysis of compound **1a** (B).

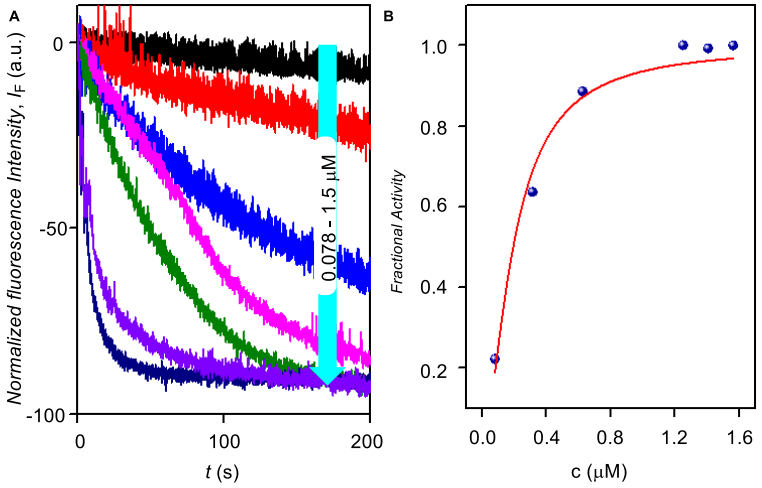

Model	Hillequation		
Equation	y = b+(a-b)/(1+(x /EC50)^n)		
Reduced Chi-Sqr	0.00203		
Adj. R-Square	0.97905		
		Value	Standard Error
C	a	0	0
C	b	1	0
C	n	1.62211	0.19004
C	EC50	0.19163	0.01924

Figure 4.12. Concentration dependent activity of compound **1b** across EYPC–LUVs⊃lucigenin. (A). Hill plot analysis of compound **1b** (B).

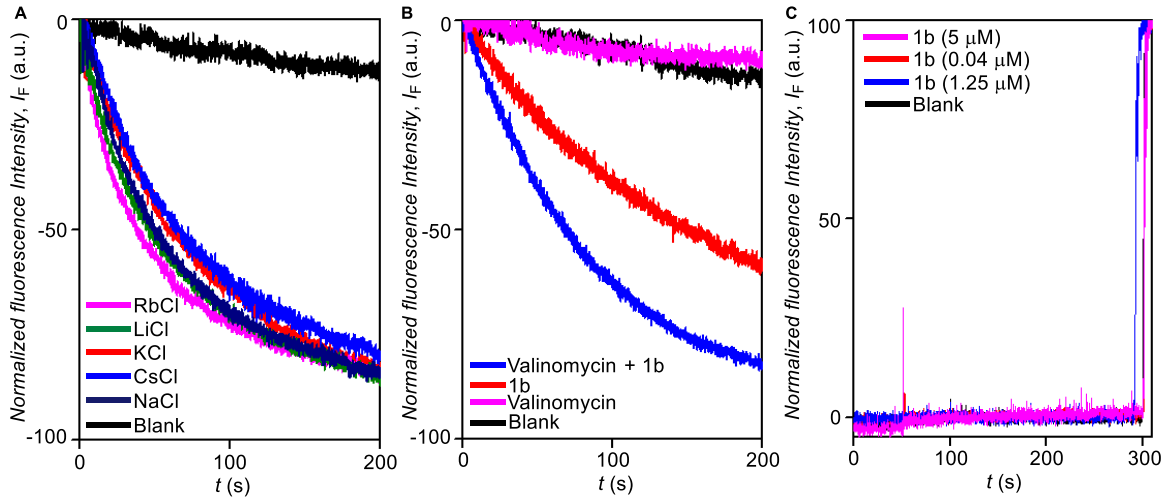

Figure 4.13. Influence of extravesicular cations in the Cl^- influx by **1b** across EYPC–LUVs⊃lucigenin (A). Comparison of Cl^- influx activity of **1b** in the absence and in the presence of valinomycin (0.312 μM) across EYPC–LUVs⊃lucigenin (B) and ANTS–DPX leakage assay in presence of compound **1b** (C).

4.2.7 Transporter Mechanism (Cholesterol Method)

To identify the kind of ion transport mechanism (carrier or channel), a cholesterol assay was conducted. The fluidity of the membrane will be reduced by cholesterol loading, which will reduce the number of ions carried by the carrier mechanism. However, there won't be a major change in how well the supramolecular channel transit works. The results of the experiment clearly revealed that the ion transport process is caused by the channel building because the transport activity remained virtually intact in the presence of cholesterol (Figure 4.14).[53]

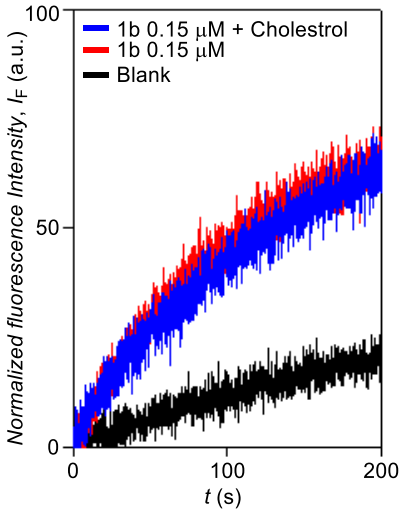

Figure 4.14. Effect of the 10 mol % of the cholesterol in the EYPC/cholesterol membrane on transport by **1b.**

4.2.8 Planar Bilayer Conductance Studies

To appraise the necessary evidence for ion channel formation by the most active compound **1b**, we measured electrical conductance across the planar lipid bilayer membrane. The planar lipid bilayer, consisting of 1,2-diphytanoyl-sn-glycero-3-phosphocholine (DPhPC) lipid, was prepared over the orifice connecting two electrolyte chambers of the instrument. Electrical conductance between two chambers, after applying a voltage, provides information about ion channel formation. Significant conduction of ions was observed by adding **1a** and **1b** (c = 5 μM) in the cis chamber of the electrolyte solution.[54] The periodic opening and closing events were also observed at different holding potentials, corroborating the ion channel formation at the planar bilayer by **1a** (Figure 4.15A) and **1b** (Figure 4.15B). The single-channel conductance G = 65 ± 0.6 pS and the diameter d = 3.81 ± 0.42 Å were calculated for the supramolecular ion channel formed by 1b. The variation of current with voltage (I–V plot) in the presence of the symmetric solution of KCl (1.0 M each) exhibited a linear variation, i.e., ohmic behaviour, confirming the channel's nondipole nature. To recognize the selectivity of **1b** towards anion in comparison with cation, the permeability ratio (P_{Cl^-}/P_{K^+}) was calculated by using the Goldman-Hodgkin-Katz equation with unsymmetrical KCl solutions (i.e., KCl_{cis} = 1 M and KCl_{trans} = 0.5 M). It was perceived that Cl^- transport rate is higher than the rate of K^+ transport with a permeability ratio (P_{Cl^-}/P_{K^+}) = 1.83 (Figure 4.16).

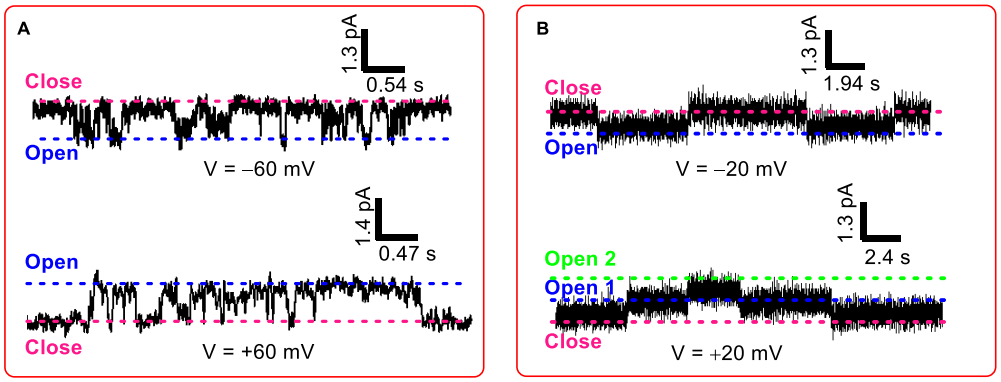

Figure 4.15. Single-channel conductance of **1a** (5 μM) recorded at –60 mV and at +60 mV (A). Single-channel conductance of **1b** (5 μM) recorded at –20 mV and at +20 mV under symmetrical KCl solution (B).

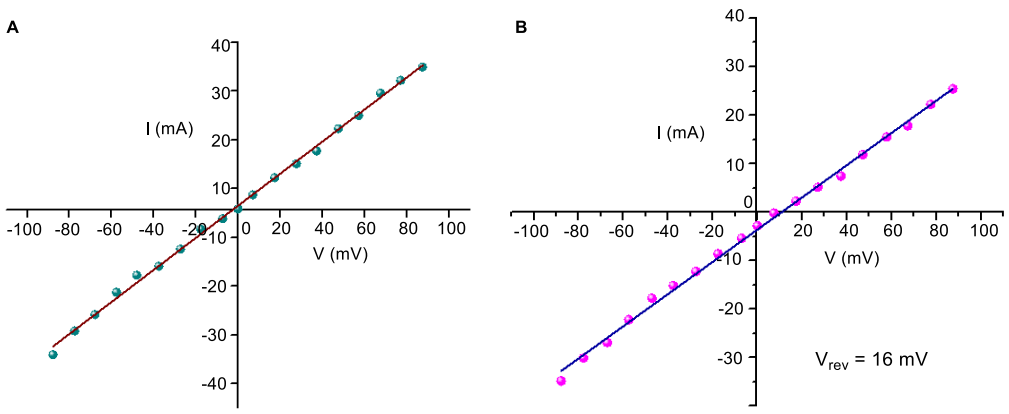

Figure 4.16. I−V plots of **1b** under symmetrical (A) and unsymmetrical (B) concentrations of KCl.

4.2.9 Molecular Modelling of Ion Channel

To gain mechanistic insights into ion transport across the artificial channel structure and evaluate the channel stability in the membrane environment, we did atomic-level molecular dynamics simulations. The synthetic channel structure, which is made up of 12 monomers organized in six successive layers, was initially minimized using the MAESTRO program.[55] Then, using CHARMM-GUI's membrane builder protocol,[56,57] the semi-minimized channel structure is used to construct the channel/membrane assembly. After system size determination, the assembly's structure is first correctly oriented and then packed within the lipid bilayer assembly. Finally, the system has achieved good equilibrium. The resulting channel/membrane complex contains the self-assembled channel structure that is located at the core of the lipid bilayer membrane. The channel is composed of six repeating layers that are collectively made up of 12 monomers. The 1,2-diphytanoyl-sn-glycero-3-phosphocholine (DPhPC) lipids that make up the membrane bilayer are distributed evenly throughout its 144 leaflets, each of which has 72 lipid units. The rectangular channel/membrane complex is eventually compressed into a box with dimensions of 7.7×7.7×9.0 nm^3. After that, enough water was added to the system to maintain a 1 M KCl salt concentration across each of the aqueous compartments that were separated from one another by a lipid bilayer. Table 4.1 lists the specifics of the simulation systems. In experimental section, the specifics of the simulation process are explained.

Box dimension	No. of water molecules	No. of K^+ ions	No. of Cl^- ions
7.7x7.7x9.0 nm^3	9407	168	168

Table 4.1. The simulation system details.

Using an umbrella sampling simulation, the free energy landscape related to the movement of chloride ions via the channel was calculated. One chloride ion was permitted to pass through the channel core in order to investigate the mechanistic insight of ion passage, and the associated coordinates were spared from starting the umbrella sampling simulation. The configurations allude to the many places where Cl^- ion can be found within the channel core, commencing with its entrance through the channel's mouth and ending with its final exit from the channel's end.

The free energy profile suggests that when the anion experiences a higher free energy (ΔG is 7 kcal/mol) barrier when it reaches the center of the channel then it stays near the water level (Figure 4.17B). On the way of its travel from one aqueous compartment to the other separated by a membrane, the anion possesses less entropic freedom as it gets inserted into the channel cavity and this is reflected in the higher free energy when the ion resides at the central part of the channel. On the other hand, as the ion progresses toward either end of the channel the corresponding free energy starts to get decreased resulting in a symmetric free energy profile on both sides. In addition to the entropic factor influenced by the structural confinement of the channel structure, the probability of accessibility of water molecules within the channel core also contributes to the nature of the free energy landscape of anion transport. Not only the ion becomes less mobile within the channel cavity but also the lesser population of water molecules within the channel (compared to either water compartment) is responsible for a higher free energy barrier when the ion reaches the center of the channel. In contrast, when the ion resides in the water interface of the lipid bilayer together with higher flexibility it would get surrounded by a substantial amount of water which stabilizes the anion with favourable H-bonding etc. It is due to the lesser solvation energy of the anion at the center of the channel that the ion needs to pay a higher energy penalty to get pass through the confined channel environment. So, both the lesser scope of ionic mobility within the channel cavity and also the poor availability of solvent molecules around the anion at the center of the channel contributes to the highest free energy barrier when the ion reaches the center of the channel and the corresponding energy decreases symmetrically on an ionic movement towards the water interface due to improved entropic freedom and favourable solvation. Together with the symmetry of the free energy curve, there are some fine curvatures in the free energy profile which suggests a considerable impact of the chemical structure of the synthetic ion channel on the chloride transport energetics.

To explore the underlying mechanism of ion transport through the channel and inspect the interactions crucial for the movement of ions along the channel here we have analyzed the intra-channel interactions and also the inter-channel interactions between the channel residues and the passing chloride ion. The blue curve depicted (Figure 4.17C) illustrates the tally of intra-channel hydrogen bonding, which refers to the formation of hydrogen bonds between the channel residues. The data indicates that as the ion approaches the center of the channel, the count of intra-channel hydrogen bonding is significantly reduced. This suggests that the chloride ion is passing through the channel by breaking the existing H-bonds between the channel residues and thus making its path easier for translocation. While it disrupts the H-bonding interaction between the channel residues, it in turn makes its own contact with the channel. When the ion sits at the center of the channel the intra-channel H-bonding interaction (cyan curve) gets impaired most while there lies the highest contacts (red curve) between the ion and the channel residues (Figure 4.17C). Since the anion needs to break the H-bonds most when it reaches at the center of the channel, the corresponding free energy barrier becomes higher at the position i.e., more energy penalty is charged for the anion at the center of the channel. Taken together, the breaking of the existing intra channel H-bonds to make ion's way more widen and simultaneously make its favourable contact with the channel residues stand as the key interaction for ion transport through the channel.

To investigate whether there is any important role of specific interaction between the passing anion and channel we have systematically analyzed the mutual interaction between the chloride ion and the channel residues. The electronegative chloride ion interacts with the N–H moieties of the channel residues through an H-bonding interaction (Figure 4.17D). Very interestingly there is special interaction between the passing chloride ion and the iodine atom of the channel monomer which is usually referred to as I–Cl^- halogen bonding interaction. Further we have calculated the distance between the anion and iodine atom during the process of transport (Figure 4.17E) and it is observed that as the ion progresses through the channel the anion comes considerably closer to the iodine atom of the channel monomers indicating the possibility of formation of I–Cl^- halogen bond. It is due to the formation of favourable halogen bonding interaction between the ion and the channel, the transport process becomes appreciably easy and smooth. This is also reflected in the considerably lower free energy barrier of the channel, making the particular synthetic channel favourable for ion transport simply due to the scope of the favourable halogen bonding interaction. This is also further supported by the count

of the number of contacts formed between the chloride ion and the iodine atom of the channel during the process of transport (Figure 4.18B).

To know how these intra and inter-channel interactions with the chloride ion impact the channel's structural stability, the radius of gyration of the channel has been calculated. The slight deformation of the channel during ion transport is caused by the passing chloride ion breaking intra-channel H-bonds and forming new chloride connections with the channel residues (Figure 4.18C). However, the fluctuation of rg does not happen to a considerably high extent indicating the overall stability of the channel structure within the membrane environment. The slight deformation of the channel upon ion transport suggests enough structural flexibility of the channel structure which helps to facilitate the transportation.

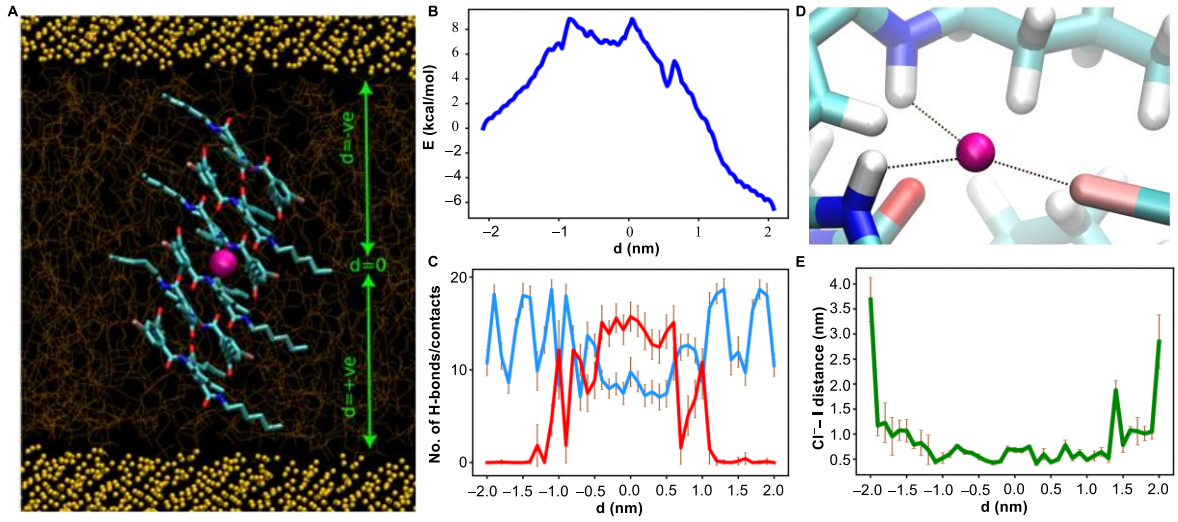

Figure 4.17. Representative snapshot describing single anion transport through the channel system embedded with the lipid bilayer membrane separating the two water compartments. The collective variable, (d) employed for umbrella sampling is also shown here (A). Free energy landscape of chloride ion transport through the channel is estimated by performing umbrella sampling simulation corresponding to the cv, d.(B) The number of hydrogen bonds (cyan) formed between the residues of the channel (intra-channel H-bonding) and the number of contacts (red) made by the passing chloride ion with the channel during its translocation along the channel is being represented with respect to the cv, d. The error bars are shown for both curves (C). The possible interactions among the channel residues and the chloride ion are shown (D). The distance between the iodine atom of the channel residues and the chloride ion during the process of its translocation is represented with error bars (E).

Next, we tested the influence of solvent molecules in the transport process of anion through the ion channel. The number of water molecules surrounding the chloride ion has calculated on the way its transported along the channel cavity (Figure 4.18A). It is found that as the ion travels

from either the end of the channel structure toward the channel center the number of water molecules accompanying the passing anion decreases gradually and as the ion reaches the center the neighbouring solvent number drops down to zero. This signifies that there is no availability of water within the channel core to help the transport of anion by allowing favourable solvation around the ion. So, through this channel the ion transport is not really guided by the water molecules rather the halogen-bonding interaction plays the key role here in assisting the passage of anion through the channel.

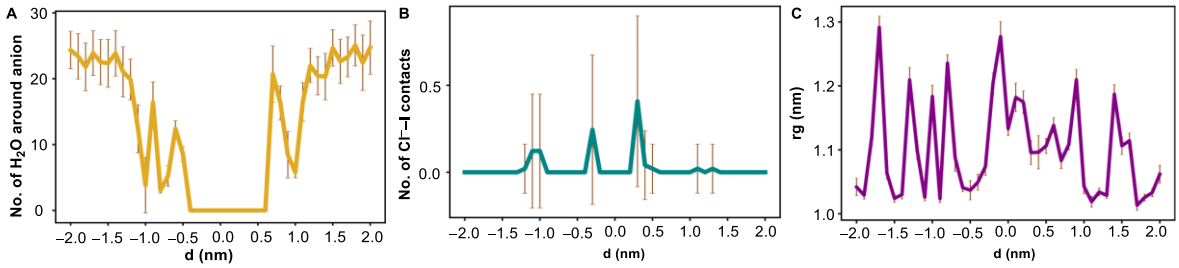

Figure 4.18. The number of water around the chloride ion is shown during the transport process of the anion through the channel (along cv, d) with error bars (A). The number of contacts between the iodine atom of the channel residues and the chloride ion during the process of its translocation is represented with error bars (B). And The radius of gyration of the synthetic channel structure is being represented (with error bars) along the progress of the ion through the channel (C).

4.3 Conclusion

To sum up, a category of synthetic chloride channels has been created through the process of directional self-assembly of polarised electron-deficient iodine atoms, resulting in channels that exhibit high activity and favourable selectivity. The linearly arrayed iodine atoms, which form a series of chloride-binding and transporting sites are responsible for facilitating chloride transport likely via a multi-ion jumping mode in a zig-zag pathway, the amide backbone enables stability of self-assembled supramolecular channel via intermolecular H-bonding. The *n*-hexyl substituted derivates turn out to be more active compared to the other two derivates. The *n*-Hexyl system favoured anion transport with prominent chloride ion selectivity, and the antiport mechanism for the anion transport was established. The transmembrane ion transport process was also operative through an ion channel constructed from the self-assembly of the *n*-Hexyl system as evident from the opening and closing events in the conductance studies. A computational model for such a supramolecular channel was also established, which shows that the transport of chloride across the bilayer is halogen-bonding driven.

4.4 Experimental Section

4.4.1 General Method

All reagents used for the synthesis were purchased from Sigma-Aldrich, Avra, TCI, Spectrochem, Alfa Aesar and used without further purification. Dry solvents, e.g., Toluene, Acetone, THF, CH_2Cl_2, and MeOH used for the synthesis, were purchased from Rankem, Merck and used without further drying. All the dry reactions were placed in oven-dried apparatus under atmospheric nitrogen conditions. The progress and completion of the reactions were monitored by performing thin-layer chromatography experiments where the plates were visualized either by short-wave UV light or by different staining reagents (Ninhydrin, PMA, etc.). Column chromatography for purification of the compound was performed using distilled organic solvents on silica gel (100–200 or 230–400 mesh). HEPES buffer, HPTS dye, Triton X–100, Lucigenin dye, NaOH, and inorganic salts (NaCl, $NaNO_3$, KCl, LiCl, CsCl, NaBr, NaI, etc.) were used in molecular biology grade purchased from Sigma-Aldrich. Egg yolk phosphatidylcholine (EYPC) lipid (25 mg/mL in chloroform), mini-extruder, and polycarbonate membranes (100 and 200 nm) were obtained from Sigma-Aldrich (Avanti Polar Lipids).

4.4.2 Physical Measurements

All ^1H and ^{13}C NMR spectra were recorded either on Bruker 400 MHz or Jeol 400 MHz spectrometers. The chemical shifts (δ) in ppm were referenced to the residual signal of deuterium solvents (^1H NMR $CDCl_3$: δ 7.26 ppm; ^{13}C NMR $CDCl_3$: δ 77.2 ppm; ^1H NMR DMSO-d_6: δ 2.5 ppm; ^{13}C NMR DMSO-d_6: δ 39.5 ppm). The multiplicities of the peaks are s (singlet), d (doublet), t (triplet), q (quartet), dd (doublet of doublet), and m (multiplet). High-resolution mass spectra (HRMS) were acquired in the ESI (+ve) mode. The measurement of pH during the preparation of the buffer solution was done by a pH meter purchased from Hanna instruments. Fluorescence spectra were recorded on a Fluoromax–4 from Horiba scientific, Jobin Yvon Edison equipped with an injector port and a magnetic stirrer. The experimental data obtained from fluorescence were processed in Origin 8.5 software. The field emission scanning electron microscopy (FESEM) images were obtained using FEI Quanta 3D dual beam ESEM at 3.0 kV.

4.4.3 Synthesis

Synthesis of compound 1: Synthesis of compound **1** was done according to known protocol.[58] At 0 °C, 5-aminoisophthalic acid (3 g, 20 mmol) in an H_2SO_4 solution was added to an aqueous solution of $NaNO_2$ (2.5 M). Afterward, urea (1.5 g) and KI (3.5 g) were added to the reaction mixture. The mixture was stirred for two hours. Following the addition of ice-cold water, the solid was filtered to get 5-iodoisophthalic acid (84% Yield). ^{1}H NMR spectrum was matched with the data of the reported compound.[58]

Synthesis of compound 1a: In a 50 mL round bottom flask, the acid **1** (500mg, 1.71 mmol, 1 eq.) was taken and dissolved in 10 mL of dry DMF. Then into the reaction mixture, cyclohexylmethylamine (581 mg, 5.13 mmol, 3 eq.), HOBt (630 mg, 4.01 mmol, 2.4 eq.), and triethylamine (0.6 mL, 4.25 mmol, 2.5 eq.) were added. At last, EDC·HCl (728 mg, 5.13 mmol, 3 eq.) was added, and the reaction mixture was then stirred at room temperature overnight under an inert atmosphere. After completion of the reaction, the reaction mixture was washed with water (3 × 10 mL) and followed by brine solution (1 × 10 mL) by extracting the compound in $CHCl_3$ (50 mL). The organic layer was then dried over Na_2SO_4, and the solvent was evaporated in a rotary evaporator to get the crude product. The crude product was purified by silica gel column chromatography using methanol (MeOH) in chloroform ($CHCl_3$) as a solvent system. The product **1a** was obtained as white solid (88 % Yield) (7 % MeOH:$CHCl_3$). **IR** (neat, ν/cm^{-1}): 3837, 3742, 2922, 2897, 2452, 1663, 1645, 1543, 1441, 619; **^{1}H NMR (400 MHz, $CDCl_3$, δ):** 8.18 (d, J = 1.5 Hz, 2H), 8.10 (d, J = 1.6 Hz, 1H), 6.37 (s, 2H), 3.29 (t, J = 6.4 Hz, 4H), 1.75 (d, J = 8.4 Hz, 8H), 1.58 (td, J = 7.9, 7.4, 3.4 Hz, 2H), 1.26 – 1.18 (m, 8H), 0.99 (d, J = 11.7 Hz, 4H). **^{13}C NMR (101 MHz, $CDCl_3$):** 165.4, 138.6, 136.9, 124.7, 94.4, 46.66, 38.1, 31.1, 26.5, 25.9. **HRMS (ESI):** Calc. for $C_{22}H_{31}IN_2O_2$ $[M+H]^+$: 483.1503; Found: 483.1503.

Synthesis of compound 1b: In a 25 mL round bottom flask, the acid **1** (200 mg, 0.68 mmol, 1 eq.) was taken and dissolved in 5 mL of dry DMF. Then into the reaction mixture, hexylamine (208 mg, 2.05 mmol, 3 eq.), HOBt (252 mg, 1.64 mmol, 2.4 eq.), and triethylamine (0.3 mL, 2.5 eq.) were added. At last, EDC·HCl (291 mg, 2.05 mmol, 3 eq.) was added, and the reaction mixture was then stirred at room temperature overnight under an inert atmosphere. After completion of the reaction, the reaction mixture was washed with water (3 × 10 mL) and followed by brine solution (1 × 10 mL) by extracting the compound in $CHCl_3$ (50 mL). The organic layer was then dried over Na_2SO_4, and the solvent was evaporated in a rotary evaporator to get the crude product. The crude product was purified by silica gel column

chromatography using methanol (MeOH) in chloroform ($CHCl_3$) as a solvent system. The product **1b** was obtained as light brown solid (90 % Yield) (7 % MeOH:$CHCl_3$). **IR** (neat, ν/cm^{-1}): 3313, 3035, 2874, 1588, 1527, 1138, 1021, 623; **^{1}H NMR (400 MHz, $CDCl_3$, δ):** 8.14 (d, *J* = 1.4 Hz, 2H), 8.05 (t, *J* = 1.4 Hz, 1H), 6.44 (s, 2H), 3.42 (q, *J* = 7.1 Hz, 4H), 1.60 (p, *J* = 7.3 Hz, 4H), 1.36 – 1.28 (m, 11H), 0.91 – 0.86 (m, 6H). **^{13}C NMR (101 MHz, $CDCl_3$):** 165.4, 138.6, 136.9, 124.6, 94.4, 77.2, 40.5, 31.6, 29.6, 26.8, 22.7, 14.2. **HRMS (ESI):** Calc. for $C_{20}H_{31}IN_2O_2$ $[M+H]^+$: 459.1503; Found: 459.1565.

Synthesis of compound 1c: In a 25 mL round bottom flask, the acid **1** (100mg, o.34 mmol, 1 eq.) was taken and dissolved in 5 mL of dry DMF. Then into the reaction mixture, butylamine (75 mg, 1.02 mmol, 3 eq.), HOBt (126 mg, 0.82 mmol, 2.4 eq.), and triethylamine (0.2 mL, 2.5 eq.) were added. At last, EDC·HCl (146 mg, 1.02 mmol, 3 eq.) was added, and the reaction mixture was then stirred at room temperature overnight under an inert atmosphere. After completion of the reaction, the reaction mixture was washed with water (3 × 10 mL) and followed by brine solution (1 × 10 mL) by extracting the compound in $CHCl_3$ (50 mL). The organic layer was then dried over Na_2SO_4, and the solvent was evaporated in a rotary evaporator to get the crude product. The crude product was purified by silica gel column chromatography using methanol (MeOH) in chloroform ($CHCl_3$) as a solvent system. The product **1c** was obtained as yellowish solid (85 % Yield) (7 % MeOH:$CHCl_3$). **IR** (neat, ν/cm^{-1}): 3316, 2941, 2852, 1638, 1549, 1515, 1126, 1021, 607;. **^{1}H NMR (400 MHz, $CDCl_3$, δ):** 8.15 (d, *J* = 1.4 Hz, 2H), 8.07 – 8.04 (m, 1H), 6.46 – 6.35 (m, 2H), 3.43 (q, *J* = 7.0 Hz, 4H), 1.59 (p, *J* = 7.4 Hz, 4H), 1.41 (dt, *J* = 15.0, 7.3 Hz, 4H), 0.95 (t, *J* = 7.3 Hz, 6H). **^{13}C NMR (101 MHz, $CDCl_3$):** 165.4, 138.6, 136.9, 124.6, 94.4, 77.2, 40.2, 31.7, 20.3, 13.9. **HRMS (ESI):** Calc. for $C_{16}H_{32}IN_2O_2$ $[M+H]^+$: 403.0877; Found: 403.0882.

4.4.4 SCXRD

The needle-shaped crystals of compound **1b** were grown in a solvent combination of MeOH/CH_2Cl_2 at room temperature. The single-crystal X-ray data of compound **2** was recorded at 150 K on a Bruker KAPPA APEX II CCD Duo diffractometer (operated at 1500 W power: 50 kV, 30 mA) using graphite-mono chromated Mo Kα radiation (λ = 0.71073 Å). The crystal was kept on a nylon Cryo-Loops (Hampton Research) with Paraton-N (Hampton Research). The data reduction and integration were computed with SAINT software.[59] A correction on multi-scan absorption was employed on the collected reflections. The structure solving was achieved by the direct method using SHELXTL[60] and was further refined on *F*2

by full-matrix least-squares technique using the SHELXL-97[61] program package within the WINGX[62] program. All the non-hydrogen atoms were refined anisotropically. All hydrogen atoms were located in successive difference Fourier maps, and they were treated as riding atoms using SHELXL default parameters. The structures were examined using the *Adsym* subroutine of PLATON[63] to ensure that no additional symmetry could be applied to the models.

Crystallographic data for compound **1b**: **CCDC 2218287** contains the supplementary crystallographic data for this paper and can be obtained free of charge from The Cambridge Crystallographic Data Centre.

Identification code	**RAS_1b**
CCDC Number	**2218287**
Empirical formula	$C_{20}H_{31}IN_2O_2$
Formula weight	459.37
Temperature	296(2) K
Wavelength	.710 Å
Crystal system	Monoclinic
Space group	P 21/c
Unit cell dimensions	a = 8.664 (2) Å α= 90. b = 40.941 (12) Å β= 98.756 (8). c = 23.819 (9) Å γ = 90.
Volume	835 (1) $Å^3$
Z	4
Density (calculated)	1.458 Mg/m^3
Absorption coefficient	1.549 mm^{-1}

F(000)	3744
Crystal size	0.200 x 0.150 x 0.150 mm^3
Theta range for data collection	1.990 to 26.000°.
Index ranges	-10<=h<=9, -50<=k<=50, -29<=l<=29
Reflections collected	152333
Independent reflections	16418 [R(int) = 0.0800]
Completeness to theta = 25.242°	99.9 %
Absorption correction	Semi-empirical from equivalents
Max. and min. transmission	1.0 and 0.75
Refinement method	Full-matrix least-squares on F^2
Data / restraints / parameters	3887/0/164
Goodness-of-fit on F^2	1.243
Final R indices [I>2sigma(I)]	R1 = 0.0560, wR2 = 0.0974
R indices (all data)	R1 = 0.0739, wR2 = 0.1016
Extinction coefficient	0.000120(16)
Largest diff. peak and hole	1.707 and -1.396 e.$Å^{-3}$

Table 4.2. Crystal data and structure refinement for compound **1b.**

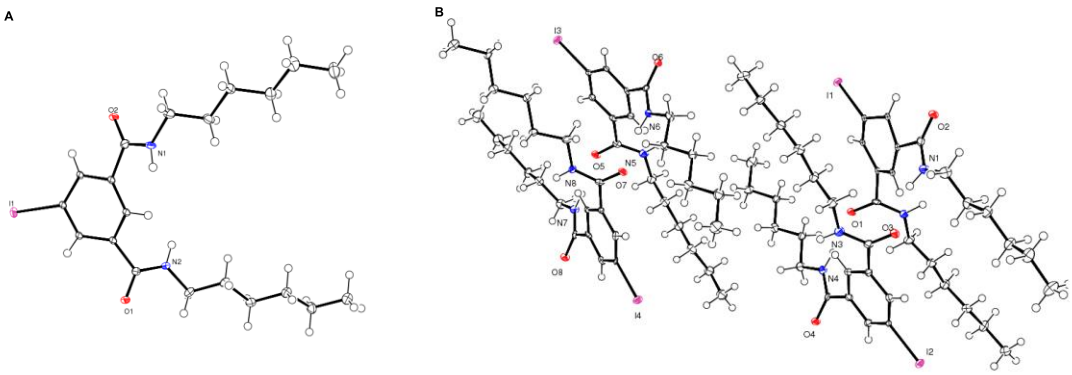

Figure 4.19. ORTEP diagram of **1b** (A) and (B).

4.4.5 FESEM

The samples were prepared by drop-casting 10 µL of **1a-1c** over silicon wafer at room temperature. The samples were dried under IR lamp for 5 minutes. Field emission scanning electron microscopy (FESEM) images were captured using a FEI Quanta 3D dual beam ESEM at 30 kV.

4.4.6 Ion Transport Studies

The ion transport studies for the compounds **1a**–**1c** were carried following the reported procedure explained in previous chapters.

4.4.7 Planar Bilayer Conductance Measurements

The ion transport studies for the compounds **1a**–**1c** were carried following the reported procedure explained in previous chapters.

4.4.8 Theoretical Calculations (*Done in collaboration with Susmita Sarkar and Dr. Jagannath Mondal from Center for Interdisciplinary Sciences, TIFR Hyderabad*)

We have performed molecular dynamics simulations at atomic resolution for gaining the mechanistic insights of ion transport through the synthetic channel structure and assessing the channel stability in the membrane environment.

Model and Methods:

System setup and simulation model: At the very beginning, the synthetic channel structure constituting 12 monomers arranged in six consecutive layers, were minimized with the software MAESTRO.[55] Then the semi-minimized channel structure is taken for building the channel/membrane assembly by utilization of the membrane builder protocol of CHARMM-GUI.[64,65] As per this protocol by Jo et al[56] the structure of the assembly is first oriented properly and then packed within the lipid bilayer assembly after system size determination. Finally, the system is equilibrated well. The channel/membrane complex thus generated contains the self-assembled channel structure lying at the center of the lipid bilayer membrane and the channel consists of six repetitive layers built with 12 monomers as a whole. The membrane bilayer is made up of 1,2-diphytanoyl-sn-glycero-3-phosphocholine (DPhPC) lipids of total 144 units equally distributed to each of the leaflet (each leaflet of the membrane consists 72 lipid units). Towards the end, the channel/membrane complex gets packed within a rectangular box of 7.7 × 7.7 × 9.0 nm^3 with dimension. Then the system was solvated with enough water maintaining 1 M KCl salt concentration over each of the aqueous compartments separated by the lipid bilayer. The simulation systems details are provided in Table 4.1.

For modelling the channel structure, the general AMBER forcefield (GAFF) were employed.[66–68] The lipid membrane in our simulation is modelled with the CHARMM36m forcefield parameters.[57,69,70] For water molecules CHARMM-TIP3P[71] parameters are employed.

Simulation method: All the simulations are done maintaining periodic boundary conditions (PBC) in all three dimensions (along x, y and z directions). For long-range electrostatic interactions the particle mesh Ewald (PME) method[72] was applied at cubic interpolation. Electrostatic interactions at the short-range were set with 1.2 nm cut-off. The neighbor lists were updated at a frequency of 20 steps. The hydrogen bonds of membrane and channel monomers were constrained by using the LINCS algorithm.[73] While the SETTLE[74] algorithm was applied for maintaining water molecule rigidity during the simulation. Lennard Jones interactions were truncated at 1.2 nm using Verlet cut-off scheme[75] considering dispersion corrections. At first, the system was energy minimized via the steepest-decent algorithm after applying some restraints on the system. Then the energy minimized system was taken for step wise equilibration through six successive steps for 10 ns each. Equilibration process was also carried out with particular restraints applied on the system but with a successive lowering of restraints value in each of the consecutive step. During the equilibration process, to maintain

an average temperature of 298 K and 1.0 bar pressure, Berendsen thermostat[76] and Berendsen barostat was employed. Finally, the equilibrated system was subjected to the final production run in NPT ensemble. Production run was continued for long 1.0 microsecond under slight restrain. During production simulation, the Nose-Hoover thermostat[77] was used to fix the system temperature at 298 K average temperature with a relaxation constant of 1.0 ps via individual coupling of three different components of the system i.e., the channel structure, membrane bilayer, and solvent. An average pressure of 1.0 bar was kept constant by applying the Parrinello-Rahman barostat[78] at a coupling constant of 5 ps and 4.5 × 10-5 bar compressibility factor. Pressure under was done in semi-isotropic condition by coupling separately in XY and Z directions of the system to keep the bilayer tensionless during the course of simulation. At the stage of production run, 2 fs time step was maintained employing leapfrog integrator. Simulations of the system were replicated twice following the similar simulation protocol. To carry out each of the simulation GROMACS software of 20x version was employed.

Free energy simulation: The free energy landscape corresponding to the chloride ion transport through the channel was computed by performing umbrella sampling simulation. To explore the mechanistic insight of ion passage, one chloride ion was allowed to move through the channel core and the corresponding coordinated were saved to initiate the umbrella sampling simulation. The configurations refer to the different location of Cl^- ion within the channel core starting from its entry through the mouth of the channel followed by its final exit from the end of the channel.

Electro-neutrality of the system containing single anion was maintained by incorporation of one K^+ ion into the system. Like equilibrium simulation, for umbrella sampling simulation also, the simulation box dimension and the water molecule number were kept the same. The collective variable (CV) of the system was chosen in Z-direction as the chloride anion travels along the channel (without considering hydrogen atoms) structure (d) as described in figure 4A. The location of the anion at the channel's upper half i.e., when the ion remains above the center of the channel (movement of the ion towards channel mouth starting from its center) is referred by negative value of d. Whereas positive d indicates that the anion resides below the channel central part i.e., at the lower half of the channel (when the anion travels from center towards the end of the channel). The location of the anion at the channel center is referred to as d = 0 nm. Configurations corresponding to the CV (d) value ranging from –2.0 nm to 2.0 nm (at a spacing of 0.1 nm of d) were generated for umbrella sampling simulation. Force

constant ranging from 7500 to 9000 kJ/mol/nm^2 was applied in simulation of each of the umbrella sampling windows for keeping the position of the anion at the desired d value. At first, energy minimization was performed via steepest-descent algorithm with each of the umbrella configurations leading to short NVT equilibration (simulation time step of 1 fs) for 500 ps. Finally, 20 ns long production run (with 2 fs time step) was performed with each of the equilibrated system in NPT ensemble at each of the windows. The same thermostat and barostat were employed for equilibration and production run in every window of the umbrella sampling simulation, as utilized during equilibrium simulation. The respective equilibrium free energy profile was computed using the weighted histogram analysis method (WHAM).[79] For executing all the simulations GROMACS software of version 20x were employed.

The free energy profile corresponding to the chloride ion passage is analyzed with our simulation. Also, to gain the insights on the detailed molecular mechanism of the transport of chloride ion through the channel, the extent of intra channel H-bonding and the number of contacts made by the passing anion with the channel residues were computed. Our calculation of radius of gyration (rg) helps to assess the stability of the synthetic channel structure within the membrane. The total number of water molecule(s) accompanying the chloride ion was estimated for investigating the contribution of the water in transporting the anion through the channel structure. Moreover, the specific interactions crucial for ion transport are also analyzed with proper details.

4.4.9 NMR Spectra

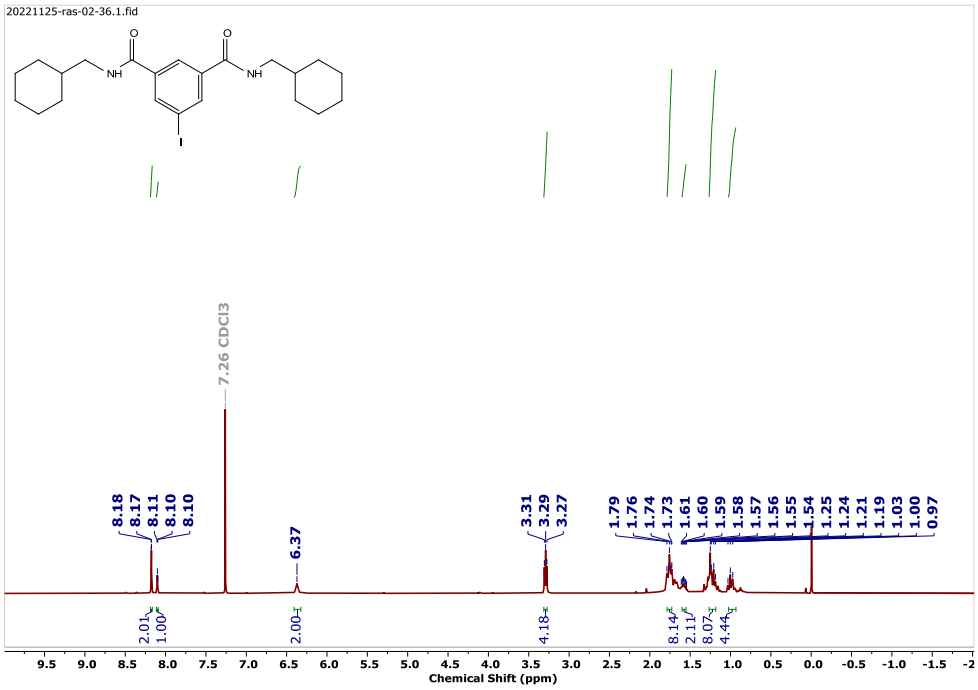

Figure 4.20. ^{1}H NMR spectrum of **1a** in $CDCl_3$.

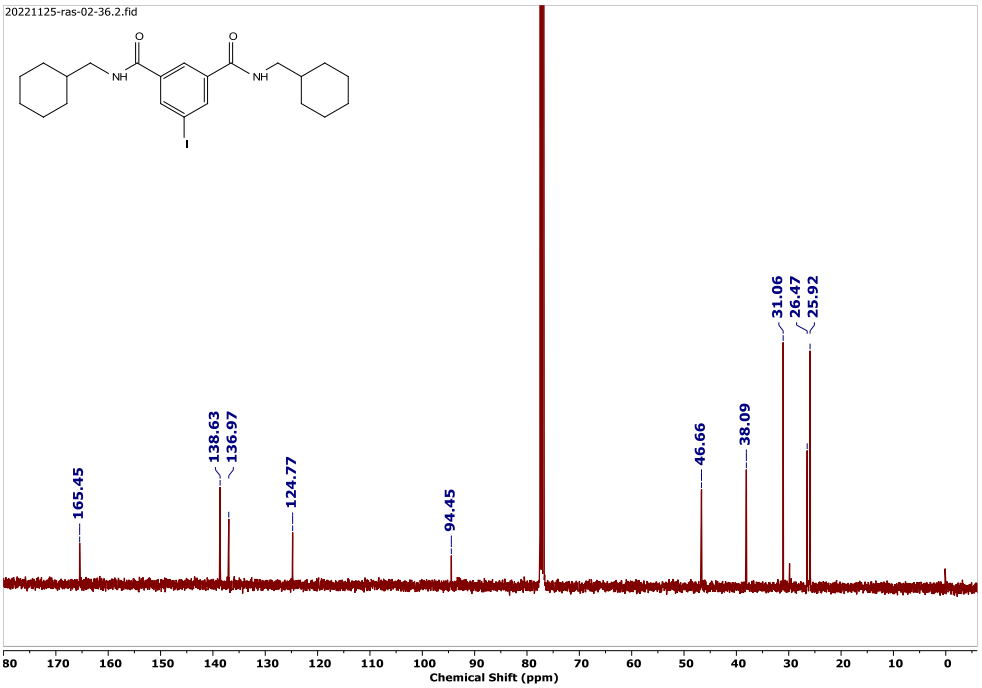

Figure 4.21. ^{13}C NMR spectrum of **1a** in $CDCl_3$.

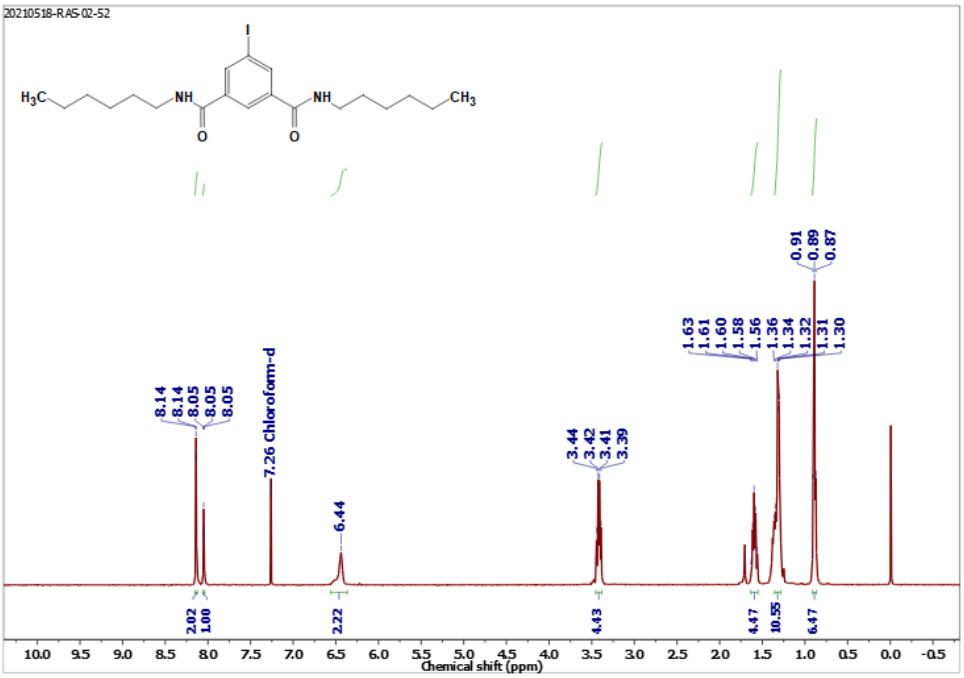

Figure 4.22. ^{1}H NMR spectrum of **1b** in $CDCl_3$.

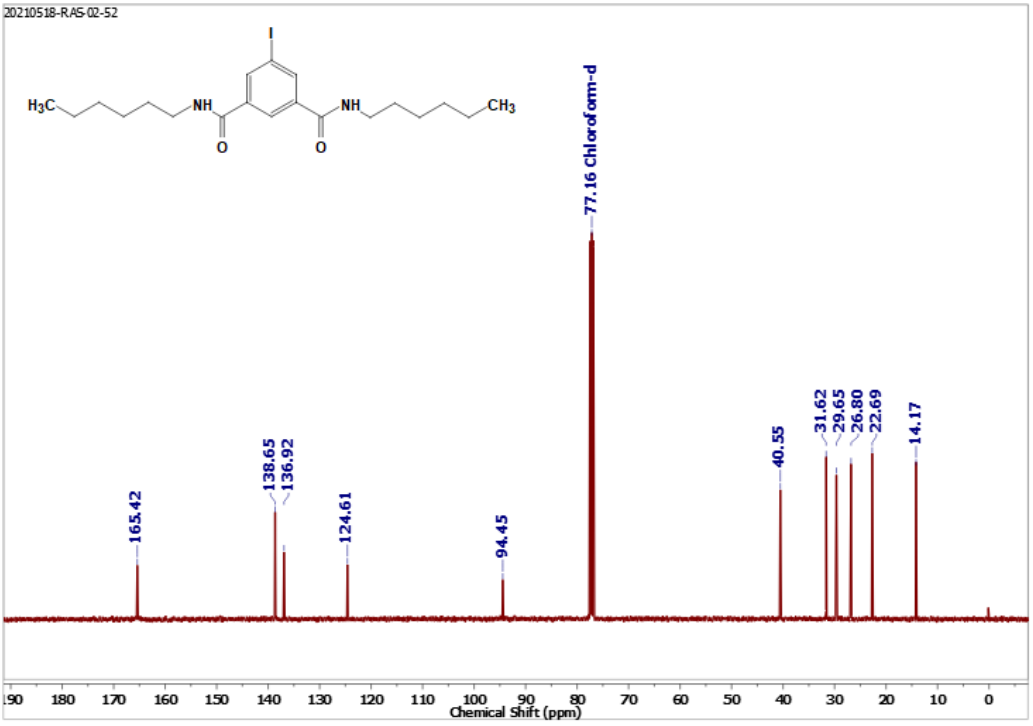

Figure 4.23. ^{13}C NMR spectrum of **1b** in $CDCl_3$.

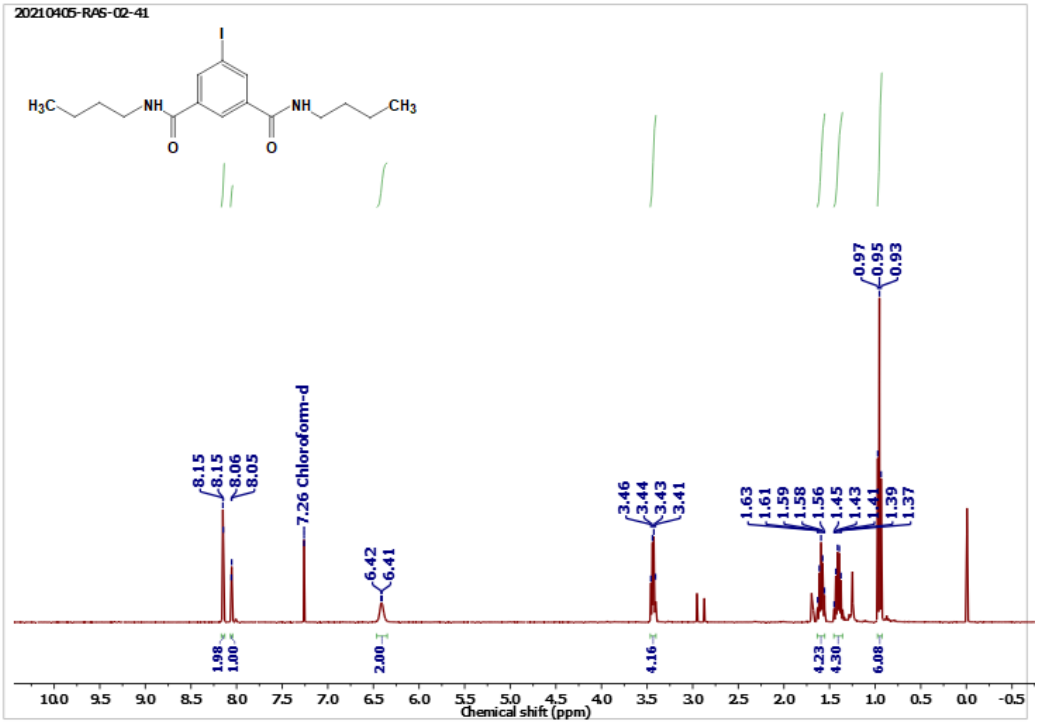

Figure 4.24. ^{1}H NMR spectrum of **1c** in $CDCl_3$.

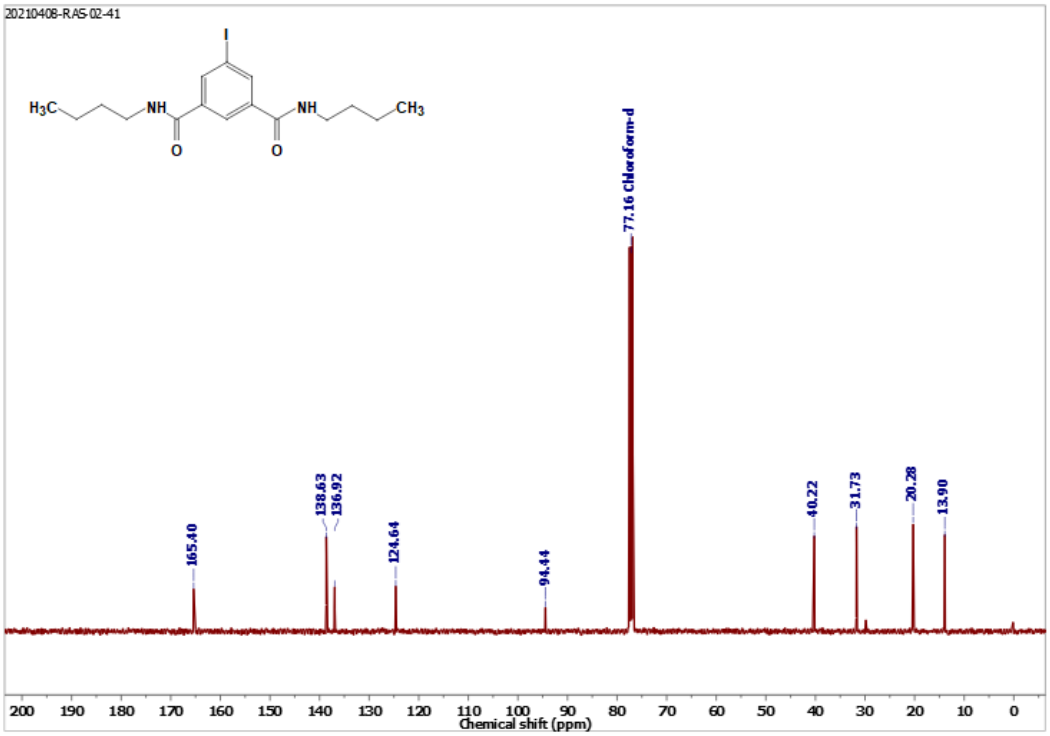

Figure 4.25. ^{13}C NMR spectrum of **1c** in $CDCl_3$.

4.5 References

1 P. A. Gale, E. N. W. Howe and X. Wu, *Chem*, 2016, 1, 351–422.

2 A. Vargas Jentzsch, D. Emery, J. Mareda, P. Metrangolo, G. Resnati and S. Matile, *Angew. Chemie - Int. Ed.*, 2011, **50**, 11675–11678.

3 A. V. Jentzsch, D. Emery, J. Mareda, S. K. Nayak, P. Metrangolo, G. Resnati, N. Sakai and S. Matile, *Nat. Commun.*, 2012, **3**, 905.

4 A. Vargas Jentzsch and S. Matile, *J. Am. Chem. Soc.*, 2013, **135**, 5302–5303.

5 G. R. Desiraju, P. Shing Ho, L. Kloo, A. C. Legon, R. Marquardt, P. Metrangolo, P. Politzer, G. Resnati and K. Rissanen, *Pure Appl. Chem.*, 2013, **85**, 1711–1713.

6 A. Brown and P. D. Beer, *Chem. Commun.*, 2016, **52**, 8645–8658.

7 Q.-Y. Wang, J. Lu, S.-M. Liao, Q.-S. Du and R.-B. Huang, *Curr. Top. Med. Chem.*, 2013, **13**, 1141–1151.

8 P. S. Ho, *Future Med. Chem.*, 2017, 9, 637–640.

9 G. Cavallo, P. Metrangolo, R. Milani, T. Pilati, A. Priimagi, G. Resnati and G. Terraneo, *Chem. Rev.*, 2016, 116, 2478–2601.

10 L. C. Gilday, S. W. Robinson, T. A. Barendt, M. J. Langton, B. R. Mullaney and P. D. Beer, *Chem. Rev.*, 2015, 115, 7118–7195.

11 T. M. Beale, M. G. Chudzinski, M. G. Sarwar and M. S. Taylor, *Chem. Soc. Rev.*, 2013, **42**, 1667–1680.

12 G. Berger, J. Soubhye and F. Meyer, *Polym. Chem.*, 2015, 6, 3559–3580.

13 G. Picci, S. Marchesan and C. Caltagirone, *Biomedicines*, 2022, **10**, 885.

14 P. Xin, L. Xu, W. Dong, L. Mao, J. Guo, J. Bi, S. Zhang, Y. Pei and C. Chen, *Angew. Chemie Int. Ed.*, 2023, **62**, e202217859.

15 C. Lang, X. Deng, F. Yang, B. Yang, W. Wang, S. Qi, X. Zhang, C. Zhang, Z. Dong and J. Liu, *Angew. Chemie - Int. Ed.*, 2017, **56**, 12668–12671.

16 P. Li, G. Xie, X. Y. Kong, Z. Zhang, K. Xiao, L. Wen and L. Jiang, *Angew. Chemie - Int. Ed.*, 2016, **55**, 15637–15641.

17 L. Leisle, K. Lam, S. Dehghani-Ghahnaviyeh, E. Fortea, J. D. Galpin, C. A. Ahern, E. Tajkhorshid and A. Accardi, *Nat. Commun.*, 2022, **13**, 7508.

18 T. Takeuchi, Y. Minato, M. Takase and H. Shinmori, *Tetrahedron Lett.*, 2005, **46**, 9025–9027.

19 J. A. Foster, M. O. M. Piepenbrock, G. O. Lloyd, N. Clarke, J. A. K. Howard and J. W. Steed, *Nat. Chem.*, 2010, **2**, 1037–1043.

20 M. G. Sarwar, D. Ajami, G. Theodorakopoulos, I. D. Petsalakis and J. Rebek, *J. Am. Chem. Soc.*, 2013, **135**, 13672–13675.

21 L. Y. You, S. G. Chen, X. Zhao, Y. Liu, W. X. Lan, Y. Zhang, H. J. Lu, C. Y. Cao and Z. T. Li, *Angew. Chemie - Int. Ed.*, 2012, **51**, 1657–1661.

22 L. Catalano, G. Cavallo, P. Metrangolo, G. Resnati and G. Terraneo, *Top. Curr. Chem.*, 2016, **373**, 289–310.

23 P. Metrangolo, Y. Carcenac, M. Lahtinen, T. Pilati, K. Rissanen, A. Vij and G. Resnati, *Science*, 2009, **323**, 1461–1464.

24 K. Rissanen, *CrystEngComm*, 2008, 10, 1107–1113.

25 O. Hassel, *Science*, 1970, **170**, 497–502.

26 A. Priimagi, G. Cavallo, P. Metrangolo and G. Resnati, *Acc. Chem. Res.*, 2013, **46**, 2686–2695.

27 G. Cavallo, P. Metrangolo, T. Pilati, G. Resnati, M. Sansotera and G. Terraneo, *Chem. Soc. Rev.*, 2010, **39**, 3772–3783.

28 D. A. Kraut, M. J. Churchill, P. E. Dawson and D. Herschlag, *ACS Chem. Biol.*, 2009, **4**, 269–273.

29 D. Lenoir and C. Chiappe, *Chem. – A Eur. J.*, 2003, **9**, 1036–1044.

30 A. Bruckmann, M. A. Pena and C. Bolm, *Synlett*, 2008, **2008**, 900–902.

31 S. M. Walter, F. Kniep, L. Rout, F. P. Schmidtchen, E. Herdtweck and S. M. Huber, *J. Am. Chem. Soc.*, 2012, **134**, 8507–8512.

32 F. Zapata, A. Caballero, N. G. White, T. D. W. Claridge, P. J. Costa, V. Félix and P. D. Beer, *J. Am. Chem. Soc.*, 2012, **134**, 11533–11541.

33 M. G. Sarwar, B. Dragisic, L. J. Salsberg, C. Gouliaras and M. S. Taylor, *J. Am. Chem. Soc.*, 2010, **132**, 1646–1653.

34 G. T. Spence and P. D. Beer, *Acc. Chem. Res.*, 2013, **46**, 571–586.

35 A. Mele, P. Metrangolo, H. Neukirch, T. Pilati and G. Resnati, *J. Am. Chem. Soc.*, 2005, **127**, 14972–14973.

36 L. A. Weiss, N. Sakai, B. Ghebremariam, C. Ni and S. Matile, *J. Am. Chem. Soc.*, 1997, **119**, 12142–12149.

37 C. Ren, X. Ding, A. Roy, J. Shen, S. Zhou, F. Chen, S. F. Yau Li, H. Ren, Y. Y. Yang and H. Zeng, *Chem. Sci.*, 2018, **9**, 4044–4051.

38 R. Wilcken, M. O. Zimmermann, A. Lange, A. C. Joerger and F. M. Boeckler, *J. Med. Chem.*, 2013, **56**, 1363–1388.

39 Y. Lu, Y. Liu, Z. Xu, H. Li, H. Liu and W. Zhu, *Expert Opin. Drug Discov.*, 2012, 7, 375–383.

40 L. A. Hardegger, B. Kuhn, B. Spinnler, L. Anselm, R. Ecabert, M. Stihle, B. Gsell, R. Thoma, J. Diez, J. Benz, J. M. Plancher, G. Hartmann, D. W. Banner, W. Haap and F. Diederich, *Angew. Chemie Int. Ed.*, 2011, **50**, 314–318.

41 P. Auffinger, F. A. Hays, E. Westhof and P. S. Ho, *Proc. Natl. Acad. Sci. U. S. A.*, 2004, **101**, 16789–16794.

42 T. Clark, M. Hennemann, J. S. Murray and P. Politzer, *J. Mol. Model.*, 2007, **13**, 291–296.

43 J. P. Behr, M. Kirch and J. M. Lehn, *J. Am. Chem. Soc.*, 1985, **107**, 241–246.

44 M. G. Sarwar, B. Dragisic, S. Sagoo and M. S. Taylor, *Angew. Chemie*, 2010, **122**, 1718–1721.

45 L. E. Bickerton, A. J. Sterling, P. D. Beer, F. Duarte and M. J. Langton, *Chem. Sci.*, 2020, **11**, 4722–4729.

46 A. Vargas Jentzsch, D. Emery, J. Mareda, P. Metrangolo, G. Resnati and S. Matile, *Angew. Chemie Int. Ed.*, 2011, **50**, 11675–11678.

47 L. M. Lee, M. Tsemperouli, A. I. Poblador-Bahamonde, S. Benz, N. Sakai, K. Sugihara

and S. Matile, *J. Am. Chem. Soc.*, 2019, **141**, 810–814.

48 A. Docker, X. Shang, D. Yuan, H. Kuhn, Z. Zhang, J. J. Davis, P. D. Beer and M. J. Langton, *Angew. Chemie Int. Ed.*, 2021, **60**, 19442–19450.

49 A. Singh, A. Torres-Huerta, T. Vanderlinden, N. Renier, L. Martínez-Crespo, N. Tumanov, J. Wouters, K. Bartik, I. Jabin and H. Valkenier, *Chem. Commun.*, 2022, **58**, 6255–6258.

50 C. Ren, X. Ding, A. Roy, J. Shen, S. Zhou, F. Chen, S. F. Yau Li, H. Ren, Y. Y. Yang and H. Zeng, *Chem. Sci.*, 2018, **9**, 4044–4051.

51 V. Gorteau, G. Bollot, J. Mareda and S. Matile, *Org. Biomol. Chem.*, 2007, **5**, 3000–3012.

52 P. Talukdar, G. Bollot, J. Mareda, N. Sakai and S. Matile, *J. Am. Chem. Soc.*, 2005, **127**, 6528–6529.

53 L. Rose and A. T. A. Jenkins, *Bioelectrochemistry*, 2007, **70**, 387–393.

54 T. Saha, S. Dasari, D. Tewari, A. Prathap, K. M. Sureshan, A. K. Bera, A. Mukherjee and P. Talukdar, *J. Am. Chem. Soc.*, 2014, **136**, 14128–14135.

55 S. Schrödinger Release 2022–1: Maestro, LLC, NewYork, NY, 2021.

56 S. Jo, J. B. Lim, J. B. Klauda and W. Im, *Biophys. J.*, 2009, **97**, 50–58.

57 J. B. Klauda, R. M. Venable, J. A. Freites, J. W. O'Connor, D. J. Tobias, C. Mondragon-Ramirez, I. Vorobyov, A. D. MacKerell and R. W. Pastor, *J. Phys. Chem. B*, 2010, **114**, 7830–7843.

58 A. Endres and G. Maas, *Tetrahedron*, 2002, **58**, 3999–4005.

59 SAINT Plus, (Version 7.03); Bruker AXS Inc.: Madison, WI, 2004.

60 G. M. Sheldrick, SHELXTL, Reference Manual: version 5.1: Bruker AXS; Madison, WI, 1997.

61 G. M. Sheldrick, Acta Crystallogr. Sect. A, 2008, 112.

62 WINGX version 1.80.05 Louis Farrugia, University of Glasgow.

63 A. L. Spek, A PLATON, Multipurpose Crystallographic Tool, Utrecht University,

Utrecht, The Netherlands, 2005.

64 J. B. Klauda, *J. Chem. Phys.*, 2018, **149**, 220901.

65 S. Jo, T. Kim, V. G. Iyer and W. Im, *J. Comput. Chem.*, 2008, **29**, 1859–1865.

66 J. Wang, R. M. Wolf, J. W. Caldwell, P. A. Kollman and D. A. Case, *J. Comput. Chem.*, 2004, **25**, 1157–1174.

67 H. Fujitani, Y. Tanida, M. Ito, G. Jayachandran, C. D. Snow, M. R. Shirts, E. J. Sorin and V. S. Pande, *J. Chem. Phys.*, 2005, **123**, 84108.

68 K. G. Sprenger, V. W. Jaeger and J. Pfaendtner, *J. Phys. Chem. B*, 2015, **119**, 5882–5895.

69 B. R. Brooks, C. L. Brooks, A. D. Mackerell, L. Nilsson, R. J. Petrella, B. Roux, Y. Won, G. Archontis, C. Bartels, S. Boresch, A. Caflisch, L. Caves, Q. Cui, A. R. Dinner, M. Feig, S. Fischer, J. Gao, M. Hodoscek, W. Im, K. Kuczera, T. Lazaridis, J. Ma, V. Ovchinnikov, E. Paci, R. W. Pastor, C. B. Post, J. Z. Pu, M. Schaefer, B. Tidor, R. M. Venable, H. L. Woodcock, X. Wu, W. Yang, D. M. York and M. Karplus, *J. Comput. Chem.*, 2009, **30**, 1545.

70 J. Huang, S. Rauscher, G. Nawrocki, T. Ran, M. Feig, B. L. De Groot, H. Grubmüller and A. D. MacKerell, *Nat. Methods*, 2017, **14**, 71–73.

71 W. L. Jorgensen, J. Chandrasekhar, J. D. Madura, R. W. Impey and M. L. Klein, *J. Chem. Phys.*, 1983, **79**, 926–935.

72 T. Darden, D. York and L. Pedersen, *J. Chem. Phys.*, 1993, **98**, 10089–10092.

73 B. Hess, H. Bekker, H. J. C. Berendsen and J. G. E. M. Fraaije, *J. Comput. Chem.*, 1997, **18**, 1463–1472.

74 S. Miyamoto and P. A. Kollman, *J. Comput. Chem.*, 1992, **13**, 952–962.

75 S. Páll and B. Hess, *Comput. Phys. Commun.*, 2013, **184**, 2641–2650.

76 H. J. C. Berendsen, J. P. M. Postma, W. F. Van Gunsteren, A. Dinola and J. R. Haak, *J. Chem. Phys.*, 1984, **81**, 3684–3690.

77 D. J. Evans and B. L. Holian, *J. Chem. Phys.*, 1985, **83**, 4069–4074.

78 M. Parrinello and A. Rahman, *J. Appl. Phys.*, 1981, **52**, 7182–7190.

79 W. T. W. H. A. M. version 2. 0. 7. A. Grossfield and Http://membrane.urmc.rochester.edu/content/wham, *Analysis*, 2004, 1–13.

Chapter 5

Transmembrane Cl^- selective channel by meta directed halogen bond donors

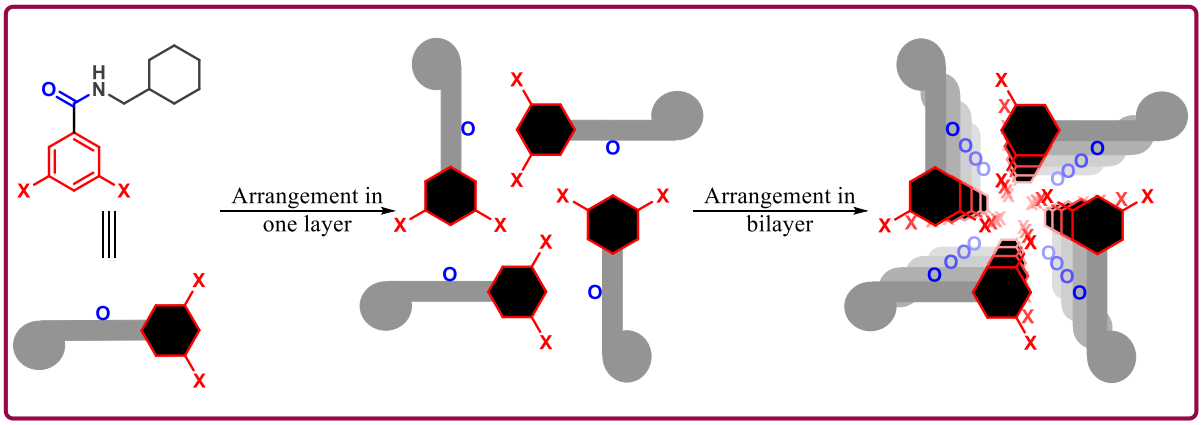

5.1 Introduction

The unique chemical properties of halogens are exploited extensively in commercially accessible compounds to improve upon or add whole new features. Recent research[1–5] found that the "halogen bonds" between halogen atoms and the carbonyl atoms in the backbones of proteins and other nucleic acids are functionally important. In addition to fundamental studies of the nature and properties of the halogen bond, one of the primary areas of interest since the beginning of the intensive research into halogen bonding at the turn of the millennium[6–9] has been the use of the halogen bond as a reliable non-covalent molecular interaction in supramolecular chemistry[10–13], and more specifically in synthetic ion transport. In organic chemistry, knowledge of short oxygen-halogen interactions dates back to the 1950s, and they have lately been utilised in the construction of supramolecular assemblies. Since few crystal structures of halogenated biomolecules are known, short halogen-oxygen interactions in biological systems are rarely characterised. Consequently, their structural and functional significance in biology have been largely overlooked. However, halogens do have crucial functions in the natural world. Short I···O interactions between tetraiodothyroxine and its transport protein transthyretin[14] show that halogen bonds play a role in the identification of naturally iodinated compounds such thyroid hormones. Important antibiotics such as chloramphenicol, 7-chlorotetracyclin, and vancomycin[15] are among the more than 3,500 halogen-containing metabolites that have been identified. The potential importance of this

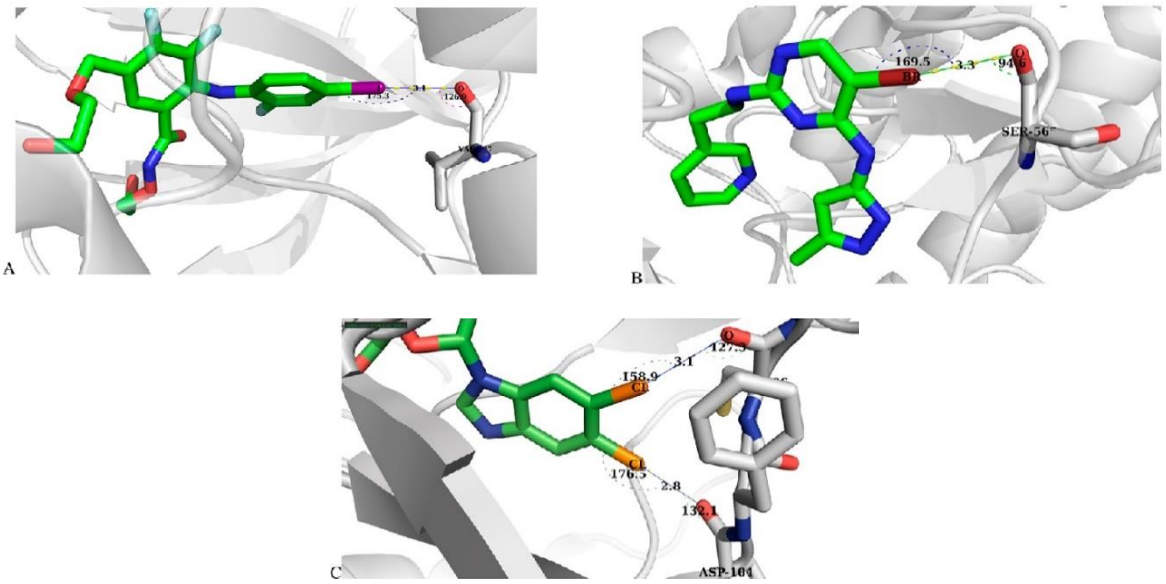

Figure 5.1. Examples of halogen bonds in protein−ligand complexes.[16]

interaction in ligand binding and recognition and molecular folding is made obvious by the review of halogen bonds in biological molecules. The CX···OY interaction is considered to be a halogen bond in biomolecules if the X···O distance is less than or equal to the sum of the van der Waals radii (3.27 for Cl···O, 3.37 for Br···O, and 3.50 for I···O) and the molecule can adopt the geometry observed in small molecules, with the CX···O angle 165° (consistent with a strong directional preference). Depending on the arrangement of the tiny molecules in the lipid bilayer, the more complex environment can impose a different geometry on the ion's route across the bilayer. Therefore, new and flexible tools are available in supramolecular chemistry thanks to the shape and variety of interaction partners of halogen bonds, allowing for the building of more efficient and selective ion transporters. In contemporary medicinal chemistry, there has been a notable surge in the utilisation of halogens. This is attributed to their elevated lipophilicity, which enhances cellular permeability.[17–19] In anticipation of enhancing the viability of synthetic ion transporters as a substitute for dysfunctional ones, we have successfully synthesized **1a-1c**.

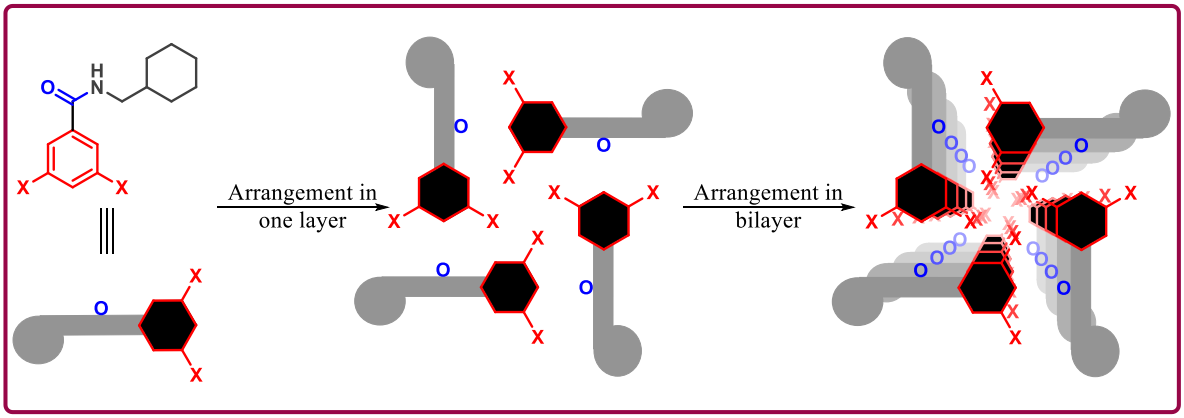

Figure 5.2. Chemical structure of compounds **1a-1c** and possible self-assembly in the lipid bilayer membrane.

5.2 Results and Discussions

5.2.1 Synthesis

By employing the diazotization reaction to transform 3,5-aminobenzoic acid **4** into 3,5-diiodobenzoic acid **1**, which was then combined with cyclohexylmethyl amines to produce the N-(cyclohexylmethyl)-3,5-diiodobenzamide, **1a** (83%). Dibromobenzoic acid and dichlorobenzoic acid were coupled with cyclohexylamine via EDC·HCl coupling to produce **1b** (67%) and **1c** (88%), respectively (Scheme 5.1). The structures of all compounds were

verified by ^{1}H NMR, ^{13}C NMR, and HRMS data after they had all been purified using column chromatography (see experimental section).

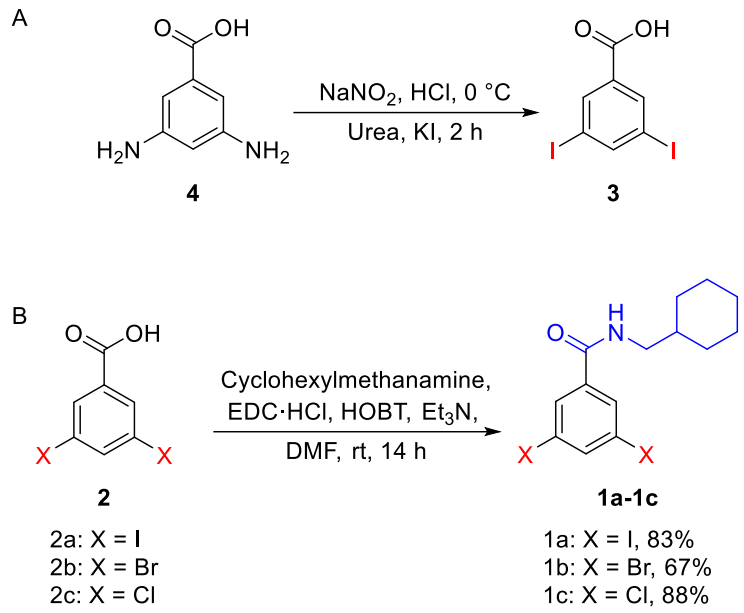

Scheme 5.1. Synthesis of compound **1a-1c**.

5.2.2 Crystallographic Studies

The rod-shaped single crystals were subjected to SC-XRD analysis, which led to the identification of the monoclinic space group. The molecular configuration within the crystals exhibits a top-and-bottom orientation where the molecules are positioned in opposite directions. The intermolecular hydrogen bonding between the carbonyl groups situated on adjacent molecules (top and bottom ones) and the amide –NH groups through N–H···O interactions has been observed to be strong (Figure 5.3A). The manifestation of the ordered structure is observed through the uninterrupted propagation of said arrangements along the a-axis. According to the SCXRD analysis, it has been observed that one iodo group is situated inside the cavity, whereas the other iodo group establishes a C=O···I bond, which leads to the creation of a four-strand assembly as depicted in Figure 5.3B. This structural analysis further supports the idea that the four iodine atoms in the cavity can act as an efficient receptor for anions, confirming the molecule's high affinity for chloride.

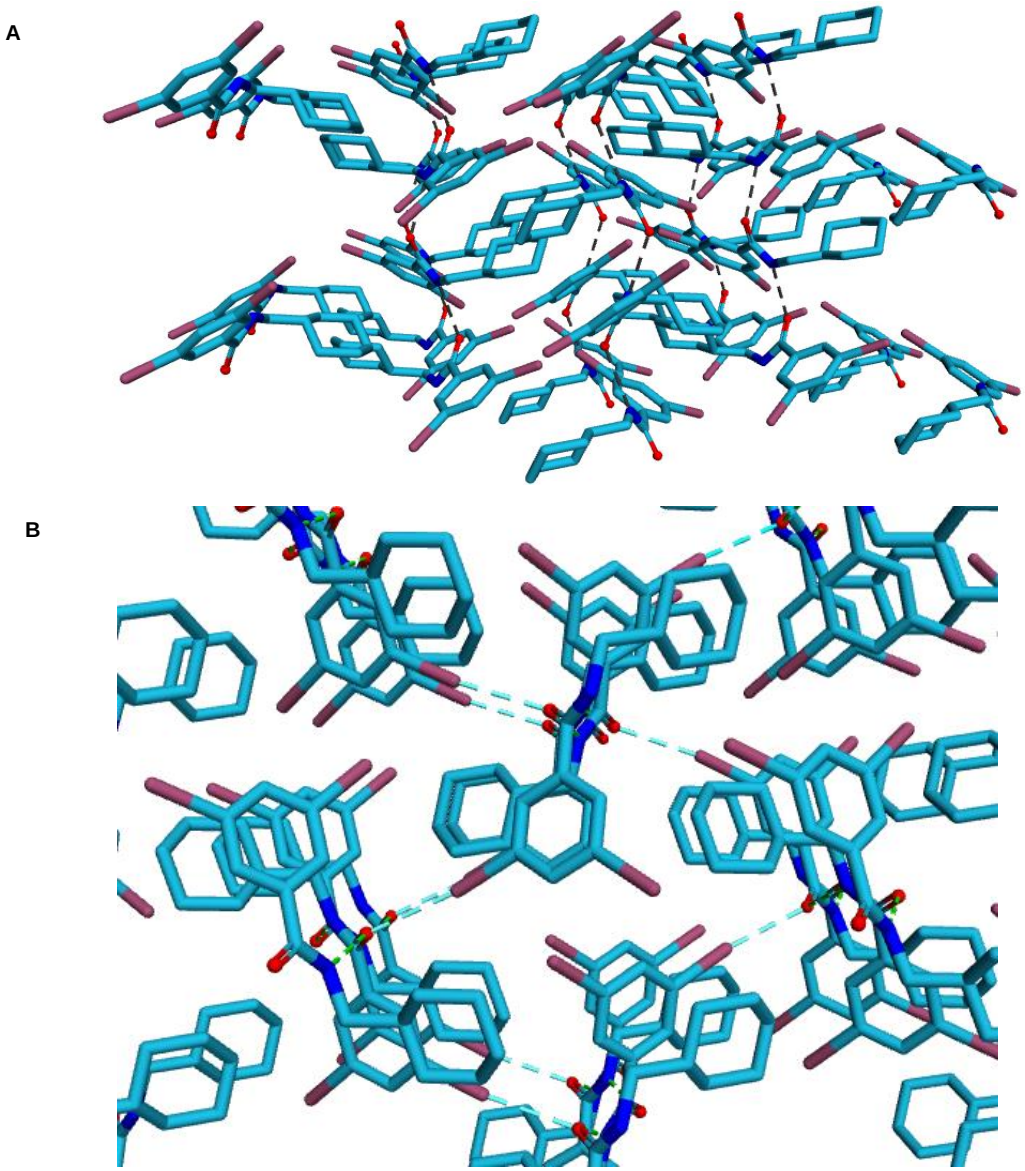

Figure 5.3. Solid state packing of **1a**, showing intermolecular H-bonding (A) and C=O···I bonding (B).

5.2.3 Certification of Self-assembly (FESEM)

The **1a-1c** sample was subjected to methanol sample preparation to obtain Field Emission Scanning Electron Microscopy (FESEM) data, as depicted in Figure 5.4. The discernment of a distinct, elongated, rod-shaped, and needle-shaped configuration holds significance as it confirms the remarkable self-assembly characteristic of **1a-1c**.

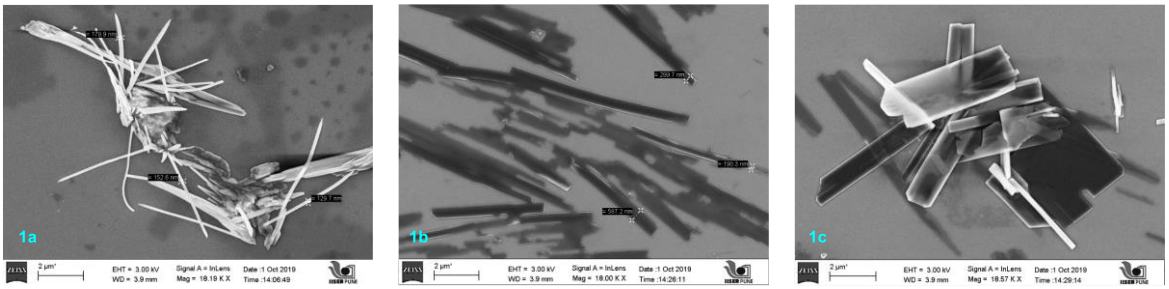

Figure 5.4. FESEM images of **1a**, **1b** and **1c** showing distinct aggregation patterns recorded in methanol.

5.2.4 Ion Transport Studies

Using 8-hydroxypyrene-1,3,6-trisulfonate (HPTS) based fluorometric techniques, the ion transport activities of compounds **1a-1c**, were assessed across large unilamellar vesicles made of egg yolk phosphatidylcholine (EYPC–LUVs⊃HPTS). The pH gradient was applied by adding NaOH (i.e., ΔpH = 0.8) to the extravesicular buffer after the EYPC vesicles containing the pH-sensitive HPTS dye (pKa = 7.2) were synthesised with internal and external pH 7.0.[20–25] The change in dye fluorescence intensity at λ_{em} = 510 nm (λ_{ex} = 450 nm) was used to track the pH gradient's collapse after the injection of **1a-1c**. According to the comparison of activities, compound **1a** functions as the most effective ion transporter, with the activity sequence being **1a** > **1c** > **1b** (Figure 5.5). The strength of a halogen bond follows the same sequence as the positive potential on halogens, which decreases in the following order: I > Br > Cl. Therefore, transport activity should decrease in that sequence if a halogen bond is present which is evident from the sequence observed. Following a Hill analysis of the dose-dependent activity data for compounds **1a-1c**, the effective concentration at 50% activity (EC_{50}) and hill coefficient (n) were determined. The determined Hill coefficient (n) values for **1a** (EC_{50} = 0.65 nM and Hill coefficient, n = 3.86) (Figure 5.12), **1b** (EC_{50} = 0.98 nM and Hill coefficient, n = 4.46) (Figure 5.13) and **1c** (EC_{50} = 31.48 μM and Hill coefficient, n = 2.37) (Figure 5.14) corroborates to the supramolecular assembly formation by all the three derivatives. The supramolecular tetrameric assembly made up of monomers of **1a** is supported by the determined hill coefficient (n) value as the active rosette structure for the supramolecular nanochannel assembly.

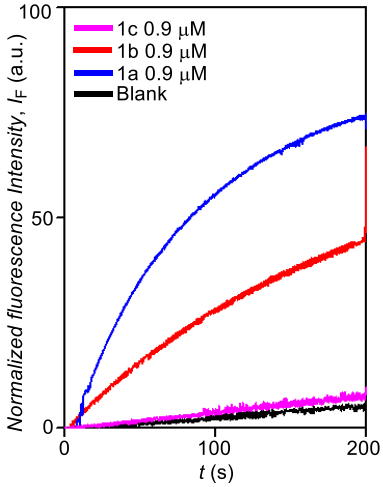

Figure 5.5. Comparison of ion transport activities of **1a-1c** across EYPC–LUVs⊃HPTS measured in the presence of an applied pH gradient (ΔpH = 0.8).

5.2.5 Ion Selectivity Studies

Compound **1a**'s noteworthy ion transport activity prompted us to investigate the compound's ion selectivity. Intravesicular NaCl and an isoosmolar extravesicular M^+/Cl^- salt (where, M^+ = Li^+, Na^+, K^+, Rb^+, and Cs^+) were utilised to assess the ion transport activity through EYPC-LUVs⊃HPTS and study the potential selectivity among the different cations.[26] No significant change in the ion transport rate was seen upon varying the external cations (M^+ = Li^+, Na^+, K^+, Rb^+, and Cs^+) in the aforementioned LUVs, demonstrating that alkali metal cations play no role in the transport process (Figure 5.6B).

Although when the anion selectivity of compound 1a was investigated by exposing it to extravesicular buffer solutions containing Na^+ salts of a variety of anions (i.e., Cl^-, Br^-, I^-, ClO_4^-, and NO_3^-) and intravesicular buffer solutions containing NaCl, a significant change in the fluorescent intensity was observed. The sequence with the highest selectivity towards Cl was $Cl^- > I^- > Br^- > NO_3^- > ClO_4^-$ as a result of the change in anions (Figure 5.6A).

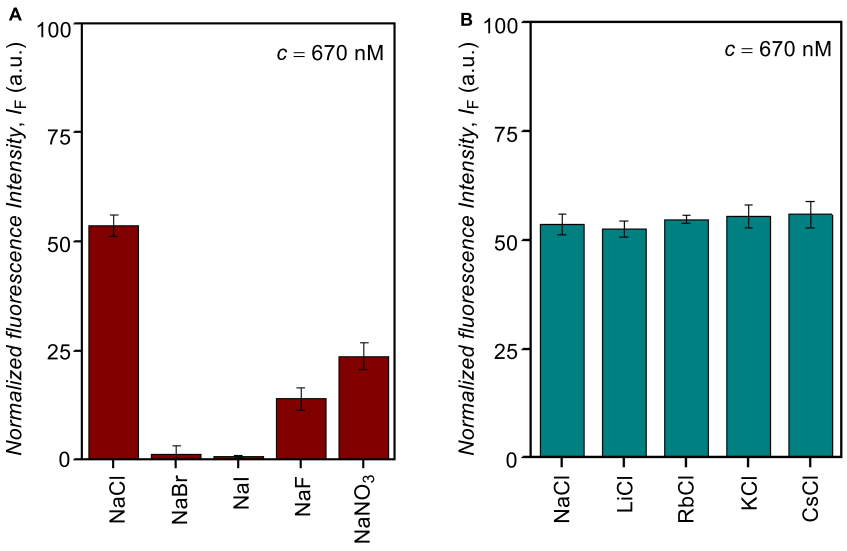

Figure 5.6. Anion selectivity (A) and cation selectivity of **1b** (B) across EYPC–LUVs⊃HPTS.

5.2.6 Chloride Transport Assay and Transport Mechanism

Subsequently, the transport of Cl^- by **1a** across EYPC–LUVs was investigated by observing the fluorescence of entrapped lucigenin, a Cl^- specific fluorescent dye.[27,28] The Cl^-/NO_3^- exchange across LUVs was assessed by introducing $NaNO_3$ and NaCl into the intravesicular and extravesicular buffers, respectively. Due to the influx of Cl^- into vesicles, concentration-dependent quenching of fluorescence was observed upon the addition of **1a** (Figure 5.7A). The Hill coefficient value further confirmed the participation of four molecules of **1a** in the formation of the supramolecular nanochannel assembly.

To learn about the operative transport mechanism, valinomycin (an electrogenic K^+- selective transporter, i.e., it causes a change in the net charge across the bilayer membrane during the transport process)[29,30] was coupled with **1a** and the ion transport rate was measured. In a symport mechanism (i.e., M^+/Cl^- cotransport), the transporter molecule alone can transport a cation along with Cl^- while maintaining charge neutrality; therefore, the addition of valinomycin to the transporter does not speed up the transport process. To maintain the overall charge neutrality, however, an antiport mechanism (i.e., Cl^-/A^- exchange) should increase the rate of Cl^- influx in the presence of valinomycin relative to the transporter alone. When KCl was added to the extravesicular buffer, followed by valinomycin and transporter **1a**, a faster Cl^- influx was observed compared to the experiment in which valinomycin was omitted (Figure 5.7C). These results suggest that transporter **1a** and valinomycin have a

synergistic effect, confirming that compound **1a** transports via the Cl^-/A^- antiport mechanism.

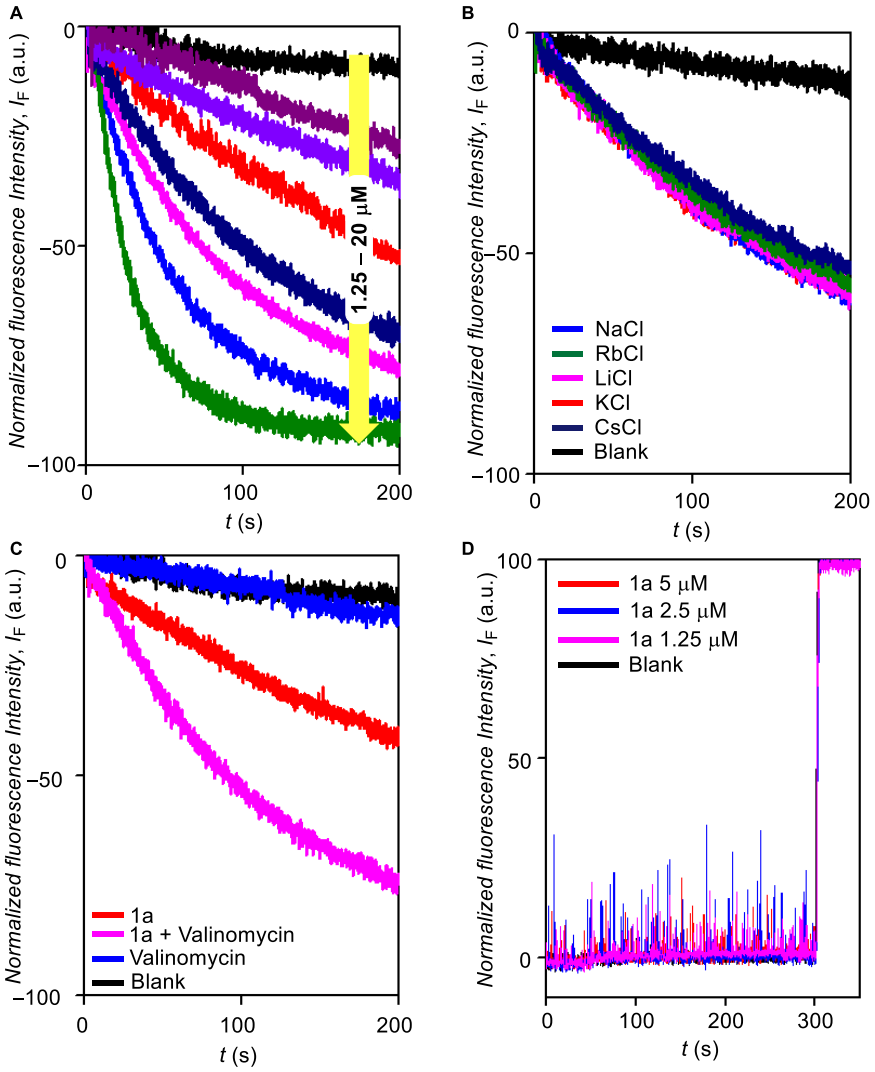

Figure 5.7. Concentration dependent activity of compound **1a** across EYPC–LUVs⊃lucigenin (A). Influence of extravesicular cations in the Cl^- influx by **1a** across EYPC–LUVs⊃lucigenin (B). Comparison of Cl^- influx activity of **1a** in the absence and in the presence of valinomycin (1.25 μM) across EYPC–LUVs⊃lucigenin (C) and ANTS–DPX leakage assay in presence of compound **1a** (D).

The transport activity of extravesicular cation salts MCl (where M represents Li^+, Na^+, K^+, Rb^+, Cs^+) across EYPC–LUVs⊃lucigenin showed no variation, thereby providing additional confirmation of the anion antiport mechanism (Figure 5.7B).

No ANTS dye leakage from EYPC–LUVs⊃ANTS/DPX (λ_{em} = 520 nm with λ_{ex} = 353 nm) was observed at varying concentrations of compound **1a**. This demonstrates that the diiodo

derivatives did not compromise the vesicle membrane (Figure 5.7D). The results cited above lend further support to the idea that the aforementioned chemical does not produce substantial transmembrane pores.

5.2.7 Transport Mechanism (Cholesterol Method)

The utilisation of a cholesterol assay facilitated the assessment aimed at determining whether the ion transport pathway operates as a carrier or a channel. Cholesterol loading induces a decrease in membrane fluidity, concomitant with a reduction in carrier-mediated ion transport.[31] The efficacy of the supramolecular channel transportation, nonetheless, will not undergo significant modifications.[32]

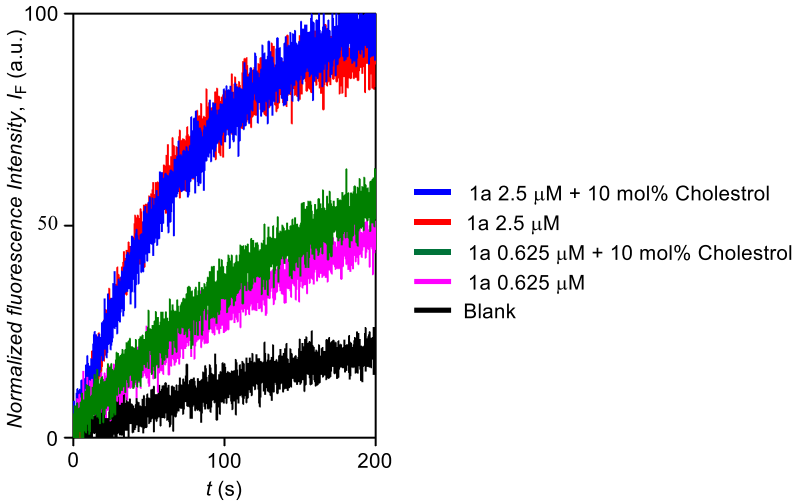

Figure 5.8. Effect of the 10 mol % of the cholesterol in the EYPC/cholesterol membrane on transport by **1a.**

The experimental results indicate that the presence of cholesterol did not result in a significant alteration in transport activity of **1a** (Figure 5.8). This provides conclusive evidence that the ion transport process is attributed to the construction of the channel.

5.2.8 Planar Bilayer Conductance Studies

In order to verify the establishment of a functional ion channel by transporter **1a**, the electrical conductance of the planar lipid bilayer membrane, which was comprised of the 1,2-diphytanoyl-sn-glycero-3-phosphocholine (DPhPC) lipid, was measured.[26,33–35] The lipid was applied to the orifice, which served as a barrier between the cis and trans compartments of the instrument that contained a solution of 1.0 M KCl. Upon the addition of compound **1a** at a concentration of 5 μM to the cis chamber, and subsequent application of either positive or

negative voltage, distinct and periodic channel opening and closing events were observed (Figure 5.9). This observation serves as a confirmation of the formation of active ion channels at the black lipid membrane (BLM). The present data enabled the calculation of the single channel conductance as 17.58 ± 0.8 pS and the determination of the channel diameter as 3.68 ± 0.12 Å through the application of Hille's equation.[36] The I–V plot in the presence of symmetric KCl solutions (1.0 M each) demonstrated a linear trend, which suggests the channel formed by **1a** (Figure 5.10A) exhibited ohmic behavior. This outcome is consistent with the nondipolar nature of the channel. Conversely, the evaluation of ion selectivity involved the utilization of dissimilar KCl solutions in the two compartments (2 M in trans and 1.0 M KCl in cis). The outcome of this assessment was a reversal potential of –4.8 mV (Figure 5.10B), which substantiates the identity of the conducting ion as Cl^-. The permeability ratio P_{Cl^-}/P_{K^+} = 4.07 calculated with the Goldman-Hodgkin-Katz equation,[36] further implies the channel formed by **1a** is anion selective.

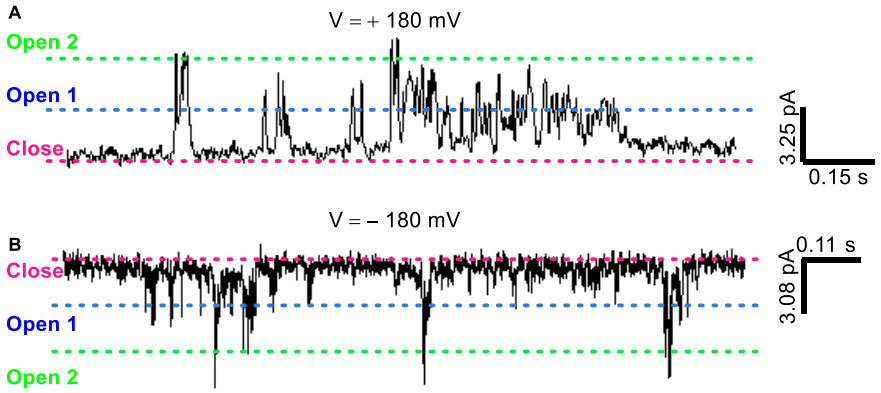

Figure 5.9. Single-channel conductance of **1a** (5 μM) recorded at +180 mV (A) and at –180 mV (B).

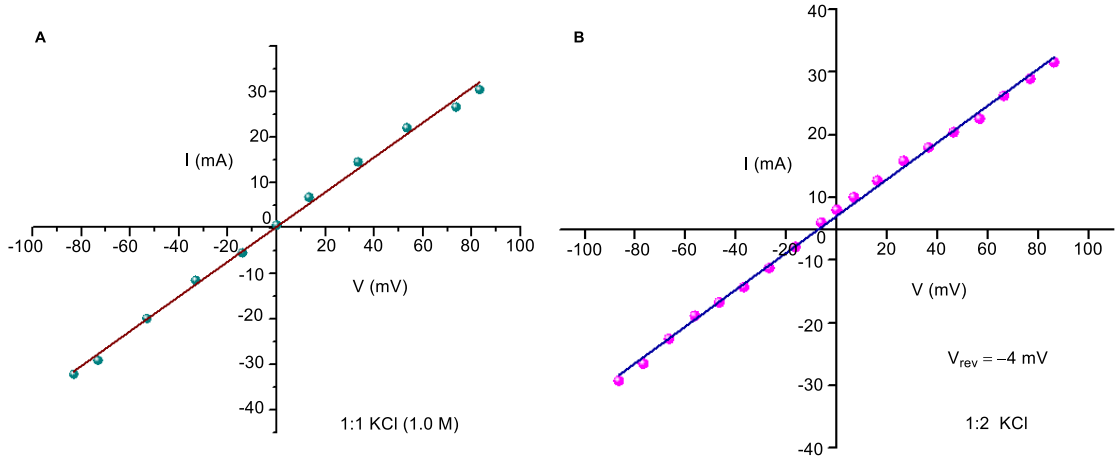

Figure 5.10. I–V plots of **1a** under symmetrical (A) and unsymmetrical (B) concentrations of KCl.

5.2.9 Molecular Modelling of Ion Channel

To study the anion transport mechanism through the synthetic channel structure and to estimate the stability of the supramolecular channel in the membrane environment we did Atomistic Molecular Dynamics (MD) simulation. At first, the channel was made up of 24 monomers stacked in six successive layers and was minimized with MAESTRO.[44] Further channel/membrane assembly was built with the semi-minimized channel structure with the help of the membrane builder protocol of CHARMM-GUI,[45,46] to construct the channel/membrane, the channel was oriented and fitted in the centre of the bilayer lipid membrane.[47] Finally, the channel/membrane complex was equilibrated in restrained MD simulation. The bilayer membrane containing 1,2-diphytanoyl-sn-glycero-3-phosphocholine (DPhPC) lipids (a total of 144 units, equally (72 units each) distributed to each of the leaflets) was utilized in the study. A rectangular simulation box of 7.9 × 7.9 × 9.0 nm^3 dimension was employed in our simulation. The system was solvated with 1 M aqueous KCl salt solution in each of the membrane-separated aqueous compartments. The specifications of the simulation systems are presented in Table 1. The simulation process is elucidated in experimental section. Umbrella sampling simulation was performed to calculate the free energy profile corresponding to the chloride ion passage through the synthetic channel embedded within the membrane.[48] The free energy landscape of chloride ion transport through the synthetic lipid membrane channel reveals distinct patterns. A significant energy barrier (7 kcal/mol) at the channel centre signifies constrained movement and reduced solvent accessibility. As the ion shifts towards channel ends, the barrier gradually lessens, reflecting improved solvation and entropic freedom (Figure 5.16). This symmetrical profile underscores equal energetic costs for ion movement to either end. The fine curvatures imply the impact of the internal channel structure. Thus, the interplay between confinement, solvation, and structural features governs the energetic behaviour of the chloride ion within the channel, with implications for molecular transport and design. To corroborate this, a quantitative analysis of adjacent water molecules in proximity to the transiting chloride ion was conducted (Figure 5.17). As the anion migrates towards the channel centre, a diminishing presence of surrounding water molecules becomes evident. Figure 5.17 illustrates that at the terminal parts of the channel, facing the aqueous environment, a substantial amount of water molecules accompanies the ion. However, this population dwindles as the ion progresses towards the centre, ultimately reaching a near absence of water molecules at the midpoint. This scarcity of water molecules within the channel core disrupts the favourable solvation environment during ion transport,

consequently contributing to the heightened free energy at the midpoint of the profile. The favourable transport of the chloride ion through the channel is guided by specific interactions. To unravel this mechanism, both intra-channel and inter-channel interactions involving the transiting ion were extensively examined. Analysis of intra-channel hydrogen bonding (Figure 5.12A, blue curve) indicates minimal disruption during ion movement, ensuring stability. In contrast, inter-channel contacts with the migrating anion intensify as it progresses toward the centre (Figure 5.12A, red curve). Evidently, the ion establishes increasingly favourable associations with channel residues. Upon reaching the centre of the channel, a peak in channel-ion contacts emerges, underscoring the pivotal role of chloride ion interaction with channel residues. This intricate interplay of interactions underscores the fundamental mechanism governing successful ion transport through the channel. To identify the specific motif of interaction of the anion with the channel residues the mutual interaction between the ion and the channel was systematically estimated. In Figure 5.11B, a representative simulation snapshot captures the trajectory of the chloride ion within the channel cavity. Intriguingly, a prominent pattern emerges– the chloride ion closely associates with the iodine atoms within the monomeric subunits. This distinctive interaction between the ion and the iodine atom likely assumes a pivotal role in the transport of the chloride ion through the channel. To substantiate the existence of the I–Cl^- halogen bonding interaction, the ion-iodine atom distance was computed throughout its journey across the channel (Figure 5.12B). This analysis unequivocally reveals that as the ion enters and advances towards the channel centre, it markedly approaches the iodine atom, suggesting plausible I–Cl^- halogen bond formation. This propensity for close ion-halogen atom proximity fosters favourable halogen bonding, rendering the transit of the ion through the channel highly favourable. This notion is further reinforced by quantifying the total count of chloride ion contacts with channel iodine atoms during its channel traversal (Figure 5.12C). This count progressively increases as the ion navigates towards the channel centre, aligning with the enhanced interaction trend observed. To investigate how the continuous formation of favourable chloride and channel contacts impacts the structural stability of the channel throughout the transport process, the radius of gyration (Rg) of the channel was assessed. As depicted in Figure 5.18, the Rg of the channel structure displays notable variation, yet the channel exhibits overall stability during ion transport. This stability arises from extensive interactions with numerous halogen atoms present within the channel. The traversal of the ion induces slight structural deformation, attributed to the extensive interactions. Notably, this minor

channel deformation can prove advantageous for ion transport, as it imparts the necessary flexibility to the confinement, facilitating the movement of the anion through the channel. This delicate interplay between deformation and stability underscores the intricate balance that underpins the successful ion transport process.

Box dimension	**No. of water molecules**	**No. of K^+ ions**	**No. of Cl^- ions**
7.9x7.9x9.0 nm^3	9737	175	175

Table 1: The simulation system details.

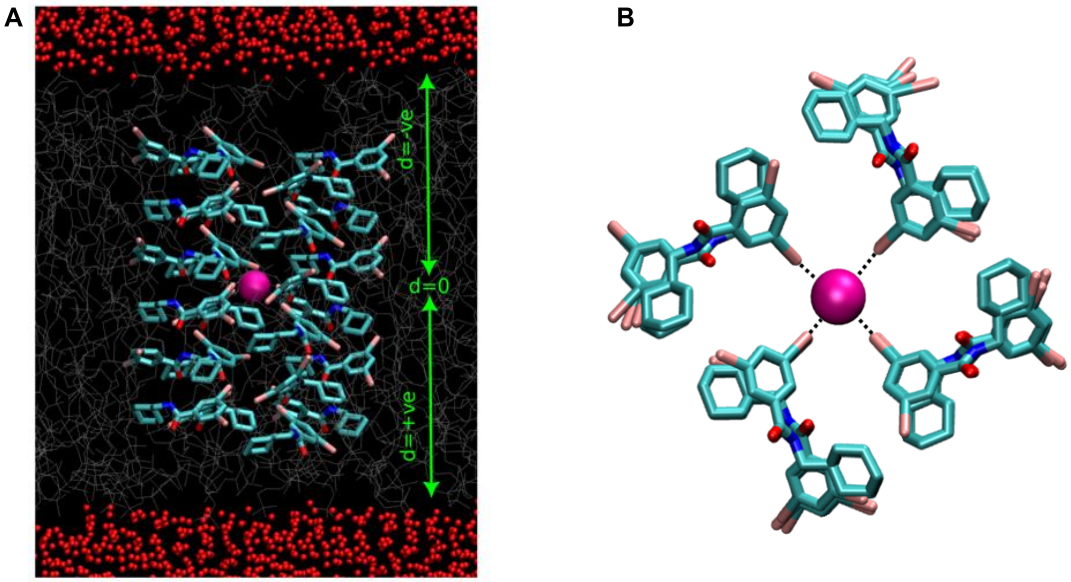

Figure 5.11. A representative snapshot showing anion transport along the synthetic channel system fitted within the lipid bilayer membrane separating the two aqueous compartments. The channel is being shown in the licorice representation without hydrogen atoms (for showing C, N, O, and I atoms cyan, blue, red, and pink colors are used respectively) The collective variable, cv (d) considered for umbrella sampling simulation is also shown in the figure (A). The possible interactions among the channel residues and the chloride ion (B).

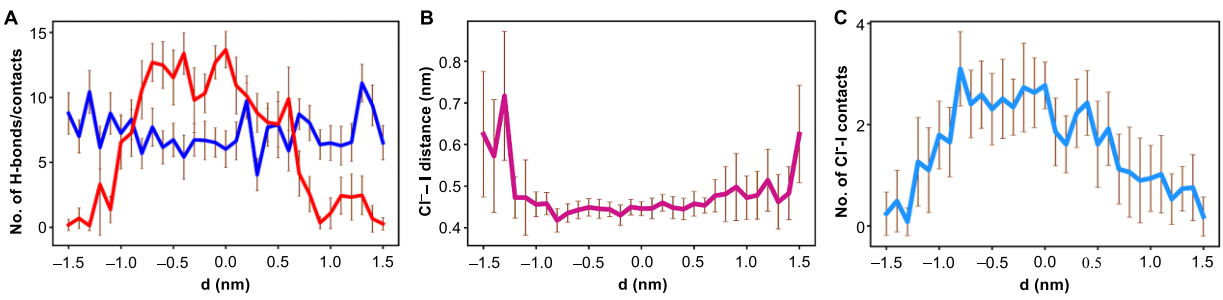

Figure 5.12. The number of intra-channel hydrogen bonds (blue) and the number of contacts (red) made by the

chloride ion with the channel residues during its passage through the channel are represented with respect to the cv, d. The error bars are shown for both curves (A). The distance between the passing chloride ion and the iodine atoms of the channel residues is represented (with error bars) during the process of its translocation (B). The number of contacts formed between the iodine atom of the channel monomers and the anion during the transport process is shown with error bars (C).

5.3 Conclusion

In summary, we have successfully synthesised a supramolecular ion channel composed of small molecules arranged in a barrel rosette structure. This ion channel exhibits selective transport of chloride ions, facilitated by halogen bonding interactions. A set of molecules were synthesised through halogen variation, resulting in modulation of the sigma hole's potency. During the course of the series, it was observed that compound **1a** exhibited greater transport activity, consistent with the theoretical literature which suggests that iodine is the most polarizable halogen. The investigation of ion selectivity through the alteration of extravesicular anionic and cationic salts has verified the superior selectivity of **1a** towards chloride ions. The investigation of the mechanism has revealed that the antiport mechanism is accountable for the conveyance of ions through the bilayer. Moreover, the lucigenin assay's dose-response studies unambiguously demonstrated the chloride influx capacity of compound **1a**. The verification of ion channel formation was ascertained through the utilisation of both the cholesterol-based assay and electrophysiological investigations. The results obtained from the electrophysiological experiments indicated that the channel diameter and single channel conductance were 3.68 ± 0.12 Å and 17.58 ± 0.8 pS, respectively. The selectivity analyses carried out in conductance studies demonstrated that the permeability of compound **1a** towards Cl^- ions is roughly 2.04 times greater than its permeability towards K^+ ions. Hence, we hold the conviction that these ion channels possess the capability to provide a fresh approach for the progression of halogen-assisted ion channels that manifest noteworthy selectivity towards chloride.

5.4 Experimental Section

5.4.1 General Methods

All reagents used for the synthesis were purchased from Sigma-Aldrich, Avra, TCI, Spectrochem, Alfa Aesar and used without further purification. Dry solvents, e.g., Toluene, Acetone, THF, CH_2Cl_2, and MeOH used for the synthesis, were purchased from Rankem, Merck and used without further drying. All the dry reactions were placed in oven-dried

apparatus under atmospheric nitrogen conditions. The progress and completion of the reactions were monitored by performing thin-layer chromatography experiments where the plates were visualized either by short-wave UV light or by different staining reagents (Ninhydrin, PMA, etc.). Column chromatography for purification of the compound was performed using distilled organic solvents on silica gel (100–200 or 230–400 mesh). HEPES buffer, HPTS dye, Triton X–100, Lucigenin dye, NaOH, and inorganic salts (NaCl, $NaNO_3$, KCl, LiCl, CsCl, NaBr, NaI, etc.) were used in molecular biology grade purchased from Sigma-Aldrich. Egg yolk phosphatidylcholine (EYPC) lipid (25 mg/mL in chloroform), mini-extruder, and polycarbonate membranes (100 and 200 nm) were obtained from Sigma-Aldrich (Avanti Polar Lipids).

5.4.2 Physical Measurements

All ^{1}H and ^{13}C NMR spectra were recorded either on Bruker 400 MHz or Jeol 400 MHz spectrometers. The chemical shifts (δ) in ppm were referenced to the residual signal of deuterium solvents (^{1}H NMR $CDCl_3$: δ 7.26 ppm; ^{13}C NMR $CDCl_3$: δ 77.2 ppm; ^{1}H NMR DMSO-d_6: δ 2.5 ppm; ^{13}C NMR DMSO-d_6: δ 39.5 ppm). The multiplicities of the peaks are s (singlet), d (doublet), t (triplet), q (quartet), dd (doublet of doublet), and m (multiplet). High-resolution mass spectra (HRMS) were acquired in the ESI (+ve) mode. The measurement of pH during the preparation of the buffer solution was done by a pH meter purchased from Hanna instruments. Fluorescence spectra were recorded on a Fluoromax–4 from Horiba scientific, Jobin Yvon Edison equipped with an injector port and a magnetic stirrer. The experimental data obtained from fluorescence were processed in Origin 8.5 software. The field emission scanning electron microscopy (FESEM) images were obtained using FEI Quanta 3D dual beam ESEM at 3.0 kV.

5.4.3 Synthesis

Synthesis of compound 1: Synthesis of compound **1** was done according to known protocol.[37,38] At 0 °C, 5-aminoisophthalic acid (3 g, 20 mmol) in an H_2SO_4 solution was added to an aqueous solution of $NaNO_2$ (2.5 M). Afterward, urea (3 g) and KI (7 g) were added to the reaction mixture. The mixture was stirred for two hours. Following the addition of ice-cold water, the solid was filtered to get 3,5-diiodobenzoic acid (70% Yield). ^{1}H NMR spectrum was matched with the data of the reported compound.[37,38]

Synthesis of compound 1a: In a 50 mL round bottom flask, the acid **1** (500mg, 1.33 mmol) was taken and dissolved in 10 mL of dry DMF. Then into the reaction mixture, cyclohexylmethylamine (227 mg, 2.00 mmol), HOBt (492 mg, 3.20 mmol), and triethylamine (0.5 mL) were added. At last, EDC·HCl (568 mg, 4.01 mmol) was added, and the reaction mixture was then stirred at room temperature overnight under an inert atmosphere. After completion of the reaction, the reaction mixture was washed with water (3 × 10 mL) and followed by brine solution (1 × 10 mL) by extracting the compound in $CHCl_3$ (50 mL). The organic layer was then dried over Na_2SO_4, and the solvent was evaporated in a rotary evaporator to get the crude product. The crude product was purified by silica gel column chromatography using methanol (MeOH) in chloroform ($CHCl_3$) as a solvent system. The product **1a** was obtained as pale white solid (83 % Yield) (5 % MeOH:$CHCl_3$). **IR** (neat, ν/cm^{-1}): 3316, 2941, 2895, 1504, 1502, 1496, 1493, 1023, 1021). **^{1}H NMR (400 MHz, $CDCl_3$, δ):** 8.16 (t, *J* = 1.5 Hz, 1H), 8.01 (d, *J* = 1.5 Hz, 2H), 6.08 (s, 1H), 3.29 – 3.25 (m, 2H), 1.79 – 1.72 (m, 5H), 1.27 – 1.20 (m, 7H). **^{13}C NMR (101 MHz, $CDCl_3$):** 166.9, 137.9, 134.5, 128.6, 98.31, 77.1, 46.45, 38.1, 31.1, 26.5, 25.9. **HRMS (ESI):** Calc. for $C_{14}H_{17}I_2NO$ $[M+H]^+$: 469.9472; Found: 469.9478.

Synthesis of compound 1b: In a 50 mL round bottom flask, the acid **2** (500mg, 1.78 mmol) was taken and dissolved in 10 mL of dry DMF. Then into the reaction mixture, cyclohexylmethylamine (303 mg, 2.67 mmol), HOBt (657 mg, 4.28 mmol), and triethylamine (0.6 mL) were added. At last, EDC·HCl (1 g, 5.35 mmol) was added, and the reaction mixture was then stirred at room temperature overnight under an inert atmosphere. After completion of the reaction, the reaction mixture was washed with water (3 × 10 mL) and followed by brine solution (1 × 10 mL) by extracting the compound in $CHCl_3$ (50 mL). The organic layer was then dried over Na_2SO_4, and the solvent was evaporated in a rotary evaporator to get the crude product. The crude product was purified by silica gel column chromatography using methanol (MeOH) in chloroform ($CHCl_3$) as a solvent system. The product **1b** was obtained as white solid (67 % Yield) (5 % MeOH:$CHCl_3$). **IR** (neat, ν/cm^{-1}): 3741, 3739, 3668, 2984, 1701, 1698, 1542, 1538, 960). **^{1}H NMR (400 MHz, $CDCl_3$, δ):** 7.80 (d, *J* = 1.7 Hz, 2H), 7.77 (t, *J* = 1.7 Hz, 1H), 6.14 (s, 1H), 3.30 – 3.26 (m, 2H), 1.80 – 1.63 (m, 6H), 1.30 – 1.16 (m, 3H), 0.99 (tt, *J* = 11.6, 6.3 Hz, 2H). **^{13}C NMR (101 MHz, $CDCl_3$):** 164.9, 138.3, 136.8, 128.9, 123.4, 46.6, 38.1, 31.1, 26.5, 25.9. **HRMS (ESI):** Calc. for $C_{14}H_{17}Br_2NO$ $[M+H]^+$: 373.9750; Found: 373.9755.

Synthesis of compound 1c: In a 50 mL round bottom flask, the acid **3** (500mg, 2.01 mmol) was taken and dissolved in 10 mL of dry DMF. Then into the reaction mixture, cyclohexylmethylamine (444 mg, 3.92 mmol), HOBt (742 mg, 4.84 mmol), and triethylamine (0.6 mL) were added. At last, EDC·HCl (858 mg, 6.95 mmol) was added, and the reaction mixture was then stirred at room temperature overnight under an inert atmosphere. After completion of the reaction, the reaction mixture was washed with water (3 × 10 mL) and followed by brine solution (1 × 10 mL) by extracting the compound in $CHCl_3$ (50 mL). The organic layer was then dried over Na_2SO_4, and the solvent was evaporated in a rotary evaporator to get the crude product. The crude product was purified by silica gel column chromatography using methanol (MeOH) in chloroform ($CHCl_3$) as a solvent system. The product **1c** was obtained as white solid (88 % Yield) (5 % MeOH:$CHCl_3$). **IR** (neat, ν/cm^{-1}): 3316, 2982, 2896, 1538, 1497, 1037, 1022, 736). **^{1}H NMR (400 MHz, $CDCl_3$, δ):** 7.61 (d, *J* = 1.9 Hz, 2H), 7.48 (t, *J* = 1.9 Hz, 1H), 6.09 (s, 1H), 3.31 – 3.27 (m, 2H), 1.76 (td, *J* = 6.3, 3.1 Hz, 6H), 1.23 (d, *J* = 11.8 Hz, 3H), 1.05 – 0.94 (m, 2H). **^{13}C NMR (101 MHz, $CDCl_3$):** 165.1, 137.9, 135.6, 131.3, 125.7, 46.6, 38.1, 31.0, 26.5, 25.9. **HRMS (ESI):** Calc. for $C_{14}H_{17}Cl_2NO$ $[M+H]^+$: 286.0760; Found: 286.0764.

5.4.4 SCXRD

The needle-shaped crystals of compound **1a** were grown in a solvent combination of MeOH/CH_2Cl_2 at room temperature. The single-crystal X-ray data of compound **1a** was recorded at 150 K on a Bruker KAPPA APEX II CCD Duo diffractometer (operated at 1500 W power: 50 kV, 30 mA) using graphite-mono chromated Mo Kα radiation (λ = 0.71073 Å). The crystal was kept on a nylon Cryo-Loops (Hampton Research) with Paraton-N (Hampton Research). The data reduction and integration were computed with SAINT software.[39] A correction on multi-scan absorption was employed on the collected reflections. The structure solving was achieved by the direct method using SHELXTL[40] and was further refined on *F*2 by full-matrix least-squares technique using the SHELXL-97[41] program package within the WINGX[42] program. All the non-hydrogen atoms were refined anisotropically. All hydrogen atoms were located in successive difference Fourier maps, and they were treated as riding atoms using SHELXL default parameters. The structures were examined using the *Adsym* subroutine of PLATON[43] to ensure that no additional symmetry could be applied to the models.

Crystallographic data for compound **1a**: **CCDC 2218310** contains the supplementary crystallographic data for this paper and can be obtained free of charge from The Cambridge Crystallographic Data Centre.

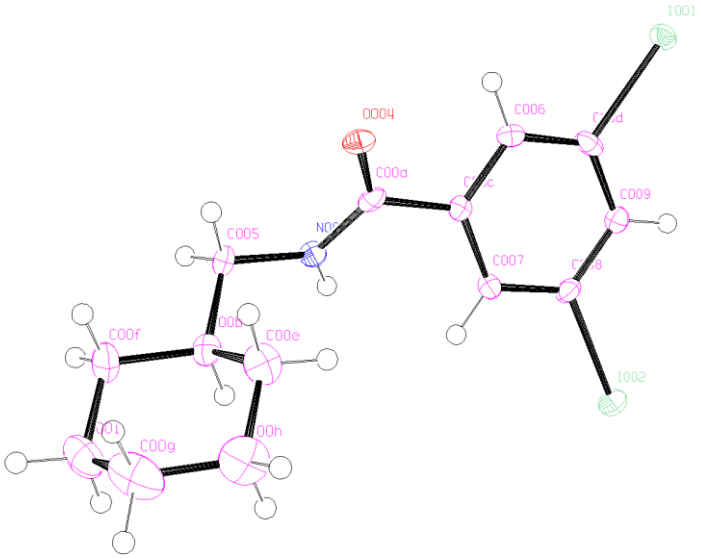

Figure 5.11. ORTEP diagrams of **1a** with 50% probability ellipsoids established by single X-ray crystallography.

Identification code	**RAS_1a**
CCDC Number	**2218310**
Empirical formula	$C_{14}H_{17}I_2NO$
Formula weight	469.08
Temperature	296(2) K
Wavelength	.710 Å
Crystal system	Orthorhombic
Space group	P 21 21 21
Unit cell dimensions	a = 9.1330 (13) Å α= 90. b = 11.7016 (15) Å β= 90. c = 14.9331 (19) Å γ = 90.

Volume	1595.9 (4) $Å^3$
Z	4
Density (calculated)	1.952 Mg/m^3
Absorption coefficient	3.931 mm^{-1}
F(000)	888
Crystal size	0.200 x 0.200 x 0.150 mm^3
Theta range for data collection	2.211 to 28.293°.
Index ranges	-11<=h<=12, -14<=k<=15, -19<=l<=19
Reflections collected	15278
Independent reflections	3887 [R(int) = 0.0475]
Completeness to theta = 25.242°	100.0 %
Absorption correction	Semi-empirical from equivalents
Max. and min. transmission	0.89 and 0.75
Refinement method	Full-matrix least-squares on F^2
Data / restraints / parameters	3887/0/164
Goodness-of-fit on F^2	1.052
Final R indices [I>2sigma(I)]	R1 = 0.0272, wR2 = 0.30467
R indices (all data)	R1 = 0.0407, wR2 = 0.0516
Extinction coefficient	0.0047 (2)
Largest diff. peak and hole	00.735 and -0.986 $e.Å^{-3}$

Table 5.1. Crystal data and structure refinement for Compound **1a.**

5.4.5 FESEM

The samples were prepared by drop-casting 5 μL of **1a, 1b** and **1c** over silicon wafer at room temperature. The samples were dried under IR lamp for 5 minutes. Field emission scanning electron microscopy (FESEM) images were captured using a FEI Quanta 3D dual beam ESEM at 30 kV.

5.4.6 Ion Transport Studies

The ion transport studies for compounds **1a**–**1c** were carried out following the reported procedure explained in previous chapters.

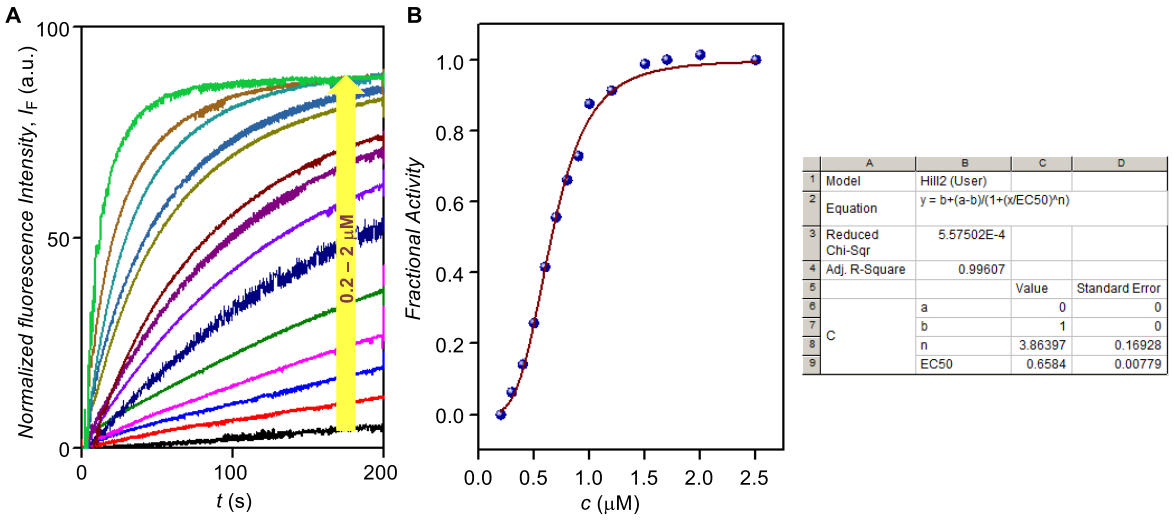

	A	B	C	D
1	Model	Hill2 (User)		
2	Equation	y = b+(a-b)/(1+(x/EC50)^n)		
3	Reduced Chi-Sqr	5.57502E-4		
4	Adj. R-Square	0.99607		
5			Value	Standard Error
6	C	a	0	0
7		b	1	0
8		n	3.86397	0.16928
9		EC50	0.6584	0.00779

Figure 5.12. Concentration dependent activity of compound **1a** across EYPC–LUVs⊃lucigenin. (**A**). Hill plot analysis of compound **1a (B)**.

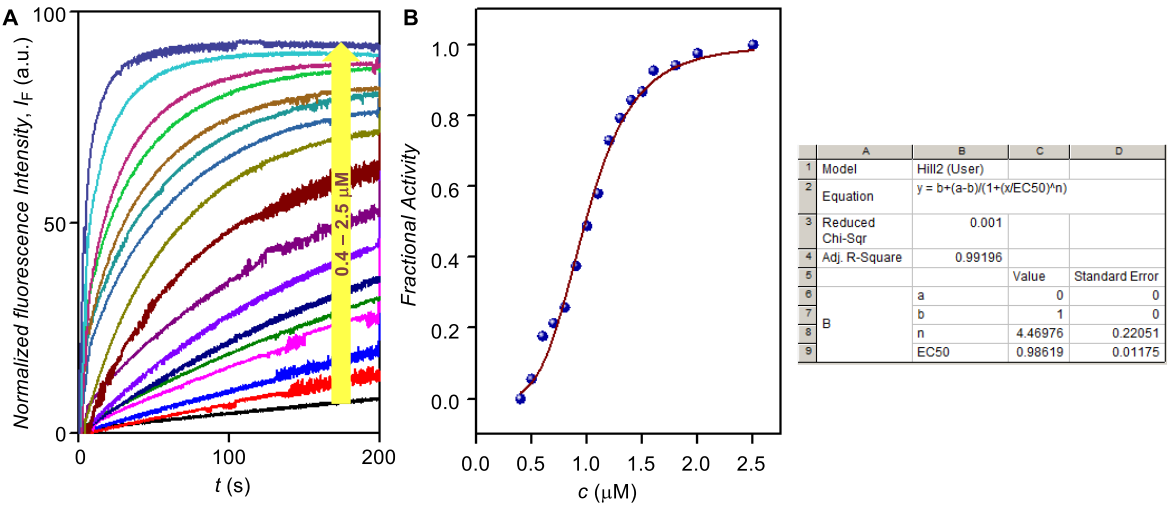

	A	B	C	D
1	Model	Hill2 (User)		
2	Equation	y = b+(a-b)/(1+(x/EC50)^n)		
3	Reduced Chi-Sqr	0.001		
4	Adj. R-Square	0.99196		
5			Value	Standard Error
6	B	a	0	0
7		b	1	0
8		n	4.46976	0.22051
9		EC50	0.98619	0.01175

Figure 5.13. Concentration dependent activity of compound **1b** across EYPC–LUVs⊃lucigenin. (**A**). Hill plot analysis of compound **1b (B)**.

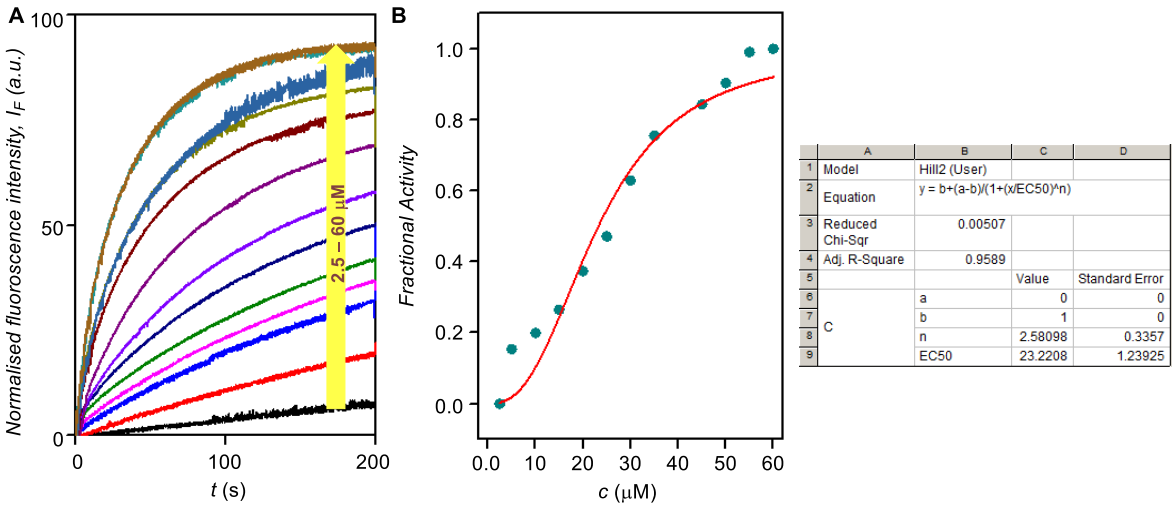

	A	B	C	D
1	Model	Hill2 (User)		
2	Equation	y = b+(a-b)/(1+(x/EC50)^n)		
3	Reduced Chi-Sqr	0.00507		
4	Adj. R-Square	0.9589		
5			Value	Standard Error
6	C	a	0	0
7		b	1	0
8		n	2.58098	0.3357
9		EC50	23.2208	1.23925

Figure 5.14. Concentration dependent activity of compound **1c** across EYPC–LUVs⊃lucigenin. (**A**). Hill plot analysis of compound **1c (B)**.

4.4.7 Planar Bilayer Conductance Measurements

The ion transport studies for compounds **1a**–**1c** were carried out following the reported procedure explained in previous chapters.

4.4.8 Molecular Modelling of Ion Channel

Atomistic Molecular dynamics (MD) simulation was performed to study the anion transport mechanism through the synthetic channel structure and to estimate the stability of the supramolecular channel in the membrane environment.

Model and Methods:

System setup and simulation model: At first, the channel made up of 24 monomers stacked in six successive layers. Further channel/membrane assembly was built with the semi-minimised channel structure with the help of the membrane builder protocol of CHARMM-GUI. To construct the channel/membrane, the channel was oriented and fitted in the center of the bilayer lipid membrane. Finally, the channel/membrane complex was equilibrated in restrained MD simulation. The bilayer membrane containing 1,2-diphytanoyl-sn-glycero-3-phosphocholine (DPhPC) lipids (total 144 units, equally (72 units each) distributed to each of the leaflet) was utilized in the study. A rectangular simulation box of 7.9 × 7.9 × 9.0 nm^3 dimension was employed in our simulation. The system was solvated with 1 M aqueous KCl salt solution in each of the membrane separated aqueous compartments. The details of simulation are provided in table 1.

The channel structure was modelled using the general AMBER forcefield (GAFF). For modelling the lipid membrane, the CHARMM36m force field parameters are utilized. The CHARMM-TIP3P water model is employed in our simulation.

Simulation method: The simulations are performed using periodic boundary conditions (PBC) along x, y and z directions. The particle mesh Ewald (PME) method was employed for long-range electrostatic interactions and for electrostatic interactions at short-range 1.2 nm cut-off were set. At a frequency of 20 steps the neighbour lists were updated. The LINCS algorithm was employed for constraining the hydrogen bonds of membrane and channel monomers. While water molecule rigidity was maintained during simulation using the SETTLE algorithm. Lenard Jones interactions were managed by the Verlet cut-off scheme (cut-off of 1.2 nm) along with dispersion corrections. Initially energy of the system was minimized with the steepest-descent algorithm considering restraints on the system. The energy minimized system was further subjected to stepwise equilibration through six consecutive steps (10 ns each). Each of the successive equilibration processes was performed keeping certain restraints on the system. However, the applied restraints were lowered gradually in each consecutive step of equilibration. An average temperature of 298 K and

pressure of 1.0 bar was maintained during the equilibration process with the Berendsen thermostat and Berendsen barostat. Finally, the production run was carried out in NPT ensemble with the equillibrated system for 1.0 microsecond under slight restrain condition subjected to the channel structure. For maintaining the average temperature of 298 K during production run, the Nose-Hoover thermostat (with a relaxation constant of 1.0 ps) was engaged by coupling the channel structure, membrane bilayer, and solvent individually. The Parrinello-Rahman barostat was applied to fix the average pressure at 1.0 bar. Pressure was maintained under semi-isotropic condition via separate coupling in XY and Z directions of the system for maintaining tensionless bilayer during the simulation. Time step of 2 fs was retained at the stage of the production run with the help of leapfrog integrator. Simulations of the channel/membrane system were replicated two times by following the similar protocol of simulation. Each of the simulations was performed with GROMACS software of 20x version.

Free energy simulation: Umbrella sampling simulation was performed to calculate the free energy profile corresponding to the chloride ion passage through the synthetic channel embedded within the membrane. To generate the initial configurations for umbrella sampling simulation one chloride ion was allowed to move along the channel core and the respective coordinates were saved individually. The configuration indicates different locations of chloride ion in the channel core starting from its entry via the mouth of the channel and its exit through the other end of the channel.

To maintain electro-neutrality of the system having one anion, one K^+ ion was added into the system. Similar to the previously described equilibrium simulation, the simulation box dimension and the number of water molecules were kept the same for umbrella sampling simulation as well. The collective variable (CV) was chosen along Z-direction following the movement of the chloride ion along the channel (without considering hydrogen atoms) structure (d) as shown in figure 6A. When the anion resides at the upper half of the channel i.e., the ion moves towards the mouth of the channel from channel centre is designated by negative value of CV, d. While a positive value of d refers that the ion stays below the channel centre i.e when it travels from centre to the end of the channel. The d = 0 nm points towards the location of the anion at the center of the channel structure. In our simulation, the CV (d) ranges from -1.5 nm to 1.5 nm (with a spacing of 0.1 nm) and the respective configurations were generated for utilization in the umbrella sampling simulation. For retaining the location of Cl^- ion at the specified d, suitable force constant of 7500 kJ/mol/nm^2 was applied during umbrella sampling simulation of each of the windows. At first, the system

was energy minimized using the steepest-descent algorithm followed by short NVT equilibration for 500 ps (1 fs simulation time step). Towards the end, the equilibrated system was subjected to NPT production run (with 2 fs time step) for 20 ns. The similar simulation strategy was followed for simulation in each of the umbrella windows. The same thermostat and barostat were employed for umbrella sampling simulation (during equilibration and production run) in each of the windows as done during equilibrium simulation. Finally employing the weighted histogram analysis method (WHAM) the respective equilibrium free energy profile was calculated. All the simulations were executed with the GROMACS software of 20x version.

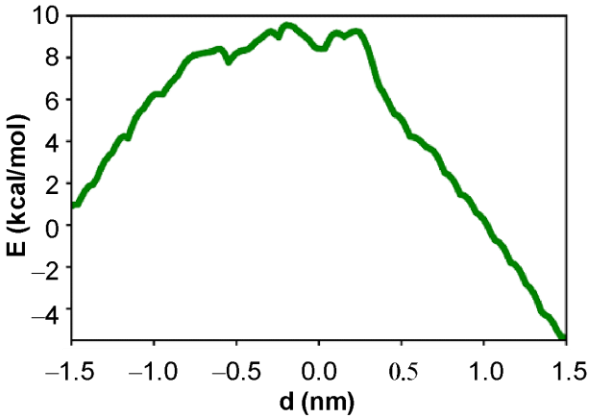

Figure 5.16. Free energy landscape of chloride ion transport through the channel is estimated by performing umbrella sampling simulation corresponding to the CV, d.

With our simulation, the free energy landscape of chloride ion transport through the channel is estimated. For gaining the mechanistic insights of the transport process, intra channel H-bonding and interactions between the passing anion with the channel were analyzed. To assess the stability of the channel embedded within the lipid bilayer membrane, radius of gyration (Rg) of the channel has been calculated as the ion passes through the channel structure. The total number of neighbouring water molecules around the chloride ion was computed. Again, the specific interactions between the transporting anion and the channel residues are also analysed which may play crucial role for the transport process.

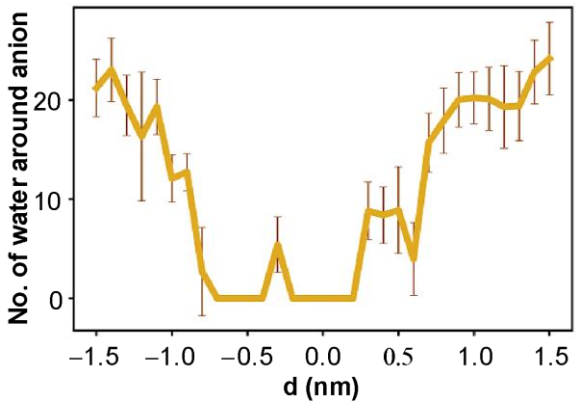

Figure 5.17. The number of water molecules near the passing chloride ion is being represented (along cv, d) with error bars.

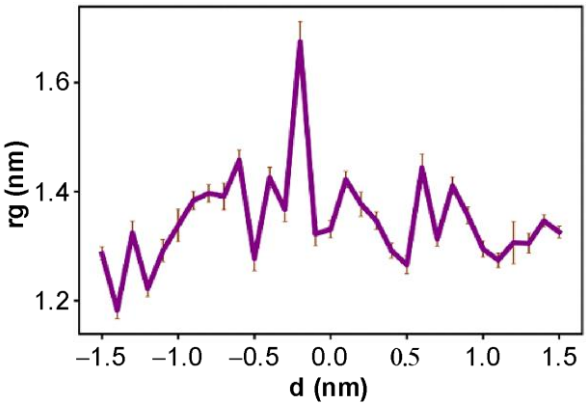

Figure 5.18. The radius of gyration (rg) of the supramolecular channel structure is shown (with error bars) during the transport of the ion through the channel.

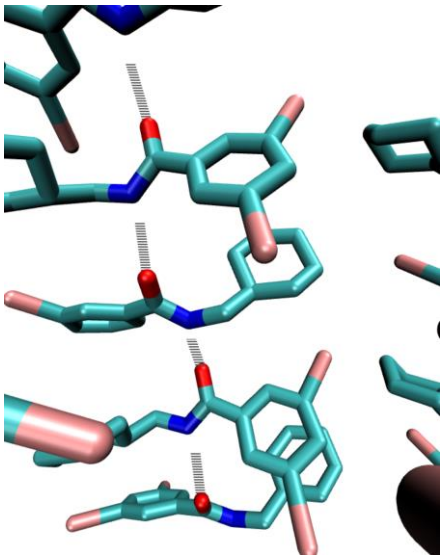

Figure 5.19. A representative snapshot showing the hydrogen bonding formation between the amide N-H moiety with the oxygen atom of the next layer.

5.4.9 NMR

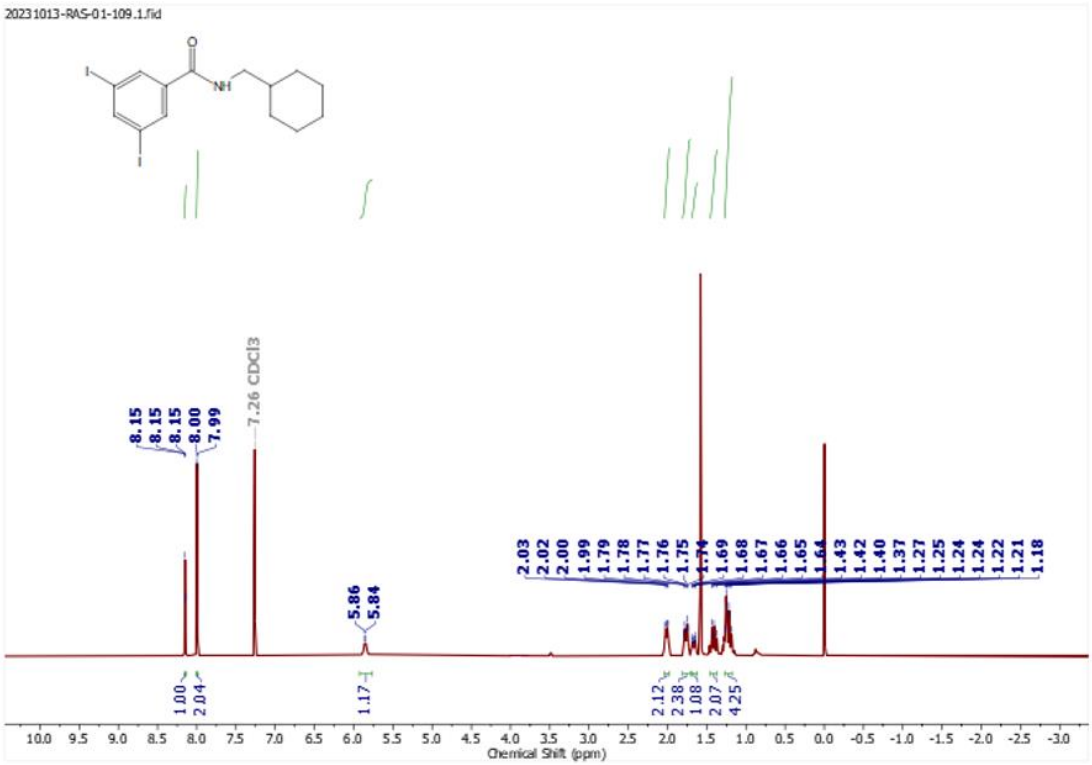

Figure 5.15. ^{1}H NMR spectrum of **1a** in $CDCl_3$.

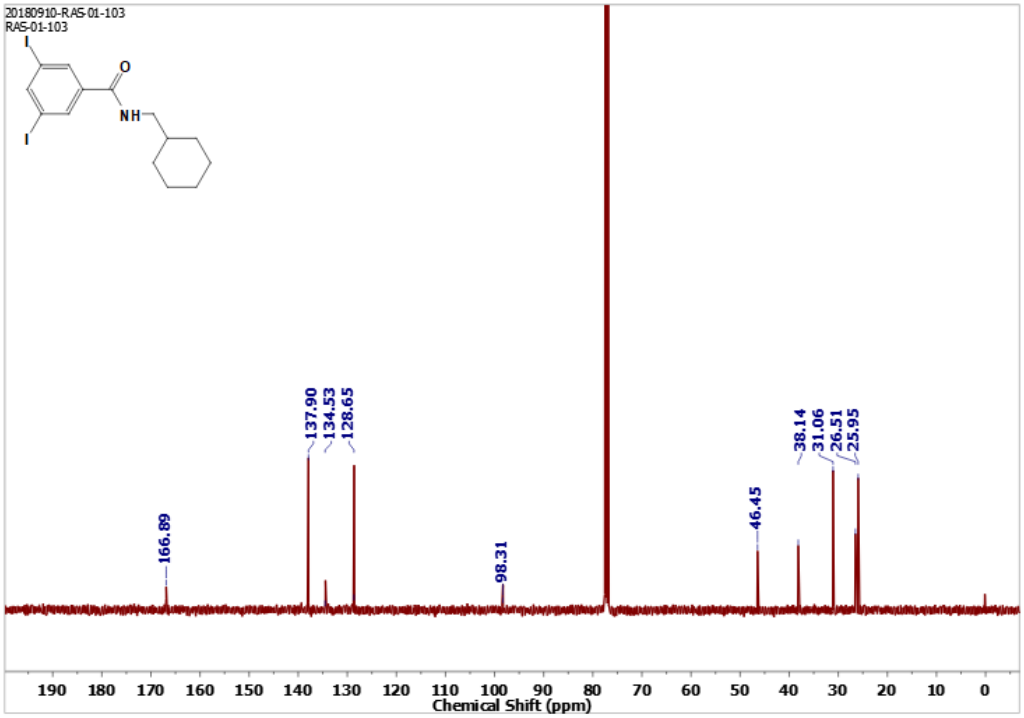

Figure 5.16.^{13}C NMR spectrum of **1a** in $CDCl_3$.

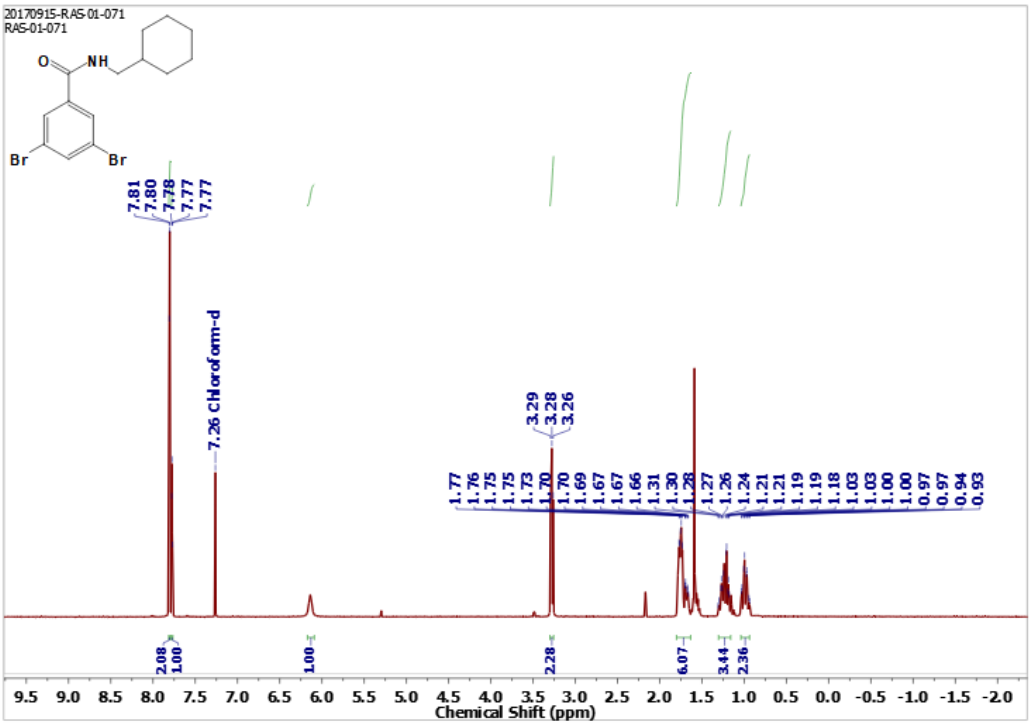

Figure 5.17. ^{1}H NMR spectrum of **1b** in $CDCl_3$.

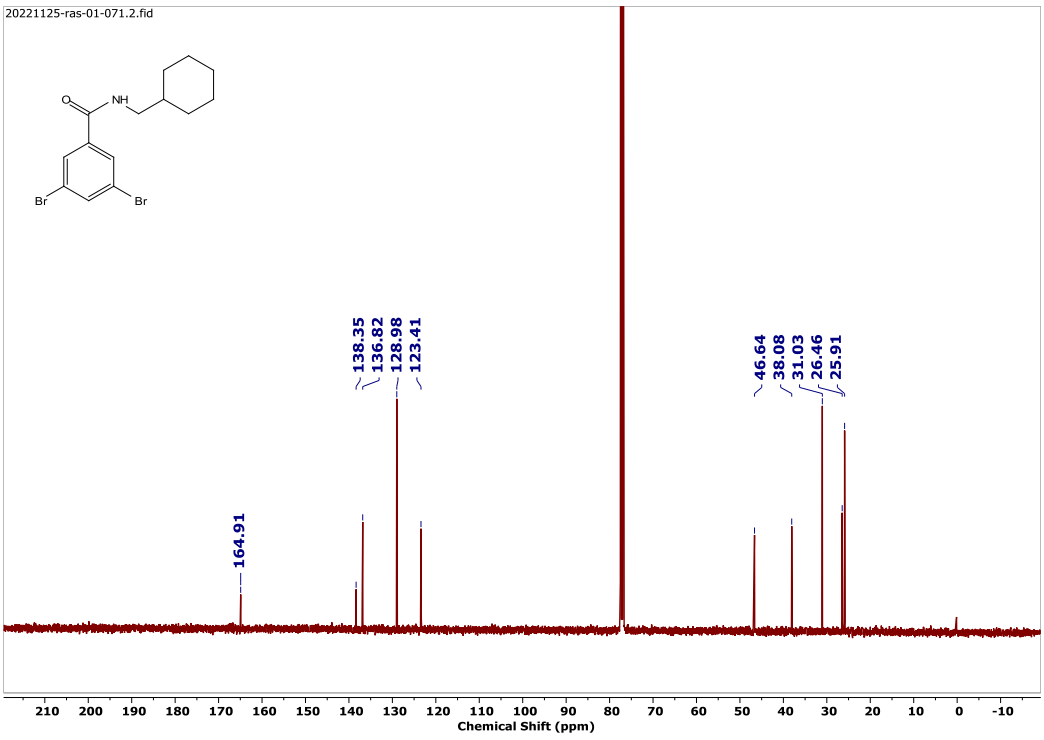

Figure 5.18. ^{13}C NMR spectrum of **1b** in $CDCl_3$.

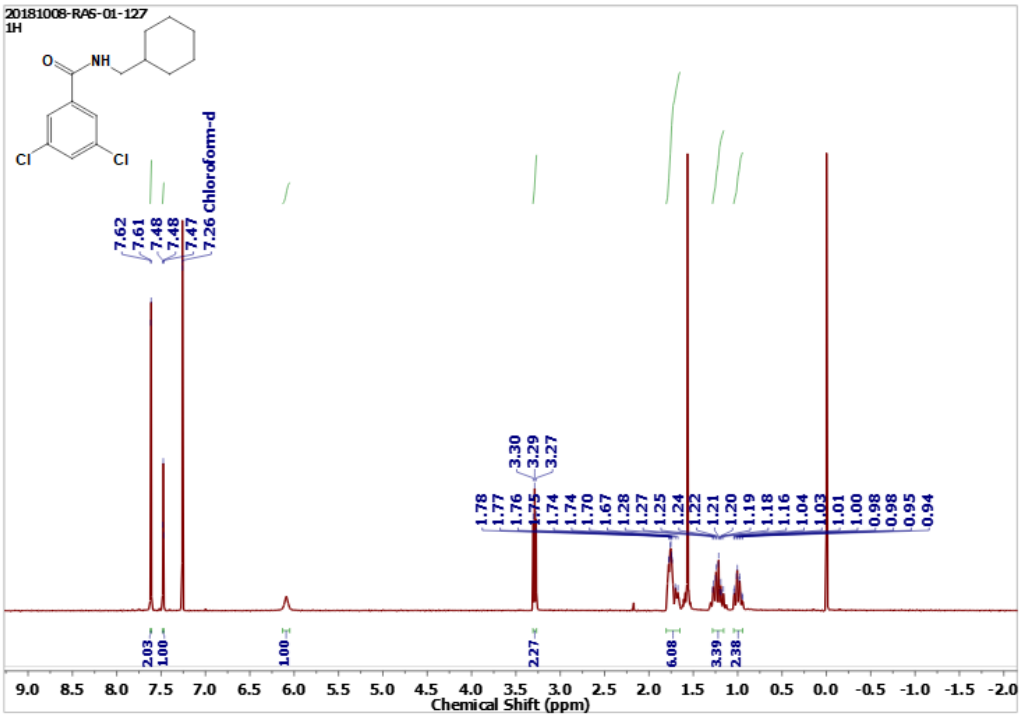

Figure 5.19. ^{1}H NMR spectrum of **1c** in $CDCl_3$.

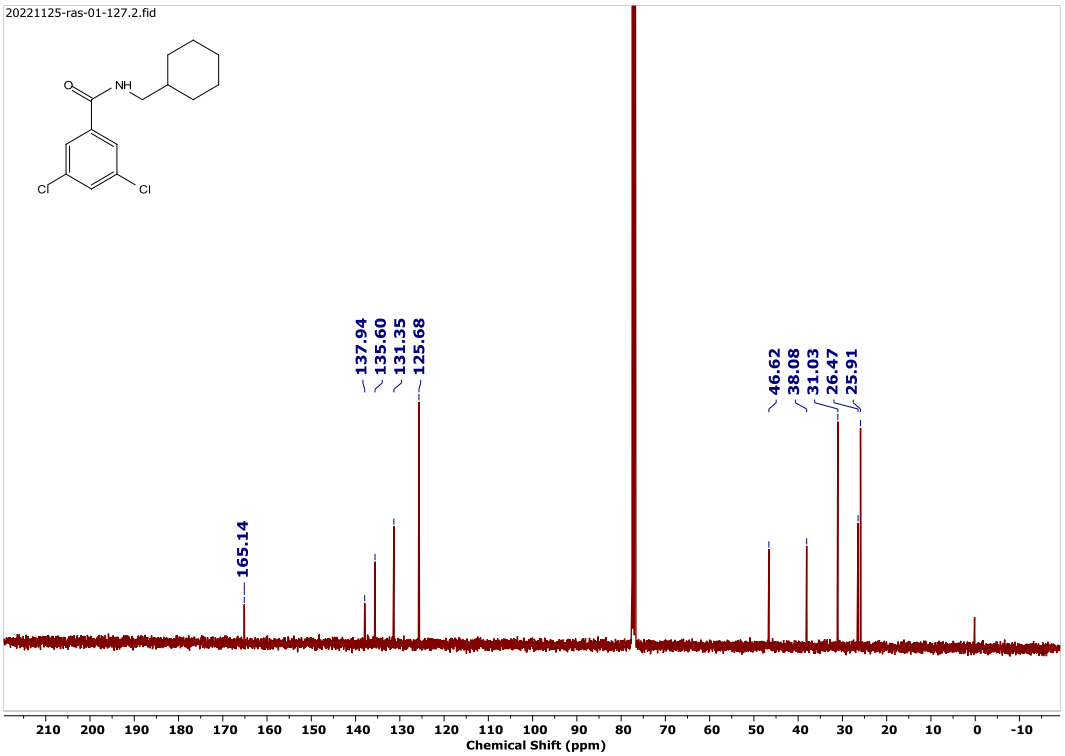

Figure 5.20. ^{13}C NMR spectrum of **1c** in $CDCl_3$.

4.5 References

1 S. Kortagere, S. Ekins and W. J. Welsh, *J. Mol. Graph. Model.*, 2008, **27**, 170–177.

2 M. Hernandes, S. M. Cavalcanti, D. R. Moreira, W. de Azevedo Junior and A. C. Leite, *Curr. Drug Targets*, 2010, **11**, 303–314.

3 Y. Lu, T. Shi, Y. Wang, H. Yang, X. Yan, X. Luo, H. Jiang and W. Zhu, *J. Med. Chem.*, 2009, **52**, 2854–2862.

4 N. Muzet, B. Guillot, C. Jelsch, E. Howardt and C. Lecomte, *Proc. Natl. Acad. Sci. U. S. A.*, 2003, **100**, 8742–8747.

5 E. I. Howard, R. Sanishvili, R. E. Cachau, A. Mitschler, B. Chevrier, P. Barth, V. Lamour, M. Van Zandt, E. Sibley, C. Bon, D. Moras, T. R. Schneider, A. Joachimiak and A. Podjarny, *Proteins Struct. Funct. Genet.*, 2004, **55**, 792–804.

6 E. Corradi, S. V. Meille, M. T. Messina, P. Metrangolo and G. Resnati, *Tetrahedron Lett.*, 1999, **40**, 7519–7523.

7 L. Brammer, A. Peuronen and T. M. Roseveare, *Acta Crystallogr. Sect. C Struct. Chem.*, 2023, **79**, 204–216.

8 C. Dalvit, C. Invernizzi and A. Vulpetti, *Chem. - A Eur. J.*, 2014, **20**, 11058–11068.

9 A. C. Legon, *Phys. Chem. Chem. Phys.*, 2014, **16**, 12415–12421.

10 G. Resnati and W. T. Pennington, *New J. Chem.*, 2018, 42, 10461–10462.

11 L. C. Gilday, S. W. Robinson, T. A. Barendt, M. J. Langton, B. R. Mullaney and P. D. Beer, *Chem. Rev.*, 2015, 115, 7118–7195.

12 J. Pancholi and P. D. Beer, *Coord. Chem. Rev.*, 2020, 416, 213281.

13 M. Erdélyi, *Chem. Soc. Rev.*, 2012, **41**, 3547–3557.

14 C. B. Aakeröy, T. K. Wijethunga and J. Desper, *J. Mol. Struct.*, 2014, **1072**, 20–27.

15 D. Cinčić, T. Friščić and W. Jones, *Chemistry*, 2008, **14**, 747–753.

16 S. Sirimulla, J. B. Bailey, R. Vegesna and M. Narayan, *J. Chem. Inf. Model.*, 2013, 53, 2781–2791.

17 H. Ungati, V. Govindaraj and G. Mugesh, *Angew. Chemie*, 2018, **130**, 9127–9131.

18 L. Mendez, G. Henriquez, S. Sirimulla and M. Narayan, *Molecules*, 2017, 22, 1397.

19 R. Wilcken, M. O. Zimmermann, A. Lange, A. C. Joerger and F. M. Boeckler, *J. Med. Chem.*, 2013, 56, 1363–1388.

20 T. Saha, A. Gautam, A. Mukherjee, M. Lahiri and P. Talukdar, *J. Am. Chem. Soc.*, 2016, **138**, 16443–16451.

21 Colchero, *Aldenderfer, Mark S., Craig, Nathan M., Speak. Robert Jeff, Popelka-Filcoff, Rachel S.*, 1997, **2**, 1–5.

22 S. P. Zheng, L. B. Huang, Z. Sun and M. Barboiu, *Angew. Chemie - Int. Ed.*, 2021, **60**, 566–597.

23 A. Mondal, J. A. Malla, H. Paithankar, S. Sharma, J. Chugh and P. Talukdar, *Org. Lett.*, 2021, **23**, 6131–6136.

24 X. Wu, L. W. Judd, E. N. W. Howe, A. M. Withecombe, V. Soto-Cerrato, H. Li, N. Busschaert, H. Valkenier, R. Pérez-Tomás, D. N. Sheppard, Y. B. Jiang, A. P. Davis and P. A. Gale, *Chem*, 2016, **1**, 127–146.

25 J. L. Sessler, L. R. Eller, W. S. Cho, S. Nicolaou, A. Aguilar, J. T. Lee, V. M. Lynch and D. J. Magda, *Angew. Chemie - Int. Ed.*, 2005, **44**, 5989–5992.

26 A. Gilles and M. Barboiu, *J. Am. Chem. Soc.*, 2016, **138**, 426–432.

27 J. Biwersi, B. Tulk and A. S. Verkman, *Anal. Biochem.*, 1994, **219**, 139–143.

28 T. Saha, M. S. Hossain, D. Saha, M. Lahiri and P. Talukdar, *J. Am. Chem. Soc.*, 2016, **138**, 7558–7567.

29 R. Sharma, A. Vijay, A. Mukherjee and P. Talukdar, *Org. Biomol. Chem.*, 2022, **20**,

2054–2058.

30 S. H. Park, S. H. Park, E. N. W. Howe, J. Y. Hyun, L. J. Chen, I. Hwang, G. Vargas-Zuñiga, N. Busschaert, P. A. Gale, J. L. Sessler and I. Shin, *Chem*, 2019, **5**, 2079–2098.

31 T. G. Johnson, A. Sadeghi-Kelishadi and M. J. Langton, *J. Am. Chem. Soc.*, 2022, **144**, 10455–10461.

32 R. Sharma, A. Vijay, S. Chattopadhayay, A. Mukherjee and P. Talukdar, *Chem. Commun.*, 2023, **59**, 3602–3605.

33 J. A. Malla, A. Roy and P. Talukdar, *Org. Lett*, 2018, **20**, 5991–5994.

34 A. Roy, A. Gautam, J. A. Malla, S. Sarkar, A. Mukherjee and P. Talukdar, *Chem. Commun.*, 2018, **54**, 2024–2027.

35 T. Saha, A. Gautam, A. Mukherjee, M. Lahiri and P. Talukdar, *J. Am. Chem. Soc.*, 2016, **138**, 16443–16451.

36 Hille, B.Ion Channels of Excitable Membranes, 3rd ed.; Sinauer Associates: Sunderland, MA, 2001.

37 S. Li, C. N. Moorefield, C. D. Shreiner, P. Wang, R. Sarkar and G. R. Newkome, *New J. Chem.*, 2011, **35**, 2130–2135.

38 A. Endres and G. Maas, *Tetrahedron*, 2002, **58**, 3999–4005.

39 SAINT Plus, (Version 7.03); Bruker AXS Inc.: Madison, WI, 2004.

40 G. M. Sheldrick, SHELXTL, Reference Manual: version 5.1: Bruker AXS; Madison, WI, 1997.

41 G. M. Sheldrick, Acta Crystallogr. Sect. A, 2008, 112.

42 WINGX version 1.80.05 Louis Farrugia, University of Glasgow.

43 A. L. Spek, A PLATON, Multipurpose Crystallographic Tool, Utrecht University, Utrecht, The Netherlands, 2005.

44 S. Schrödinger Release 2022–1: Maestro, LLC, NewYork, NY, **2021**.

45 J. B. Klauda, *J. Chem. Phys.* 2018, **149**, 220901.

46 S. Jo, J. B. Lim, J. B. Klauda, W. Im, *Biophys. J.* 2009, **97**, 50–58.

47 S. Jo, T. Kim, V. G. Iyer, W. Im, *J. Comput. Chem.* 2008, **29**, 1859–1865.

48 G. M. Torrie, J. P. Valleau, *J. Comput. Phys.* 1977, **23**, 187–199.

Overall Conclusion

The primary objective of my doctoral research was to elucidate the fundamental principles underlying ion channel formation through non-covalent interactions and to investigate their anion selectivity within the lipid bilayer. In summary, the research findings support the intended aim of the study. The present studies focus on elucidating the fundamental principles underlying the self-assembly behavior of low-molecular-weight compounds that exhibit the ability to form transmembrane ion channels and facilitate ion transport through the utilization of hydrogen and halogen bonding interactions. The focus of the thesis pertains to the development, chemical production, and analysis of a biomimetic synthetic ion channel. The induction of chloride-mediated apoptosis within cancer cells is a well-established phenomenon that is attributed to the transportation of chloride ions. Nevertheless, conventional transporters exhibit a deficiency in selectivity, which can result in harm to both healthy tissues and malignant cells. The augmentation of ion transport across the bilayer membrane can be achieved by modifying the self-assembly of the individual monomeric units to involve multiple ion binding sites. In addition, the selectivity of ions can be altered by incorporating multiple ion-binding sites and influencing the mechanism of ion transport mediation.

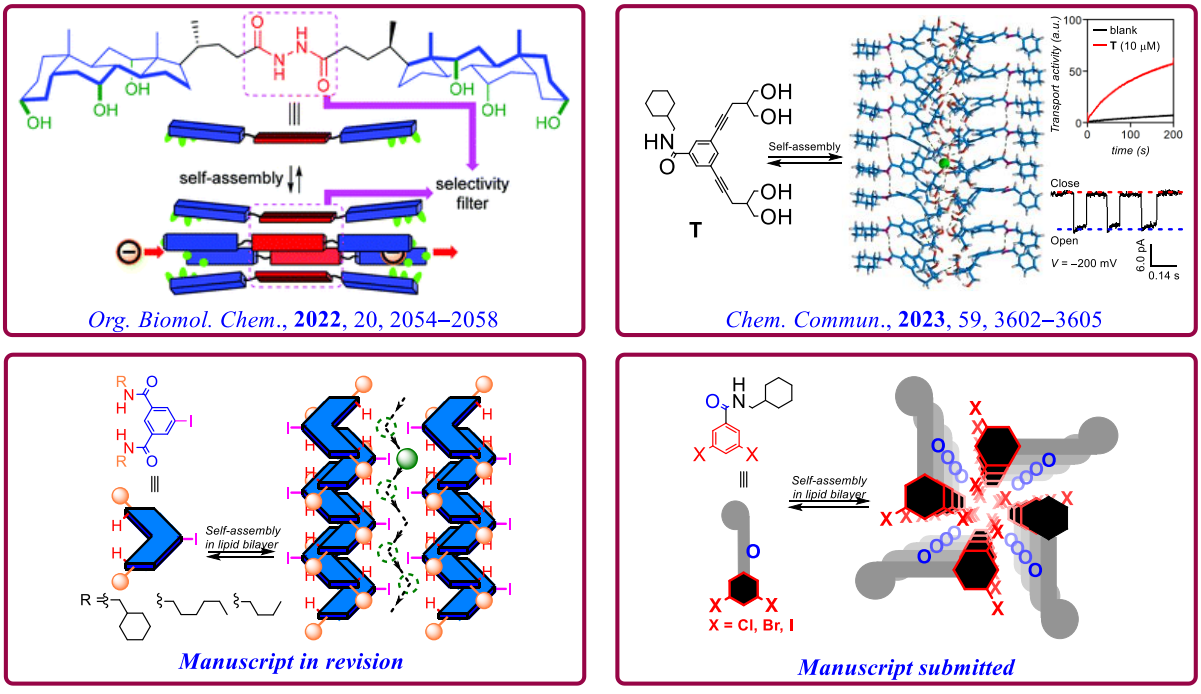

Figure: Schematic illustration of chloride selective ion channels discussed in the thesis.

Research Publications

1. Bis(cholyl)-based chloride channels with oxalamide and hydrazide selectivity filters.
R. Sharma, A. Vijay, A. Mukherjee* and P. Talukdar*.
Org. Biomol. Chem., **2022,** *20,* 2054–2058.

2. Self-assembled anion channel formation by bis(1,3-propanediol)-linked meta-dipropynylbenzene-based small molecules.
R. Sharma, A. Vijay, S. Chattopadhayay, A. Mukherjee* and P. Talukdar*.
Chem. Commun., **2023**, 59, 3602–3605.

3. Halogen bond-driven artificial Cl^- selective channel constructed from 5-iodoisophthalamide-based molecules.
R. Sharma, S. Sarkar, S. Chattopadhayay, J. Mondal* and P. Talukdar*.
Manuscript in revision (Angew. Chem.Int. Ed.).

4. Transmembrane Cl^- selective channel by meta directed halogen bond donors.
R. Sharma, S. Sarkar, S. Chattopadhayay, J. Mondal* and P. Talukdar*.
Manuscript submitted.

5. Supramolecular Barrel-Rosette Ion Channel Based on 3,5-Diaminobenzoic Acid for Cation-Anion Symport. Sandip Chattopadhayay, Anupam Ghosh, Titas Kumar Mukhopadhyay, Rashmi Sharma, Ayan Datta,* Pinaki Talukdar.
S. Chattopadhayay, A. Ghosh, T. K. Mukhopadhyay, **R. Sharma**, A. Datta*, P. Talukdar*
Angew. Chem. Int. Ed., ***2023****,* 62, e2023137.